Experimental and Numerical Investigations of Wettability of Positive Electrodes for Li−O_2 Batteries

By

Fangzhou Wang

2019

Submitted to the graduate degree program in Mechanical Engineering and the Graduate Faculty of the University of Kansas in partial fulfillment of the requirements for the degree of Doctor of Philosophy.

Chair: Assistant Professor **Xianglin Li**
Dept. of Mechanical Engineering, University of Kansas

Professor **Trung Van Nguyen**
Dept. of Chemical & Petroleum Engineering, University of Kansas

---

Professor **Ronald Dougherty**
Dept. of Mechanical Engineering, University of Kansas

Associate Professor **Christopher Depcik**
Dept. of Mechanical Engineering, University of Kansas

Assistant Professor **Lin Liu**
Dept. of Mechanical Engineering, University of Kansas

Date Defended: 24 April 2019

The dissertation committee for Fangzhou Wang certifies that this is the approved version of the following dissertation:

Experimental and Numerical Investigations of Wettability of Positive Electrodes for Li−O_2 Batteries

Chair: Assistant Professor **Xianglin Li**

Dept. of Mechanical Engineering, University of Kansas

Date Approved: 26 April 2019

Abstract

The objective of this dissertation is to characterize the positive electrode wettability and its effects on the performance (e.g., discharge capacity) of Li−O_2 batteries. The investigations include an experimental study of discharging electrodes with various wettabilities, proposing and examining the intermittent discharge strategy, and the numerical simulation of the distribution of the electrolyte at various saturations and of the discharge performance of Li−O_2 batteries at the pore scale. Future work will measure the structure of positive electrodes using advanced imaging technology such as transmission X-ray microscopy.

First, I fabricated the electrodes and adjusted their wettability by mixing acetylene black carbon particles with various binders. The wettability was quantitatively characterized by the contact angle and ionic resistance. The customized electrodes were then discharged in Li−O_2 batteries at 0.1 mA/cm^2 through which the relationship between electrode wettability and discharge capacity was obtained. The discharge capacity of the electrode with 15% PVDF (36.5°) binder was 1665.8 mAh/g while the customized electrode with 15% PTFE (128.4°) binder had a discharge capacity of 4160.8 mAh/g. The effects of lyophobicity on O_2 transfer in the porous electrode have been proved. A positive electrode with mixed wettability was designed and tested, which acquired the highest specific discharge capacity of 5149.5 mAh/g. The structure of this electrode included two lyophobic carbon coatings on top and bottom and one lyophilic carbon coating in the middle. Further design may focus on appropriately configuring the wettability to balance the gas paths for O_2 diffusion and wetted area for reaction sites.

A novel strategy for discharging Li−O_2 batteries was then proposed and identified. The battery was periodically discharged and rested, which can enhance O_2 availability and increase the discharge capacity. Periodically resting the battery increased the specific discharge capacity

by at least 50% at various current densities (0.1 - 1.5 mA/cm^2). Afterward, the investigation combined the electrode wettability and the intermittent strategy. Compared with the continuous strategy, the capacity of lyophobic electrodes increased by over 100% when the intermittent strategy was applied. Besides, a multi-step discharge strategy can provide greater capacity when the battery is discharged at decreasing current rates (2.0, 1.5, and 1.0 mA/cm^2). The importance of O_2 diffusion is emphasized and provide practical strategies are proposed to improve the deep discharge capacity of Li-O_2 batteries, especially at high current rates (> 1.0 mA/cm^2).

Finally, a numerical study was conducted to investigate the electrode with different saturations of the electrolyte. The effects of electrolyte saturation levels and the distribution of electrolyte have been demonstrated by comparing the corresponding discharge performance of Li-O_2 batteries. It was found that fully saturated electrodes (100% saturation) have high oxygen transfer resistance, which will result in the lowest discharge capacity of 7.41 Ah/g. On the contrary, over-dried battery (with < 50% saturations) electrodes have poor electrochemical performance since dry pores are inactive for electrochemical reactions. Carefully designed electrodes with a mixture of hydrophilic and hydrophobic pores could achieve a discharge capacity (> 7 Ah/g) at high current (20 A/m^2) similar to hydrophilic electrodes which are fully saturated by the electrolyte at low current (1 A/m^2). The modeling study found that designing the electrode with a mixture of lyophilic and lyophobic pores is critical to significantly increasing (by orders of magnitude) the operating current and power of the Li–O_2 battery. In the future, plans are to characterize the geometry of the positive electrode using the imaging techniques (e.g., transmission X-ray microscopy) and gas sorption method. Based on the characterization of the porous structure, the relationship between the porous structure and the mass transport phenomena will be clarified.

Acknowledgments

I gratefully acknowledge the Startup Fund from KU Mechanical Engineering Department, KU New Faculty General Research Fund, KU General Research Fund, as well as National Science Foundation (EPSCoR Research Infrastructure #1833048) for funding my research endeavors. The work was performed at the Department of Mechanical Engineering, at the University of Kansas from August 2015 to May 2019 under the supervision of the main supervisor Professor Xianglin Li.

First and foremost, I would like to thank my adviser, Dr. Xianglin Li, for empowering me as a researcher, guiding me over the research and nurturing my researching intuition. Our detailed weekly meeting and discussions are invaluable to my understanding of the work. Your careful revisions of publications have substantially improved my writing. I am also thankful for other committee members, Professors Christopher Depcik, Ronald L. Dougherty, and Lin Liu of the Department of Mechanical Engineering and Professor Trung Van Nguyen of the Department of Chemical & Petroleum Engineering.

I would like to thank many collaborators who have shared their time, equipment, and ideas with me the last few years, especially Dr. Qiang (Charles) Ye (KU Institute for Bioengineering Research Laboratories), Ms. Heather Shinogle (KU Microscopy and Analytical Imaging Laboratory), Dr. Vincent de Andrade (Argonne National Laboratory), and Charles Gabel (KU Machine Shop).

I am grateful for my colleagues in the Lab. Thank you Farhad Mohazabrad, Ning Tian, Pengjian Guan and Derek Barnes for your partnership, and for helpful research discussions. Thank you to all of the labmates and visiting scholars who provided friendship over the years.

To my Master's degree adviser, Dr. Fengwu Bai, thank you for always encouraging me and equipping me with the basis of energy storage research. I thank Dr. Chao Xu and Dr. Xin Li for your recommendation when I applied for the Ph.D. position at the University of Kansas.

I express my thanks to Dr. Jianyu Tan and Dr. Xiaowen Hao for your mentoring during my undergraduate. I would not have pursued a master's and then a doctorate if you were not introducing me to the researching field of energy storage. I also thank Ms. Xiaojie Li for her English teaching that contributes to my study abroad.

I want to thank my friends, especially Benyi Xu, Shuai Liu, Ke Chen, Panying Yu, Frank Hua, Mei Feng, Limiao Wang, Xiangtian Tao, Crystal Shi, Jessica Won, Wen Du, Guangrui Zu, Qing Li, Zhi Li, and Mengran Xu, for your love and support. I am also thankful for the friends from Sina Microblog. Their nicknames are Masuoyuwei and Kay.

I would like to express my appreciation to my parents and other family members, who have always been deeply supporting me.

Lastly, and most importantly, thank you Yanjie Li for your smile, support, and love.

Research Publications

This dissertation is mainly based on my first-authored journal articles (**P1 – P5**). I also made contributions to the other peer-reviewed journal articles (**P6 – P9**) during my PhD study.

P1: Fangzhou Wang, and Xianglin Li. Effects of the electrode wettability on the deep discharge capacity of Li–O_2 batteries. *ACS Omega* 3.6 (2018): 6006-6012.

This study aims at (i) fabricating electrodes with different wettability and characterizing their wettability; (ii) obtaining the relationship between electrode wettability (e.g., lyophobicity, and lyophilicity) and the discharge capacity; (iii) demonstrating that lyophobic electrodes (contact angle > 90°) can enhance O_2 diffusion; (iv) designing novel electrodes with mixed wettability. Dr. Li and I conceived the original idea, and I designed the experiment. In addition, my contributions include conducting all of the experiments, analyzing data, as well as preparing the manuscript.

P2: Fangzhou Wang, and Xianglin Li. Discharge Li-O_2 batteries with intermittent current. *Journal of Power Sources* 394 (2018): 50-56.

In this work, an innovative discharging strategy (e.g., discharging for 5 min, resting for 10 min) is proposed that discharges and rests the battery periodically. The experimental work includes: (i) investigating the effects of this new strategy by comparing the discharge capacity obtained from intermittent and continuous strategies; (ii) increasing the discharge capacity using a multistep strategy at decreasing current rates (2.0, 1.5, and 1.0 mA/cm^2); (iii) conducting a joint research of the electrode wettability and the intermittent strategy; (iv) customizing the intermittent strategy to both save discharging time and obtain a high capacity; (v) identifying

effects of the intermittent strategy on the cycling performance. Dr. Li and I developed the idea of periodically discharging batteries. My contributions consist of planning and carrying out all of the experiments, analyzing data, and writing the manuscript.

P3: Fangzhou Wang, and Xianglin Li. Pore-scale simulations of porous electrodes of Li–O_2 batteries at different saturation levels. *ACS Applied Materials & Interfaces* 10.31 (2018): 26222-26232.

A numerical model is utilized to simulate the electrochemical process in the positive electrode of Li−O_2 batteries. The numerical study consists of (i) reconstructing a 3-D geometry of the electrode; (ii) comparing the discharge performance of electrodes with different saturations (100%, 87.5%, 75%, and 50%); (iii) proving the feasibility of discharging a battery at a higher current rate (20 A/m^2); (iv) providing a valuable reference for electrode design. Dr. Li developed the theoretical model, and performed the simulation. Dr. Li and I contributed to preparing the manuscript. My contributions also include experimentally obtaining the scanning electron microscopy (SEM) images, deriving the correlation functions for the reconstruction, and reviewing the manuscript.

P4: Fangzhou Wang, and Xianglin Li. The stagnant thermal conductivity of porous media predicted by the random walk theory. *International Journal of Heat and Mass Transfer* 107 (2017): 520-533.

This numerical study provides a predictive tool to calculate the stagnant thermal conductivity of porous materials considering detailed pore geometries. The imaging technique of micro-CT and the method of random walk theory are utilized in this simulation. The model

proposed in this study can simulate porous media with a wide range of porosities and geometries. Dr. Li and I developed this idea and performed the computational work. I prepared a portion of this manuscript. Moreover, my contributions focus on using the micro-CT to obtain the geometry and providing the experimental data for model calibration.

P5: Fangzhou Wang, P. K. Kahol, Ram Gupta, Xianglin Li. Experimental studies of carbon electrodes with various surface area for Li−O_2 batteries. *ASME Journal of Electrochemical Energy Conversion and* Storage. (2019): 1-16.

This work gives results of a systematically study of the influence of surface area on Li−O_2 batteries. Both commercial carbon and recycled carbon material are investigated after comparing their discharge performance. The imaging technique and gas sorption method are employed to characterize materials with different surface areas. Dr. Li and I developed the original idea of this study. I contribute to preparing for electrodes, conducting experiments, analyzing data, and writing manuscript.

P6: Farhad Mohazabrad, **Fangzhou Wang**, and Xianglin Li. Experimental studies of Salt concentration in electrolyte on the performance of Li-O_2 batteries at various current densities. *Journal of the Electrochemical Society* 163.13 (2016): A2623-A2627.

This experimental study investigates the effects of the electrolyte concentration on the electrochemical performance of Li−O_2 batteries at various current densities. After adding electrolytes with different concentrations, the initial discharge capacity and the first discharge-charge cycle of Li−O_2 batteries are compared and analyzed. An appropriate electrolyte concentration needs to balance the ionic conductivity and viscosity, which results in a decent

performance. Farhad setup the experiments, initially started the experiments, and contributed to the draft manuscript. My contributions include continuing collecting and analyzing data as well as preparing the manuscript.

P7: Farhad Mohazabrad, **Fangzhou Wang**, and Xianglin Li. Influence of the oxygen electrode open ratio and electrolyte evaporation on the performance of Li–O_2 batteries. *ACS Applied Materials & Interfaces* 9 (18) (2017): 15459-15469.

This paper consists of both an experimental study and a simulation of Li–O_2 batteries. The positive electrodes with various open ratios are investigated by discharging Li–O_2 batteries at different current densities. The model is developed to simulate the electrolyte evaporation and its effects on the discharge capacity of batteries. Farhad has setup the experiment, carried out the model simulations, and contributed to the draft manuscript. My contributions are composed of improving the experimental setup, continuing collecting and analyzing data as well as preparing the manuscript.

P8: Camila Zequine, **Fangzhou Wang**, Xianglin Li, Deepa Guragain, S. R. Mishra, K. Siam, P. K. Kahol, and Ram K. Gupta. nanosheets of $CuCo_2O_4$ as a high-performance electrocatalyst in urea oxidation. *Applied Sciences.* 9 (4) (2019): 793.

P9: Camila Zequine, Sanket Bhoyate, **Fangzhou Wang**, Xianglin Li, Khamis Siam, P. K. Kahol, and Ram K. Gupta. Effect of solvent for tailoring the nanomorphology of multinary $CuCo_2S_4$ for overall water splitting and energy storage. *Journal of Alloys and Compounds* 784 (2019): 1-7.

Papers P8 and P9 are the resulting publications of the collaborative work between our lab and the research group of KSU. I mainly complete the imaging characterization of materials analyzed in those two papers.

Table of Contents

List of Figures

List of Tables

List of Abbreviations and Symbols

2D	Two dimensional
3D	Three dimensional
BET	Brunauer, Emmet, and Teller
BJH	Barrett, Joyner, and Halenda
CV	Cyclic voltammetry
DFT	Density function theory
DME	Dimethoxyethane
DSMO	Dimethyl sulfoxide
EC	Ethylene carbonate
EIS	Electrochemical impedance spectroscopy
EV	Electric vehicle
FIB-SEM	Focused ion beam scanning electron microscopy
$LiPF_6$	Lithium hexafluorophosphate
LiTFSI	Lithium bis(trifluoromethanesulfonyl)imide
Micro-CT	Micro computed tomography
MOF	Metal organic framework
PC	Propylene carbonate
PTFE	Polytetrafluoroethylene
PVDF	Polyvinylidene fluoride
SEM	Scanning electron microscope
TEGDME	Tetraethylene glycol dimethyl ether
TXM	Transmission X-ray microscopy

A_{active}	Active area of electrode per volume (m^2/m^3)
A_{ED}	Total specific surface area (m^2/m^3)
A_{sl}	Wetted pore surface (m^2)
C	Double layer capacitance (μF)
d	Double layer thickness (μm)
$D_{\text{Li+,EL}}$	Diffusivity of lithium ion in the electrolyte (m^2/s)
$D_{\text{O2,EL}}$	Diffusivity of oxygen in the electrolyte (m^2/s)
$D_{\text{Li+}}^{\text{eff}}$	Effective Diffusivity of lithium ion (m^2/s)
$D_{\text{O2}}^{\text{eff}}$	Diffusivity of oxygen (m^2/s)
E^0	Thermodynamic equilibrium voltage (VDC)
ΔE	Energy difference of two correlation functions
F	Faraday constant (A/mol)
$F(x)$	Distribution of each phase
i_0	Exchange current density (A/m^2)
i_{EL}	Current density in the electrolyte (A/m^2)
I	Discharge Current (A/cm^2)
k_{ORR}	Reaction constant
$\dot{m}_{\text{Li+}}$	Consumption rate of lithium ion (g/s)
$\dot{m}_{\text{O2}}$	Consumption rate of lithium ion (g/s)
$M_{\text{Li+}}$	Molecular weight of lithium ion (g/mol)
M_{O2}	Molecular weight of oxygen (g/mol)
p	Criterion to switch two points
q	Specific discharged electricity (C/m^2)

R_1	Ohmic resistance (Ω)
R_2	Charge transfer resistance (Ω)
R_3	Mass transfer resistance (Ω)
R_{ORR}	Reaction rate of the oxygen reduction reaction (mol/m^3/s)
S_2	Probability of two randomly points
S	Specific surface of a 3D medium (m^3)
S_{total}	Total specific surface area (m^2/g$_{carbon}$)
$S_{micro}{}^a$	Micro specific surface area (m^2/g$_{carbon}$)
$S_{external}{}^b$	External specific surface area (m^2/g$_{carbon}$)
t_+	Transference number of lithium ion
V	Battery voltage (VDC)
V_{ED}	Total specific volume (m^3/g)
V_{total}	Total specific volume (m^3/g$_{carbon}$)
V_{micro}	Micro specific volume (m^3/g$_{carbon}$)
W_4	Warburg impedance (Ω)
α	Transfer coefficient
ε	Porosity
ε_r	Relative permittivity of electrolyte
ε_0	Permittivity of the vacuum (F/m)
η	Over-potential (VDC)
θ_c	Contact angle (°)
ρ_C	Density of carbon (g/cm^3)
ρ_{Li2O2}	Density of lithium peroxide (g/cm^3)

ρ_{EL}	Density of the electrolyte (g/cm^3)
σ_{ED}	Conductivity of the electrode (S/cm)
σ_{ED}^{eff}	Effective conductivity of the electrode (S/cm)
σ_{EL}	Conductivity of electrolyte (S/cm)
σ_{Li2O2}	Conductivity of Li_2O_2 (S/cm)
x_{EL}	Fraction of wetted surface
ω_{Li+}	Concentration of lithium ion (kg/kg)
$\omega_{Li+,\ ref}$	Reference concentration of lithium ion (kg/kg)
ω_{O2}	Concentration of O_2 (kg/kg)
$\omega_{O2,\ ref}$	Reference concentration of O_2 (kg/kg)

Chapter 1: Introduction

1.1 Background

The current growth of the economy and population results in an increasing consumption of fossil fuels for personal transportation. The electric vehicle (EV) has been playing an important role in mobility in recent years [1]. Even though the usage of EV is more popular, driving range anxiety is a major obstacle for the development of EVs. Li-ion batteries have been widely applied to power EVs. Li-ion batteries utilize an intercalated lithium compound as the positive electrode. Thus, the energy density (e.g. energy per mass) is given by the storage capacity of lithium. However, the current Li-ion batteries cannot fully satisfy the EVs since its energy density is limited by the intercalation chemistry [2-3]. This can be one of the most crucial driving-force for innovative battery technologies. Nowadays, advanced battery technologies are being continuously developed [4-9]. Rechargeable batteries with a higher energy density and lower cost are the main targets of current research. The Li−O_2 battery is one of the candidates that are promising to offer solutions for improvements in the energy density of batteries.

The Li−O_2 battery is similar to the Li-air battery under the assumption that oxygen is taken from the ambient atmosphere. Since the CO_2 and H_2O from the atmosphere can contaminate the battery by reacting with active materials [10], a rechargeable Li-air battery has not been realized by the current time. Most of the investigations of Li−O_2 batteries have so far been conducted in the pure O_2 atmosphere [11-12]. As a result, the term of Li−O_2 battery is presented throughout this dissertation. Typically, four types of Li−O_2 batteries have been categorized based on the electrolytes utilized in them [8, 13-14]. The all-solid-state Li−O_2 battery is troubled with a low ionic conductivity of the electrolyte [9, 15-16]. The energy density of aqueous Li−O_2 battery is limited by the solubility of discharge products and the weight of the

negative electrode protection membrane [17-19]. This also negatively affects the hybrid aqueous/aprotic Li−O_2 battery. Therefore, the study has mainly focused on the aprotic Li−O_2 battery in this dissertation.

The rechargeable aprotic Li−O_2 battery was originally demonstrated and reported by Abraham and Jiang [20]. Basically, the current aprotic Li−O_2 battery consists of a lithium negative electrode, an aprotic electrolyte dissolving with a lithium salt and a porous carbon positive electrode soaked by the electrolyte, which is shown in Figure 1. When the Li−O_2 battery is discharged, the Li metal is oxidized at the negative electrode to generate Li^+ that transfers through the electrolyte and reaches the porous positive electrode. The Li^+ reacts with O_2 from the atmosphere or gas channels and generates Li_2O_2 at the positive electrode. The charging process is performed via the decomposition of Li_2O_2. The Li metal is deposited on the negative electrode and the O_2 is released at the positive electrode. The specific energy of a Li−O_2 battery is estimated to be 3330 Wh/kg on the basis of 1 kg active material of Li_2O_2. The discharging and charging processes are represented by the following reactions. Therefore, the ideal overall reaction is depicted in reaction 1.3 and the reversible cell voltage is 2.96 VDC [21].

$$Negative: \mathrm{Li} \underset{\text{Charge}}{\overset{\text{Discharge}}{\rightleftharpoons}} \mathrm{Li^+} + \mathrm{e^-} \tag{1.1}$$

$$Positive: \mathrm{O_2} + 2\mathrm{e^-} + 2\mathrm{Li^+} \underset{\text{Charge}}{\overset{\text{Discharge}}{\rightleftharpoons}} \mathrm{Li_2O_2\ (s)} \tag{1.2}$$

$$Overall: 2\mathrm{Li} + \mathrm{O_2} \underset{\text{Charge}}{\overset{\text{Discharge}}{\rightleftharpoons}} \mathrm{Li_2O_2\ (s)} \tag{1.3}$$

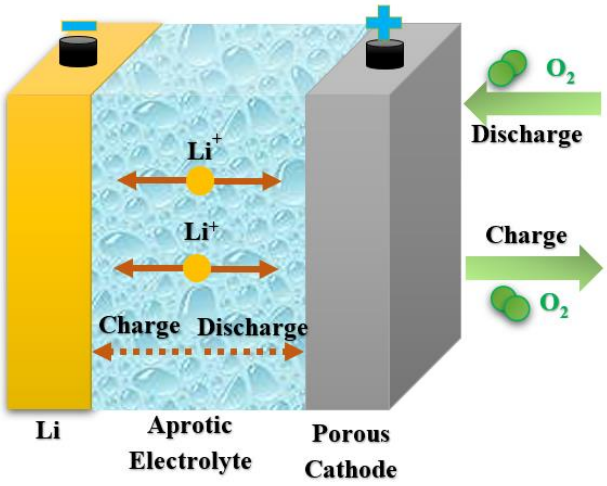

Figure 1: The schematic of an aprotic Li−O_2 battery.

1.2 Challenges

Recently, researchers have made numerous achievements to further develop Li−O_2 technology. For example, various aprotic electrolyte solvents and positive electrode materials for Li−O_2 batteries have been found to meet the required electrochemistry of both discharging and charging processes [22-26]. However, several unresolved fundamental issues are hindering the realization of Li−O_2 batteries, which have been summarized in Figure 2. Several studies have demonstrated that Li negative electrode can react with aprotic electrolytes, which reduces the capacity and cycling life of Li−O_2 batteries [9, 27-28]. Moreover, Li dendrites forming during the discharging and charging processes can penetrate the separator and cause a short circuit. This may threaten battery safety and degrade its performance [29-30]. The electrolytes play a significant role in aprotic Li−O_2 batteries and should have two main functions in mass transfer: (i) transport the Li^+ from the negative electrode to the positive electrode for the oxygen reduction reaction (ORR); (ii) dissolve the O_2 and then transport it to the reaction sites to participate the

ORR. The stability of aprotic electrolytes is a major concern in developing Li−O_2 batteries. For example, propylene carbonate (PC) was once considered a promising carbonate-based electrolyte since it had the advantages of low volatility and good capability of Li^+ transport [31-32]. Unfortunately, PC has been found to be unstable because it is decomposed by Li_2O_2 [33] and the observation of Li_2CO_3 as the main product after discharge directly has been proved [34]. Even though dimethyl sulfoxide (DMSO) leads to a solution mechanism of the discharge process and increase the discharge capacity [35], the formation of LiOH is caused by the reaction between DMSO and Li_2O_2 [36]. The discharge product of Li_2O_2 is a wide-bandgap insulator and forms as a conformal film at the positive electrode due to its insolubility in aprotic electrolytes. Researchers have confirmed that the exchange current density falls rapidly and then the battery suffers from a "sudden death" when the Li_2O_2 film grows to ~5 nm [37-38]. In other words, the accumulation of Li_2O_2 passivates the positive electrode and shortens the discharging process. Besides, less effective transportation of O_2 and Li^+ limits the performance of Li−O_2 batteries, which is associated with lower solubility and diffusivity of O_2 and Li^+ in aprotic electrolytes and an inappropriately-structured porous carbon electrode.

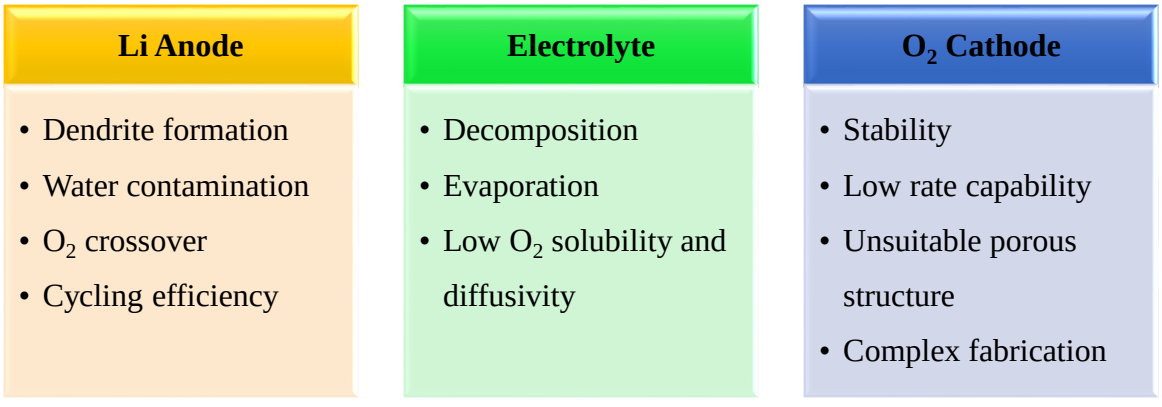

Figure 2: Critical challenges facing Li−O_2 batteries.

These fundamental challenges regarding three major components, especially at the positive electrode, hinder the development of Li−O_2 technology. As a results, the high-energy-

density, stably-operated Li−O_2 batteries may not be realized without overcoming those limitations. It is necessary to address those challenges on both theoretical and engineering aspects, significantly motivating this study. Therefore, this study concerns a need for positive electrode configuration and engineering to achieve a high-capacity Li−O_2 battery at high current density.

1.3 Electrode Surface Area

Studies targeting to improve the practical energy density of Li−O_2 batteries typically tackle with the positive electrode. The electrode serves as a reservoir to accommodate insoluble discharge products (i.e., Li_2O_2) [39]. Previously, it assumed that pore-clogging can be the main factor resulting in the "cell death" in the Li−O_2 battery [40]. The porous electrode cannot provide enough space to accommodate the discharge product so that the discharge capacity of the Li−O_2 battery is limited. However, several studies [41-42] showed that the passive layer of discharge products was regarded as the main factor to determine the discharge capacity of the Li−O_2 battery. In our previous study [43], the discharged electrodes were measured by the scanning electron microscope (SEM). Results showed that the discharge current affected the morphology of the main discharge product (Li_2O_2). At low current, the needle-like particles were detected while the film-like discharge products were deposited at high current on the electrode surface. In addition, the positive electrode derived from metal organic frameworks (MOFs) can also increase the capacity of discharge and stabilize the Li−O_2 battery discharge voltage plateau due to hierarchical mesoporous nanocomposites [44-45]. Hence, it is worthwhile to pay more attention to the structure of the porous electrode.

All the above research suggests that the Li−O_2 battery's discharge capacity is proportional to active carbon surface of the porous electrode. Access to the electrolyte and O_2 should be

possible for the active carbon surface referring to the reaction sites. Overall, the capacity for discharge should increase as the specific area of the active surface increases. However, in the porous electrode, only a few studies focus on the influence of the specific surface area [40, 46-47]. Meini et al. [46] investigated the effect of the specific surface area of carbon (e.g. Vulcan XC 72, BP2000 and KB600) on both the first discharge capacity and the Li−O_2 battery cycling performance. All electrodes had similar surface-standardized discharge capacities and the passivating Li_2O_2 layer was deposited on the carbon surface. Besides, other studies found that the discharge capacity increased with the total volume of mesopores [47] and was proportional to the average pore diameter [48]. However, the above studies did not investigate the carbon electrode with mixed type of carbons. Zhang et al.[49] paid attention to the use of mixed carbon materials. It was found that the carbon mixture of KB600 and Super P could increase the discharge capacity by enhancing the O_2 mass transport.

In Paper **P5**, electrodes were fabricated from different carbons, including both commercial carbon blacks (i.e., acetylene black, Super P, and Vulcan XC 72) and carbon materials activated from recycled tea leaves. Li−O_2 batteries with electrodes coated by those carbons were discharged at 0.5 mA/cm^2 to examine the effect of specific surface area on the discharge capacity. Porous structures of all electrodes were characterized by the N_2 adsorption/desorption technique. A summary of the structural properties of different carbon materials is shown in both Table 1. The type IV isotherms are observed clearly for the acetylene black and Super P in N_2 adsorption/desorption measurement, which indicates mesoporous structures in corresponding electrodes. The total specific surface area of ~70 m^2/g mainly results from mesopores. Isotherms of other carbon samples have the characteristics of both type I and type IV, indicating that both the micropores and mesopores exist in samples. For example,

activated tea leaves have an extremely high specific surface area of 2868.4 m^2/g which is confirmed by the previous study [50]. The high specific surface area is due to the large proportion of micropores. The microporous specific surface area of the tea carbon is 2091.1 m^2/g. The specific volume of the pores generally shows similar trends to those shown in the specific area of the surface. Because of the lack of micro pores, the specific volume of acetylene black and Super P carbon is zero. In contrast, Vulcan XC 72 contains micro pores and activated tea leaves. When the mass fraction of micro pores increases, it will attribute more specific volume of pore to specific volumes of micro pore.

Table 1: The specific surface area and pore volume of different carbon samples.

Sample	S_{total} (m^2/g_c)	S_{micro}[a] (m^2/g_c)	$S_{external}$[b] (m^2/g_c)	V_{total} (cc/g)	V_{micro}[c] (cc/g)
Acetylene black	76.5	0	76.5	0.25	0
Super P	60.9	0	60.9	0.16	0
Vulcan XC 72	264.1	97.5	166.6	0.43	0.05
Activated Tea leaves	2868.4	2091.1	777.3	1.16	1.03

$Li-O_2$ batteries with electrodes made from commercial carbons are firstly discharged at a very high current density of 0.5 mA/cm^2. Despite the fact that the Vulcan XC 72 has the largest specific surface area, three commercial carbons achieve similar discharge capacities of 2.50 Ah/g shown in Figure 3. The previous studies suggest that the carbon electrode with higher mesoporous volume can enhance the discharge capacity [51-52]. The volume of micropores has no significant impact on the capacity of discharge because the micropores cannot accommodate discharge products such as Li_2O_2. Even the specific mesoporous surface area of Vulcan XC 72 is 166.6 m^2/g, the volume of the mesopore was not fully utilized. The electrode surface of mesopores can be active only when it is accessible to O_2 and electrolyte. It is speculated that the micropores may block the effective use of the mesopores. While numerous efforts have been

made to optimize the structure of positive electrodes, it is also important to reduce costs and use more natural materials to develop Li−O_2 batteries. Carbon materials such as carbon nanotubes and graphene can achieve decent discharge capacity, but the high cost has negative effects on the Li−O_2 battery marketing [24, 53]. Positive electrodes made from natural wood have been utilized in Li−O_2 batteries[54-55]. As far as reported, the electrode made from activated tea leaves is firstly used in Li−O_2 batteries though tea leaves have been widely employed to fabricate supercapacitor electrodes [50, 56]. However, results prove that larger specific surface area cannot help to achieve higher discharge capacity because micropores are unable to accommodate Li_2O_2 and the active surface area are not effectively used. Moreover, it is much difficult to exactly measure the porous structure of the activated tea leaves with a high surface area. Therefore, I paid more attention to enhancing the mass transport of O_2 in positive electrode in this dissertation.

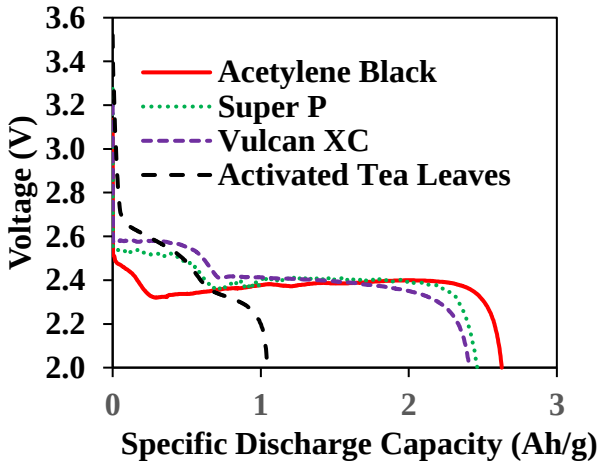

Figure 3: Discharge curves of Li−O_2 batteries with activated tea leaves electrodes and commercial carbon electrodes at 0.5 mA/cm^2.

1.4 Scope of the Dissertation

This dissertation aims to investigate mass transfer in the positive electrode by analyzing the effects of electrode wettability on the performance of Li−O_2 batteries. It details both the experimental study of examining positive electrodes with various wettability and engineering discharge strategies and the numerical study of clarifying the relationship between electrolyte saturation levels and discharge capacity of Li−O_2 batteries.

Firstly, the performance of Li−O_2 batteries with electrodes of various wettability is investigated in Paper **P1**. Mixing commercial carbon powders with various binders alters the wettability of electrodes. To characterize the different wettability of electrodes, the static contact angles between the electrode surface and non-aqueous electrolytes, the ionic resistance, and the double layer capacitance are measured, respectively. Once the wettability is characterized, the deep discharge capacity of all electrodes is obtained and compared. Those results are used to analyze the effects of electrode wettability on the deep discharge capacity of Li−O_2 batteries.

Secondly, innovative strategies of discharging Li−O_2 batteries are put forward in Paper **P2**, following the previous investigation of electrode wettability. Discharging and resting Li−O_2 batteries is applied to improve the oxygen transfer and utilize more active surface within the porous electrode. The performance of Li−O_2 batteries has been proven to be enhanced using the intermittent strategy at various current densities. Furthermore, I perform experiments to interpret the coupled effects of electrode wettability and intermittent discharging strategy. The results emphasize the importance of O_2 diffusion and provide practical strategies to improve the deep discharge capacity of Li-O_2 batteries, especially at high current rates.

On the other hand, the numerical study sheds light on researching the effects of electrolyte saturation level on the performance of Li-O_2 batteries. I reconstruct pore-scale

structures of battery electrodes from SEM images, and quantitatively obtain the distribution of the electrolyte at various saturations, and simulate the discharge performance of Li-O_2 batteries in Paper **P3**. Since the liquid-gas two-phase mass transfer within the porous electrode plays a significant role in the electrochemical performance of batteries, the study focuses on designing electrodes the mixture of lyophilic and lyophobic pores. Reasonably designed electrodes can enable Li-O_2 batteries to achieve decent discharge capacity at high current rates. Findings in Paper **P3** promote further research to significantly increase (by orders of magnitude) the operating current and power of the Li–O_2 battery and accelerate its deployment to transport and stationary applications.

Imaging techniques are widely employed in the research work. The work in Paper **P4** presents a predictive tool to investigate the stagnant thermal conductivity of porous materials. I use the micro-CT to obtain the structure of the aluminum foam and develop the model based on the random walk theory. The importance of imaging technology has been proven in this work. Therefore, I am now trying to obtain the structure of the positive electrode using the transmission X-ray microscopy located at the Advanced Photon Source of Argonne National Laboratory. The ongoing project shows great potential that the transmission X-ray microscopy can measure the detailed pore-scale geometry of samples in a few minutes. The measuring time is critical for *in situ* experiments that capture evolutions of pore-scale geometries. I will exploit more in this researching field in future work.

Overall, this dissertation is presented based on published articles. **Chapter 2** and **Chapter 3** focus on the experimental study. **Chapter 2** outlines the fabrication of electrodes with different wettability, methods of characterizing the wettability, the prototype of Li-O_2 batteries, experimental setups of testing Li-O_2 batteries and instruments utilized in post-

processing of discharged electrodes (Papers **P1** and **P2**). **Chapter 3** and **Chapter 4** includes key results and discussion of the effects of electrode wettability and intermittent discharging strategies (Papers **P1** and **P2**), respectively. **Chapter 5** is dedicated to simulate electrodes at different saturating levels and map electrolyte distribution in the porous electrode (Paper **P3**). **Chapter 6** introduces a predictive tool that is based on random walk theory. The importance of imaging techniques is addressed in this chapter. The micro-CT can measure the structure of aluminum foams. At the same time, I am making efforts to measure the geometry of positive battery electrodes using the transmission X-ray microscopy. This method is still under development will be further studied in the future. **Chapter 7** contains a summary and an outlook, which is followed by references for all chapters. Overall, this dissertation begins with a brief introduction, followed by a summary of the experimental methodology. The core of this dissertation is the discussion of key results in Papers **P1**, **P2, P3,** and **P4**, respectively. Finally, this dissertation ends with a summary. Note that the definitions of variables have been introduced in the corresponding papers.

Chapter 2: Experimental Methodology

Chapter **2** presents the experimental methods utilized in this dissertation, which are adapted from Papers **P1** and **P2**. The descriptions mainly include positive electrode preparation, pre-characterization of the electrode, discharging-charging test, and post-characterization of the electrode.

2.1 Positive Electrode

The positive electrode typically consists of a carbon cloth substrate and three coating layers. AvCarb 1071 HCB plain carbon cloth fabric purchased from the Fuel Cell Store is used as the substrate of the customized electrode at the positive electrode. Coating layers are made of commercial carbon powers and binders. Conductive acetylene black (purchased from MTI Corporation) is mixed with various mass fractions of polytetrafluoroethylene (PTFE) binder. Afterward, the mixture is dissolved in an ethanol solution to form the carbon slurry. The substrate carbon cloth is dipped into the carbon slurry and dried in the atmosphere for 24 h. Then, the coated electrode is heat-treated at 350°C for 30 min. This heat treatment is to ensure the uniform distribution of the binder and avoid its degradation. The PTFE mass fractions in those customized electrodes are 5%, 15%, 25% and 35%, respectively. Similarly, electrodes with 15% polyvinylidene fluoride (PVDF) carbon coatings and electrodes with mixed carbon coatings (both 15% PTFE and 15% PVDF) are prepared following the same procedure. The structures of electrodes are described in Figure 4. The measured carbon weight of each fabricated electrode is ~3 mg. A higher carbon loading will result in cracks within the electrode. Before the battery assembly, all electrodes are stored in the glovebox where the H_2O and O_2 contents are below 1 ppm.

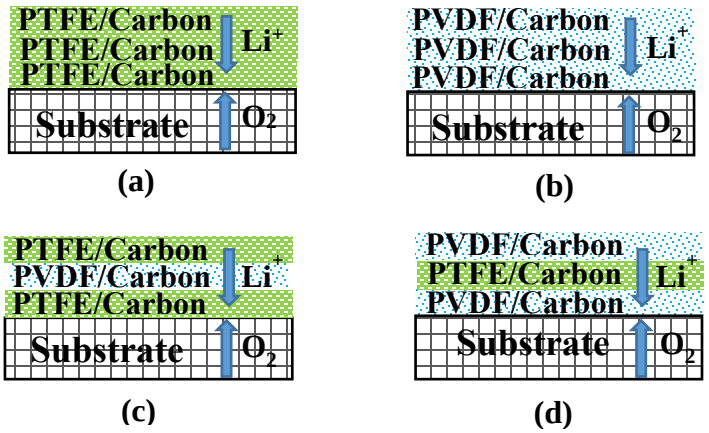

Figure 4: Structural views of customized electrodes using (a) PTFE binder, (b) PVDF binder, (c) mixed binders I (PTFE+PVDF+PTFE) and (d) mixed binders II (PVDF+PTFE+PVDF).

2.2 Lab-scale Li−O_2 Battery

The prototype of the Li−O_2 battery shown in Figure 5 has been extensively used in the research. The battery consists of two current collectors, a lithium chip negative electrode with a diameter of 1.56 cm, a porous positive electrode, a gasket (to prevent short between two electrodes), an O-ring (to seal the battery), and a separator. Two valves are installed at the inlet and outlet of the positive electrode current collector. Oxygen is supplied through the inlet during discharge-charge cycle tests. The current collectors on both the negative electrode and positive electrode sides are home-designed and made from highly corrosion-resistant Grade 2 titanium purchased from McMaster-Carr. The open ratio of the oxygen diffuser is 50% and the separator is a Whatman GF/B glass fiber filter from Fisher Scientific with a diameter of 2.1 cm. The lithium chip is purchased from MTI Corporation. The battery is then constructed by sandwiching the oxygen diffuser, a customized positive electrode, a separator and a lithium chip in the battery frame. All batteries are assembled in the glove box by adding 60 μL of electrolyte in the separator and in the positive electrode, respectively. Adding the electrolyte separately can

guarantee a better distribution of electrolyte, and, therefore a good ionic conductivity. The electrolyte used in Papers **P2** and **P3** is 1 mol/L bis(trifluoromethane) sulfonimide lithium salt (LiTFSI) in tetraethylene glycol dimethyl ether (TEGDME). The concentration of the electrolyte has been studied and optimized in our previous study [57].

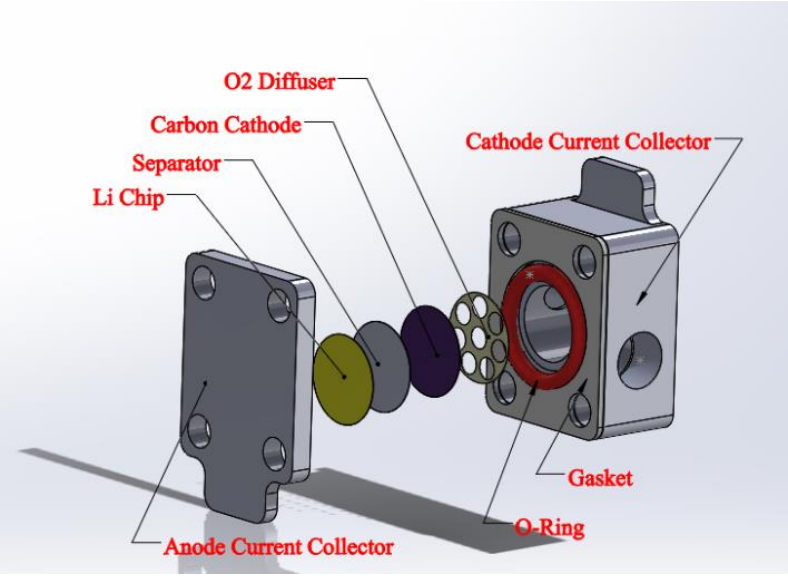

Figure 5: The schematic of lab-scale Li−O_2 battery.

2.3 Discharge-charge Test

Assembled batteries are moved to the test station from the glovebox with all the valves closed to prevent H_2O and CO_2 contamination. Batteries are purged by pure oxygen for 30 s and rested for one hour before starting the discharge and charge cycles. The pure oxygen is supplied at a flow rate of 0.5~1.2 sccm. Besides, the pressure of the pure oxygen is maintained at 10 kPa gauge pressure using a pressure controller (T-68027-64, Cole-Parmer) and a flow controller (T-32907-55, Cole-Parmer). The discharge-charge tests are performed using a 4-channel Arbin MSTAT4 battery tester at room temperature. The cut-off potentials are 2.0 VDC and 4.5 VDC for discharging and charging, respectively. The current densities of galvanostatic tests range from 0.1 mA/cm^2 to 2 mA/cm^2. The geometric surface area for calculating the current density is

1.27 cm^2, which is used throughout the dissertation. The cycling performance of $Li-O_2$ batteries includes the first discharge-charge cycle and multi-cycling with a cut-off capacity. All experimental cases are summarized in Table 2.

Table 2: A summary of experimental cases.

Electrode	**Current Density**	**Strategy**
5% PTFE	0.1 mA/cm^2	Continuous Discharge
15% PTFE	0.1 mA/cm^2	Continuous Discharge
25% PTFE	0.1 mA/cm^2	Continuous Discharge
35% PTFE	0.1 mA/cm^2	Continuous Discharge
15% PVDF	0.1 mA/cm^2	Continuous Discharge
15% Mixed I	0.1 mA/cm^2	Continuous Discharge
15% Mixed II	0.1 mA/cm^2	Continuous Discharge
15% PTFE	0.1 mA/cm^2 (50min) – 0 mA/cm^2 (10min)	Intermittent Discharge
15% PTFE	0.5 mA/cm^2	Continuous Discharge
15% PTFE	0.5 mA/cm^2 (10min) – 0 mA/cm^2 (10min)	Intermittent Discharge
15% PTFE	1.0 mA/cm^2	Continuous Discharge
15% PTFE	1.0 mA/cm^2 (5min) – 0 mA/cm^2 (10min)	Intermittent Discharge
15% PTFE	1.5 mA/cm^2	Continuous Discharge
15% PTFE	1.5 mA/cm^2 (4min) – 0 mA/cm^2 (10min)	Intermittent Discharge
15% PTFE	2.0 mA/cm^2	Continuous Discharge
15% PTFE	2.0 mA/cm^2 (2.5min) – 0 mA/cm^2 (10min)	Intermittent Discharge
15% PTFE	2.0 mA/cm^2 -1.5 mA/cm^2 -1.0 mA/cm^2	Muti-step Discharge
15% PVDF	1.0 mA/cm^2	Continuous Discharge

15% PVDF	1.0 mA/cm^2 (5min) – 0 mA/cm^2 (10min)	Intermittent Discharge
Mixed I	1.0 mA/cm^2	Continuous Discharge
Mixed I	1.0 mA/cm^2 (5min) – 0 mA/cm^2 (10min)	Intermittent Discharge
Mixed I	1.0 mA/cm^2 (10min) – 0 mA/cm^2 (10min)	Intermittent Discharge
Mixed I	1.0 mA/cm^2 (2min) – 0 mA/cm^2 (10min)	Intermittent Discharge
Mixed I	1.0 mA/cm^2 (5min) – 0 mA/cm^2 (5min)	Intermittent Discharge
Mixed I	1.0 mA/cm^2 (5min) – 0 mA/cm^2 (15min)	Intermittent Discharge
Mixed I	1.0 mA/cm^2 1000 mA h/g cut-off capacity	Multi-cycle
Mixed I	1.0 mA/cm^2 (5min) – 0 mA/cm^2 (5min) 1000 mA h/g cut-off capacity	Multi-cycle
Mixed I	0.1 mA/cm^2 1000 mA h/g cut-off capacity	Multi-cycle
PTFE 15%	0.1 mA/cm^2 1000 mAh cut-off capacity	Multi-cycle
PTFE 15%	0.1 mA/cm^2	First-cycle
PVDF 15%	0.1 mA/cm^2	First-cycle
Mixed I	0.1 mA/cm^2	First-cycle
Li chip	0.1 mA/cm^2	Multi-cycle
Li chip	1.0 mA/cm^2	First-cycle
Li chip	5.0 mA/cm^2	First-cycle
Li chip	10.0 mA/cm^2	Multi-cycle

Note: Mixed I and Mixed II electrodes are displayed in Figure 4. The current density is based on the geometric surface area of 1.27 cm^2.

2.4 Pre-characterization Methodology

2.4.1 Wettability Measurement. To quantify the wettability of the electrode, both surface and internal measurements are conducted. The static contact angle (to be maintained for 120 s) is defined to quantify the surface wettability between 1 M LiTFSI/TEGDME and surfaces of customized electrodes. The measurement is done using Ramé-hart Model 190 Contact Angle Goniometer at the room temperature. The volume of electrolyte drop is 5 μL and each measurement is conducted at three different locations to guarantee the consistency. Besides, I apply the electrochemical impedance spectroscopy (EIS) measurement to the internal wettability using the SP 150 potentiostat from BioLogic Science Instrument. The equivalent ionic resistance of each electrode is obtained and compared. In addition, double layer capacitance of each electrode is measured by cyclic voltammetry (CV) tests performed from -0.2 to 0.2 VDC at the scanning rate of 0.2 VDC/s. The trend of wettability difference among all electrodes can be confirmed even though larger errors appear in the double layer capacitance measurement.

2.4.2 Pore Size Analysis. The porous structure of the positive electrode plays an important role in Li−O_2 batteries due to its dual functions. The O_2 and Li^+ are transported to the reaction sites in the positive electrode. At the same time, the discharge product of Li_2O_2 is accommodated in the positive electrode. The N_2 gas adsorption/desorption method is used to measure the pore size distribution, specific surface area, and pore volume of carbon samples in this dissertation. The physisorption measurement is performed at 77 K by the surface and pore size analyzer (NOVAtouch N2TLX – 1, Quantachrome Instrument, U.S.). All samples are degassed at 300 °C for 3 hours before adsorption/desorption measurements. Degassing the sample in the above manner (at 300 °C for 3 hours) fully removes the moisture since the water content will greatly affect the gas sorption measurement. The amount adsorbed vs. the adsorptive

pressure (P), relative to the saturated vapor pressure over the bulk liquid (P_0) is obtained and used as isotherms of the adsorption and desorption. The surface area is analyzed by the Brunauer, Emmet, and Teller (BET) method, the pore size distribution is evaluated by the Barrett, Joyner, and Halenda (BJH) and the Density Function Theory (DFT) methods.

2.5 Electrode Surface Characterization

The scanning electron microscopy (SEM) images of customized electrode surface are scanned using FEI Versa 3-D Dual Beam Electron Microscopy. SEM images of both fresh electrodes and discharged electrodes are obtained. For all samples, measurements are conducted in high vacuum at 10 kV accelerating voltage. Preparations for imaging vary somewhat between different samples. The sample of the fresh electrode is stuck on the sample holder by a carbon tape. The discharged electrode is rinsed by the electrolyte to remove the unnecessary glass fibers, after which portions of the discharge electrode is stuck on the sample holder as well.

In chapter 2, the experimental methodologies in this dissertation have been introduced. Positive electrodes with various wettability are fabricated by mixing acetylene black carbon with PTFE (and/or PVDF) binders. The wettability is characterized by the surface contact angle, ionic resistance and double layer capacitance. All positive electrodes are discharged using the self-designed $Li-O_2$ batteries at different experimental conditions. Moreover, the gas adsorption/desorption techniques are utilized to characterize the porous structure of the positive electrodes, obtaining the pore volume, pore size distribution and specific surface area. In general, the experimental methodologies mentioned in this chapter benefits the experimental research as well as the numerical study in this dissertation.

Chapter 3: Experimental Study of Electrodes with Various Wettability

This chapter is adapted from Paper **P1**.

3.1 Introduction

The investigation of electrode wettability is critical to understand the two-phase mass transfer in the porous positive electrode. Reaction 1.2 indicates that the O_2 is diffusing into the electrode and then reduced into Li_2O_2 at the reaction sites. During the operation of a Li−O_2 battery, ORR can only happen at the region where the electrode surface is wetted by the electrolyte. Therefore, wetting pores are necessary for discharging Li−O_2 batteries. Even though the dissolved O_2 and Li^+ in the electrolyte participate in the ORR, the saturated electrode with all pores wetted is undesirable. The solubility and diffusivity of O_2 in aprotic electrolytes are far from the requirement of operating the Li−O_2 battery practically [58-61]. The saturated electrode reduces O_2 accessibility at the reaction sites. Subsequently, the discharge current density decreases and the ORR will be quickly terminated. Therefore, O_2 availability for the ORR is determined by both diffusions in non-wetting and wetting pores and solubility in the electrolyte. The improvement of O_2 solubility in aprotic electrolytes may require a breakthrough in material research in the future. Meanwhile, increasing the O_2 diffusion is the other way to provide more O_2 for the ORR. The O_2 diffusion coefficient in the air is 10^4 higher than that in the liquid electrolyte [62]. Thus, constructing a porous electrode with a reasonable distribution of wetting and non-wetting pores can significantly improve the O_2 diffusion, increasing the operating current density of Li−O_2 batteries. Paper **P1** focuses on alternating the electrode wettability and quantitatively compare the discharge performance of Li−O_2 batteries with various electrode wettability.

Many studies have paid considerable attention to the O_2 diffusion in the porous positive electrode since the O_2 diffusion in the porous positive electrode is critical for the discharge capacity of Li−O_2 batteries [49, 54, 63-65]. The O_2 diffusion in the porous positive electrode are related to carbon loading[66], pore clogging induced by the deposition of solid lithium peroxide[38, 67-69], and the partial pressure of oxygen[58]. In addition, the wettability between the electrolyte and electrode also significantly affects the performance of Li−O_2 batteries because the O_2 diffusion coefficient in air is several orders of magnitude higher than that in the liquid electrolyte. The electrolyte contact angle on the carbon electrode surface increases when the difference between the electrolyte and the carbon electrode is greater in the dielectric constant. The larger contact angle electrolyte is less likely to humidify the carbon electrode. Xu et al. [64] show that the wettability affects the O_2 diffusion in the porous electrode, which then influences the discharge and charge capacity. The measured contact angles between various non-aqueous solvents and the surface of both carbon and Teflon show that the discharge capacity is improved when the contact angle increases. For example, the contact angle of 1M LiTFSI in PC / ethylene carbonate (EC) (1:1 wt%) on the surface of carbon is 47°. Another contact angle of 1M LiTFSI in PC / dimethoxyethane (DME) (1:1 wt) on the surface of carbon is 5°. The discharge capacity decreases from 167.5 mAh/g to 27.4 mAh/g when the contact angle decreases from 47° to 5°. Binders such as PVDF and PTFE are used to combine different types of small particles together and adjust the wettability of the positive electrode in Li−O_2 batteries. Moreover, the electrode made from Super P carbon mixed with PTFE (8:2 wt%) has the contact angle of 99° while the electrode consisting of KB 600 carbon mixed with PTFE (8:2 wt%) has the contact angle of 56°. On the other hand, strongly lyophobic electrodes may deteriorate the discharge−charge performance. The Li−O_2 battery with a lyophobic electrode (99°) obtains a higher discharge

capacity of 3175 mAh/g. However, the discharge capacity is only 798 mAh/g when the electrode is lyophilic [49]. Based on the research conducted by Chen et al. [65], electrodes with strong lyophobicity may deteriorate the discharge-charge performance. Experimental data show that the specific discharge capacity increases from 1365 to 2365 mAh/g when the PTFE mass fraction increases from 0 to 30%. However, the electrode composed of 40 wt% PTFE reduces the specific discharge capacity to 2130 mAh/g. The PTFE mass fraction should be optimized because of a higher PTFE content will reduce the amounts of wetting pores, which are necessary for the electrochemical reactions.

The non-wetting pores result from the lyophobicity while the wetting pores are related to the lyophilicity. Due to the significant difference of O_2 diffusivity between wetting and non-wetting pores, a reasonable construction of electrode wettability may potentially both facilitate the O_2 diffusion and reserve adequate reaction sites for Li−O_2 batteries. The wettability of electrode was adjusted by mixing carbon powders with different binders (PTFE and PVDF) at various weight ratios. The stability of binders has been systematically examined[70] in the presence of commercial Li_2O_2, which showed that PVDF was unstable because of the presence of highly electron-withdrawing functional groups and an α or β hydrogen atom next to them. The PTFE binder was demonstrated to be stable in the presence of Li_2O_2. In addition, the PVDF binder was confirmed to degrade in Li−O_2 batteries[71]. The products formed in the PVDF degradation was measured by Raman spectroscopy and showed the Raman shifts of ~1123 and 1525 cm^{-1}. However, the degradation can be prevented by drying the electrode under higher temperature such as 200 °C. Thus, the stability of PTFE and PVDF binders can be guaranteed in this study if the electrodes are prepared according to the process in experimental section. Therefore, the study in Paper **P1** has conducted a systematic investigation of the effects of electrode wettability toward organic

electrolyte (including both lyophilicity and lyophobicity) and its effects on the deep discharge capacity of Li−O_2 batteries. The study sheds light on criteria to improve the O_2 diffusion and increase the specific discharge capacity of Li−O_2 batteries.

3.2 Results and Discussion

3.2.1 Surface Wettability. The contact angle shown in Figure 6 is measured as the angle where a liquid or a vapor interacts with a solid surface. The angle represents the wettability of a solid surface wetted by a liquid via the Young equation. The surface wettability of the electrode in the Li−O_2 battery is often quantified by the contact angle measurement [72-74]. A high contact angle indicates that the liquid droplet will maintain the droplet form. A low contact angle indicates that the surface has the high wetting ability and the water droplet spreads out more on the surface. The difference between the solid surface energy and the surface tension of a liquid will affect the wettability of the solid to the liquid. The liquid with a larger contact angle is less likely to wet the solid surface.

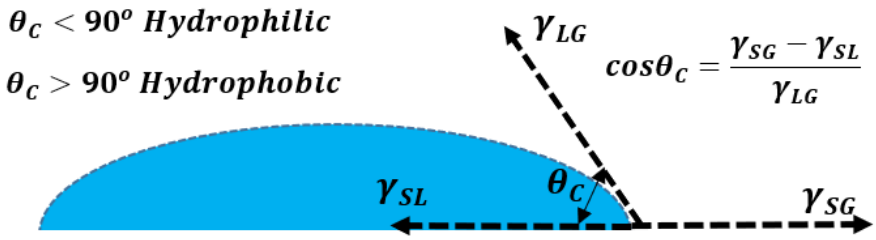

Figure 6: Schematic of a liquid drop showing a contact angle in Young's equation.

In paper **P1**, the static contact angle is applied to characterize surface wettability of electrodes with various content of PTFE and PVDF binders. Figure 7 shows static contact angles of 1 M of LiTFSI/TEGDME electrolyte (5 μL per drop) dropped on the surfaces of electrodes. The electrode containing the PTFE binder has higher surface energy than the PVDF binder. The

measurement of static contact angle is unsuccessful when the electrolyte drop is dripped on the surface of customized electrode containing 5% PTFE because the electrolyte droplet quickly spreads into the electrode. It indicates that the surface of 5% PTFE is lyophilic and is more easily wetted by the electrolyte. When the PTFE content increases from 15% to 35%, the electrode becomes more lyophobic and the static contact angle increases from 128.4° to 138.5°. The mixed I electrode, which consists of one 15% PVDF coating sandwiched by two 15% PTFE coatings, displays a slightly lower static contact angle (118.8°) than the electrode with 15% PTFE. It may be caused by the fact that a small amount of PVDF binder is mixed on the top layer of carbon coating during the fabrication. In addition, the contact angles of customized electrodes with 15% PVDF carbon coatings as well as the mixed II electrode consisting of one 15% PTFE carbon coating sandwiched by two 15% PVDF carbon coatings are less than 90° and are unstable.

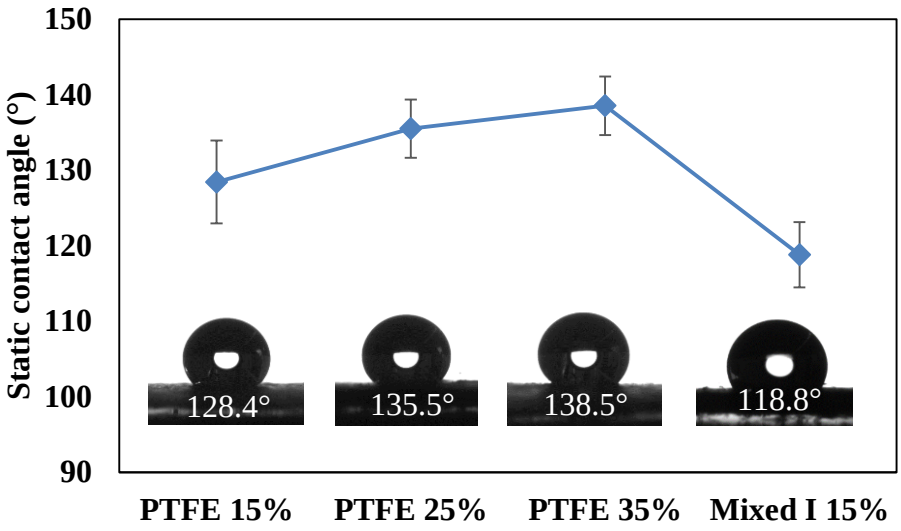

Figure 7: Static contact angle measurements on customized electrode surfaces.

3.2.2 Internal Wettability. Considering an electrode made of carbon powder and binders, the wetting characteristics range widely since the non-uniform distribution or

malfunction of PTFE treatment, rendering part of the pores lyophilic. Additionally, surface defects and impurities may lead to a reduction in the lyophobicity. Therefore, a measurement internal wettability is necessary to investigate the effects of electrode wettability on the performance of the $Li-O_2$ battery. For those porous electrodes, wetting behavior is related to the solid-liquid interfacial interactions. I perform EIS and CV measurements to obtain the ionic resistance and double layer capacitance, which can represent the internal wettability.

During discharge, Li metal is oxidized at the negative electrode, Li^+ ions are delivered to the reaction sites through the electrolyte, which is crucial to complete the ORR at the positive electrode. The ionic resistance is directly related to the electrolyte and its distribution in the positive electrode. Measuring the ionic resistance can provide a decent understanding of internal wettability. In Paper **P1**, the ionic resistance of electrodes with various wettability are experimentally measured and shown in Figure 8. The Electrochemical Impedence Spectroscopy (EIS) is applied to carry out electrical resistance measurement on $Li-O_2$ batteries with customized electrodes of various wettability. The Nyquist plots of fitted data using the equivalent circuit is shown in Figure 9. The equivalent circuit includes an ohmic resistance (R_1), which considers the electronic resistance of the electrodes, current collectors, and ionic resistance of the electrolyte, as well as the contact resistance between these components. R_2 and R_3 are due to the charge transfer resistance and mass transfer resistance at the two electrodes. The diagonal line at low frequencies represents the Warburg impedance (W_4), which is due to the diffusion impedance of the oxidant and reductant. C_2 and C_3 denote the double layer capacitance formed when a non-conducting media separates two conducting electrodes. Due to the same configuration of $Li-O_2$ batteries, the variations of R_1 can be attributed to the electrode resistance which is dominated by the ionic resistance.The PVDF 15% electrode has the lowest ionic

resistance which indicates that wetting area is the largest and the electrode is the most lyophilic. More lyophobic electrodes impede the ionic transfer by increasing the ionic resistance. Additionally, the resistance displays the same trend as the static contact angle.

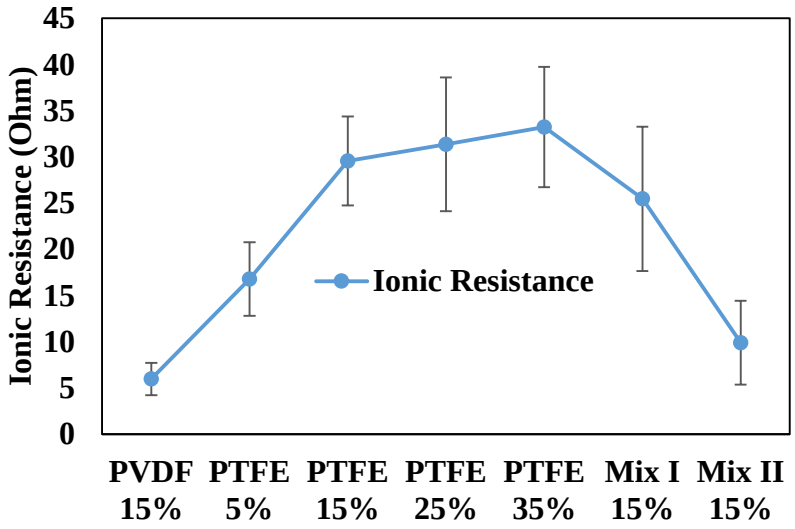

Figure 8: Equivalent ionic resistance of the batteries with customized electrodes of different wettability.

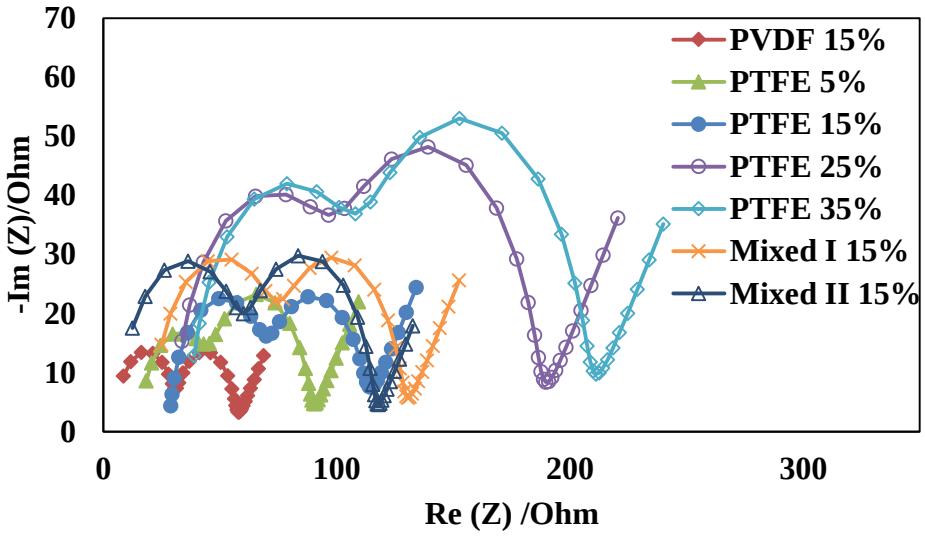

Figure 9: Nyquist plots of batteries with customized electrode with different wettability.

The double layer capacitance of customized electrodes is also measured to quantify the internal wettability. I employ an electrochemical approach to quantify the solid-liquid interfacial

area and promote the understanding of wettability within customized electrodes [75]. The electrical double layer is created on the electrode surface that is wetted by the electrolyte because the customized electrode made of carbon powders are electrically conductive. A simple calculation of this capacitance in a planar system with only electrical energy is related to the geometric capacitance expression:

$$C = \varepsilon_r \varepsilon_0 \frac{A_{sl}}{d} \tag{3.1}$$

where C is the capacitance, ε_r is the relative permittivity of the electrolyte, ε_0 is the permittivity of the vacuum, d is the double layer thickness which can be approximated as Debye length and A_{sl} represents the wetted pore surface. For an electrolyte with the given composition measured at the room temperature, parameters of $\varepsilon_r, \varepsilon_0$ and d can be considered as constants. Therefore, the change of the area of the wetted pore surface is proportional to the variation of the double layer capacitance.

The 1 M LiTFSI/TEGDME electrolyte is added to the surface of the electrode using a pipette. The relationship between electrolyte volume and the double layer capacitance is shown in Figure 10. A separator is inserted in the battery to avoid a short circuit phenomenon. The double layer capacitance is related to the wetted pore surface in the electrode as well as the wetted area in the current collector. Thus, it is necessary to measure the capacitance when only the strongly lyophilic separator is inserted in the battery. Generally, as more electrolyte is added, more pore surface is wetted so that the double layer capacitance increases. The customized electrode containing 15% PVDF has larger capacitances than that with 35% PTFE because the former electrode is more lyophilic, and more pores are wetted by electrolyte. For example, the capacitance of the electrode with 15% PVDF was 12.9 μF more than that of the electrode with 35% PTFE at the volume of 20 μL. The capacitance of 35%-PTFE electrode combined with the separator is only

slightly higher (< 5μF in all volumetric cases) than that of a single separator as shown in Figure 4. It indicates that most of the electrolyte added into the lyophobic electrode is repelled into the lyophilic separator. The double layer capacitance increases almost linearly with the amount of added electrolyte when the electrolyte is less than 60 μL. As the electrolyte is added, more electrolyte spreads into the separator. Therefore, the wetted surface in the current collector may account for a larger fraction of the double layer capacitance. The sudden rise in the capacitance after 100 μL may be attributed to the fact that electrolyte is squeezed out from the battery frame and the extra double layer is created. Although the compression during battery assembly may partially compensate the capillary pressure within the electrode and cause measuring errors, especially when the electrolyte was more than 60 μL, the measurement of double layer capacitance demonstrates the general trend that more pores are wetted by the electrolyte in the lyophilic electrodes.

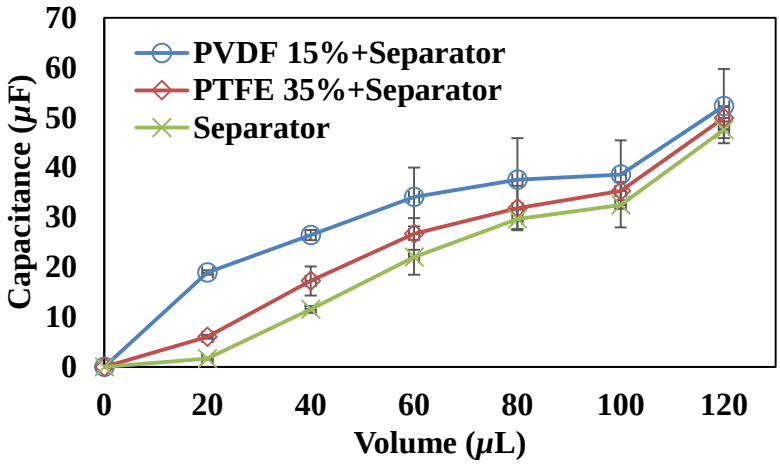

Figure 10: Double layer capacitance vs volume of electrolyte in electrodes.

3.2.3 Deep Discharge Test. When the wettability of each type of the electrode is characterized, the discharge tests are performed at 0.1 mA/cm^2. The discharge capacity of electrodes with variable wettability is shown in Figure 11. The discharge capacity of raw carbon

cloth is negligible (< 100 mAh/g) due to the low specific surface area. Therefore, the reported specific discharge capacity is calculated based on the weight of carbon powders coated on the electrode without considering the weight of raw carbon cloth substrate and binders. The lowest specific discharge capacity of 1665.8 mAh/g is achieved by the electrode with 15% PVDF carbon coatings. On the other hand, the specific discharge capacities of Li−O_2 batteries increase from 3145.8 to 4160.8 mAh/g when the mass fraction of PTFE binder increases from 5% to 15%. However, the specific discharge capacity decreases to 3109.5 and 2822.9 mAh/g when the mass fraction of PTFE binder further increases to 25% and 35%. The significant variation of specific discharge capacity can be attributed to the difference among the electrode wettability. More lyophobic electrodes facilitate O_2 diffusion by creating more gas paths. The improvement of O_2 transfer enhancing the O_2 availability at the reaction sites which results in higher specific discharge capacity. However, the specific discharge capacity of the electrode decreases after further increasing the PTFE content to more than 15%. The influences of PTFE content on specific discharge capacity possesses good consistency with the published data [65]. Further increasing the PTFE content generates more lyophobic pores that reduce the number of reaction sites for the ORR and increases the ionic resistance. In order to facilitate the oxygen diffusion without significantly sacrificing the ionic conductivity, electrodes with mixed wettability have been designed and tested. In mixed I electrode, the top and bottom layers with 15% PTFE are lyophobic and the middle layer with 15% PVDF is lyophilic. The battery with mixed I electrode achieves the highest specific discharge capacity of 5149.5 mAh/g. Because of the lyophobicity of both the top and the bottom coatings, O_2 can diffuse into the electrode without much diffusion resistance and reach the electrolyte that accumulates in the lyophilic coating in the middle. This design utilizes the porous structure inside the electrode more effectively. Also, adding a lyophilic layer in the middle of

electrode may reduce the O_2 diffusion length compared with the fully lyophobic electrode. The combined effects lead to the highest specific capacity. In comparison, the mixed II electrode is composed of one carbon coating with 15% PTFE layer sandwiched by two carbon coatings with 15% PVDF. This electrode only results in 2700.6 mAh/g deep discharge capacity because that the lyophilic top and bottom layers impose more resistance in O_2 diffusion. Comparing with the electrode with 15% PVDF, applying one lyophobic layer in the middle of mixed II electrode increases the discharge capacity by about 1000 mAh/g. The result is consistent with the previous conclusion as well as the study conducted by Xia et al.[76] that partially wetted electrodes perform better than electrodes fully saturated by the electrolyte. The mixed I customized electrode with stacking coatings (lyophobic coatings on top and bottom with a lyophilic coating in the middle) can be beneficial to promote the design of air electrodes and provide a valuable reference to fabricate high-capacity electrodes.

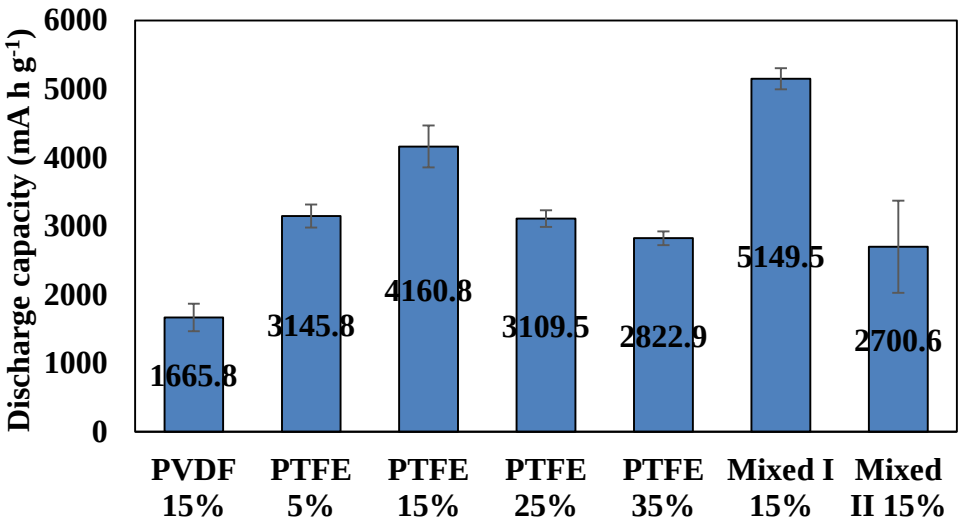

Figure 11: Deep discharge Li−O_2 batteries using customized electrodes.

3.2.4 First Discharge-Charge Cycle. Although this study is focusing on the deep discharge capacity of Li−O_2 batteries with customized electrodes, the cycling performance is

also investigated and analyzed. The first discharge-charge cycles of Li−O_2 batteries with customized electrodes at 0.1 mA/cm^2 are shown in Figure 12. The cut-off voltage of charging is set at 4.5VDC. The Mixed I 15% electrode, as well as the PTFE 15% electrode, results in a discharge-charge cycle with the average coulombic efficiency close to 85% while the battery with 15% PVDF electrode achieves a slightly higher coulombic efficiency of 93%. The lower coulombic efficiencies of Mixed I 15% electrode and PTFE 15% electrode can be contributed to the fact that more electrolyte in the lyophobic electrode evaporates because of a longer discharge and charge time, which may increase the ionic resistance during charge and, thus, deteriorate the coulombic efficiency [77]. Besides, PVDF favors the thin Li_2O_2 film formed on the surface of the electrode while PTFE results in more Li_2O_2 toroids which are more difficult to decompose during the charging process [78].

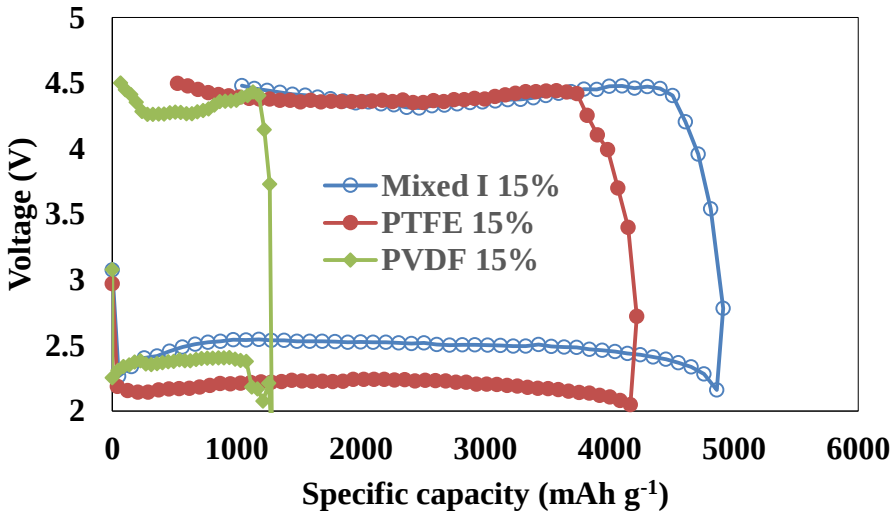

Figure 12: First discharge-charge cycle of Li−O_2 batteries with customized electrodes.

In Paper **P1**, electrodes with various wettability are fabricated and tested in Li−O_2 batteries. Different approaches are utilized to characterize the electrode wettability. The wettability of electrode was mainly altered by mixing acetylene black carbons with PTFE and/or PVDF binders at various weight ratios. The customized electrodes containing PVDF binder or less PTFE binder

(< 15%) were lyophilic and their corresponding discharge capacities were lower than those of lyophobic electrodes. The electrode with 15% PTFE exhibited the deep discharge capacity of 4160.8 mAh/g because lyophobic electrode provided more gas path for O_2 diffusion. This study also designed customized electrodes with stacked layers by combing the lyophilic layers with lyophobic layers. The mixed I electrode (15% PTFE carbon coatings on top and bottom, one 15% PVDF carbon coating in the middle) showed the highest deep discharge capacity of 5149.5 mAh/g among all the experimental cases. The mixed wettability promoted the oxygen diffusion without significantly lowering the ionic conductivity or reducing the number of reaction sites. Therefore, configuring the wettability in the electrode design is an important direction to increase the discharge capacity of Li−O_2 batteries.

It is challenging to accurately measure the difference of wettability among all electrodes in this chapter. However, an innovative method is required to improve the accuracy of wettability measurement. I may design a new experimental configuration to characterize the electrode wettability with much fewer errors. After comparing the deep discharge capacity of each electrode, lyophobic electrodes perform better than lyophilic ones due to the fast O_2 diffusion in gas paths. The mixed wettability promotes the O_2 diffusion without significantly lowering the ionic conductivity or reducing the number of reaction sites. Therefore, configuring the wettability in the electrode design is an important direction to increase the discharge capacity of Li−O_2 batteries.

Chapter 4: Experimental Study of Intermittent Discharge Strategy

Chapter 4 is adapted from Paper **P2**.

4.1 Introduction

As discussed in Section 1.2, the fundamental issues of Li−O_2 batteries, including the reaction mechanism, the electrochemical stability of positive electrode, and the electrolyte and Li negative electrode, are not fully understood. More specifically, the low discharge/charge rate capability, poor cycle life, and low round-trip efficiency are the crucial factors that prevent the practical operation of Li−O_2 batteries [79-83]. Since the Li−O_2 battery is regarded as a promising candidate to replace the Li-ion battery, powering EVs may be a major application when it is commercialized. However, the practical applications of EVs require that the discharge current density should be two orders of magnitude higher than the present current density applied in discharging the Li−O_2 batteries (e.g., 0.1 mA/cm^2) [84]. Therefore, it is urgent to increase the discharge/charge rate capability of Li-O_2 batteries.

Multiple numerical and experimental studies demonstrated that the discharge capacity would be reduced significantly if the Li−O_2 batteries are discharged at high current density [15, 57, 77, 85-89]. For instance, Han et al.[87] stated that the discharge voltage plateau decreased by 0.2 V and discharge capacity decreased from 6219 to 1251 mAh/g when the current density increases from 0.1 mA/cm^2 to 0.4 mA/cm^2. Mohazabrad et al.[57] showed that the specific discharge capacity decreased from 461.53 mAh/g to 106.07 mAh/g when the current density increased from 0.1 mA/cm^2 to 0.5 mA/cm^2. Tremendous efforts have been paid to clarify the dominated factor that affect the discharge capacity of Li−O_2 batteries at high current density. The electrical passivation of positive electrode caused by Li_2O_2 film and poor O_2 transportation

limited by pore clogging are claimed as two major factors that limit the discharge capacity. For example, Adams et al. [38] reported that Li_2O_2 particles nucleated at low current densities (5-25 $\mu A/cm^2$), and amorphous thin films of Li_2O_2 formed by electro-reduction reaction on the electrode surface at high current densities (50-100 $\mu A/cm^2$). The investigation by Adams et al.[38] also showed that the direct electron transfer would incur a significant voltage drop at high current density which indicates the thickness and conductivity of the Li_2O_2 film become more important for discharging $Li-O_2$ batteries at high current density. The electrical conductivity of Li_2O_2 film was investigated both experimentally and numerically [37]. Results show that the critical thickness of Li_2O_2 film is ~ 5 nm above which the exchange current density fell rapidly below ~10^{-7} A/cm^2 and the ORR was no longer supported, leading to "sudden death" of $Li-O_2$ batteries. The electrical conductivity of Li_2O_2 was estimated to be in the range of 10^{-12} to 10^{-13} S cm^{-1} and the critical thickness of 5 nm was confirmed by Lu et al [90]. Mirzaeian et al. [88] examined the operation effect on the performance of $Li-O_2$ batteries systematically. The discharge capacity decreased from 2387 mAh/g to 364 mAh/g as the current density varied from 10 mA/g to 150 mA/g. The discharge ceased when the discharge products occupied almost all the pores at lower current density. Another study[91] argued that the Li_2O_2 deposition only covers the electrode external surface by forming a thin film rather than filling the interior pores in the electrode at high current density. Therefore, the capacity loss can be attributed to the fast deposition of Li_2O_2 on the electrode surface which limits the transportation of O_2 and Li^+ and blocks the inner active surface. However, the morphology of discharge products such as the primary product of Li_2O_2 is not only influenced by the current density but other factors such as the electrode structure [63] and the electrolyte [92-93]. Thus, it is very challenging to control the morphology of discharge products to improve the rate capability of $Li-O_2$ batteries.

On the other hand, studies [58, 94] claimed that the poor rate capability of Li-O_2 batteries was mainly due to sluggish O_2 transportation in the organic electrolyte of flooded electrodes, which was also reported by the numerical studies [86, 95]. The 1M electrolytes with different constituents display various viscosity such that the corresponding O_2 diffusion coefficients estimated by Stokes-Einstein equation are also different [58]. For example, 1M lithium hexafluorophosphate ($LiPF_6$) in propylene carbonate (PC) has the viscosity of 8.06 cP while the viscosity of 1M LiPF6 in PC: dimethoxyethane (DME) (1:2) is 1.98 cP. When discharge the Li-O_2 batteries with 1M $LiPF_6$/PC and 1M $LiPF_6$/PC:DME (1:2) at 0.1 mA/cm^2, the discharge capacities were 380 and 1095 mAh/g, respectively. When discharging those batteries at 0.5 mA/cm^2, the discharge capacity corresponding to 1M $LiPF_6$/PC was 85 mAh/g while it was 363 mAh/g for 1M $LiPF_6$/PC:DME (1:2). The three times increase of capacity showed that promoting O_2 diffusion in the electrode can reduce the capacity loss at high current density. In other words, the poor O_2 diffusion may dominate the performance of Li−O_2 batteries at high current density.

The debate on the determining factor of capacity loss of Li−O_2 batteries at high current density may continue until the fundamental mechanism is fully understood. However, possible approaches which include intermittent operating procedure and modifying the electrode wettability[96] can be applied to enhance the O_2 diffusion in the electrode and thus improve the rate capability of Li−O_2 batteries. In Paper **P2**, an intermittent operating procedure along with modifying the electrode wettability is applied to enhance the O_2 diffusion in the electrode and, thus, improve the rate capability of Li-O_2 batteries. Electrodes of different wettability are discharged at various current densities (0.1 – 2.0 mA/cm^2). Cycling experiments of Li-O_2 batteries are also studied to determine the effect of discharge strategy on discharge-charge cycles.

4.2 Results and Discussion

4.2.1 Intermittent Strategy vs. Continuous Strategy. I first compare the specific discharge capacity of Li-O_2 batteries using the intermittent and continuous discharging strategies. The electrode with 15% PTFE binder, lyophobic with the static contact angle of 128.4°, achieves higher discharge capacity than that of lyophilic electrode [96]. Thus, electrodes with PTFE 15% binder are tested in this subsection. Figure 13 and Table 3 show the results of specific discharge capacity when Li-O_2 batteries are discharged under continuous or intermittent currents of 0.1, 0.5, 1.0, and 1.5 mA/cm^2. The intermittent current strategy periodically discharges and rests the battery. The time for the discharging process is proportional to the given current and the rest time is kept as 10 min. For example, the battery is discharged for 10 min at 0.5 mA/cm^2 and for 5 min at 1.0 mA/cm^2. Results show that both the continuous discharge capacity and the intermittent discharge capacity decrease when the current density increases from 0.1 to 1.5 mA/cm^2. The discharge capacity is lower at higher current density because of the increased polarization of positive electrode, which has been already examined in other studies [57]. The specific discharge capacities of Li-O_2 batteries discharged by intermittent current are ~50% higher than these obtained by continuous current. For example, the specific discharge capacity is 1629.5 ± 124.0 mAh/g at intermittent discharge current of 1.0 mA/cm^2 while it is 1031.0 ± 22.8 mAh/g at continuous discharge current of 1.0 mA/cm^2. Since the O_2 diffusion plays a significant role in determining the discharge capacity, the Li−O_2 battery will achieve higher discharge capacity if more O_2 is available. When the Li−O_2 battery is discharged intermittently, O_2 can diffuse into the electrode while the battery is at rest and compensate the O_2 consumed during discharge. Thus, the capacity loss caused by sluggish O_2 diffusion is alleviated and the discharge capacity is increased by ~50% at various current densities.

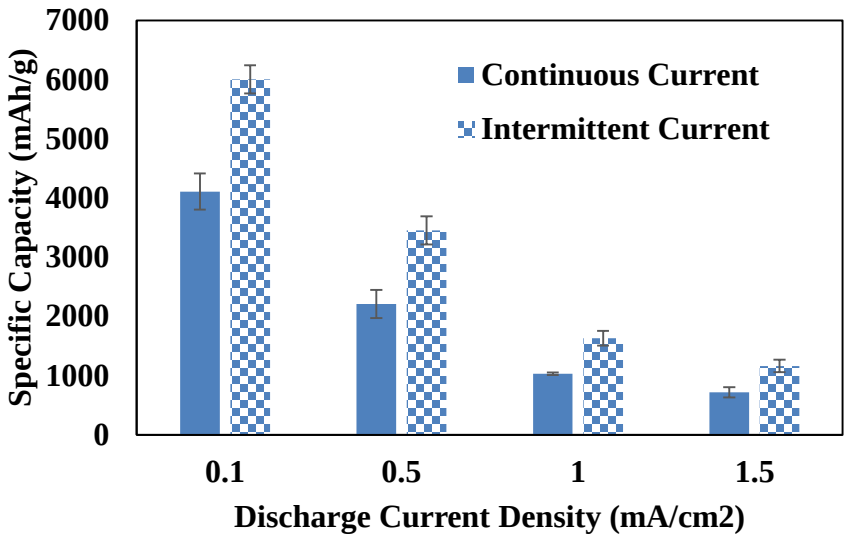

Figure 13: Specific discharge capacities of Li–O_2 batteries with PTFE 15% electrodes at continuous and intermittent current densities.

Table 3: A summary of discharge capacity using different strategies.

Strategy	Current Density (mA/cm^2)	Discharge Capacity (mAh/g)
Intermittent	0.1	6005 ± 237.3
Continuous	0.1 (50min) – 0 (10min)	4106.8 ± 305.1
Intermittent	0.5	3451.1 ± 237.0
Continuous	0.5 (10min) – 0 (10min)	2210.5 ± 237.2
Intermittent	1.0	1629.5 ±124.0
Continuous	1.0 (5min) – 0 (10min)	1030.9 ± 22.8
Intermittent	1.5	1161.5 ± 105.8
Continuous	1.5 (4min) – 0 (10min)	716.5 ± 87.7

The discharge curves of Li−O_2 batteries with continuous and intermittent 0.5 mA/cm^2 is shown in Figure 14. The voltages of Li−O_2 batteries using the intermittent strategy jump back to

~2.8 V when the batteries are at rest. This innovative strategy elongates and stabilizes the discharge plateaus as shown in Figure 14. The Type IV isotherm is observed in N_2 adsorption/desorption measurement. The relatively long linear part indicates the completion of the monolayer and the isotherm characterizes a mesoporous structure in the porous electrode. Results calculated based on the isotherm also show that the acetylene black carbon has the BET surface area of 76.5 m^2/g and most of the pores are in the range of 2-50 nm. The results of surface area and pore size distribution confirms that the electrode has a mesoporous structure and the O_2 diffusion will not be impeded due to the electrode structure. I measure electrodes after discharge using the SEM instrument. The obtained images are shown in Figure 15. At low currents, the needle-like Li_2O_2 can be detected on the electrode surface and the film-like Li_2O_2 forms at high currents. The discharge products gradually form large agglomerates that hinder the O_2 mass transfer. The morphologies of Li_2O_2 are similar when they are deposited under those two strategies. This similarity demonstrates that the increase of discharge capacity at the intermittent current has no relationship with the morphological variations of Li_2O_2. Thus, the discharge capacity can be improved due to sufficient O_2 supply by periodically resting the $Li-O_2$ battery.

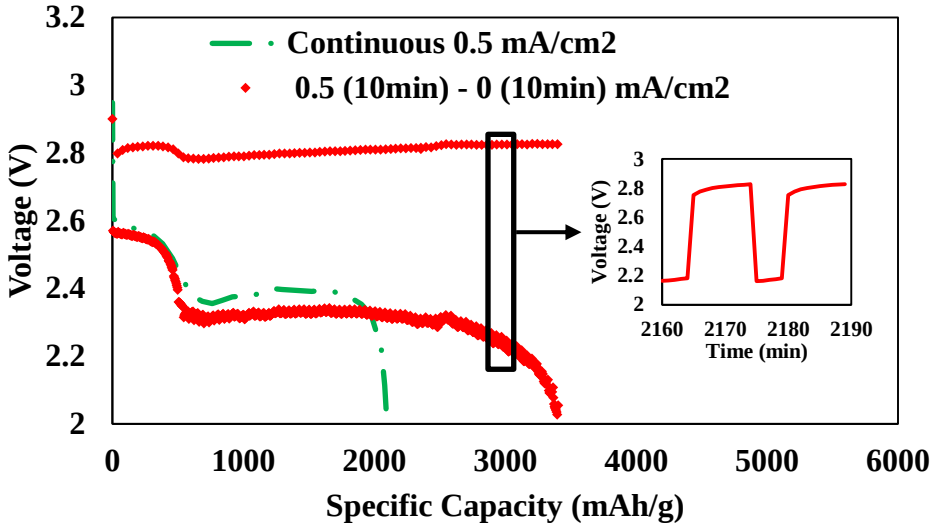

Figure 14: Discharge curves of Li–O_2 batteries with PTFE 15% electrodes at continuous and intermittent 0.5 mA/cm^2.

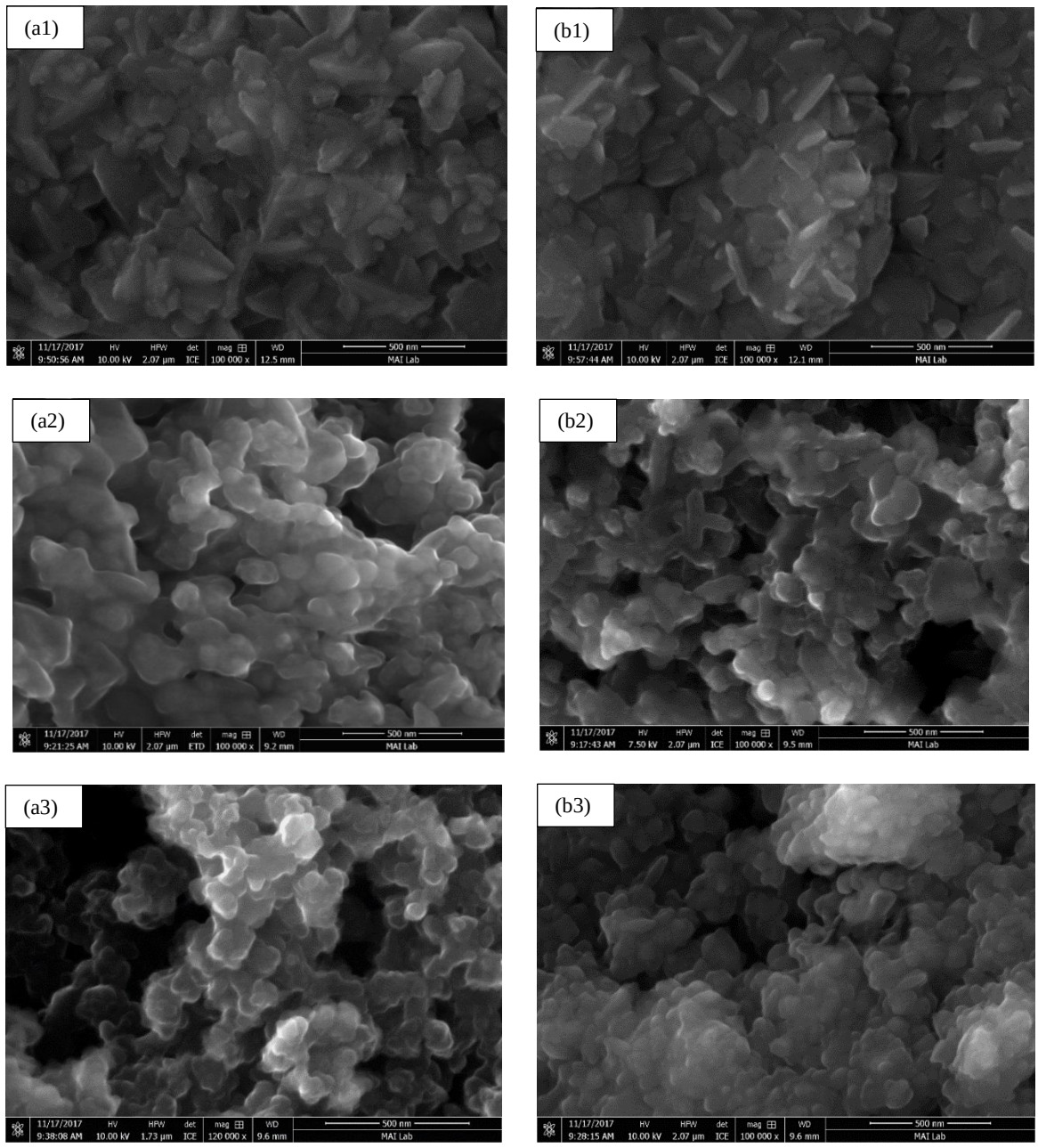

Figure 15: SEM images of PTFE 15% electrodes after (a1) continuous and (b1) intermittent discharge at 0.5 mA/cm^2, (a2) continuous and (b2) intermittent discharge at 1.0 mA/cm^2, (a3) continuous and (b3) intermittent discharge at 1.5 mA/cm^2.

4.2.2 Multi-Step Strategy.The existing studies usually report the Li−O_2 batteries discharged at a current density on the order of 0.1 mA/cm^2 which is too low compared with the operating current density of Li-ion batteries. I make efforts to increase the capacity at much

higher current densities in Paper **P2**. When the current density is set at 2.0 mA/cm^2 and the discharge cut-off is 2.0 VDC, the intermittent and continuous strategies show little difference in discharge capacity. The continuous discharge capacity is 423.4 ± 29.1 mAh/g and the intermittent discharge capacity is 436. 4 ± 45.5 mAh/g. Thus, the intermittent discharge strategy only slightly increases the specific discharge capacity by 3%. Based on the results shown in Figure 16, the battery stops discharging because the over-potential caused by polarization exceeds the difference between open-circuit voltage and a cut-off voltage of 2.0 VDC. When the discharge cut-off voltage is changed into 1.0 V, the intermittent discharge capacity reaches 1683.9 ± 148.7 mAh/g while it is only 800.2 ± 162.1 mAh/g at continuous discharge current. This reveals that the battery may be further discharged even after it reaches the cut-off voltage at a high current density. The discharge curves at 2.0 VDC cut-off voltage drop linearly towards 2.0 VDC without forming a discharge plateau. The battery stops discharging because the over-potential caused by polarization exceeds the difference between open-circuit voltage and cut-off voltage of 2.0 VDC. When the cut-off voltage is set at 1.0 VDC, the plateaus are built and the discharge capacities are increased. This reveals that the battery may be further discharged even after it reaches the cut-off voltage at high current density. This finding leads to the study of multistep discharging at decreasing current rates. Moreover, the discharge cut-off voltage cannot go below 2.0 VDC since the Li_2O is generated under 2.0 VDC. This discharge product is undesired due to its irreversible during the charging process. Thus, I propose a multi-step strategy for discharging the battery at a high current density which is shown in Figure 17. The discharge capacity increases to 855 ± 49.9 mAh/g when the battery is further discharged at 1.5 and 1.0 mA/cm^2.

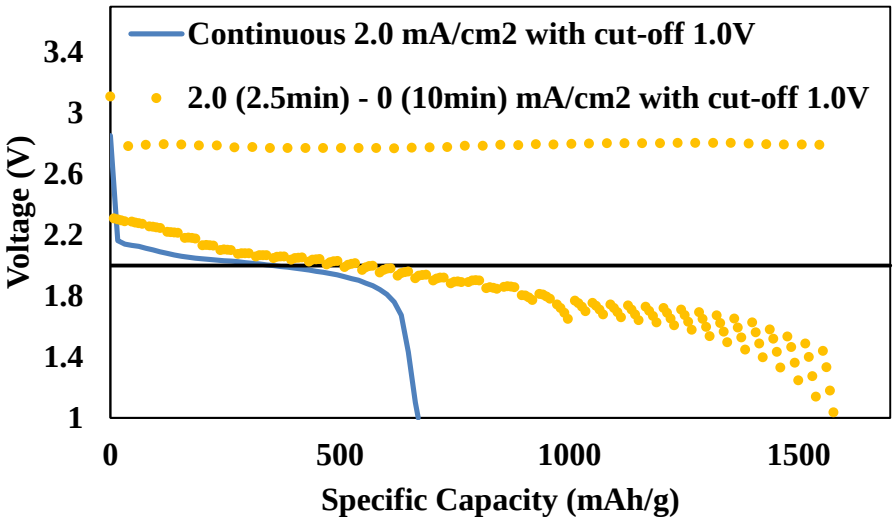

Figure 16: Discharge curves of Li–O_2 batteries with PTFE 15% electrodes discharged at (a) 2.0 mA/cm^2 continuously and intermittently.

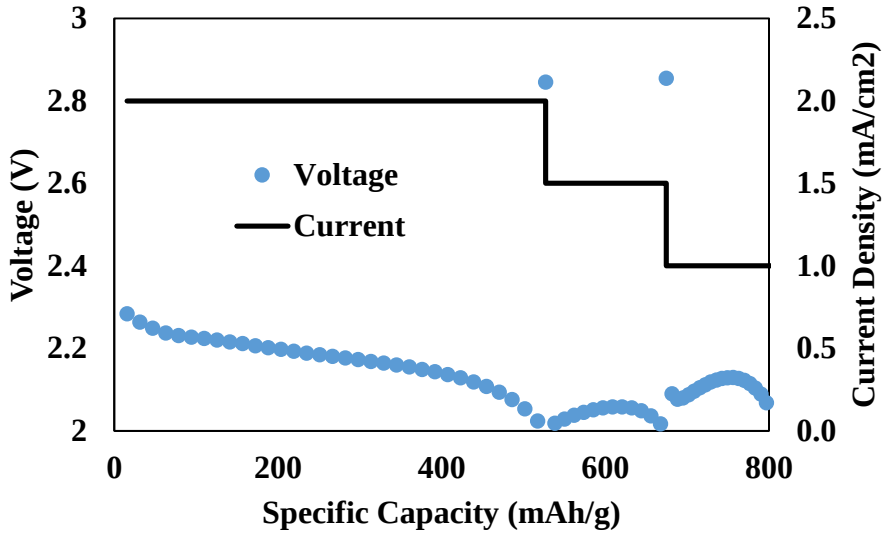

Figure 17: Discharge curves of Li–O_2 batteries with PTFE 15% electrodes discharged at a multi-step current.

4.2.3 Coupled Effects of Electrode Wettability and Intermittent Strategy. As discussed in Chapter 3, O_2 diffusion is also affected significantly by the electrode wettability. Three kinds of electrodes (PVDF 15%, PTFE 15% and Mixed I 15%) for Li-O_2 batteries are selected and experimented in Paper **P2**. Electrodes with PTFE 15% and Mixed I 15% binders are

lyophobic which can promote the O_2 diffusion. The electrode with PVDF 15% binder is lyophilic which is able to provide adequate reaction sites. The results of the intermittent and continuous discharge capacity at 1.0 mA/cm^2 are shown in Figure 18 and Table 4. The specific discharge capacity of Li-O_2 battery with mixed binders increases from 1645.9 ± 98.3 mAh/g to 2256.7 ± 225.8 mAh/g when the operation changes from continuous discharge current to intermittent discharge current. The specific discharge capacity of the PVDF 15% electrode is 1664.8 ± 259.6 mAh/g at intermittent current but it is only 807.6 ± 137.6 mAh/g at continuous 1.0 mA/cm^2. The discharge capacity is improved by 106.2%, much higher than those of the PTFE 15% electrode (51%) and the mixed 15% electrode (38%). The lyophilic PVDF 15% electrode is completely wetted by the electrolyte. The number of reaction sites increases but the O_2 diffusion is impeded due to the low O_2 diffusivity in the liquid electrolyte. Therefore, enhancing O_2 supply may be more urgent in this case. Experimental results demonstrate that Li−O_2 batteries with lyophilic electrodes are more sensitive to the intermittent discharge current and the discharge capacity can be increased more significantly. The mixed 15% electrode results in the highest discharge capacity which coincides well with results in previous study [96]. This is because the balance is achieved between dried regions for fast O_2 diffusion and wetted areas for electrochemical reactions. The discharge curves shown in Figure 19 followed the trend in Figure 14 in general. At the end of discharge, the potential decreases significantly and then increase gradually every time when the battery is discharged after the rest. As more Li_2O_2 is deposited in the electrode, the potential drop when the current changes from 0 to 1.0 mA/cm^2 is more obvious. When the potential drops below 2.0 VDC, the "sudden death" occurs and the battery stops discharging. The voltage of discharge plateau of the Li−O_2 battery with mixed 15% electrode is slightly higher (0.05 VDC < ΔV<0.1VDC) than these of the batteries with the other two kinds of electrodes,

which agrees well with its highest discharge capacity. The results demonstrate that Li−O_2 batteries with lyophilic electrodes are more sensitive to the intermittent discharge current and the discharge capacity can be increased more significantly.

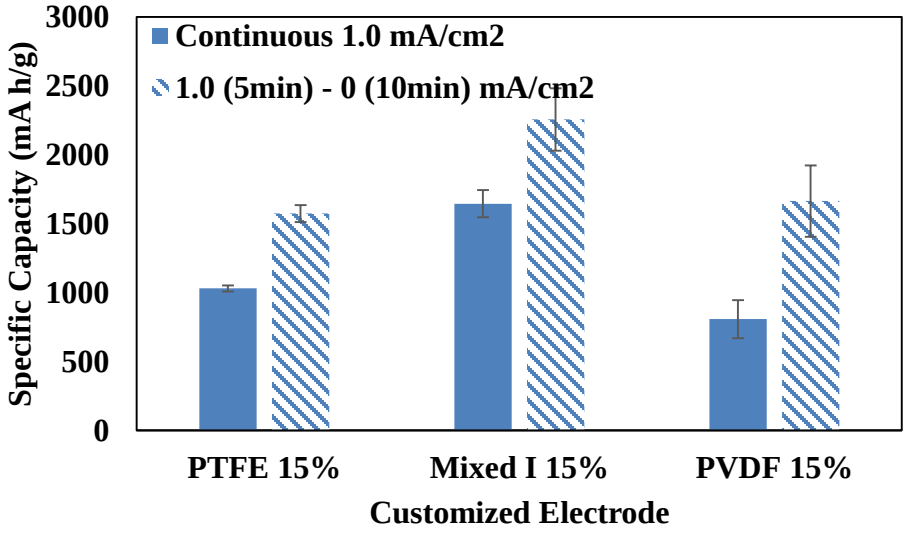

Figure 18: Results of Li−O_2 batteries with electrodes of different wettability discharged at 1.0 mA/cm^2 continuously and intermittently.

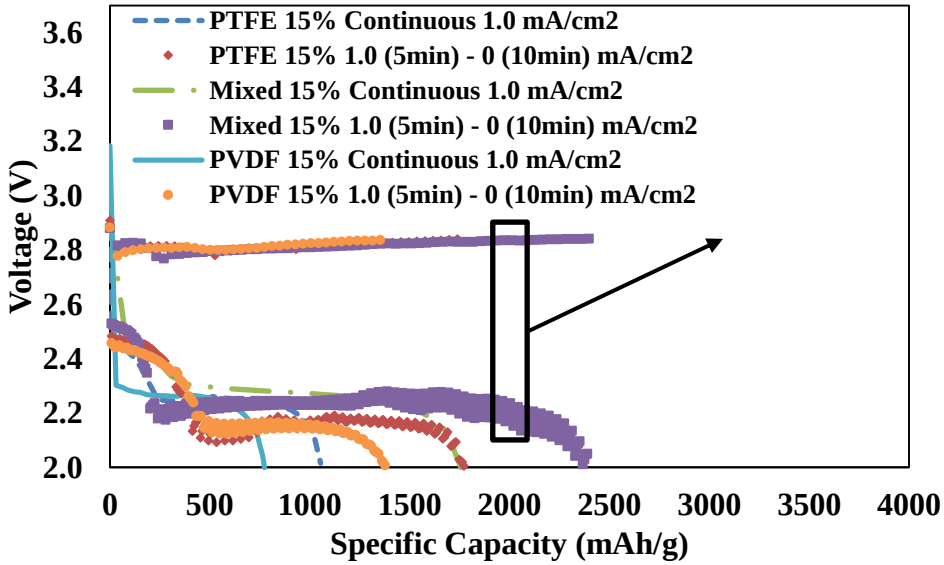

Figure 19: Discharge curves of Li−O_2 batteries with electrodes of different wettability discharged at 1.0 mA/cm^2 continuously and intermittently.

Table 4: Discharge capacity of electrodes with various wettability at intermittent and continuous currents.

Electrode	Strategy	Discharge Capacity (mAh/g)
PTFE 15%	Continuous 1.0 mA/cm^2	1030.9 ± 22.8
PTFE 15%	1.0 (5min) – 0 (10min) mA/cm^2	1629.5 ± 124.0
Mixed I 15%	Continuous 1.0 mA/cm^2	1645.9 ± 98.3
Mixed I 15%	1.0 (5min) – 0 (10min) mA/cm^2	2256.7 ± 225.9
PVDF 15%	Continuous 1.0 mA/cm^2	807.6 ± 137.6
PVDF 15%	1.0 (5min) – 0 (10min) mA/cm^2	1664.8 ± 259.7

4.2.4 Customized Strategy. In previous experiments, the estimated time of discharging for 5 min and resting for 10 min may not be suitable for all experimental cases. Thus, different intermittent discharge strategies are investigated experimentally, which are shown in Figure 20 and Table 5. The subsection tests the mixed 15% electrode at discharge current of 1.0 mA/cm^2. With the rest time of 10 min, the specific discharge capacities decrease slightly from 2298.1 ± 135.1 mAh/g to 2256.7 ± 225.8 mAh/g as the discharge time varies from 2 min to 5 min. Although the capacity difference is negligible, the strategy of intermittent current 1.0 (2 min) – 0 (10 min) mA/cm^2 is less time-efficient. Discharging the battery for 10 min and resting for 10 min suffers the lack of O_2 supply which results in lower discharge capacity of 1941.6 ± 110.3 mAh/g. When the discharge time is set to be 5 min, the specific discharge capacity decreases gradually from 2357.5 ± 138.2 mAh/g to 2121.0 ± 191.8 mAh/g when the rest time increases from 5 min to 15 min, which may be mainly due to the electrolyte evaporation [77]. Considering the time efficiency and the capacity increase, the optimized strategy for the Li−O_2 battery with the mixed 15% electrode at 1.0 mA/cm^2 is discharging for 5 min and resting for 5 min. The intermittent

discharge strategy may need to be customized based on the wettability and discharged current densities.

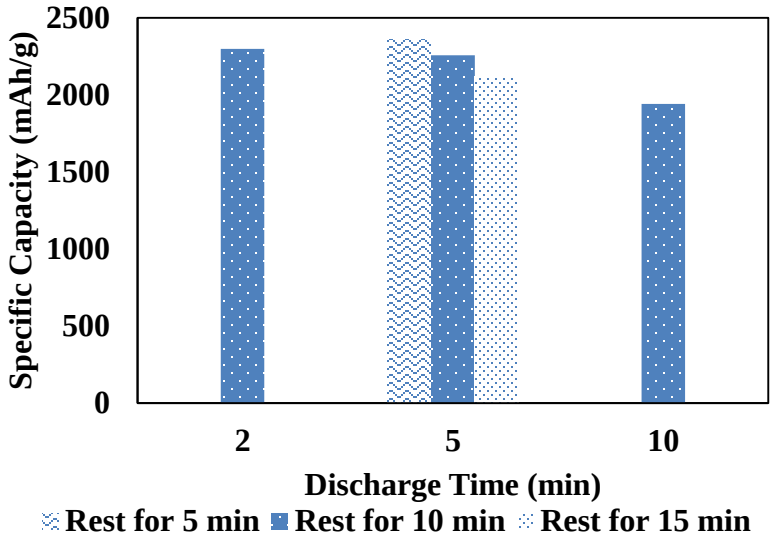

Figure 20: Specific discharge capacities of Li−O_2 batteries with mixed 15% electrodes at 1.0 mA/cm^2 with different intermittent discharge strategies.

Table 5: Customized strategies of Mixed I 15% electrode at 1.0 mA/cm^2.

Discharge Time (min)	Rest Time (min)	Discharge Capacity (mAh/g)
2	10	2298.1
5	10	2256.7
10	10	1941.6
5	5	2357.5
5	15	2121.0

4.2.5 Cycling Performance. The electrodes with mixed 15% binders are discharged and charged with the cut-off capacity of 1000 mAh/g and 1500 mAh/g, respectively. Discharge strategies include continuous 0.1 mA/cm^2 and 1.0 mA/cm^2 and intermittent 1.0 (5 min) – 0 (5

min) mA/cm^2 but all batteries are charged at a continuous current of 0.1 mA/cm^2. Figure 21 shows that the cycle numbers vary between 7 and 9 and the coulombic efficiencies are above 85%. After the last cycle, the voltages of $Li-O_2$ batteries reach the cut-off voltage of 2.0 VDC and thus the tests stop. The cycling performance of $Li-O_2$ batteries are similar despite of the discharge current. We speculate that failures of cycling tests are mainly attributed to the Li anode which may be contaminated by the water in the atmosphere. The symmetrical battery with Li chips on both anode and positive electrode is cycled and analyzed to validate the assumption. The cycling performance of $Li-O_2$ batteries is similar despite the discharge current. I speculate that failures of cycling tests are mainly attributed to the Li negative electrode which may be contaminated by the water in the atmosphere. The symmetrical battery with Li chips on both negative electrode and positive electrode is cycled and analyzed to validate the assumption. The over-potential caused by water contamination on Li chip is more than 1.0 VDC after 14 cycles. The cycle can continue with almost 100% coulombic efficiency after replacing the Li chip. Applying the intermittent discharge strategy is advantageous over the continuous discharge strategy since it can cycle the batteries with higher cut-off capacity (e.g., 1500 mAh/g), which has been proved in Figure 21.

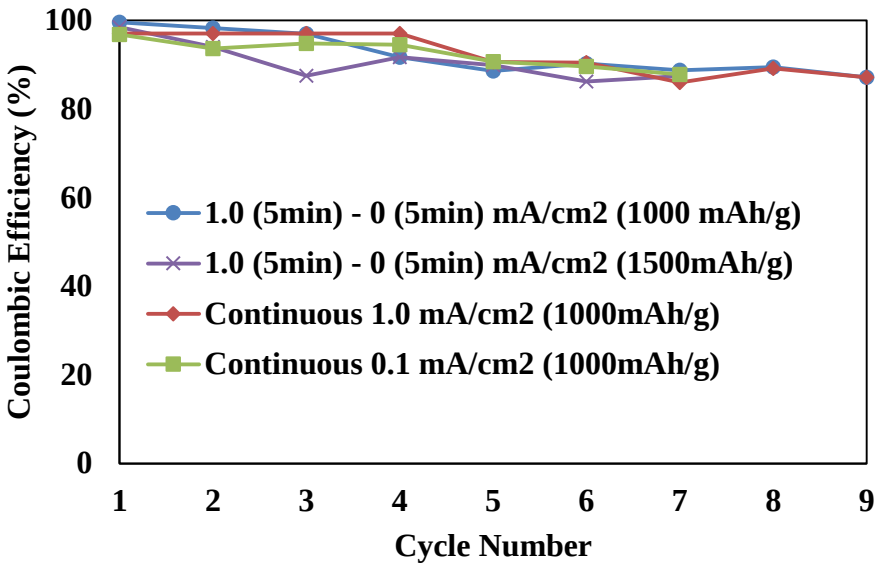

Figure 21: Coulombic efficiencies of Li−O_2 batteries discharged in the cycling tests.

4.2.6 Li Symmetric Battery. I investigate the effects of electrode wettability and discharge strategy on the performance of Li−O_2 batteries in Chapter 3 and Chapter 4. Commonly, results indicate that O_2 diffusion in the positive electrode mainly controls the discharging and cycling performance. In order to double-check the limiting factor, we apply the Li symmetric battery into the experiment. The Li chips are inserted in both the negative electrode and the positive electrode, which is shown in Figure 22. Figure 23 displays the voltages of Li symmetric batteries at 1.0, 5.0, and 10.0 mA/cm^2. The potentials caused by the Li chip during both the charging and discharging processes are less than 1.0 VDC. Therefore, the feasibility of discharging and charging Li−O_2 batteries is not prevented by the Li chip, and the O_2 diffusion in the positive electrode has been demonstrated to be the limiting factor. Moreover, the cycling experiment of Li symmetric batteries is conducted at 10.0 mA/cm^2. As shown in Figure 24, the Li symmetric battery is able to cycle at high current density. In conclusion, it is urgent to

improve the O_2 diffusion in the positive electrode and the efforts I have made in this dissertation is of great importance.

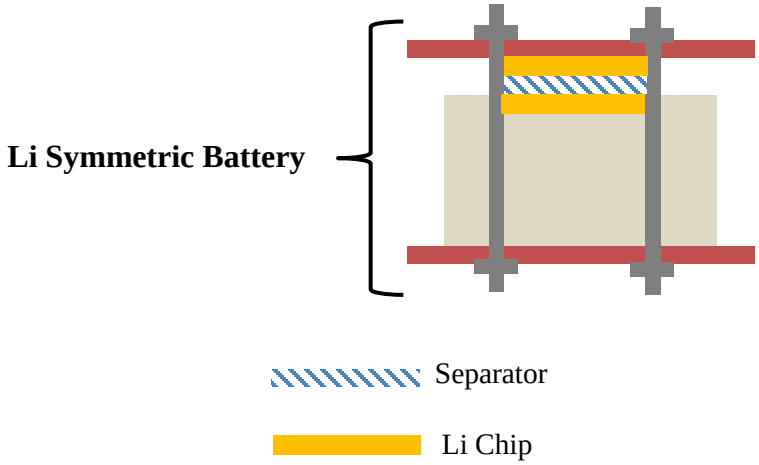

Figure 22: The schematic of a Li symmetric battery.

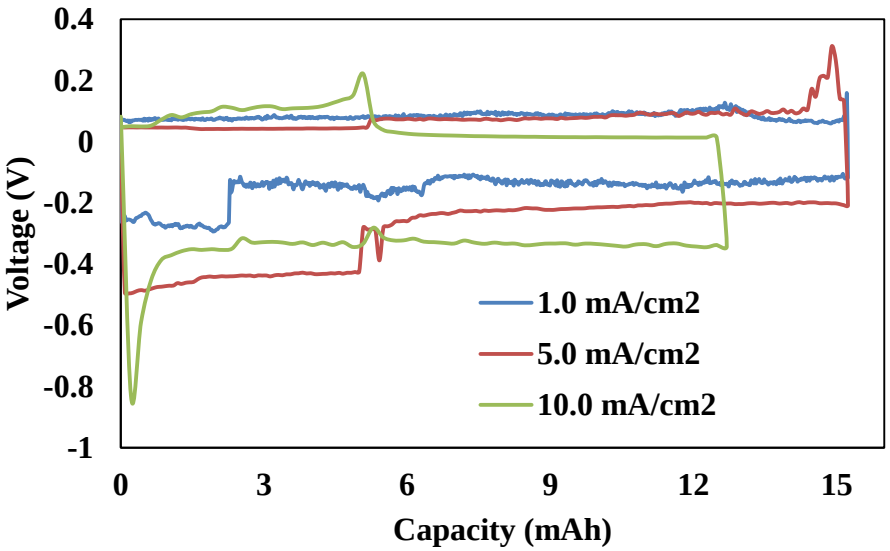

Figure 23: Voltages of Li symmetric batteries at various current densities.

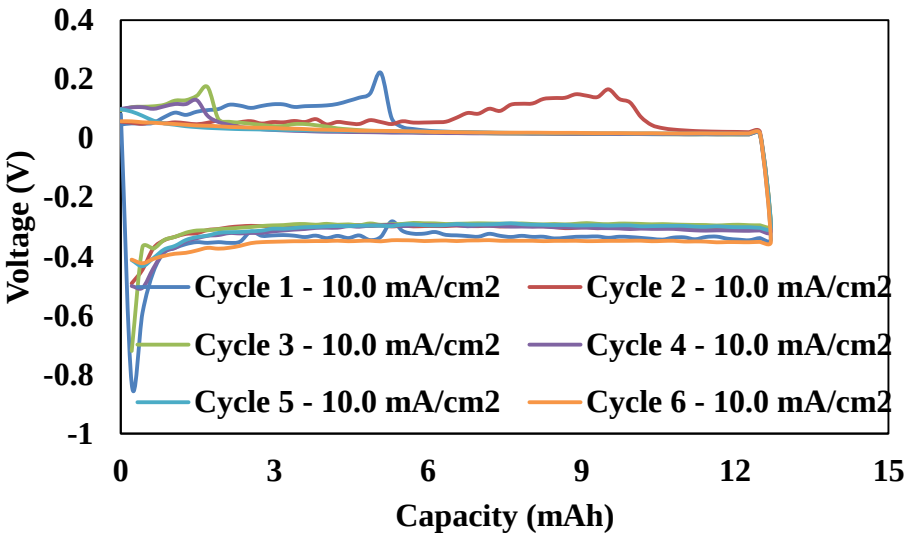

Figure 24: Cycling performance of Li symmetric batteries at 10.0 mA/cm^2.

In Paper **P2**, the intermittent discharge approach can serve as a practical way to improve the deep discharge capacity even at high current densities (> 1.0 mA/cm^2). The Li-O_2 batteries were discharged and rested periodically when intermittent strategy was applied. The intermittent discharge current can enhance the O_2 diffusion and increase the discharge capacity due to sufficient O_2 supply. Battery stacks for transportation or stationary applications will likely be composed of thousands of single cells. These single cells can be easily grouped and controlled separately following strategies investigated in this study: while some cells are discharging, other cells could be at rest to recover the oxygen. The discharge capacities of Li-O_2 batteries with PTFE 15% electrodes increased by 50% when these batteries were discharged at intermittent currents of 0.1, 0.5, 1.0 and 1.5 mA/cm^2. The discharge capacity was doubled when the battery was discharged at intermittent 2.0 mA/cm^2 with 1.0 cut-off voltage. Besides, the Li-O_2 batteries can be further discharged at lower current densities (1.5, 1 mA/cm^2 etc.) after it reaches the discharge cut-off voltage at a high current (2.0 mA/cm^2). The Li-O_2 batteries with lyophilic electrodes such as PVDF 15% electrodes were more sensitive to the intermittent discharge current. More than 100% increase on the discharge capacity was observed when the Li-O_2

batteries with PVDF 15% electrodes were discharged at intermittent 1.0 mA/cm^2. Mixed 15% electrodes balanced the wetted regions for reactions and dried paths for O_2 diffusion and increased the discharge capacity. The Li-O_2 batteries with mixed 15% electrodes gained the highest capacity of 2256.7 ± 225.8 mAh/g at the intermittent current of 1.0 mA/cm^2. The optimized intermittent discharge strategy depended on the electrode wettability and discharge current. For the Li-O_2 batteries with mixed 15% electrode at intermittent 1.0 mA/cm^2, the discharge time was determined to be 5 min and resting time for O_2 diffusion was also 5 min.

Chapter 5: Numerical Investigation of Electrolyte Saturations

Chapter 5 is adapted from Paper **P3**.

5.1 Introduction

The previous Chapter 3 and Chapter 4 focused on the experimental study of electrode wettability, which shows that O_2 diffusion is a key factor that limits the discharge capacity of Li−O_2 batteries. In Chapter 5, I use a numerical approach to investigate the distribution of the electrolyte at various saturations and obtain the corresponding discharge performance of Li−O_2 batteries. Compared with the experimental method, the numerical approach is more effective to capture and analyze the electrochemical process during the operation of batteries. Paper **P3** focuses on effects of liquid-gas two-phase mass transfer within the porous electrode on the electrochemical performance of batteries.

The spatial distributions of the liquid and vapor phases in the porous electrode is governed by the evaporation of the electrolyte, volume change of solid materials, pore size, wettability, and connectivity of pores. Our recent study of Li-O_2 batteries indicated that the amount of the electrolyte strongly affected the specific discharge capacity [77]. The discharge capacity is strongly affected by both the initial amount of the electrolyte and its evaporation rate (controlled by the cathode open ratio). The maximum discharge capacity was achieved at 25% open ratio among the selected open ratios (0% - 100%) at the current density of 0.1 mA/cm^2. As the open ratio increased from 25% to 100%, the specific discharge capacity decreased from 995 to 397 mAh/g_{carbon}. The fast evaporation of electrolyte at higher open ratios resulted in the decrease of the discharge capacity with increasing open ratio. A similar experiment carried out by Jiang et al.[97] also studied the effects of the oxygen window on the capacity of Li−O_2 batteries. In this work, a single hole with different diameters was machined on the oxygen side of

the coin-cell battery as the oxygen window. It should be noted that the maximum open ratio (ratio between oxygen window area to the total electrode surface area) was only 19.5%. The battery used 50 μL of $LiCF_3SO_3$-TEGDME (1:4 molar ratio) as the organic electrolyte solution. The first discharge-charge cycle of the Li−O_2 batteries at a current of 0.1 mA showed that battery capacity increases linearly with the size of the oxygen window.

During the charge and discharge cycles of the battery, the volume of both the solid materials change significantly due to the consumption/generation of Li_2O_2 at the cathode and the deposition/consumption of Li metal at the anode. As a result, the electrolyte redistributes in pores during the battery operation. Yoo et al. [98] developed a model to study the significance of the volume change of the Li anode corresponding to the discharge performance of the battery. During discharge, the decomposition of lithium metal at the anode leads to a gap between the separator and Li anode. The gap grew bigger with discharge due to the decomposition of lithium metal, and gap was assumed to be always filled with the electrolyte. Meanwhile, the porosity and pore volume of the cathode electrode decreased with discharge because of the deposition of Li_2O_2, which expelled excess electrolyte from the cathode. The leakage of the electrolyte is proportional to the discharge capacity and 2.15% of the electrolyte leaked out at the specific capacity of 650 mAh/g.

The direct measurement of the distribution and evaporation of the electrolyte by experiments is very challenging due to the small pore size and complex geometry of the pores. Therefore, models provide detailed information on the transport phenomena in liquid-vapor two-phase flow in the porous electrode. Our recent study [77] has carried out a simple model to simulate the discharge capacity considering the evaporation of the electrolyte. The model simplified the evaporation of the electrolyte as the moving of the electrolyte-air interface at a

constant speed (which is proportional to the cathode open ratio). Huang and Faghri [99] developed a 2-D model that captured electrolyte evaporation into the air chamber of the battery. The evaporation rate was a function of the partial pressure of solvent vapor and air chamber size. A highly volatile electrolyte, DMF, and a less volatile electrolyte, TEGDME, were compared in this study. The evaporation rate decreased with discharge and stopped once the partial pressure of the solvent in the air chamber reached saturation. The evaporation of the electrolyte had a significant influence on the Li_2O_2 distribution and discharge capacity. The reaction sites with the fastest reaction rate moved with the electrolyte-air interface away from the air inlet. The whole electrode was better utilized due to the improved oxygen supply. After considering the evaporation of the electrolyte, the specific discharge capacity of the battery increased by 22.5% and 14.9% with DMF and TEGDME electrolytes, respectively. It was also demonstrated that the size of the air chamber was critical: increasing the air chamber radius from 5 cm to 15 cm led to a capacity increase of 72%. The analytical model developed by Ye et al. [100] also showed that a flooded electrode negatively impacts the battery performance. A partially wetted electrode was preferred to promote the diffusion in the gas phase and decrease the concentration over-potential.

The wettability of the electrode, which determines the distribution of the electrolyte, is a critical factor on battery capacity. Our experimental studies customized battery electrodes using Acetylene Black carbon powder and different polymer binders (PVDF and PTFE) [62]. The different surface energy of the polymer binders leads to variations of electrode wettability. It was found that slightly hydrophobic electrodes (with 15wt% PTFE) are more favorable than hydrophilic electrodes (with PVDF) for higher discharge capacities. The higher discharge capacity is resulted from the improved oxygen transfer due to more available gas phase. Strongly hydrophobic electrodes (with 30wt% PTFE), however, have low discharge capacity due to the

over dry of the electrode. Considering the balance of improved mass transfer with the available reaction sites, this study proposed electrodes with combined hydrophilic and hydrophobic layers. The specific capacity of the electrode with mixed wettability was more than three times (1665.8 vs. 5149.5 mAh/g) higher than the hydrophilic electrode. Although the improved mass transfer at the pore scale results in superior electrochemical performance, direct observations of the pore-scale transport phenomena by experiments are extremely difficult. The distribution of the electrolyte and mechanism of the liquid-gas multi-phase transfer at the pore scale is unclear. Therefore, it is important to study the pore-scale distribution of each phase to resolve key scientific issues and engineer advanced battery electrodes to meet the target specific energy and current density.

Extensive experimental studies and numerical simulations have been carried out to investigate the statistical and spatial distributions of the pore size in electrodes of fuel cells [101-102], super capacitors[103], and redox flow batteries[104]. Only limited number of experiments[105-106] and numerical simulations[107-108] studied the pore size distribution of Li-O_2 batteries. Since smaller pores lead to higher surface area per volume and provide more reaction sites, experiments attempted to decrease the pore size to increase the specific capacity of the battery. However, there is no obvious correlation between the specific energy of the battery and the surface area or porosity. Numerical simulations also try to consider the effect of pore size on the discharge capacity of batteries. Xue et al.[107] developed a model that considers the passivation of the electrode surface by the deposition of Li_2O_2. The model assumed that the pore becomes inactive either once it is completely blocked by the Li_2O_2 film or the thickness of Li_2O_2 is more than 10 nm. The performance of two electrodes with different pore size distributions made from Super P and Ketjen Black, respectively, are the compromise between the high initial

surface area and low degradation rate of active surface area. Andrei and Bevara [108] simplified the battery electrode as a bunch of cylindrical pores with a distribution of diameters. It was found that electrodes with the same mean diameter (20 nm) but different standard deviations could have very different discharge performance due to the different characteristics of small and large pores.

The above mentioned experimental and numerical studies haven't considered the fact that very small pores (~ nm) may not be available for reactions, therefore do not contribute to the battery capacity, if they are isolated or have extremely high mass transfer resistance. In comparison, the surface areas per volume of large pores are low, although they have low mass transfer resistance. The different mass transfer characteristics of pores with different sizes lead to the hypothesis that micro pores that are smaller than the critical pore size does not contribute to the discharge and charge of electrochemical devices due to the limited mass transfer capability. To understand the effect of critical pore size, Li [109] developed a statistics model to simulate the microstructural evolution of porous electrodes. The model assumed that pores smaller than a critical pore size have too high mass transfer resistance so that they do not contribute to the discharge of the battery. The micro structural change was also coupled with a computational fluid dynamics model to simulate the discharge performance. Effects of electrode properties, operating parameters, as well as the pore size distributions have been investigated. At a given critical pore size (10 nm), the discharge capacity first increased with the increase of the average pore size (from 10 to 50 nm) due to the improved mass transfer, followed by a capacity decrease when the average pore size further increased to 100 nm due to the decrease of the effective surface area.

The detailed distributions of electrolyte and pore requires the clear understanding of pore-scale structure of the electrode. However, the complex microstructure of electrodes is very difficult to measure and reconstruct and none of the previously mentioned studies directly measure and consider the spatial distributions of pores and electrolyte. Although pore-scale structure reconstruction and simulations have been carried out in fuel cells [110-111], the authors are not aware of detailed measurements and model simulations pore structures of $Li-O_2$ battery electrodes. To fill this knowledge gap, Paper **P3** includes developing an electrochemical model, based on reconstructed pore-scale geometries of porous electrodes, to simulate the discharge performance (current, voltage, local reaction rates etc.) of the electrode with various saturations of the electrolyte. This model considers the multi-phase mass transfer in porous electrodes and sheds lights on the critical role of liquid-gas two-phase mass transfer within the porous electrode on the electrochemical performance of batteries. The findings from this study enables further research to significantly increase (by orders of magnitude) the operating current and power of the $Li–O_2$ battery and accelerate its deployment to transport and stationary applications.

5.2 Reconstruction of Electrode

The reconstructing procedure begins with obtaining a series of scanning electron microscope (SEM) images. Then, the correlation function is applied to complete the reconstruction of the battery electrode. Basically, the SEM images of dozens of electrode slices are produced by the focused ion beam (FIB). The SEM images have the resolution of 1.34 nm per pixel in order to see the pore structures of the electrode slices. The field of view, however, is limited to be $1.136 \times 1.136\ \mu m^2$. The small field of view cannot provide a representative unit of the electrode (~200 μm thick) to investigate the mass transfer coupled with electrochemical reactions. Therefore, this study will generate a digital battery electrode (with the size of

186.0×5.8 μm^2) with detailed pore-scale structures using correlation functions as a representative unit of the model simulation. The target two-point correlation function is then used to reconstruct electrodes iteratively. The summary of processing SEM images is shown in Figure 25 and the equations used in reconstruction are provided in

Table 6. Figure 26 shows the flowchart of the entire reconstruction process. Once a digital electrode is numerically generated, its pore size distribution and the effective surface area can be derived statistically using the erosion-dilation method[112]. The erosion process can erase any foreground pixel (pore) that has at least one neighbor that is the background pixel (solid) in the binary images. While the dilation process erases any background pixel (solid) that has at least one neighbor that is the foreground pixel (pore). The erosion and dilation processes start with a small circular structuring element (with only one voxel) and are repeated with larger and larger circular structuring elements. The change of the cumulative volume fraction of foreground pixel with the size of circles leads to the histogram of pore size distribution. The surface area of the digital electrode is calculated by tracking the amount of carbon/pore interface. The accuracy of the reconstructed geometries has been validated by comparing pore size distributions and effective surface area of numerically generated electrode with experimental measurements by the NOVA Touch pore size analyzer. Once the digital electrode is reconstructed and validated, slices of the porous electrode will be applied to electrochemical models to simulate the species distribution, reaction rate, and pore-scale structure change of the electrode during discharge.

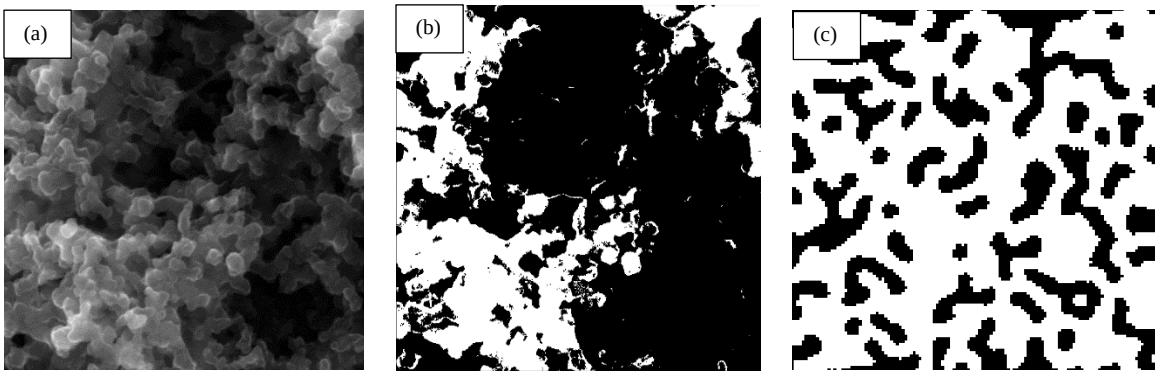

Figure 25: (a) The original SEM image; (b) the binary image of a customized battery electrode, and (c) part of the reconstructed electrode (128×128 pixels) from the binary image.

Table 6: A summary of equations for the reconstruction.

Number	Equation	Description
5.1	$F(\vec{x}) = \begin{cases} 0 & \text{Gas} \\ 1 & \text{Solid} \end{cases}$	distribution of each phase within the electrode, $\vec{x}$ is the position of the selected point
5.2	$s_2(\vec{x}_1, \vec{x}_2) = < F(\vec{x}_1)F(\vec{x}_2) >$	the probability that two randomly selected points $\vec{x}_1$ and $\vec{x}_2$ fall into the same phase
5.3	$\left.\frac{ds_2(r)}{dr}\right\|_{r=0} = -S/4$	the specific surface of a 3D medium
5.4	$E^i = \sum_r \left[s_2^i(r) - s_{2,\text{target}}(r)\right]^2$	the energy difference *E* between these two correlation functions
5.5	$p = \begin{cases} 1 & \text{when } \Delta E < 0 \\ \exp\left(\frac{\Delta E}{T}\right) & \text{when } \Delta E > 0 \end{cases}$	The criterion to switch two selected points

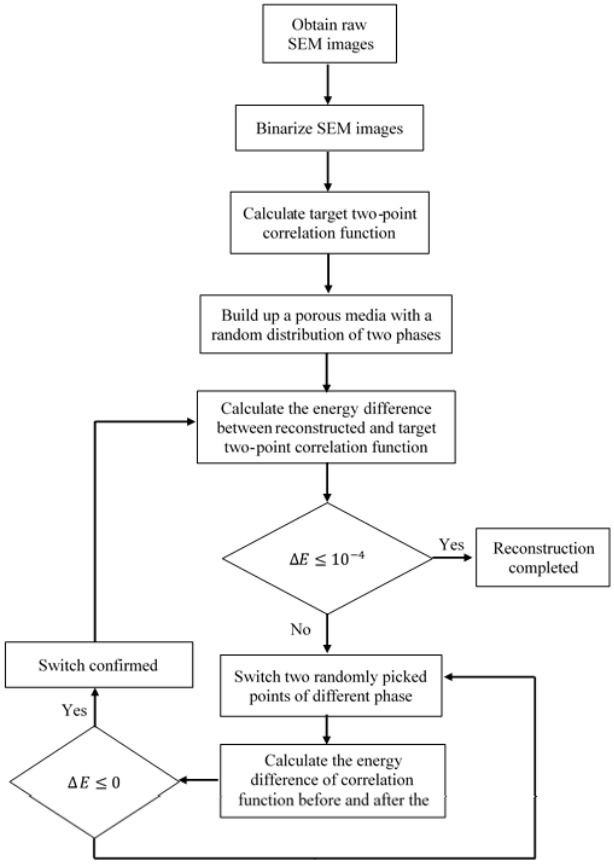

Figure 26: A flowchart of the reconstruction process.

5.3 Electrochemical Model

After the digital electrode is reconstructed, it can be imported into CFD models based on a finite volume method (FVM) to simulate the mass transfer coupled with electrochemical reactions at the pore scale. The computational domain includes the whole porous electrode partially filled with electrolyte. The typical battery electrodes have very high aspect ratios. The height of the electrode is on the order of centimeter while the thickness of the electrode is on the order of hundreds of micrometers. Since the transport phenomena along the height of the electrode are very similar or follow a repeat pattern, it's reasonable to simulate a representative unit of the electrode in order to save computational time. Therefore, a representative unit shown in Figure 27 is selected and applied to the electrochemical model. The equations used to describe

the electrochemical process are summarized in Table 7 and the parameters used in this model is shown in Table 8.

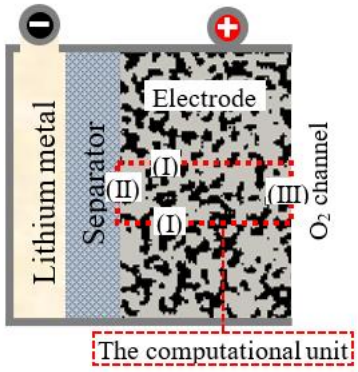

Figure 27: The computational domain and the boundary conditions of a Li−O_2 battery using organic electrolyte.

Table 7: A summary of equations in the electrochemical model.

Number	Equation	Description
5.6	$\frac{\partial(\rho_{EL}\omega_{Li+})}{\partial t} = \nabla\cdot\left(\rho_{EL}D_{Li+}^{eff}\nabla\omega_{Li+}\right) - \nabla\cdot\left(\frac{i_{EL}t_+}{F}M_{Li+}\right) + \dot{m}_{Li+}$	ω_{Li+} is the concentration of lithium ion, $\dot{m}_{Li+}$ is the consumption rate of lithium ion, i_{EL} is the current density, and t_+ is the transference number of Li^+
5.7	$\frac{\partial(\rho_{EL}\omega_{O2})}{\partial t} = \nabla\cdot\left(\rho_{EL}D_{O2}^{eff}\nabla\omega_{O2}\right) + \dot{m}_{O2}$	ω_{O2} is The concentration of oxygen in the electrolyte, $\dot{m}_{O2}$ is the consumption rate of oxygen
5.8	$\dot{m}_{Li+} = -\frac{R_{ORR}}{F}M_{Li+}$	R_{ORR} is the reaction rate of the oxygen reduction reaction (ORR), and M_{Li+} is the molecular weight of lithium ion
5.9	$\dot{m}_{O2} = -\frac{R_{ORR}}{2F}M_{O2}$	M_{O2} is the molecular weight of oxygen
5.10	$D_i^{eff} = D_i\varepsilon^{1-0.77\ln\varepsilon}$	D_i^{eff} is the effective diffusivity, D_i is the diffusion coefficient, ε is the porosity
5.11	$\varepsilon_{Li2O2}(t) = \frac{\int R_{ORR}\cdot dt}{2F}\frac{M_{Li2O2}}{\rho_{Li2O2}}$	ε_{Li2O2} is the local volume fraction of Li_2O_2
5.12	$R_{ORR} = k_{ORR}\cdot\frac{A_{active}}{V_{ED}}\cdot\left\{\left(\frac{\omega_{Li+}}{\omega_{Li+}^{ref}}\right)^2\cdot\left(\frac{\omega_{O2}}{\omega_{O2}^{ref}}\right)\cdot\exp\left(\frac{\alpha F\eta}{RT}\right) - \left(\frac{\omega_{Li2O2}}{\omega_{Li2O2}^{ref}}\right)\cdot\exp\left[-\frac{(1-\alpha)F\eta}{RT}\right]\right\}$	k_{ORR} is the standard constant rate of ORR, A_{ctive} is the active surface area of the electrode, V_{ED} is per volume of electrode, α is the transfer coefficient, and η is the over-potential
5.13	$A_{active} = A_{ED}\cdot x_{EL}$	A_{ED} is the total surface area of the electrode, x_{EL} is the fraction of the carbon surface wetted by the electrolyte

5.14	$k_{\mathrm{ORR}} = \begin{cases} i_0 \cdot \frac{A_{\mathrm{active}}}{V_{\mathrm{ED}}} \cdot \left(1 - 0.9 \cdot \frac{q}{7}\right) & \text{for } q \le 7\ \mathrm{C/m^2} \\ 0.15245\ i_0 \cdot \frac{A_{\mathrm{active}}}{V_{\mathrm{ED}}} \cdot 10^{-0.02616q} & \text{for } q > 7\ \mathrm{C/m^2} \end{cases}$	i_0 is the exchange current density, q is the quantity of discharged electricity per active surface area of the electrode
5.15	$q(t) = \frac{\int R_{\mathrm{ORR}} \cdot dt}{A_{\mathrm{active}}/V_{\mathrm{ED}}}$	
5.16	$V = E^0 - \eta - I \times \frac{0.5\delta_{\mathrm{ED}}}{\sigma_{\mathrm{ED}}^{\mathrm{eff}}}$	δ_{ED} is the thickness of the electrode and $\sigma_{\mathrm{ED}}^{\mathrm{eff}}$ is the effective ionic conductivity of the electrode

Symmetric boundaries are applied to the upper and lower boundaries (I) of the representative computational unit:

$$\frac{\partial \omega_{\mathrm{Li+}}}{\partial y} = \frac{\partial \omega_{\mathrm{O2}}}{\partial y} = 0 \tag{5.17}$$

When the electrode wettability is alternated along the *y*-direction, the non-flux boundary is applied to Li^+ and the constant concentration boundary condition is applied to O_2 at the upper and lower boundaries (I):

$$\left.\frac{\partial \omega_{\mathrm{Li+}}}{\partial y}\right|_{(\mathrm{I})} = 0 \text{ and } \omega_{\mathrm{O2}}|_{(\mathrm{I})} = \omega_{\mathrm{O2}}^0 \tag{5.18}$$

At the interface of the separator in the electrode (II), the flux of Li^+ is proportional to the discharge current density and the flux of O_2 is 0:

$$\rho D_{\mathrm{Li+}}^{\mathrm{eff}} \left.\frac{\partial \omega_{\mathrm{Li+}}}{\partial x}\right|_{(\mathrm{II})} = \frac{I}{F} M_{Li+} \text{ and } \left.\frac{\partial \omega_{\mathrm{O2}}}{\partial x}\right|_{(\mathrm{II})} = 0 \tag{5.19}$$

At the electrode – oxygen interface (III), the non-flux boundary applies to Li^+ and the O_2 concentration is set as the reference concentration:

$$\left.\frac{\partial \omega_{\mathrm{Li+}}}{\partial x}\right|_{(\mathrm{III})} = 0 \text{ and } \omega_{\mathrm{O2}}|_{(\mathrm{III})} = \omega_{\mathrm{O2}}^0 \tag{5.20}$$

The following results and discussions are based on the validated model and parameters.

Table 8: Electrochemical and physical parameters used in the model.

Parameter	**Symbol**	**Value**
Active area of electrode per volume	A_{ED}	1.43×10^{8} m^2/m^3
Thermodynamic equilibrium voltage	E^0	3.1 VDC [113]
Solubility of oxygen in electrolyte		4.395×10^{-3} mol/L [58]
Reference concentration of O_2	$\omega_{O2,\ ref}$	1.23×10^{-4} kg/kg
Reference concentration of lithium ion	$\omega_{Li+,\ ref}$	8.866×10^{-2} kg/kg
Conductivity of electrolyte	σ_{EL}	5×10^{-3} S/cm
Conductivity of the electrode	σ_{ED}	3 S/cm
Conductivity of Li_2O_2	σ_{Li2O2}	1×10^{-12} S/cm
Density of carbon	ρ_C	2.26 g/cm^3
Density of lithium peroxide	ρ_{Li2O2}	2.31 g/cm^3
Density of the electrolyte	ρ_{EL}	1.011 g/cm^3[58]
Exchange current density	i_0	3.11×10^{-6} A m^{-2} [86]
Diffusivity of oxygen in the electrolyte	$D_{O2,EL}$	9.12×10^{-10} m^2/s[58]
Diffusivity of lithium ion in the electrolyte	$D_{Li+,EL}$	8×10^{-11} m^2/s [81]

5.4 Results and Discussion

5.4.1 Electrochemical Model Validation. The typical battery electrodes have very high aspect ratios. The height of the electrode is on the order of centimeter while the thickness of the electrode is on the order of dozens or hundreds of micrometers. Since the transport phenomena along the height of the electrode are very similar or follow a repeat pattern, it's not uncommon to simulate a representative unit of the electrode in order to save computational time. As a result,

this model simulates a representative unit of a lithium-oxygen battery electrode with 186.0-μm thick and 5.8-μm high. The simulation results of discharge capacity vs. cell voltage at various discharge current densities are compared to the experiment data in Figure 28. The calculated specific capacities by our model agree well with experimental results and the following results and discussions are based on the validated model and parameters.

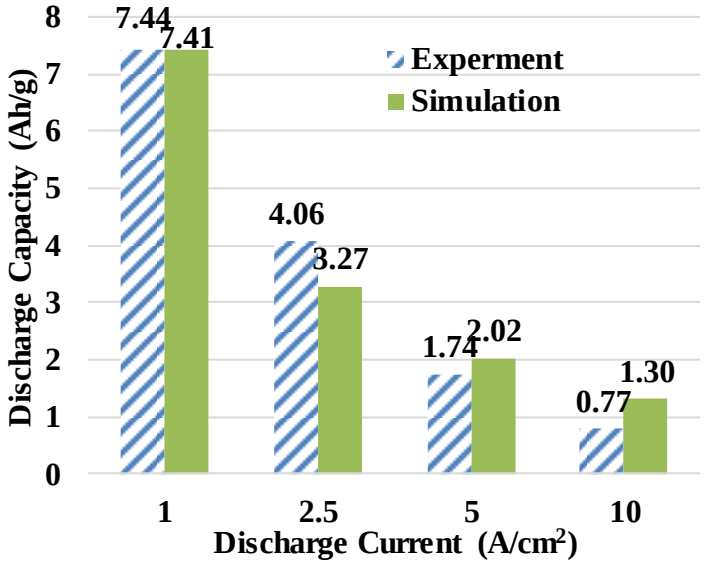

Figure 28: Discharge capacities of electrodes with 100% saturation at various discharge current densities: Experiments vs. Simulations.

5.4.2 Oxygen Distribution in Fully Saturated Electrode. The distributions of oxygen at 1 A/m^2 are also plotted in Figure 29. As can be seen from the plot, the oxygen concentration decreases from the saturated oxygen concentration (1.23×10^{-4} kg/kg) due to reactions. The deposition of Li_2O_2 reduces the porosity of the porous electrode, therefore, increase the mass transfer resistance of oxygen and lithium ion in the electrolyte. Most of the Li_2O_2 generated by the reaction deposits at the vicinity of the oxygen channel and blocks the transfer of oxygen. At the end of the discharge, the oxygen concentration reduces to less than 1.0×10^{-4} kg/kg in most of the electrode. As a result, reaction within the electrode stopes due to the lack of oxygen. The

high oxygen concentration along the depth of the electrode is caused by the low diffusivity of oxygen in the liquid electrolyte (2.17×10^{-6} cm^2/s). As a comparison, oxygen diffusivity in the gas phase (0.219 cm^2/s) is about 5 orders of magnitudes higher than that in the liquid electrolyte. In order to facilitate the oxygen transfer within the electrode and improve the electrochemical reaction deep in the electrode, this study investigates electrodes that are partially saturated by the electrolyte. The gas phase serves as the oxygen transfer media and significantly improves the mass transfer of oxygen.

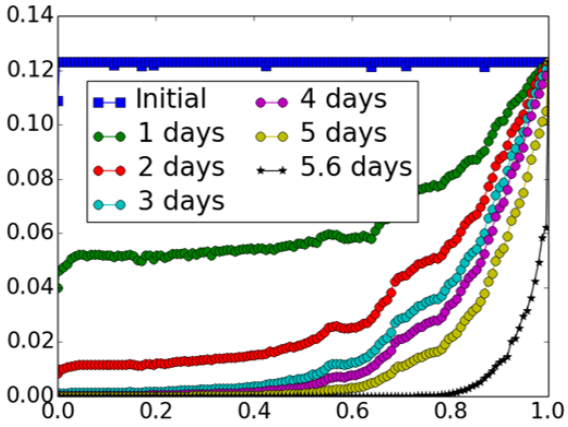

Figure 29: The distributions of O_2 when the battery is discharged at 1 A/m^2.

5.4.3 Electrode at Different Saturation Levels. The investigation starts with simplified distributions of the electrolyte. The electrolyte is assumed to occupy pores in the middle of the electrode first, which is shown in Figure 30. The volume fraction of the pores occupied by the electrolyte is proportional to the given saturation (100%, 87.5%, 75%, etc.). Figure 31 shows the discharge capacity of batteries with various electrolyte saturations (100%, 87.5%, 75%, and 50%). The discharge capacity increases significantly from 7.41 to 19.31 Ah/g when the saturation decreases from 100% to 87.5% since oxygen is more abundant. The increase of the discharge capacity is mainly driven by the improved oxygen transfer within the electrode. When the electrolyte fully saturates the electrode, the oxygen concentration within the electrode is

relatively low. While the oxygen concentration is much higher when the electrode is partially (87.5%) saturated by the electrolyte. The availability of the dry pores at the top and bottom of the electrode significantly improve the oxygen transfer through the gas phase. Therefore, the oxygen supply is more sufficient during discharge in partially saturated electrodes. On the other hand, when the saturation is further decreased to 75% and 50%, the discharge capacity decreases to 16.94 and 15.41 Ah/g. The decrease of the capacity is caused by the balance of improved oxygen transfer and availability of active reaction sites within the electrode. Since the discharge reaction (ORR) requires both oxygen and lithium ion, only carbon surface that has direct contact with the electrolyte can serve as the active reaction site. Reactions only happen when oxygen and lithium ion, that are dissolved within the electrolyte, reach the electric-conductive carbon surface. This model quantitatively exam the active surface area of the electrode by checking the pixels that are in the electrolyte phase and have carbon as neighbor cells.

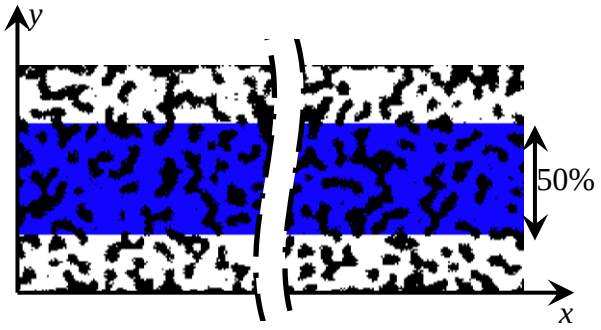

Figure 30: The distribution of the electrolyte (blue) within the porous electrode (black) at the saturation of 50%.

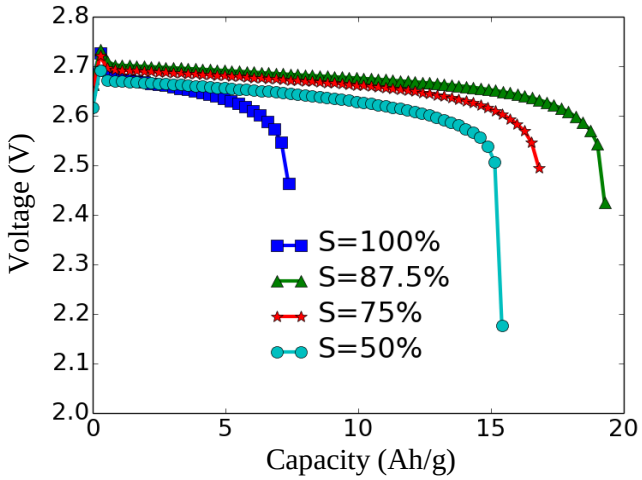

Figure 31: The corresponding discharge performance of electrodes with various electrolyte saturations at 1 A/m^2.

Figure 32 shows the oxygen concentration of electrodes with 100% and 87.5% of electrolyte saturations when the electrodes are discharged for 24 hours. The equivalent discharge capacity is 3.18 Ah/g for both electrodes. Most of the oxygen has been consumed in electrode with 100% saturation after 24 hours discharge (Figure 32 (a)). The evolution of the volume fraction of Li_2O_2 indicates that the volume fraction in the majority of electrode is below 0.2 at the end of discharge, although the porosity of the electrode is 0.65. The volume fraction of Li_2O_2 is proportional to the discharge capacity. Although the electrode with 100% saturation is still capable to host more solid product, the insufficient oxygen supply stopped the discharge. The depletion of oxygen within the electrode saturated by the electrolyte leads to the death of the battery fully saturated by the electrolyte. For comparison, the oxygen concentration in the electrode with 87.5% saturation is still relatively high after 24 hours discharge (Figure (b)). As a result, most of the electrode has sufficient O_2 for discharge and the volume fraction of Li_2O_2 reaches above 0.4 at the end of discharge. The dry pores near the top and bottom of the computational unit provide fast oxygen path. The diffusional length of the oxygen in the liquid

electrolyte is significantly decreased from the thickness of the electrode (~200 μm) to the height of the representative unit (~5 μm), which greatly improve the oxygen transfer. The electrode with 87.5% saturation continued discharging until the Li_2O_2 completely filled pores.

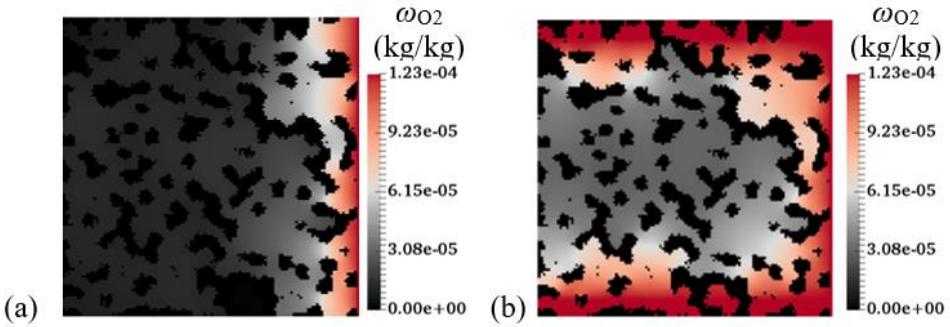

Figure 32: Distributions of O_2 in electrodes with (a) 100% and (b) 87.5% electrolyte saturations after discharging at 1 A/m^2 for 24 hours (3.18 Ah/g).

5.4.4 Electrolyte Distribution. Since the electrolyte is assumed to occupy the center of the electrode, the amount of the active reaction sites change in proportional to the saturation: 48.49% (50% saturation), 73.22% (75% saturation), 85.38% (87.5% saturation), and 100% (fully saturated). In real electrodes that are partially saturated by the electrolyte, the distribution of the electrolyte is governed by the capillary pressure. As a result, the amount of the action reaction site depends not only on the saturation but also the spatial distribution of the electrolyte. The solid matrix of the porous electrode is composed of carbon and binding polymer (PVDF, PTFE, Nafion etc.). The properties and distributions of carbon and binding polymers lead to different distributions of the wettability and pore size. Both the pore size and the wettability (contact angle) determine the capillary pressure, therefore, the distribution of the electrolyte. This study further investigates the distribution of the electrolyte with a given saturation. If the electrode matrix is assumed hydrophilic (when Nafion® or PVDF is applied as the binding polymer), electrolyte will occupy small pores first due to the higher capillary pressure in small pores.

This study applies the ball moving approach [114] to identify the diameter of pores in the regenerated porous electrode. All pores are assumed to be hydrophilic throughout the electrode. When the electrolyte fills the electrode, it will occupy small pores first due to the high capillary pressure within small pores. Figure 33 shows electrodes with different saturations (0 - 100%) of the electrolyte. The percentages of the active electrode surface (surface that is wetted by the electrolyte) are 0%, 40.87%, 65.07%, 83%, 91.07%, 95.98%, 98.60%, and 100% at the saturation levels of 0%, 16.57%, 36.13%, 58.88%, 72.91%, 84.66%, 93.46% and 100%, respectively. The discharge performance of electrodes with simulated distributions of electrolyte Figure 33 are compared with the performance of the electrode saturated with electrolyte in Figure 34. Since pore surfaces in the electrode are assumed to be hydrophilic, the electrolyte prefers to wet the electrode surface. The simulated discharge capacity increases from 7.41 to 21.38 Ah/g when the saturation decreases from 100% to 84.66% (which has 95.98% active surface area). In the electrode that is fully saturated by the liquid electrolyte, the insufficient oxygen concentration deep inside the electrode limits the reaction rates and the discharge current. When the saturation of the electrode decreases due to the available gas phase, oxygen could transfer deep into the electrode much easier through the gas phase. The improved oxygen transfer leads to the significantly increase of discharge capacity. However, when the saturation of the electrode is further reduced to 36.14%, only 65.07% of the electrode is wetted by the electrolyte and a large fraction of the electrode becomes inactive. As a result, the discharge capacity decreases to 15.79 Ah/g. The electrode with 36.14% saturation stops discharge because active pores have been completely filled with Li_2O_2 although sufficient oxygen is still available within the electrode.

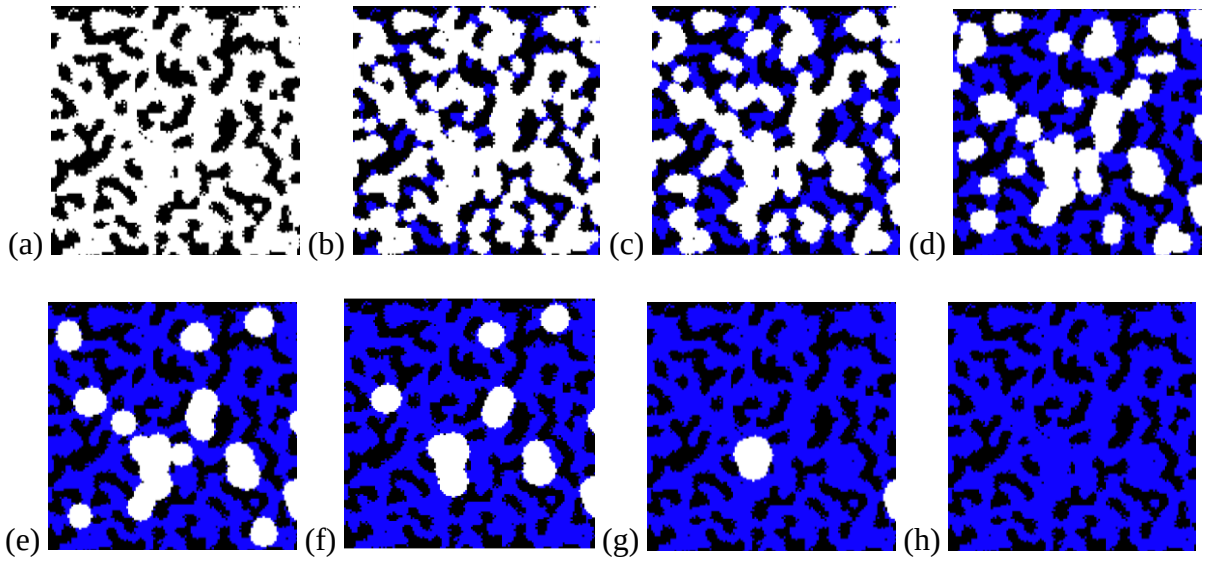

Figure 33: Battery electrodes with (a) 0%, (b) 16.57%, (c) 36.13%, (d) 58.88%, (e) 72.91%, (f) 84.66%, (g) 93.46% and (h) 100% saturation.

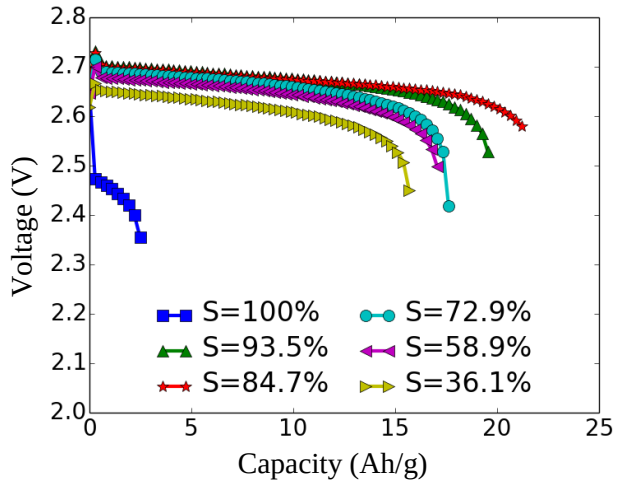

Figure 34: Discharge curves of batteries with various electrolyte saturations at 1 A/m^2.

5.4.5 Discharge Batteries at High Current Densities. Although 1 A/m^2 is commonly used in existing experimental and modeling studies, this extremely low current density leads to very low power density. The total active area of batteries has to be very large in order to provide the required power. This not only drives up the cost but also the weight of the battery pack. Li-O_2 batteries that are capable to achieve high discharge and charge capacity at current rates, much

higher than 1 A/cm^2, are required for practical applications. The model simulates in this study discharge electrodes with different electrolyte saturations at very high current densities (up to 50 A/m^2) to investigate the feasibility of the cell design. Figure 35 (a) compares the simulated discharge capacity at various current rates. Results show that electrodes that are partially wetted by the electrolyte could achieve similar capacity (Ah/g) at 20 A/cm^2 with electrodes that are fully saturated with the electrolyte at 1 A/cm^2 (Ah/g). The partially saturated (S=84.7%) electrodes could operate at 20 A/cm^2 and generate the same capacity with the electrode that is fully saturated by electrode at 1 A/cm^2. In other words, the partially saturated electrode increases the power density (voltage times the current density) by 20 times. With dry pores within the electrode, the diffusion path of oxygen in liquid electrode has been significantly decreased compared with the fully saturated electrode. Partially wetted electrodes have better utilization of the reaction sites deep into the electrode. On the contrary, a fully saturated electrode easily consumed up the oxygen and stops discharge. Although partially wetted electrodes achieve similar capacity with fully saturated electrode, the distributions of the reaction are very different. As a result, the volume fraction of the Li_2O_2 at the end of the discharge, Figure 35 (b), are significantly different. In Figure 35 (b), the total amount of Li_2O_2 is proportional to the discharge capacity, while the local volume fraction of Li_2O_2 is determined by the cumulative local reaction rates. In a fully saturated electrode, the volume fraction of Li_2O_2 next to the oxygen channel (x=1) is close to the porosity (0.65) but the volume fraction decreases very fast moving deep into the electrode. While in a partially wetted electrode (S=84.7), the distribution of Li_2O_2 volume fraction is more uniform due to the sufficient oxygen supply deep within the electrode.

Simulated results in this study, that a partially wetted electrode outperform a fully saturated electrode, is consistent with my recently published experiments in Paper **P2**. Although

the simulation does not exactly match experimental data, the overall trends are similar. The mismatch between simulation and experiments is mainly due to the fact that it's extremely difficult to engineer the distribution of wettability within the electrode by experiments to have exactly electrolyte distributions simplified in models. In addition, the model assumes that all the dry pores are connected, therefore, the oxygen can easily fill all the dry pores due to the high diffusivity in gas phase. However, only dry pores that are in direct connection with the environment has access to oxygen. Since each phase connects in all three dimensions, 3-D models that can capture the connectivity of all three phases will lead to more accurate simulation results on electrodes that are partially filled with liquid electrode. Further experiments and numerical simulations are being carried out in our lab to further elucidate the impact of electrolyte saturation and electrode wettability.

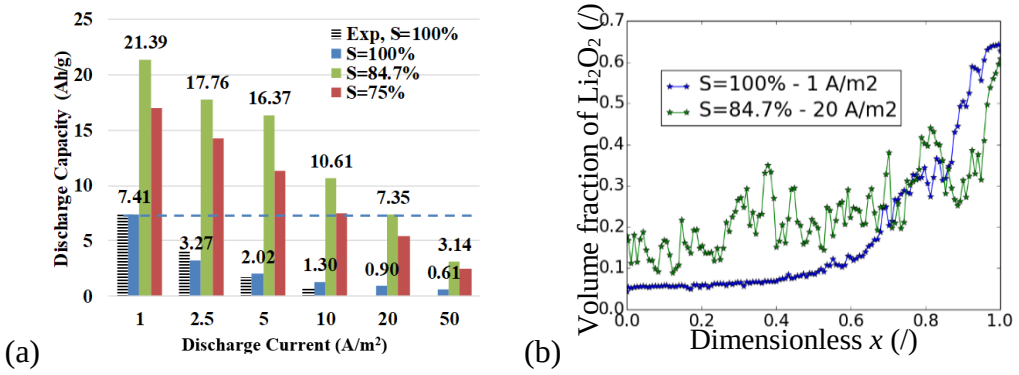

Figure 35: (a) Discharge capacities at different current rates when the electrode has different saturation levels and (b) the volume fraction of Li_2O_2 in the electrode at the end of discharge.

In Paper **P3**, I reconstruct 3D porous structures of porous electrodes from 2-D SEM images, and quantitatively study the distribution of the electrolyte at various saturations, and simulate the discharge performance of a Li−O_2 battery. The low operating current density and power density of Li−O_2 batteries are both limited by the availability of reactants (oxygen and

lithium ion) during operation. This study reconstructs 3-D porous structures of porous electrodes from 2-D SEM images, quantitatively studies the distribution of the electrolyte at various saturations, and simulates the discharge performance of a $Li-O_2$ battery. This research sheds lights on the critical role of liquid-gas two-phase mass transfer within the porous electrode on the electrochemical performance of $Li-O_2$ batteries. Fully saturated electrodes (100% saturation) have high oxygen transfer resistance, which will impede the battery performance at typical electrode thickness (~200 μm). On the other hand, over-dried battery (with 50% or less saturations) electrodes have poor electrochemical performance due to low connectivity of the electrolyte phase. It leads to not only the low ionic conductivity of the electrolyte but also the high mass transfer resistance of the lithium ion. The mixture of hydrophilic and hydrophobic pore makes it possible to achieve high discharge capacity (> 7 Ah/g) at high current (~20 A/cm^2). The design of the battery electrode should consider both the thickness of the electrode, the initial amount of the electrolyte, and the evaporation of the electrolyte during operation. These findings enable the design of advanced $Li-O_2$ battery electrodes with high capacity at high operating current and power densities, which are critical to accelerate the deployment of this beyond Li-ion battery technology to transport and stationary applications.

In this chapter, the problems exist in computationally reconstruct and simulate the geometry, which is less time-efficiency. I will address those issues in chapter 6 and propose the potential approach in chapter 7. This research sheds lights on the critical role of liquid-gas two-phase mass transfer within the porous electrode on the electrochemical performance of $Li-O_2$ batteries.

Chapter 6: Additional Imaging Techniques

Besides the experimental methods introduced in Chapter 2, various imaging techniques are utilized. This chapter is based on Paper **P4** and an ongoing project. It includes a predictive tool and proposed use of advanced imaging technique.

6.1 Introduction

Porous media are widely used in the energy storage system and categorized into packed beds and open foam structures. Various theoretical and experimental research on the stagnant thermal conductivity of porous materials has been performed and summarized [115]. The thermal conductivity of both packed beds and the solid matrix is strongly affected by properties of constituent materials and the porosity. However, the thermal conductivity predicted by models is significantly different from each other. The major limitation is that most of these models only apply to certain geometry of matrix material, or a narrow range of the porosity, or a range of fluid conductivities. Besides, models derived based on packed beds cannot investigate foam materials and vice versa, because the connectedness of packed beds is considerably different from that of foam materials. The errors between the predicted stagnant conductivity and experimental measurements are unacceptable [116-118]. Therefore, a predictive tool is developed that can more commonly describe the stagnant thermal conductivity of porous media in Paper **P4**. This model considers the detailed pore geometry (sphere, cube, or irregular; no contact, point contact or surface contact etc.), material properties (conductivities of the solid matrix and the filling material) and porosity (from less than 0.5 to higher than 0.9).

Though the simulation of the stagnant thermal conductivity is less related to the electrode wettability, in this chapter, I mainly address the importance of imaging techniques in the research

and present ongoing project of measuring the structure of positive electrode using transmission X-ray microscopy.

6.2 Metal Foam Reconstruction by Micro-CT

I employ the micro-CT to measure the geometry of the metal foams and reconstruct it using home-written codes based on Python 2.7.6. This method overcomes the shortcomings caused by the simplified geometries of the matrix. The stagnant thermal conductivity of Al-foams is directly simulated using pore geometries measured by Micro-CT. In this work, Al-foams with different pore sizes, 5, 10, 20, and 40 PPI show the porosities of 0.907, 0.899, 0.909, and 0.874, respectively. Cylindrical Al-foam samples (with 25 mm in diameter and 7 mm in height) are measured with an Xradia MicroXCT-400 tomographic X-ray microscope. The resolution of the micro CT image is 1 μm. I present three-dimensional (3-D) views of Al-foam samples with the pore size of 5, 10, 20 and 40 PPI in Figure 36. The 2D slices of four Al-foam samples are shown in Figure 37. The three-dimensional image is obtained by the image processing software of the X-ray microscope. Meanwhile, all two-dimensional slices are processed to remove the noise and convert images from grayscale to binary, which is prepared for the reconstruction. The processed binary data of each slice are reconstructed to three-dimensional computational domain. Figure 38 shows the reconstructed three-dimensional geometries of four samples. The reconstructed geometries consider the details of Al-foams and therefore guarantee the accuracy of the simulation.

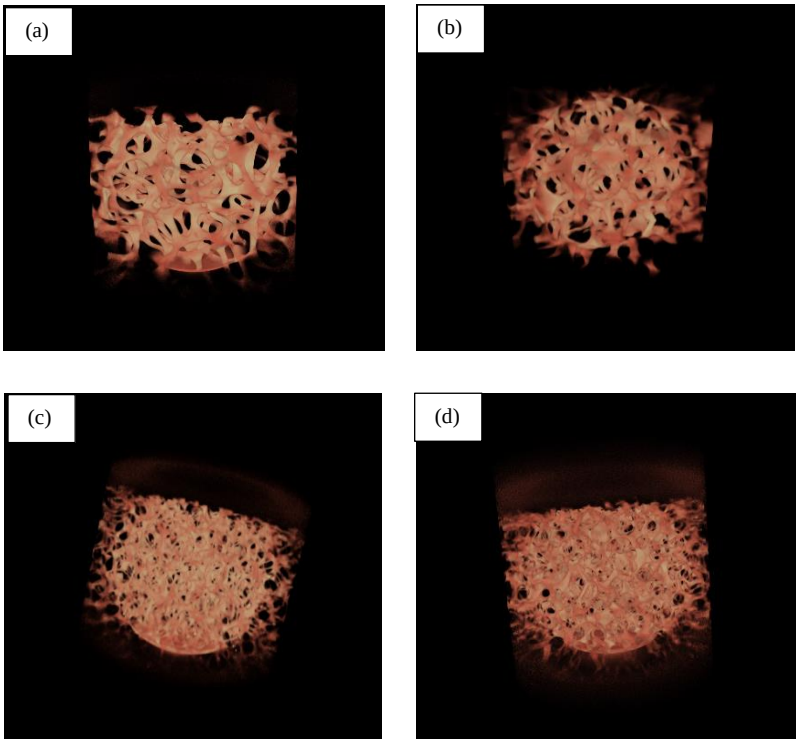

Figure 36: The three-dimensional views of Al foams with the pore sizes of (a) 5 PPI, (b) 10 PPI, (c) 20 PPI, and (d) 40 PPI.

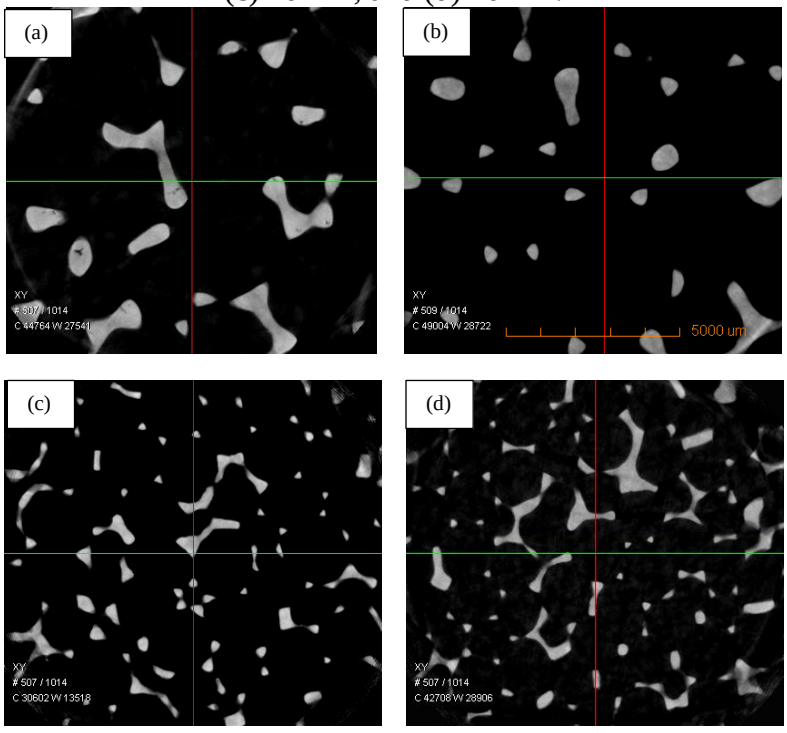

Figure 37: The 2D slices of Al foams with pore sizes of (a) 5 PPI, (b) 10 PPI, (c) 20 PPI, and (d) 40 PPI.

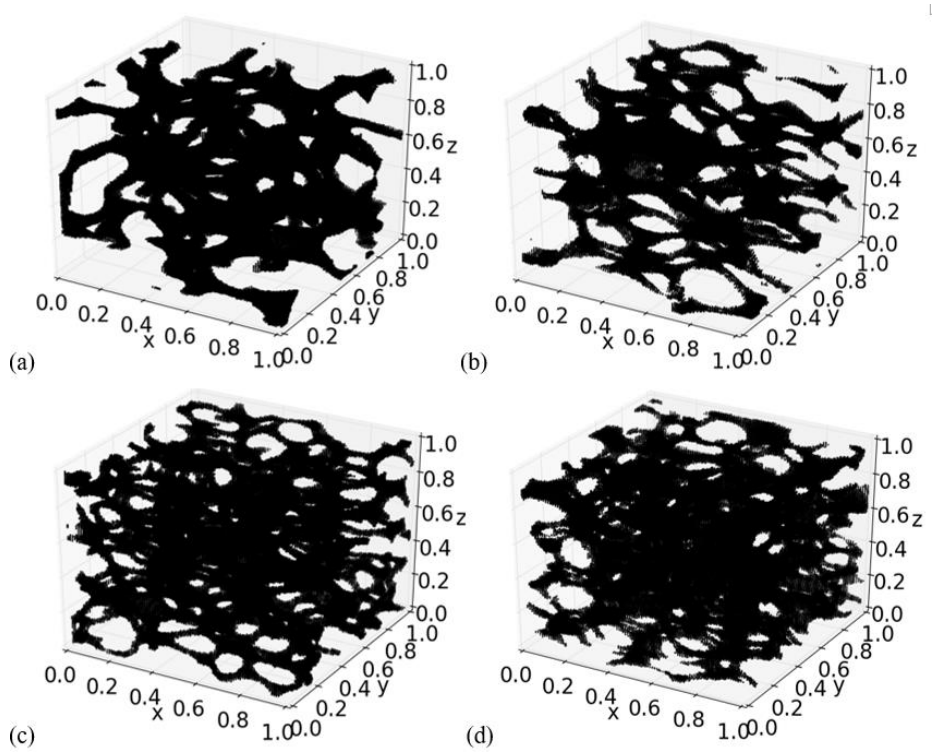

Figure 38: Reconstructed three-dimensional structures of Al foams with the pore sizes of (a) 5 PPI, (b) 10 PPI, (c) 20 PPI, and (d) 40 PPI.

6.3 Transmission X-ray Microscopy

As discussed in Chapter 5, the numerical approach is more suitable to research the electrochemical processes happening in the electrode. Obtaining the geometry of the electrode is necessary for the simulation. I have successfully reconstructed the geometry of the positive electrode using the 2D slices obtained by focused ion beam scanning electron microscopy (FIB-SEM) in Paper **P3**. The overall procedure is binarizing the images and then using the computational algorithm to complete the reconstruction. However, this procedure can be time-consuming and computationally expensive.

To our knowledge, the synchrotron X-ray technology has been employed to measure and reconstruct the 3D geometry of a sample [119-120]. Synchrotron radiation results from bending or

steering a high energy electron beam with bending magnets into a continuous circular or ring path. This is achieved within a series of particle accelerators in a synchrotron light source. The use of synchrotron radiation as an X-ray source can enhance the image quality and phase contrast resolution due to higher X-ray flux [121]. Compared with the FIB-SEM technique, the synchrotron X-ray can perform the measurement without destroying the sample. Furthermore, this technology is more time-saving compared with the above procedure. Therefore, I choose this imaging technique to measure the geometry of the customized electrode used in my experimental study.

The 32-ID-C Transmission X-ray Microscopy is located at the Advanced Photon Source (Argonne National Laboratory). It can provide an image with a 16 nm spatial resolution. The facility at APS includes nano-scale imaging with absorption, phase contrast, and spectroscopy techniques. Moreover, it can be operated in a wide range of sample's environments. The carbon electrode is made of the acetylene black and the polytetrafluoroethylene (PTFE) binder. The prepared electrode is measured by the 32-ID-C Transmission X-ray Microscopy. During the measurement, the software collects projection radiographs over an angle range of 180°. The individual exposure time of 1 s per radiograph and the beam energy is 8 keV. After acquiring the raw volumetric data, the reconstruction is performed to generate an image stack of 2D slices.

6.4 Image Processing

ImageJ is known as a public domain multi-platform software written for image analysis. This software focuses more on quantification, measuring and mathematical processing of images. Recently, the development of major microscopic techniques is thriving in many research fields such as medical science and engineering. These techniques allow me to receive images of higher resolution and obtain true 3D volumetric data. In order to process those data such as

visualization and quantification, multiple software has been developed and utilized. Here We present the procedure of reconstructing 3D geometry from 2D slices using ImageJ.

6.4.1 Filtering. I employ the software ImageJ to process the obtained image stack of 2D slices. After importing all the 2D slices into the ImageJ, it is necessary to correlate the image dimensions in the pixel to physical dimensions. Based on the measured parameters, the pixel size is calculated as 54 nm in the image stack. Afterward, the filter is applied to reduce the noise by which the image stack is prepared for the binarization. In this work, I choose the bandpass filter which is a 2D Fourier filter in the ImageJ. Basically, this filter can remove high spatial frequencies (blurring the image) and low spatial frequencies (similar to subtracting a blurred image). It can also suppress horizontal or vertical stripes that are created by scanning an image line by line. For the image stack in my study, I apply the bandpass filter to remove high-frequency noise. Therefore, the quality of the image stack is improved. After filtering, the image stack is more qualified for the binarization. For example, Figure 39 shows one 2D slice before and after the filtering process.

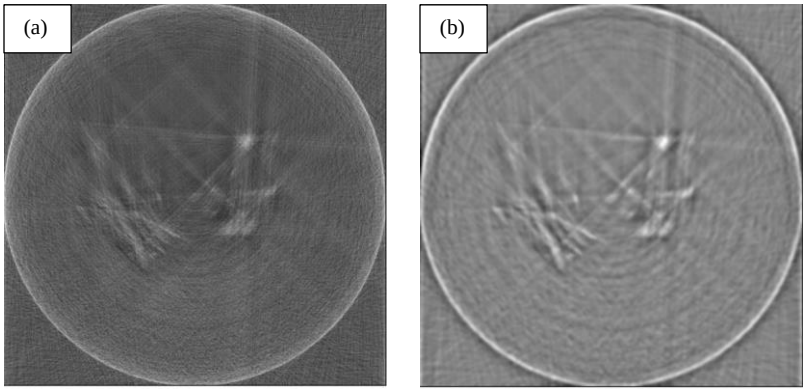

Figure 39: The image (a) before and (b) after the filtering process.

6.4.2 Binarization. Image processing algorithms require a binary image that can be produced by converting the 8-bit image. The thresholding is a technique for dividing an image into two (or more) classes of pixels, which are typically called "foreground" and "background." The adjust threshold tool helps in determining the threshold, an interval of values is manually

selected and applied. In this work, I set the lower threshold value of 0 and the upper threshold value of 160, which segments gray-scale images into features of interest and background. The procedure of binarization is shown in Figure 40. Proceeding the binarization produces the proper binary image stack for further reconstruction. Since the sample only occupies the central area of the image, the cropping tool is applied to trim the image stack. For example, the selected area in Figure 40 (b) is 200 × 200 pixels.

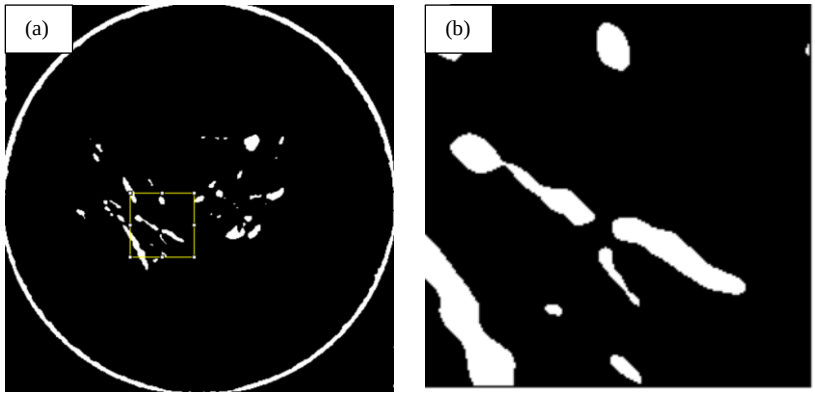

Figure 40: (a) The binary image and (b) the selected part in this image.

6.4.3 3D Visualization. Interpreting the image stack of 2D slices into 3D geometry may sometimes be the most complicated task of the image processing. Due to the development of powerful computers and 3D graphics cards, the visualization can now be performed easily on most computers. A plugin 3D Viewer is a powerful tool for 3D visualization in ImageJ. The 3D geometry is represented as a succession of 2D slices in the Z direction. The reconstructed 3D geometry is shown in Figure 41. This is the first time that I can directly measure the 3D geometry of the positive electrode in this dissertation.

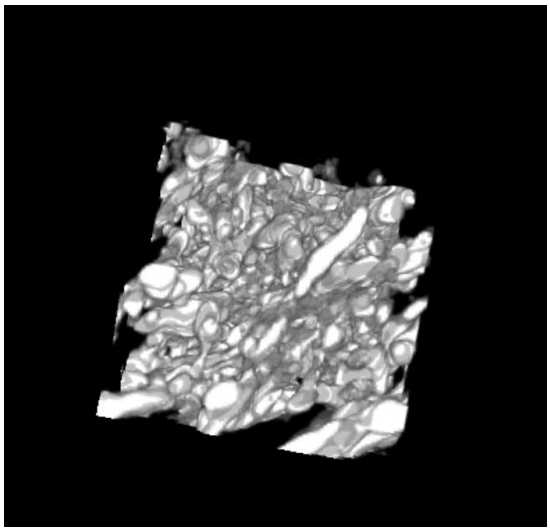

Figure 41: The generated 3D geometry using ImageJ.

6.4.4 Image Analysis. Once the image stack of 2D slices is segmented and reconstructed, the image analysis will be performed. This part is going to compute the porosity and surface area of the sample. The basic imageJ is suitable to deal with the 2D image in terms of measuring the porosity and particle size. For the 3D geometry, the Bonej plugin is installed and utilized. Bonej has the function of volume fraction that can calculate the porosity of porous media. Besides, the commands of surface area and particle analyzer can calculate the surface area and pore size, respectively. Results of image analysis obtained by BoneJ show that the total volume is 2.52×10^{12} nm^3 and the volume of pores is 2.10×10^{12} nm^3. The porosity is 0.833. The image histogram result shows that the number of 0 pixels is 2669669 and the number of 1 pixel is 13370331. The porosity based on the histogram is 0.833. Therefore, the results calculated by BoneJ is verified. The surface area obtained from Bonej is 6.08×10^9 nm^2. The total volume of the analyzed sample is 2.52×10^{12} nm^3. Meanwhile, the volume of carbon coatings in the electrode is 2 cm^2 × 200 μm = 4×10^{-8} m^3 and the weight of coatings is 6 mg. Therefore, the weight of the analyzed sample is 3.78×10^{-10} g. The calculated specific surface area is 16.08 m^2/g. The surface area of acetylene black measured by N_2 adsorption/desorption is 76.5 m^2/g. Considering the resolution

of 54 nm and the agglomerates formed in the coatings, the result calculated by BoneJ seems to be reasonable. The plugin BoneJ has a function of particle analyzer which can be used to analyze the particles in a 3D geometry. In my work, the particle analyzer can be used to analyze pores since the dark color represents pores. The pores are labeled in a 3D view which is shown in Figure 42. Assuming the pores are a spherical shape, the calculated pore size distribution is shown in Figure 43. The pore size distribution analyzed by BoneJ confirms that the resolution of this measurement is 54 nm. Results can be regarded as compensation for pore size analysis since the N_2 adsorption/desorption method mainly measures the mesopores (2-50 nm).

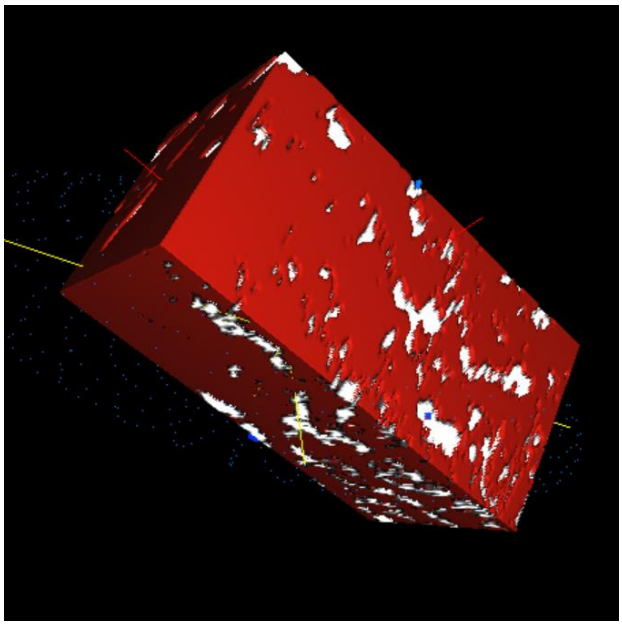

Figure 42: The 3D view of the geometry with labeled pores.

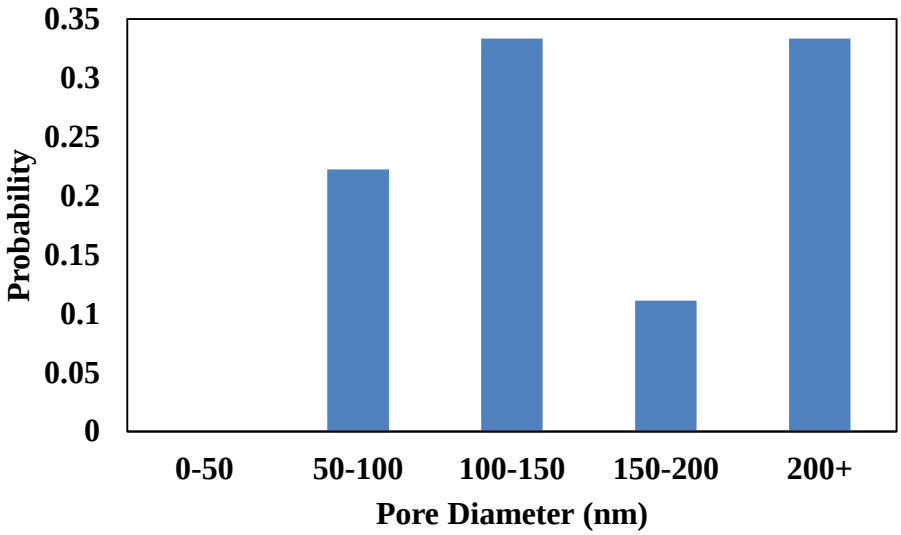

Figure 43: Pore size distribution obtained by BoneJ.

In this chapter, I introduce imaging techniques that can efficiently reconstruct the geometry of different samples. The micro-CT is suitable for the object with micropores. For the nanoscale pores, the transmission X-ray microscope can be applied. In practice, the geometry of Al-foam is measured and reconstructed after which the stagnant thermal conductivity of porous media is investigated. Moreover, I propose the use of a transmission X-ray microscope and ImageJ for reconstructing a 3D geometry and evaluating the porosity and surface area of the positive electrode in Li−O_2 batteries. This method can more quickly obtain the volumetric data and more conveniently conduct the image analysis. The proposed procedure is more useful in the dimensional characterization of carbon electrodes. This can be used as a great tool to investigate the porous structure of positive electrodes for Li−O_2 batteries. The ongoing project shows the great potential of benefiting the understanding of two-phase mass transfer in Li−O_2 batteries.

Chapter 7: Conclusion and Future Work

7.1 Conclusion

Li−O_2 batteries have been highlighted as a promising technology in the field of energy storage. It is still at the infant stage, although significant achievements have been made since it was first reported. In this dissertation, I mainly research the effects of electrode wettability on the performance of Li−O_2 batteries.

Based on the experimental study, the customized electrodes containing PVDF binder or less PTFE binder are lyophilic and their corresponding discharge capacity is lower than those of lyophobic electrodes. The lyophobic electrode can provide more gas paths for O_2 diffusion and enhance the O_2 availability for the ORR. The mixed wettability can balance the promotion of oxygen diffusion and the adequate number of reaction sites. Therefore, configuring the wettability in the electrode design is an important direction to increase the discharge capacity of Li−O_2 batteries. Secondly, an innovative strategy of periodically discharging and resting batteries is proposed and examined. The discharge capacity of Li-O_2 batteries is increased by 50% when these batteries are discharged at intermittent currents of 0.1, 0.5, 1.0 and 1.5 mA/cm^2. After the battery is discharged at a high current density of 2.0 mA/cm^2, the Li-O_2 batteries can be further discharged at lower current densities (1.5, 1 mA/cm^2 etc.). The Li-O_2 batteries with lyophilic electrodes, such as PVDF 15% electrodes, can gain more discharge capacity at intermittent discharge current. The cycling performance is also promoted by increasing the cut-off capacity.

The numerical study in this dissertation demonstrates that neither the fully saturated electrode nor the over-dried electrode is suitable for Li−O_2 batteries. More wetted pores in the electrode result in higher O_2 transfer resistance and more dried pores lead to the reduction of

reaction sites. The mixture of lyophilic and lyophobic pore makes it possible to achieve high discharge capacity (> 7 Ah/g) at high current (~20 A/cm^2). The design of the battery electrode should consider both the thickness of the electrode, the initial amount of the electrolyte, and the evaporation of the electrolyte during operation. Although the simulation does not exactly match experimental data, the overall trends are similar. These findings enable the design of advanced electrodes with high capacity at high operating current and power densities, which are critical to accelerating the launch of $Li-O_2$ batteries.

7.2 Future Work

The suggested future work targets at the optimization of positive electrodes and the understanding of two-phase mass transfer in porous media.

For the positive electrodes, the porous structure of the positive electrode affects the mass transport of O_2 and Li^+ in parallel with the importance of aprotic electrolytes. I will try to find a suitable combination of mesopores and macropores due to their ability to balance the surface area and mass transport. More experiments are required to examine the coupled effects of (i) surface area, (ii) pore volume, and (iii) pore size on the performance of $Li-O_2$ batteries.

Secondly, carbon materials (e.g., carbon blacks and nanotubes) are still a major choice for fabricating positive electrodes. The cost of fabricating carbon electrodes should also be considered. Using natural materials, such as woods and tea leaves, are more promising for the development of the porous positive since those materials are less expensive and more environmentally friendly. I will apply different materials in fabricating the positive electrodes. Besides, other materials such as Co_9S_8 will be used to fabricate the positive electrode due to its catalytic property.

Thirdly, since the imaging techniques such as FIB-SEM and TXM show the capability of measuring the geometry of objects, I will continue the ongoing project mentioned in Chapter 6.

The aim is to find an appropriate method to obtain the detailed geometry of the positive electrode. This method should both guarantee the accuracy of describing the porous structure and save time in the measurement. It is crucial to distinguish the carbon particle phase and the binder phase. When the geometry is successfully reconstructed and different phases are correctly labeled, a home-made code based on the finite element method will be used to simulate the two-phase mass transfer in the electrode. The obtained results may shed light on clarifying the electrode wettability and improving the electrode design for $Li{-}O_2$ batteries.

References

1. Rahman, I.; Vasant, P. M.; Singh, B. S. M.; Abdullah-Al-Wadud, M.; Adnan, N., Review of recent trends in optimization techniques for plug-in hybrid, and electric vehicle charging infrastructures. *Renewable and Sustainable Energy Reviews* **2016,** *58*, 1039-1047.
2. Etacheri, V.; Marom, R.; Elazari, R.; Salitra, G.; Aurbach, D., Challenges in the development of advanced Li-ion batteries: a review. *Energy & Environmental Science* **2011,** *4* (9), 3243-3262.
3. Manthiram, A., An outlook on lithium ion battery technology. *ACS Central Science* **2017,** *3* (10), 1063-1069.
4. Rahman, M. A.; Wang, X.; Wen, C., High energy density metal-air batteries: a review. *Journal of the Electrochemical Society* **2013,** *160* (10), A1759-A1771.
5. Lee, J. S.; Tai Kim, S.; Cao, R.; Choi, N. S.; Liu, M.; Lee, K. T.; Cho, J., Metal–air batteries with high energy density: Li–air versus Zn–air. *Advanced Energy Materials* **2011,** *1* (1), 34-50.
6. Cheng, F.; Chen, J., Metal–air batteries: from oxygen reduction electrochemistry to cathode catalysts. *Chemical Society Reviews* **2012,** *41* (6), 2172-2192.
7. Rosenman, A.; Markevich, E.; Salitra, G.; Aurbach, D.; Garsuch, A.; Chesneau, F. F., Review on Li- sulfur battery systems: An integral perspective. *Advanced Energy Materials* **2015,** *5* (16), 1500212-1500233.
8. Lu, J.; Li, L.; Park, J. B.; Sun, Y. K.; Wu, F.; Amine, K., Aprotic and aqueous Li–O2 batteries. *Chemical Reviews* **2014,** *114* (11), 5611-5640.
9. McCloskey, B. D.; Bethune, D.; Shelby, R.; Mori, T.; Scheffler, R.; Speidel, A.;

Sherwood, M.; Luntz, A., Limitations in rechargeability of Li-O2 batteries and possible origins. *The Journal of Physical Chemistry Letters* **2012,** *3* (20), 3043-3047.

10. Gowda, S. R.; Brunet, A.; Wallraff, G.; McCloskey, B. D., Implications of CO2 contamination in rechargeable nonaqueous Li–O2 batteries. *The Journal of Physical Chemistry Letters* **2012,** *4* (2), 276-279.
11. Lei, Y.; Lu, J.; Luo, X.; Wu, T.; Du, P.; Zhang, X.; Ren, Y.; Wen, J.; Miller, D. J.; Miller, J. T., Synthesis of porous carbon supported palladium nanoparticle catalysts by atomic layer deposition: application for rechargeable lithium–O2 battery. *Nano Letters* **2013,** *13* (9), 4182-4189.
12. Qin, Y.; Lu, J.; Du, P.; Chen, Z.; Ren, Y.; Wu, T.; Miller, J. T.; Wen, J.; Miller, D. J.; Zhang, Z., In situ fabrication of porous-carbon-supported α-MnO2 nanorods at room temperature: application for rechargeable Li–O2 batteries. *Energy & Environmental Science* **2013,** *6* (2), 519-531.
13. Padbury, R.; Zhang, X., Lithium–oxygen batteries—Limiting factors that affect performance. *Journal of Power Sources* **2011,** *196* (10), 4436-4444.
14. Girishkumar, G.; McCloskey, B.; Luntz, A. C.; Swanson, S.; Wilcke, W., Lithium-air battery: promise and challenges. *The Journal of Physical Chemistry Letters* **2010,** *1* (14), 2193-2203.
15. Kumar, B.; Kumar, J.; Leese, R.; Fellner, J. P.; Rodrigues, S. J.; Abraham, K., A solid-state, rechargeable, long cycle life lithium–air battery. *Journal of the Electrochemical Society* **2010,** *157* (1), A50-A54.
16. Armand, M.; Tarascon, J.-M., Building better batteries. *Nature* **2008,** *451* (7179), 652-657.

17. Zheng, J.; Andrei, P.; Hendrickson, M. A.; Plichta, E., The theoretical energy densities of dual-electrolytes rechargeable Li-air and Li-air flow batteries. *Journal of the Electrochemical Society* **2011,** *158* (1), A43-A46.

18. Shimonishi, Y.; Zhang, T.; Imanishi, N.; Im, D.; Lee, D. J.; Hirano, A.; Takeda, Y.; Yamamoto, O.; Sammes, N., A study on lithium/air secondary batteries—Stability of the NASICON-type lithium ion conducting solid electrolyte in alkaline aqueous solutions. *Journal of Power Sources* **2011,** *196* (11), 5128-5132.

19. He, P.; Wang, Y.; Zhou, H., A Li-air fuel cell with recycle aqueous electrolyte for improved stability. *Electrochemistry Communications* **2010,** *12* (12), 1686-1689.

20. Abraham, K.; Jiang, Z., A polymer electrolyt-based rechargeable lithium/oxygen battery. *Journal of the Electrochemical Society* **1996,** *143* (1), 1-5.

21. Lu, Y. C.; Gasteiger, H. A.; Parent, M. C.; Chiloyan, V.; Shao-Horn, Y., The influence of catalysts on discharge and charge voltages of rechargeable Li–oxygen batteries. *Electrochemical and Solid-State Letters* **2010,** *13* (6), A69-A72.

22. Mizuno, F.; Nakanishi, S.; Shirasawa, A.; Takechi, K.; Shiga, T.; Nishikoori, H.; Iba, H., Design of non-aqueous liquid electrolytes for rechargeable Li-O2 batteries. *Electrochemistry* **2011,** *79* (11), 876-881.

23. Li, Y.; Wang, X.; Dong, S.; Chen, X.; Cui, G., Recent advances in non-aqueous electrolyte for rechargeable Li–O2 batteries. *Advanced Energy Materials* **2016,** *6* (18), 1600751-1600777.

24. Wang, Z. L.; Xu, D.; Xu, J. J.; Zhang, L. L.; Zhang, X. B., Graphene oxide gel-derived,free-standing, hierarchically porous carbon for high-capacity and high-rate rechargeable Li-O2 Batteries. *Advanced Functional Materials* **2012**, *22* (17), 3699-

3705.

25. Wu, D.; Guo, Z.; Yin, X.; Pang, Q.; Tu, B.; Zhang, L.; Wang, Y. G.; Li, Q., Metal–organic frameworks as cathode materials for Li–O2 batteries. *Advanced Materials* **2014,** *26* (20), 3258-3262.

26. Liu, Q. C.; Li, L.; Xu, J. J.; Chang, Z. W.; Xu, D.; Yin, Y. B.; Yang, X. Y.; Liu, T.; Jiang, Y. S.; Yan, J. M., Flexible and foldable Li–O2 battery based on paper-ink cathode. *Advanced Materials* **2015,** *27* (48), 8095-8101.

27. Assary, R. S.; Lu, J.; Du, P.; Luo, X.; Zhang, X.; Ren, Y.; Curtiss, L. A.; Amine, K., The effect of oxygen crossover on the anode of a Li–O2 battery using an ether- based solvent: insights from experimental and computational studies. *ChemSusChem* **2013,** *6* (1), 51-55.

28. Zhang, X.; Xie, Z.; Zhou, Z., Recent progress in protecting lithium anodes for Li-O2 batteries. *ChemElectroChem*. **2019,** *6* (7), 1969-1977.

29. Liu, Q. C.; Xu, J. J.; Yuan, S.; Chang, Z. W.; Xu, D.; Yin, Y. B.; Li, L.; Zhong, H. X.; Jiang, Y. S.; Yan, J. M., Artificial protection film on lithium metal anode toward long-cycle- life lithium–oxygen batteries. *Advanced Materials* **2015,** *27* (35), 5241-5247.

30. Yu, B. C.; Park, K.; Jang, J. H.; Goodenough, J. B., Cellulose-based porous membrane for suppressing Li dendrite formation in lithium–sulfur battery. *ACS Energy Letters* **2016,** *1* (3), 633-637.

31. Hall, D. S.; Self, J.; Dahn, J., Dielectric constants for quantum chemistry and Li-ion batteries: solvent blends of ethylene carbonate and ethyl methyl carbonate. *The Journal of Physical Chemistry C* **2015,** *119* (39), 22322-22330.

32. Takezawa, H.; Ito, S.; Yoshizawa, H.; Abe, T., Surface composition of a SiOx film anode cycled in carbonate electrolyte for Li-ion batteries. *Electrochimica Acta* **2017,** *229*, 438-

444.

33. Laino, T.; Curioni, A., A new piece in the puzzle of lithium/air batteries: computational study on the chemical stability of propylene carbonate in the presence of lithium peroxide. *Chemistry–A European Journal* **2012,** *18* (12), 3510-3520.

34. Zhang, Z.; Lu, J.; Assary, R.S.; Du, P.; Wang, H.H.; Sun, Y.K.; Qin, Y.; Lau, K.C.; Greeley, J., Redfern, P.C. and Iddir, H., Increased stability toward oxygen reduction products for lithium-air batteries with oligoether-functionalized silane electrolytes. *The Journal of Physical Chemistry C* **2011,** *115* (51), 25535-25542.

35. Xu, D.; Wang, Z.L.; Xu, J.J.; Zhang, L.L.; Zhang, X.B., Novel DMSO-based electrolyte for high performance rechargeable Li–O2 batteries. *Chemical Communications* **2012,** *48* (55), 6948-6950.

36. Kwabi, D. G.; Batcho, T. P.; Amanchukwu, C. V.; Ortiz-Vitoriano, N.; Hammond, P.; Thompson, C. V.; Shao-Horn, Y., Chemical instability of dimethyl sulfoxide in lithium–air batteries. *The Journal of Physical Chemistry Letters* **2014,** *5* (16), 2850-2856.

37. Viswanathan, V.; Thygesen, K. S.; Hummelshøj, J.; Nørskov, J. K.; Girishkumar, G.; McCloskey, B.; Luntz, A., Electrical conductivity in Li2O2 and its role in determining capacity limitations in non-aqueous Li-O2 batteries. *The Journal of Chemical Physics* **2011,** *135* (21), 214704-214714.

38. Adams, B. D.; Radtke, C.; Black, R.; Trudeau, M. L.; Zaghib, K.; Nazar, L. F., Current density dependence of peroxide formation in the Li–O2 battery and its effect on charge. *Energy & Environmental Science* **2013,** *6* (6), 1772-1778.

39. Huang, J.; Tong, B.; Li, Z.; Zhou, T.; Zhang, J.; Peng, Z., Probing the reaction interface in li–oxygen batteries using dynamic electrochemical impedance spectroscopy:

discharge-charge asymmetry in reaction sites and electronic conductivity. *The Journal of Physical Chemistry Letters* **201**8, *9*.12 (2018): 3403-3408.

40. Sandhu, S. S.; Fellner, J. P.; Brutchen, G. W., Diffusion-limited model for a lithium/air battery with an organic electrolyte. *Journal of Power Sources* **2007,** *164* (1), 365-371.

41. Albertus, P.; Girishkumar, G.; McCloskey, B.; Sánchez-Carrera, R. S.; Kozinsky, B.; Christensen, J.; Luntz, A. C., Identifying capacity limitations in the Li/oxygen battery using experiments and modeling. *Journal of the Electrochemical Society* **2011,** *158* (3), A343-A351.

42. Hummelshøj, J. S.; Blomqvist, J.; Datta, S.; Vegge, T.; Rossmeisl, J.; Thygesen, K. S.; Luntz, A.; Jacobsen, K. W.; Nørskov, J. K., Communications: Elementary oxygen electrode reactions in the aprotic Li-air battery. *The Journal of Chemical Physics* **2010,** *132* (7), 071101-071106

43. Wang, F.; Li, X., Discharge Li-O2 batteries with intermittent current. *Journal of Power Sources* **2018,** *394*, 50-56.

44. Chen, W.; Zhang, Z.; Bao, W.; Lai, Y.; Li, J.; Gan, Y.; Wang, J., Hierarchical mesoporous γ-Fe2O3/carbon nanocomposites derived from metal organic frameworks as a cathode electrocatalyst for rechargeable Li-O2 batteries. *Electrochimica Acta* **2014,** *134*, 293-301.

45. Li, Q.; Xu, P.; Gao, W.; Ma, S.; Zhang, G.; Cao, R.; Cho, J.; Wang, H. L.; Wu, G., Graphene/graphene- tube nanocomposites templated from cage- containing metal-organic frameworks for oxygen reduction in Li–O2 batteries. *Advanced Materials* **2014,** *26* (9), 1378-1386.

46. Meini, S.; Piana, M.; Beyer, H.; Schwämmlein, J.; Gasteiger, H. A., Effect of carbon

surface area on first discharge capacity of Li-O2 cathodes and cycle-life behavior in e ether-based electrolytes. *Journal of the Electrochemical Society* **2012,** *159* (12), A2135-A2142.

47. Kuboki, T.; Okuyama, T.; Ohsaki, T.; Takami, N., Lithium-air batteries using hydrophobic room temperature ionic liquid electrolyte. *Journal of Power Sources* **2005,** *146* (1-2), 766-769.

48. Yang, X.; He, P.; Xia, Y., Preparation of mesocellular carbon foam and its application for lithium/oxygen battery. *Electrochemistry Communications* **2009,** *11* (6), 1127-1130.

49. Zhang, Y.; Zhang, H.; Li, J.; Wang, M.; Nie, H.; Zhang, F., The use of mixed carbon materials with improved oxygen transport in a lithium-air battery. *Journal of Power Sources* **2013,** *240*, 390-396.

50. Bhoyate, S.; Ranaweera, C. K.; Zhang, C.; Morey, T.; Hyatt, M.; Kahol, P. K.; Ghimire, M.; Mishra, S. R.; Gupta, R. K., Eco-friendly and high performance supercapacitors for elevated temperature applications using recycled tea leaves. *Global Challenges* **2017,** *1* (8), 1700063-1700075.

51. Li, L.; Chen, C.; Chen, X.; Zhang, X.; Huang, T.; Yu, A., Structure and catalyst effects on the electrochemical performance of air electrodes in lithium-oxygen batteries. *ChemElectroChem*. **2018**, *5* (18): 2666-2671.

52. Olivares-Marín, M.; Palomino, P.; Enciso, E.; Tonti, D., Simple method to relate experimental pore size distribution and discharge capacity in cathodes for Li/O2 batteries. *The Journal of Physical Chemistry C* **2014,** *118* (36), 20772-20783.

53. Lim, H. D.; Park, K. Y.; Song, H.; Jang, E. Y.; Gwon, H.; Kim, J.; Kim, Y. H.; Lima, M.

D.; Robles, R. O.; Lepró, X., Enhanced power and rechargeability of a Li−O2 battery based on a hierarchical- fibril CNT electrode. *Advanced Materials* **2013,** *25* (9), 1348-1352.

54. Song, H.; Xu, S.; Li, Y.; Dai, J.; Gong, A.; Zhu, M.; Zhu, C.; Chen, C.; Chen, Y.; Yao, Y., Hierarchically porous, ultrathick,"breathable" wood-derived cathode for lithium-oxygen batteries. *Advanced Energy Materials* **2018,** *8* (4), 1701203-1701211.

55. Zhu, C.; Du, L.; Luo, J.; Tang, H.; Cui, Z.; Song, H.; Liao, S., A renewable wood-derived cathode for Li–O2 batteries. *Journal of Materials Chemistry A* **2018,** *6* (29), 14291-14298.

56. Peng, C.; Yan, X..; Wang, R.; Lang, J.; Ou, Y.; Xue, Q., Promising activated carbons derived from waste tea-leaves and their application in high performance supercapacitors electrodes. *Electrochimica Acta* **2013,** *87*, 401-408.

57. Mohazabrad, F.; Wang, F.; Li, X., Experimental studies of salt concentration in electrolyte on the performance of Li-O2 batteries at various current densities. *Journal of the Electrochemical Society* **2016,** *163* (13), A2623-A2627.

58. Read, J.; Mutolo, K.; Ervin, M.; Behl, W.; Wolfenstine, J.; Driedger, A.; Foster, D., Oxygen transport properties of organic electrolytes and performance of lithium/oxygen battery. *Journal of the Electrochemical Society* **2003,** *150* (10), A1351-A1356.

59. Liu, B.; Xu, W.; Zheng, J.; Yan, P.; Walter, E. D.; Isern, N.; Bowden, M. E.; Engelhard, M. H.; Kim, S. T.; Read, J., Temperature dependence of the oxygen reduction mechanism in nonaqueous Li–O2 batteries. *ACS Energy Letters* **2017,** *2* (11), 2525-2530.

60. Lindberg, J.; Endrődi, B. z; Åvall, G.; Johansson, P.; Cornell, A.; Lindbergh, G. r., Li

salt anion effect on O2 solubility in an Li–O2 battery. *The Journal of Physical Chemistry C* **2018,** *122* (4), 1913-1920.

61. Gittleson, F. S.; Jones, R. E.; Ward, D. K.; Foster, M. E., Oxygen solubility and transport in Li–air battery electrolytes: establishing criteria and strategies for electrolyte design. *Energy & Environmental Science* **2017,** *10* (5), 1167-1179.

62. Wang, F.; Li, X., Effects of the electrode wettability on the deep discharge capacity of Li–O2 batteries. *ACS Omega* **2018,** *3* (6), 6006-6012.

63. Yang, Y.; Zhang, T.; Wang, X.; Chen, L.; Wu, N.; Liu, W.; Lu, H.; Xiao, L.; Fu, L.; Zhuang, L., Tuning the morphology and crystal structure of Li2O2: A graphene model electrode study for Li–O2 battery. *ACS Applied Materials & Interfaces* **2016,** *8* (33), 21350-21357.

64. Xu, W.; Xiao, J.; Zhang, J.; Wang, D.; Zhang, J. G., Optimization of nonaqueous electrolytes for primary lithium/air batteries operated in ambient environment. *Journal of the Electrochemical Society* **2009,** *156* (10), A773-A779.

65. Chen, M.; Jiang, X.; Yang, H.; Shen, P. K., Performance improvement of air electrode for Li/air batteries by hydrophobicity adjustment. *Journal of Materials Chemistry A* **2015,** *3* (22), 11874-11879.

66. Beattie, S.; Manolescu, D.; Blair, S., High-capacity lithium–air cathodes. *Journal of the Electrochemical Society* **2009,** *156* (1), A44-A47.

67. Horstmann, B.; Gallant, B.; Mitchell, R.; Bessler, W. G.; Shao-Horn, Y.; Bazant, M. Z., Rate-dependent morphology of Li2O2 growth in Li–O2 batteries. *The Journal of Physical Chemistry Letters* **2013,** *4* (24), 4217-4222.

68. Li, X.; Huang, J.; Faghri, A., A critical review of macroscopic modeling studies on LiO2

and Li–air batteries using organic electrolyte: Challenges and opportunities. *Journal of Power Sources* **2016,** *332*, 420-446.

69. Zhang, W.; Shen, Y.; Sun, D.; Huang, Z.; Huang, Y., Objectively evaluating the cathode performance of lithium- oxygen batteries. *Advanced Energy Materials* **2017,** *7* (24): 1602938.

70. Amanchukwu, C. V.; Harding, J. R.; Shao-Horn, Y.; Hammond, P. T., Understanding the chemical stability of polymers for lithium–air batteries. *Chemistry of Materials* **2015,** *27* (2), 550-561.

71. Papp, J. K.; Forster, J. D.; Burke, C. M.; Kim, H. W.; Luntz, A. C.; Shelby, R. M.; Urban, J. J.; McCloskey, B. D., Poly (vinylidene fluoride)(pvdf) binder degradation in Li–O2 batteries: a consideration for the characterization of lithium superoxide. *The Journal of Physical Chemistry Letters* **2017,** *8* (6), 1169-1174.

72. Balaish, M.; Ein-Eli, Y., The role of air–electrode structure on the incorporation of immiscible pfcs in nonaqueous Li–O2 battery. *ACS Applied Materials & Interfaces* **2017,** *9* (11), 9726-9737.

73. Balaish, M.; Ein-Eli, Y., Enhancing oxygen adsorption capabilities in Li–O2 battery cathodes through solid perfluorocarbons. *Journal of Materials Chemistry A* **2017,** *5* (27), 14152-14164.

74. Meng, C.; Wang, B.; Gao, Z.; Liu, Z.; Zhang, Q.; Zhai, J., Insight into the role of surface wettability in electrocatalytic hydrogen evolution reactions using light-sensitive nanotubular TiO2 supported pt electrodes. *Scientific Reports* **2017,** *7*, 41825-41833.

75. Sow, P. K.; Lu, Z.; Talebian, H.; Damron, L.; Mérida, W., Double layer capacitance measurements to characterize the water intrusion into porous materials. *The Journal of*

Physical Chemistry C **2016,** *120* (43), 24794-24802.

76. Xia, C.; Bender, C. L.; Bergner, B.; Peppler, K.; Janek, J., An electrolyte partially-wetted cathode improving oxygen diffusion in cathodes of non-aqueous Li–air batteries. *Electrochemical Communications.* **2013,** *26*, 93-96.

77. Mohazabrad, F.; Wang, F.; Li, X., Influence of the oxygen electrode open ratio and electrolyte evaporation on the performance of Li–O2 batteries. *ACS Applied Materials & Interfaces* **2017,** *9* (18), 15459-15469.

78. Geaney, H.; O'Dwyer, C., Examining the role of electrolyte and binders in determining discharge product morphology and cycling performance of carbon cathodes in Li-O2 batteries. *Journal of the Electrochemical Society* **2016,** *163* (2), A43-A49.

79. Sharon, D.; Hirshberg, D.; Afri, M.; Frimer, A. A.; Noked, M.; Aurbach, D., Aprotic metal-oxygen batteries: recent findings and insights. *Journal of Solid State Electrochemistry* **2017**, *21* (7) 1-18.

80. Vegge, T.; Garcia-Lastra, J. M.; Siegel, D. J., Lithium–oxygen batteries: At a crossroads? *Current Opinion in Electrochemistry* **2017**, *6* (1): 100-107.

81. Lu, Y. C.; Kwabi, D. G.; Yao, K. P.; Harding, J. R.; Zhou, J.; Zuin, L.; Shao-Horn, Y., The discharge rate capability of rechargeable Li–O2 batteries. *Energy & Environmental Science* **2011,** *4* (8), 2999-3007.

82. Girishkumar, G.; McCloskey, B.; Luntz, A.; Swanson, S.; Wilcke, W., Lithium−air battery: promise and challenges. *The Journal of Physical Chemistry Letters* **2010,** *1* (14), 2193-2203.

83. Débart, A.; Bao, J.; Armstrong, G.; Bruce, P. G., An O2 cathode for rechargeable lithium batteries: the effect of a catalyst. *Journal of Power Sources* **2007,** *174* (2), 1177-1182.

84. Wagner, F. T.; Lakshmanan, B.; Mathias, M. F., Electrochemistry and the future of the automobile. *The Journal of Physical Chemistry Letters* **2010,** *1* (14), 2204-2219.

85. Li, X.; Huang, J.; Faghri, A., Modeling study of a Li–O2 battery with an active cathode. *Energy* **2015,** *81*, 489-500.

86. Li, X.; Faghri, A., Optimization of the cathode structure of lithium-air batteries based on a two-dimensional, transient, non-isothermal model. *Journal of the Electrochemical Society* **2012,** *159* (10), A1747-A1754.

87. Han, S. M.; Kim, J. H.; Kim, D. W., Evaluation of the electrochemical performance of a lithium-air cell utilizing diethylene glycol diethyl ether-based electrolyte. *Journal of the Electrochemical Society* **2014,** *161* (6), A856-A862.

88. Mirzaeian, M.; Hall, P. J.; Sillars, F. B.; Fletcher, I.; Goldin, M. M.; Shitta-bey, G. O.; Jirandehi, H. F., The effect of operation conditions on the performance of lithium/oxygen batteries. *Journal of the Electrochemical Society* **2013,** *160* (1), A25-A30.

89. Chen, X.; Bevara, V.; Andrei, P.; Hendrickson, M.; Plichta, E.; Zheng, J., Combined effects of oxygen diffusion and electronic resistance in Li-air batteries with carbon nanofiber cathodes. *Journal of the Electrochemical Society* **2014,** *161* (12), A1877-A1883.

90. Lu, Y.-C.; Shao-Horn, Y., Probing the reaction kinetics of the charge reactions of nonaqueous Li–O2 batteries. *The Journal of Physical Chemistry Letters* **2012,** *4* (1), 93-99.

91. Mirzaeian, M.; Hall, P. J., Characterizing capacity loss of lithium oxygen batteries by impedance spectroscopy. *Journal of Power Sources* **2010,** *195* (19), 6817-6824.

92. Aetukuri, N. B.; McCloskey, B. D.; García, J. M.; Krupp, L. E.; Viswanathan, V.; Luntz, A. C., Solvating additives drive solution-mediated electrochemistry and enhance toroid growth in non-aqueous Li–O2 batteries. *Nature Chemistry* **2015,** *7* (1), 50-56.

93. Geaney, H.; O'Dwyer, C.T, The influence of electrolyte salt and solvent on the morphology of Li2O2 formed on Li-air cathodes, *ECS Meeting Abstracts* **2014**, *3*, 547-547.

94. Read, J., Characterization of the lithium/oxygen organic electrolyte battery. *Journal of the Electrochemical Society* **2002,** *149* (9), A1190-A1195.

95. Andrei, P.; Zheng, J. P.; Hendrickson, M.; Plichta, E. J., Some possible approaches for improving the energy density of Li-air batteries. *Journal of the Electrochemical Society* **2010,** *157* (12), A1287-A1295.

96. Wang, F.; Li, X., Effects of the electrode wettability on the deep discharge capacity of Li−O2 batteries. *Journal of the Electrochemical Society* **2018,** *3* (6):6000-6012.

97. Jiang, J.; Deng, H.; Li, X.; Tong, S.; He, P.; Zhou, H., Research on effective oxygen window influencing the capacity of Li–O2 batteries. *ACS Applied Materials & Interfaces* **2016,** *8* (16), 10375-10382.

98. Yoo, K.; Banerjee, S.; Dutta, P., Modeling of volume change phenomena in a Li–air battery. *Journal of Power Sources* **2014,** *258*, 340-350.

99. Huang, J.; Faghri, A., Analysis of electrolyte level change in a lithium air battery. *Journal of Power Sources* **2016,** *307*, 45-55.

100. Ye, L.; Wang, X.; Lv, W.; Fei, J.; Zhu, G.; Liang, Y.; Song, Y.; Zhai, J.; He, W., Analytical insight into the oxygen diffusion in wetted porous cathodes of Li-air

batteries. *Energy* **2015,** *93*, 416-420.

101. Inoue, G.; Yokoyama, K.; Ooyama, J.; Terao, T.; Tokunaga, T.; Kubo, N.; Kawase, M., Theoretical examination of effective oxygen diffusion coefficient and electrical conductivity of polymer electrolyte fuel cell porous components. *Journal of Power Sources* **2016,** *327*, 610-621.

102. Hwang, G.; Weber, A., Effective-diffusivity measurement of partially-saturated fuel-cell gas-diffusion layers. *Journal of the Electrochemical Society* **2012,** *159* (11), F683-F692.

103. Salitra, G.; Soffer, A.; Eliad, L.; Cohen, Y.; Aurbach, D., Carbon electrodes for double-layer capacitors I. Relations between ion and pore dimensions. *Journal of the Electrochemical Society* **2000,** *147* (7), 2486-2493.

104. Andisheh-Tadbir, M.; El Hannach, M.; Kjeang, E.; Bahrami, M., An analytical relationship for calculating the effective diffusivity of micro-porous layers. *International Journal of Hydrogen Energy* **2015,** *40* (32), 10242-10250.

105. Tran, C.; Yang, X. Q.; Qu, D., Investigation of the gas-diffusion-electrode used as lithium/air cathode in non-aqueous electrolyte and the importance of carbon material porosity. *Journal of Power Sources* **2010,** *195* (7), 2057-2063.

106. Ding, N.; Chien, S. W.; Hor, T. A.; Lum, R.; Zong, Y.; Liu, Z., Influence of carbon pore size on the discharge capacity of Li–O2 batteries. *Journal of Materials Chemistry A* **2014,** *2* (31), 12433-12441.

107. Xue, K. H.; Nguyen, T. K.; Franco, A. A., Impact of the cathode microstructure on the discharge performance of lithium air batteries: a multiscale model. *Journal of the Electrochemical Society* **2014,** *161* (8), E3028-E3035.

108. Andrei, P.; Bevara, V. V., Effects of pore size distribution on the discharge

characteristics of Li-air batteries with organic electrolyte. *ECS Transactions* **2014,** *61* (27), 193-212.

109. Li, X., A modeling study of the pore size evolution in lithium-oxygen battery electrodes. *Journal of the Electrochemical Society* **2015,** *162* (8), A1636-A1645.

110. Mukherjee, P. P.; Wang, C. Y., Stochastic microstructure reconstruction and direct numerical simulation of the PEFC catalyst layer. *Journal of the Electrochemical Society* **2006,** *153* (5), A840-A849.

111. Mukherjee, P. P., Kang, Q., and Wang C. Y., Pore-scale modeling of two-phase transport in polymer electrolyte fuel cells—progress and perspective. *Energy & Environmental Science* **2011,** *4* (2), 346-369.

112. Crabtree Jr, S. J.; Yuan, L. P.; Ehrlich, R., A fast and accurate erosion-dilation method suitable for microcomputers. *CVGIP: Graphical Models and Image Processing* **1991,** *53* (3), 283-290.

113. Patankar, S., *Numerical Heat Transfer and Fluid Flow*. CRC press: 1980.

114. Schulz, V. P.; Becker, J.; Wiegmann, A.; Mukherjee, P. P.; Wang, C.-Y., Modeling of two-phase behavior in the gas diffusion medium of PEFCs via full morphology approach. *Journal of the Electrochemical Society* **2007,** *154* (4), B419-B426.

115. Ranut, P., On the effective thermal conductivity of aluminum metal foams: Review and improvement of the available empirical and analytical models. *Applied Thermal Engineering* **2016,** *101*, 496-524.

116. Yao, Y.; Wu, H.; Liu, Z., A new prediction model for the effective thermal conductivity of high porosity open-cell metal foams. *International Journal of Thermal Sciences* **2015,** *97*, 56-67.

117. Schmierer, E. N.; Razani, A., Self-consistent open-celled metal foam model for thermal applications. *Journal of Heat Transfer* **2006,** *128* (11), 1194-1203.

118. Boomsma, K.; Poulikakos, D., The effects of compression and pore size variations on the liquid flow characteristics in metal foams. *Journal of Fluids Engineering* **2002,** *124* (1), 263-272.

119. Grew, K. N.; Chu, Y. S.; Yi, J.; Peracchio, A. A.; Izzo, J. R.; Hwu, Y.; De Carlo, F.; Chiu, W. K., Nondestructive nanoscale 3D elemental mapping and analysis of a solid oxide fuel cell anode. *Journal of the Electrochemical Society* **2010,** *157* (6), B783-B792.

120. Shearing, P. R.; Gelb, J.; Brandon, N. P., X-ray nano computerised tomography of SOFC electrodes using a focused ion beam sample-preparation technique. *Journal of the European Ceramic Society* **2010,** *30* (8), 1809-1814.

121. Pike, E. R.; Sabatier, P. C., *Scattering, Two-Volume Set: Scattering and Inverse Scattering in Pure and Applied Science*. Elsevier: 2001.

Paper P1

Effects of the Electrode Wettability on the Deep Discharge Capacity of Li–O_2 Batteries

ACS OMEGA

Article

Cite This: ACS Omega 2018, 3, 6006 6012

Effects of the Electrode Wettability on the Deep Discharge Capacity of Li−O_2 Batteries

Fangzhou Wang and Xianglin Li*

Department of Mechanical Engineering, University of Kansas, Lawrence, Kansas 66045, United States

Supporting Information

ABSTRACT: The wettability of customized Li−O_2 battery electrodes is altered by mixing acetylene black carbon particles with various binders. The wettability of the electrode can be characterized by the static contact angles between the electrode surface and nonaqueous electrolyte, which is 1 M bis(trifluoromethane)sulfonimide lithium salt (LiTFSI) dissolved in tetraethylene glycol dimethyl ether, and the double-layer capacitance measured by the cyclic voltammetry. Results show that electrodes containing poly(vinylidene difluoride) (PVDF) binder are lyophilic and increasing the fraction of poly(tetrafluoroethylene) (PTFE) increases the lyophobicity of electrodes. Li−O_2 batteries are discharged at 0.1 mA/cm^2 with the cut-off voltage of 2.0 V. The discharge capacity of the electrode with 15% PVDF (36.5°) carbon coatings is 1665.8 mAh/g, whereas the customized electrode with 15% PTFE (128.4°) carbon coatings obtains the discharge capacity of 4160.8 mAh/g. However, the discharge capacity decreases to 3109.5 and 2822.9 mAh/g as the PTFE content further increases to 25% (135.5°) and 35% (138.5°), respectively. The electrode composed of two lyophobic carbon coatings on top and bottom and one lyophilic carbon coating in the middle has the static contact angle of 118.8° and acquires the highest specific discharge capacity of 5149.5 mAh/g.

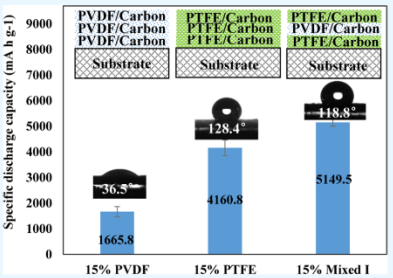

1. INTRODUCTION

Greenhouse gas emissions from the production and consumption of fossil fuels have resulted in global climate change, acid rain, as well as other environmental consequences, which attract growing concerns from the world. Thus, renewable energy is emerging and thriving globally to replace the fossil fuels. However, the lower energy density and intermittency of renewable energy, such as solar energy and wind energy, limit their commercialization.[1] Currently, the rechargeable battery is considered as one of the compromising technologies to efficiently store renewable energy. Among rechargeable batteries, the Li-ion battery has achieved a great success and has been widely applied in many devices and instruments, including mobile phones and electrical vehicles.[2] The practical specific energy of the Li-ion battery (~200 Wh/kg), however, has already approached the theoretical specific energy (~600 Wh/kg).[3]

The Li−air battery using O_2 from the atmosphere displays a much higher theoretical energy density (~11 000 Wh/kg based on Li anode) than other rechargeable batteries.[4] However, many obstacles, such as the low discharge−charge current rate, low charge discharge energy efficiency, and poor cycle life need to be overcome to commercialize the Li−air battery.[5,6] Since CO_2 and H_2O in air would react with active components in batteries and deteriorate the performance, most laboratory experiments were conducted under pure O_2 environment.[7,8] Experiments in this study has utilized pure O_2 so that the term Li−O_2 battery is presented throughout this paper. Generally, a rechargeable Li−O_2 battery using organic electrolyte consists of a lithium metal anode, a separator saturated with the organic electrolyte, and a porous cathode electrode (typically made from carbon or catalysts). The electrochemical reactions occurring on the anode and cathode as well as the overall reaction are shown below. The reversible cell voltage is 2.96 V.[9]

$$\text{anode: } \mathrm{Li} \underset{\text{charge}}{\overset{\text{discharge}}{\rightleftharpoons}} \mathrm{Li^+} + \mathrm{e^-} \quad (1)$$

$$\text{cathode: } \mathrm{O_2} + 2\mathrm{e^-} + 2\mathrm{Li^+} \underset{\text{charge}}{\overset{\text{discharge}}{\rightleftharpoons}} \mathrm{Li_2O_2(s)} \quad (2)$$

$$\text{overall: } 2\mathrm{Li} + \mathrm{O_2} \underset{\text{charge}}{\overset{\text{discharge}}{\rightleftharpoons}} \mathrm{Li_2O_2(s)} \quad (3)$$

During the discharge operation, the Li metal is oxidized at the anode to generate lithium ion that transfers through the separator and reaches the porous cathode. The lithium ion reacts with oxygen from the ambient or gas channels and generates lithium peroxide (Li_2O_2) at the cathode. The oxygen reduction reaction (ORR) should occur both on triphase boundaries formed by the electrode material, the electrolyte and oxygen, as well as the interface of electrode material and electrolyte. The charging reactions at the anode and cathode

Received: April 25, 2018
Accepted: May 23, 2018
Published: June 4, 2018

DOI: 10.1021/acsomega.8b00808
ACS Omega 2018, 3, 6006−6012

are reversed from discharging reactions in which lithium peroxide is decomposed and oxygen is released at the cathode and lithium metal is deposited at the anode.

The O_2 diffusion in the porous cathode is a key factor that determines the discharge capacity of Li−O_2 batteries.[10,11] Therefore, many studies on Li−O_2 batteries have paid considerable attention to the O_2 diffusion in the porous cathode because poor O_2 diffusion will reduce the capacity. The O_2 diffusion in the porous cathode is related to carbon loading,[12] pore clogging induced by the deposition of solid lithium peroxide,[13−16] and the partial pressure of oxygen.[17] In addition, the wettability between the electrolyte and electrode also significantly affects the performance of Li−O_2 batteries because the O_2 diffusion coefficient in air is several orders of magnitude higher than that in the liquid electrolyte. For instance, the O_2 diffusion coefficient[18] in nonaqueous electrolyte calculated by the Stokes−Einstein equation is on the order of 10^{-6}, whereas the diffusion coefficient is on the order of 10^{-2} in air.[19] The contact angle is often applied to characterize the wetting behavior between the liquid and solid surface. The electrolyte and carbon material in electrode possess different dielectric constants, which affect the wettability of the solid to the liquid. The contact angle of the electrolyte on the surface of carbon electrode increases when the difference of dielectric constant between the electrolyte and carbon electrode is larger. The electrolyte with a larger contact angle is less likely to wet the carbon electrode. Xu et al.[20] showed that the wettability affected the O_2 diffusion in the porous electrode and thus the discharge and charge capacities. The measured contact angles of 1 M bis(trifluoromethane)sulfonimide lithium salt (LiTFSI) in various nonaqueous solvents and their mixtures on the surface of both carbon and Teflon showed that the discharge capacity was improved when the contact angle increased. For example, the contact angle of 1 M LiTFSI in propylene carbonate (PC)/ethylene carbonate (EC) (1:1 wt) on the surface of carbon was 47°, whereas that of 1 M LiTFSI in PC/dimethoxyethane (DME) (1:1 wt) on the surface of carbon was 5°. The discharge capacity with the PC/EC solvent was 167.5 mAh/g, whereas the capacity was only 27.4 mAh/g with the PC/DME solvent. Binders such as poly(vinylidene difluoride) (PVDF) and poly(tetrafluoroethylene) (PTFE) are used to combine different types of small particles together and adjust the wettability of cathode electrode in Li−O_2 batteries. Zhang et al.[21] investigated the wettability of carbon electrodes using the electrolyte of 1 M $LiPF_6$ in PC/EC with a weight ratio of 1:1. The electrode made from Super P carbon mixed with PTFE (8:2 wt) had the contact angle of 99°, whereas the electrode made from KB 600 carbon mixed with PTFE (8:2 wt) had the contact angle of 56°. The battery with lyophobic electrode obtained a higher discharge capacity (3175 mAh/g) than the battery with a lyophilic electrode (798 mAh/g).

On the other hand, strongly lyophobic electrodes may deteriorate the discharge−charge performance. The Li−O_2 battery using lyophobic electrode was researched by Chen et al.,[22] in which the experimental data showed that the specific discharge capacity increased from 1365 to 2365 mAh/g when the PTFE weight ratio increased from 0 to 30%. However, the electrode composed of 40 wt % PTFE deteriorated the performance of Li−O_2 battery such that the specific discharge capacity decreased to 2130 mAh/g. The PTFE weight ratio should be optimized because a higher PTFE content will reduce the amounts of triphase boundaries for the electrochemical reactions battery electrode. The contact angles of water on the surface of raw carbon paper and carbon paper with 30 wt % PTFE were measured to be 136.6 and 148.3°, respectively. It should be noted that the water and liquid electrolytes have very different dielectric constants: the dielectric constant of water is 78.3[23] at 25 °C, whereas that of tetraethylene glycol dimethyl ether (TEGDME) is 7.9.[24] Therefore, the contact angle measured by water cannot represent the surface wettability between electrode and liquid electrolyte.

Because of the significantly different O_2 diffusivity in gas phase and electrolyte phase, electrodes with mixed wettability could create triphase boundaries that facilitate the oxygen transfer through gas phase (nonwetted pores). However, too many nonwetted pores will decrease the ionic conductivity of electrodes. Therefore, this study has conducted a systematic investigation on the effects of wettability of electrodes toward organic electrolyte (including both lyophilicity and lyophobicity) and its effects on the deep discharge capacity of Li−O_2 battery. The wettability of electrode was adjusted by mixing carbon powders with different binders (PTFE and PVDF) at various weight ratios. The stability of binders has been systematically examined[25] in the presence of commercial Li_2O_2, which showed that PVDF was unstable because of the presence of highly electron-withdrawing functional groups and an α or β hydrogen atom next to them. The PTFE binder was demonstrated to be stable in the presence of Li_2O_2. In addition, the PVDF binder was confirmed to degrade in Li−O_2 batteries.[26] The products formed in the PVDF degradation was measured by Raman spectroscopy and showed the Raman shifts of ∼1123 and 1525 cm^{-1}. However, the degradation can be prevented by drying the electrode under higher temperature, such as 200 °C. Thus, the stability of PTFE and PVDF binders can be guaranteed in this study if the electrodes are prepared according to the process in Experimental Section. The wettability of various customized electrodes was indicated by the contact angles of 1 M LiTFSI/TEGDME electrolyte on the customized electrode surface as well as the double-layer capacitance, which is proportional to the area of wetted pore surface in the electrode.[27] After comparing the specific discharge capacities of electrodes with lyophilic and lyophobic carbon coating layers, the electrodes consisting of mixed coating layers were produced and tested to optimize the discharge−charge performance. The study shed light on the criteria to improve the O_2 diffusion and increase the specific discharge capacity of Li−O_2 batteries.

2. RESULTS AND DISCUSSION

2.1. Initial Deep Discharge. All these customized electrodes are tested by the deep discharge experiments at the current density of 0.1 mA/cm^2. The discharge capacity of raw carbon cloth is negligible (<100 mAh/g) due to the low specific surface area. Therefore, the reported specific discharge capacity is calculated on the basis of the weight of carbon powders coated on the electrode without considering the weight of raw carbon cloth substrate and binders. The discharge curves with the highest discharge capacity among three repeated experiments of each electrode are shown in Figure 1, and the discharge capacities are compared in Figure 2. The lowest specific discharge capacity of 1665.8 mA/h g is achieved by the electrode with 15% PVDF carbon coatings. When the PTFE binder is used in the customized electrode, the electrode becomes more lyophobic. The specific discharge capacities of Li−O_2 batteries increase from 3145.8 to 4160.8 mAh/g when the mass fraction of PTFE binder increases from 5 to 15% but

DOI: 10.1021/acsomega.8b00808
ACS Omega 2018, 3, 6006−6012

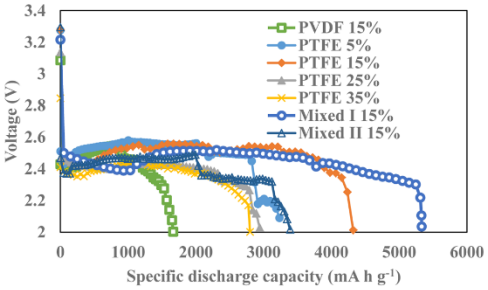

Figure 1. Deep discharge curves of Li−O_2 batteries with customized electrodes.

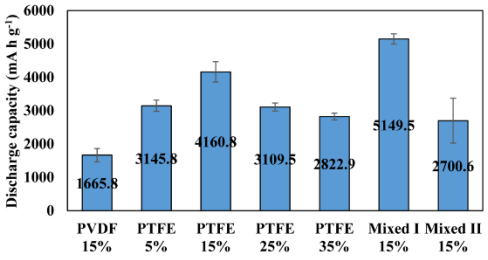

Figure 2. Deep discharge Li−O_2 batteries using customized electrode.

decreases to 3109.5 and 2822.9 mAh/g when the mass fraction of PTFE binder further increases to 25 and 35%. The significant variation of specific discharge capacity can be attributed to the wettability change. To quantitatively correlate the discharge capacity with the electrode wettability, both the static contact angle and the double-layer capacitance of customized electrodes are measured and exhibited.

2.2. Contact Angle Measurement. The static contact angle between electrolyte and electrode surface is measured to indicate the surface wettability difference among customized electrodes with various contents of PTFE and PVDF binders. Instead of measuring contact angle between a water drop and electrode surface,[22] the 1 M LiTFSI/TEGDME electrolyte (5 μL per drop) is dropped on the surface of customized electrodes to measure the static contact angle. The measured static contact angles (<90° for lyophilic surface and >90° for lyophobic surface) as well as images of electrolyte drops on electrode surfaces are shown in Figure 3.

The measurement of static contact angle is unsuccessful when the electrolyte drop is dripped on the surface of customized electrode containing 5% PTFE because the electrolyte droplet quickly spreads into the electrode. It indicates that the surface of 5% PTFE is lyophilic and is more easily wetted by the electrolyte. When the PTFE content increases from 15 to 35%, the electrode becomes more lyophobic and the static contact angle increases from 128.4 to 138.5°. The mixed I electrode, which consists of one 15% PVDF coating sandwiched by two 15% PTFE coatings, displays a slightly lower static contact angle (118.8°) than the electrode with 15% PTFE. It may be caused by the fact that a small amount of PVDF binder is mixed on the top layer of carbon coating during the fabrication. In addition, the contact angles of

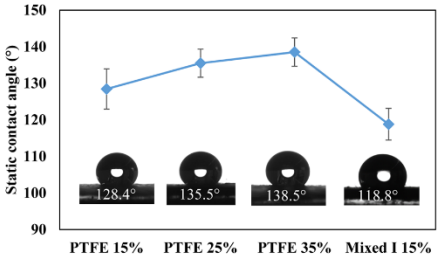

Figure 3. Results of static contact angle measurements on customized electrode surface.

customized electrodes with 15% PVDF carbon coatings as well as the mixed II electrode consisting of one 15% PTFE carbon coating sandwiched by two 15% PVDF carbon coatings are less than 90° and are unstable.

2.3. Double-Layer Capacitance Measurement. Since static contact angles represent the surface rather than internal wettability of customized electrodes, the double-layer capacitance of customized electrodes is also measured. This study employs an electrochemical approach[27] to quantify the solid−liquid interfacial area and promote the understanding of wettability within customized electrodes. The electric double layer is created on the electrode surface that is wetted by the electrolyte because the customized electrode made of carbon powders is electrically conductive. The double-layer capacitance is related to the wetted interfacial area via the following equation

$$C = \varepsilon_r \varepsilon_0 \frac{A_{sl}}{d} \tag{4}$$

where C is the capacitance, ε_r is the relative permittivity of the electrolyte, ε_0 is the permittivity of the vacuum, d is the double-layer thickness, which can be approximated as Debye length, and A_{sl} represents the wetted pore surface. For an electrolyte with the given composition measured at the room temperature, parameters of ε_r, ε_0, and d can be considered as constants. Therefore, the change of the area of the wetted pore surface is proportional to the variation of the double-layer capacitance.

Figure 4 exhibits the relationship between the volume of added electrolyte and the measured double-layer capacitance. Considering the battery frame shown in Figure 8, the double-layer capacitance is related to the wetted pore surface in the electrode as well as the wetted area in the current collector. Thus, it is necessary to measure the capacitance when only the

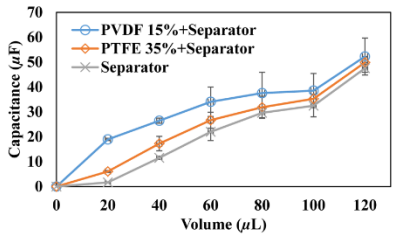

Figure 4. Double-layer capacitance vs volume of electrolyte added on the customized electrode.

DOI: 10.1021/acsomega.8b00808
ACS Omega 2018, 3, 6006−6012

strongly lyophilic separator is inserted in the battery. Generally, as more electrolyte is added, more pore surface is wetted so that the double-layer capacitance increases. The customized electrode containing 15% PVDF has larger capacitances than that with 35% PTFE because the former electrode is more lyophilic and more pores are wetted by electrolyte. For example, the capacitance of the electrode with 15% PVDF was 12.9 μF more than that of the electrode with 35% PTFE at the volume of 20 μL. The capacitance of 35%-PTFE electrode combined with the separator is only slightly higher (<5 μF in all volumetric cases) than that of a single separator, as shown in Figure 4. It indicates that most of the electrolyte added into the lyophobic electrode is repelled into the lyophilic separator. The double-layer capacitance increases almost linearly with the amount of added electrolyte when the electrolyte is less than 60 μL. As the electrolyte is added, more electrolyte spreads into the separator. Therefore, the wetted surface in the current collector may account for a larger fraction of the double-layer capacitance. The sudden rise in the capacitance after 100 μL may be attributed to the fact that electrolyte is squeezed out from the battery frame and the extra double layer is created. Although the compression during battery assembly may partially compensate the capillary pressure within the electrode and cause measuring errors, especially when the electrolyte was more than 60 μL, the measurement of double-layer capacitance demonstrates the general trend that more pores are wetted by the electrolyte in the lyophilic electrodes.

2.4. Discussion. More lyophobic electrodes facilitate O_2 diffusion by creating more gas paths. The improvement of O_2 transfer results in a higher specific discharge capacity. However, the specific discharge capacity of the electrode decreases after further increasing the PTFE content to more than 15%. The influences of PTFE content on specific discharge capacity possesses good consistency with the published data.[22] Further increasing the PTFE content generates more lyophobic pores that reduce the number of triphase boundaries for the ORR reaction and decreases the ionic conductivity. In Figure 5, the

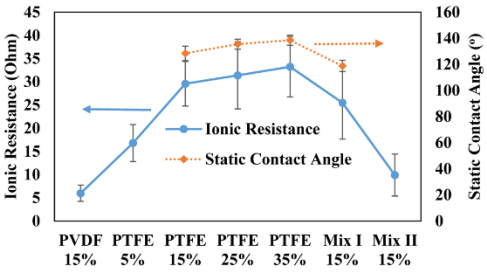

Figure 5. Equivalent ionic resistance of the batteries with customized electrode of different wettabilities.

equivalent resistance measured by electrochemical impedance spectroscopy (EIS) mainly includes the electronic resistance of the electrodes, current collectors, and ionic resistance of the electrolyte, as well as the contact resistance between these components. All electrodes are tested in the same battery frame design with the same electrolyte. Therefore, variations of the equivalent resistance can be attributed to changes of the ionic resistance. More lyophobic electrode impedes the ionic transfer by decreasing the ionic conductivity. The resistance displays the same trend as the static contact angle. In addition, the unstable discharge curves at the end of discharging process imply that lyophobic electrodes still experience O_2 starvation on cathode, which increases the overpotential and causes the sudden death of the battery.

To facilitate the oxygen diffusion without significantly sacrificing the ionic conductivity, electrodes with mixed wettability have been designed and tested. The mixed electrode structures shown in Figure 1c,d consist of three carbon coatings. In mixed I electrode, the top and bottom layers with 15% PTFE are lyophobic and the middle layer with 15% PVDF is lyophilic. The battery with mixed I electrode achieves the highest specific discharge capacity of 5149.5 mAh/g. Because of the lyophobicity of both the top and the bottom coatings, O_2 can diffuse into the electrode without much diffusion resistance and reach the electrolyte that accumulates in the lyophilic coating in the middle. This design utilizes the porous structure inside the electrode more effectively. Also, adding a lyophilic layer in the middle of electrode may reduce the O_2 diffusion length compared with the fully lyophobic electrode. The combined effects lead to the highest specific capacity. In comparison, the mixed II electrode is composed of one carbon coating with 15% PTFE layer sandwiched by two carbon coatings with 15% PVDF. This electrode only results in 2700.6 mAh/g deep discharge capacity because the lyophilic top and bottom layers impose more resistance in O_2 diffusion. Comparing with the electrode with 15% PVDF, applying one lyophobic layer in the middle of mixed II electrode increases the discharge capacity by about 1000 mAh/g. The result is consistent with the previous conclusion as well as the study conducted by Xia et al.[28] that partially wetted electrodes perform better than electrodes fully saturated by the electrolyte. The mixed I customized electrode with stacking coatings (lyophobic coatings on top and bottom with a lyophilic coating in the middle) can be beneficial to promote the design of air electrodes and provide a valuable reference to fabricate high-capacity electrodes.

2.5. Discharge−Charge Cycle. Although this study is focusing on the deep discharge capacity of Li−O_2 batteries with customized electrodes, the cycling performance is also investigated and analyzed. The first discharge−charge cycles of Li−O_2 batteries with customized electrodes at 0.1 mA/cm^2 are shown in Figure 6. The cut-off voltage of charge is set as 4.5 V. The mixed I 15% electrode as well as PTFE 15% electrode result in a discharge−charge cycle with the average coulombic efficiency close to 85%, whereas the battery with 15% PVDF

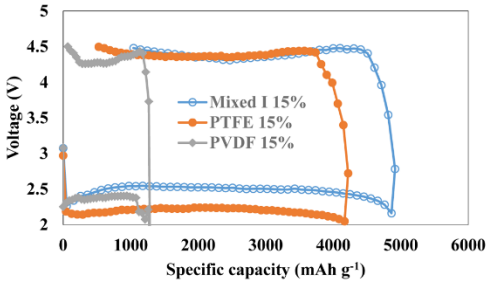

Figure 6. First discharge−charge cycle of Li−O_2 batteries with customized electrode.

DOI: 10.1021/acsomega.8b00808
ACS Omega 2018, 3, 6006−6012

achieves a slightly higher coulombic efficiency of 93%. The lower coulombic efficiencies of mixed I 15% electrode and PTFE 15% electrode can be contributed to the fact that more electrolyte in the lyophobic electrode evaporates because of much longer discharge and charge time, which may increase the ionic resistance during charge and thus deteriorate the coulombic efficiency.[29] Besides, PVDF favors the thin Li_2O_2 film formed on the surface of electrode, whereas PTFE results in more Li_2O_2 toroids, which are more difficult to decompose during charging.[30] The cycling performance of Li−O_2 batteries with PTFE 15% electrodes is also studied with the cut-off capacity of 1000 mAh/g. Figure 7 shows that coulombic

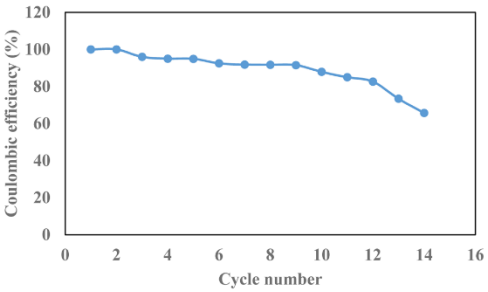

Figure 7. Coulombic efficiencies of Li−O_2 batteries with PTFE 15% electrode.

efficiency is more than 90% in the first nine cycles and the discharge−charge curves are shown in Figure S4. The cycling performance of Li−O_2 batteries using customized electrodes is validated. Further study will focus on optimizing the design of customized electrode since the rational structure can increase the cycle life of Li−O_2 batteries.[31,32]

3. CONCLUSIONS

The wettability of electrode was mainly altered by mixing acetylene black carbons with PTFE and/or PVDF binders at various weight ratios. The customized electrodes containing PVDF binder or less PTFE binder (<15%) were lyophilic, and their corresponding discharge capacities were lower than those of lyophobic electrodes. The electrode with 15% PTFE exhibited the deep discharge capacity of 4160.8 mAh/g because lyophobic electrode provided more gas path for O_2 diffusion. This study also designed customized electrodes with stacked layers by combining the lyophilic layers with lyophobic layers. The mixed I electrode (15% PTFE carbon coatings on top and bottom, one 15% PVDF carbon coating in the middle) showed the highest deep discharge capacity of 5149.5 mAh/g among all of the experimental cases. The mixed wettability promoted the oxygen diffusion without significantly lowering the ionic conductivity or reducing the number of reaction sites. Therefore, configuring the wettability in the electrode design is an important direction to increase the discharge capacity of Li−O_2 batteries. Further study may focus on improving the configuration of customized electrode wettability considering the spatial distribution of pore size[31] and specific pore volume of various carbon powders.

4. EXPERIMENTAL SECTION

4.1. Electrolyte Preparation. TEGDME (99%) purchased from Sigma-Aldrich was used as received to prepare the electrolyte. The electrolyte was prepared in a glovebox with <1 ppm water and <5 ppm oxygen. The electrolyte salt, LiTFSI (99.95%), from Sigma-Aldrich, was dissolved in TEGDME and the concentration was 1 mol/L.

4.2. Air Cathode Preparation. AvCarb 1071 HCB plain carbon cloth fabric purchased from Fuel Cell Store was used as the substrate of the customized cathode electrode on cathode. Conductive acetylene black (purchased from MTI Corporation) mixed with various weight ratios of PTFE was dissolved in the ethanol solution to form the carbon slurry. The substrate carbon cloth was dipped into the carbon slurry and dried in the atmosphere for 24 h. Then, the electrode was heat-treated at 350 °C for 30 min. The electrodes with customized coatings of 5, 15, 25, and 35% (in weight) of PTFE were obtained. In addition, electrodes with 15% PVDF carbon coatings and electrodes with mixed carbon coatings (both 15% PTFE and 15% PVDF) were prepared following the same procedure aforementioned. The schematic views on the structure of the customized electrodes are displayed in Figure 8. The targeted carbon loadings of all customized electrodes were 2 mg/cm^2. The measured carbon loadings of the fabricated electrodes were 2.1 ± 0.1 mg/cm^2.

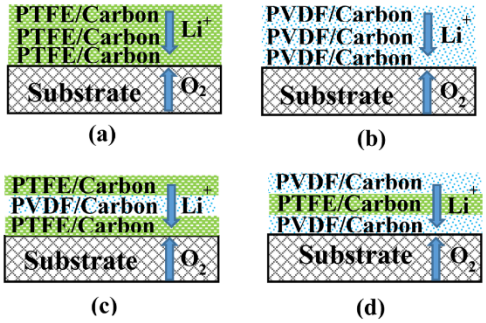

Figure 8. Structural views of customized electrodes with carbon coatings using (a) PTFE binder, (b) PVDF binder, (c) mixed binders I (PTFE + PVDF + PTFE), and (d) mixed binders II (PVDF + PTFE + PVDF) in this study.

4.3. Battery Assembly. The battery was constructed by sandwiching the oxygen diffuser, customized cathode electrode, separator, and lithium chip in the battery frame shown in Figure 9[29] The battery frame was customer-designed and made from highly corrosion-resistant grade 2 titanium. The open ratio of oxygen diffuser was 50% and the separator was a Whatman GF/B glass fiber filter from Fisher Scientific with the diameter of 2.1 cm. The lithium chip with the diameter of 1.56 cm was purchased from MTI Corporation. The PTFE gasket and O-ring purchased from McMaster-Carr were inserted to prevent oxygen leaking. All batteries were assembled in the glovebox by adding 60 μL of electrolyte in the separator and in the cathode electrode. The substrate layer faced the O_2 side and the 1 M LiTFSI/TEGDME electrolyte was added on the coating layer.

4.4. Wettability Measurements. The contact angles between 1 M LiTFSI/TEGDME and surfaces of customized

DOI: 10.1021/acsomega.8b00808
ACS Omega 2018, 3, 6006−6012

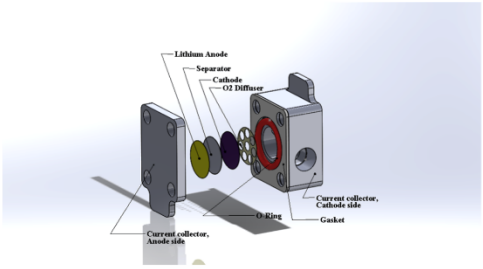

Figure 9. Li–O_2 battery frame and its components.[29]

electrodes were measured using ramé-hart Model 190 contact angle goniometer at the room temperature. The static contact angle, which can be maintained for 120 s during measurement, was used to characterize the surface wettability. Each measurement was conducted at three different locations on the surface of customized electrodes using 5 μL of electrolyte drops. Double-layer capacitance measurement was carried out by the cyclic voltammetry (CV) tests with SP 150 potentiostat from BioLogic Science Instrument. The experimental setup was the same as the battery assembly in the discharge experiment. The 1 M LiTFSI/TEGDME electrolyte was added on the surface of the electrode by a pipette. All CV measurements were performed from −0.2 to 0.2 V at the scanning rate of 0.2 V/s and repeated at least three times. The EIS data were analyzed by the EC Lab software (V11.02).

4.5. Deep Discharge Measurements. Assembled batteries were connected to a four-channel Arbin MSTAT4 battery tester. The pure oxygen was supplied at a flow rate of 0.3 sccm, and the pressure of the pure oxygen was maintained at 10 kPa gauge pressure. After resting for 1 h, deep discharge tests were conducted at room temperature and repeated at least three times.[18] First discharge–charge cycles of Li–O_2 batteries with Mixed I, 15% PTFE and 15% PVDF carbon coatings, were also tested and analyzed.

■ ASSOCIATED CONTENT

Supporting Information

The Supporting Information is available free of charge on the ACS Publications website at DOI: 10.1021/acsomega.8b00808.

Nyquist plots of batteries with customized electrode with different wettabilities, scanning electron microscopy images of customized electrodes with carbon coatings with 15% PVDF and 15% PTFE after discharge, the pore size distribution of electrodes, and discharge–charge cycles of Li–O_2 batteries with PTFE 15% electrodes (PDF)

■ AUTHOR INFORMATION

Corresponding Author

*E-mail: xianglinli@ku.edu. Phone: +1 (785) 864 8165.

ORCID

Xianglin Li: 0000-0002-0193-9410

Notes

The authors declare no competing financial interest.

■ ACKNOWLEDGMENTS

The authors greatly appreciate Dr. Gibum Kwon and his student Mr. Nathan Klein for their assistance on the contact angle measurement using ramé-hart goniometer.

■ REFERENCES

(1) Apergis, N.; Payne, J. E. Renewable and non-renewable energy consumption-growth nexus: Evidence from a panel error correction model. *Energy Econ.* **2012**, *34*, 733–738.

(2) Abraham, K. M. Prospects and limits of energy storage in batteries. *J. Phys. Chem. Lett.* **2015**, *6*, 830–844.

(3) Aurbach, D.; McCloskey, B. D.; Nazar, L. F.; Bruce, P. G. Advances in understanding mechanisms underpinning lithium–air batteries. *Nat. Energy* **2016**, *1*, No. 16128.

(4) Zheng, J.; Liang, R.; Hendrickson, M. a; Plichta, E. Theoretical energy density of Li–air batteries. *J. Electrochem. Soc.* **2008**, *155*, A432–A437.

(5) Padbury, R.; Zhang, X. Lithium–oxygen batteries—limiting factors that affect performance. *J. Power Sources* **2011**, *196*, 4436–4444.

(6) Girishkumar, G.; McCloskey, B.; Luntz, A.; Swanson, S.; Wilcke, W. Lithium–air battery: promise and challenges. *J. Phys. Chem. Lett.* **2010**, *1*, 2193–2203.

(7) Lei, Y.; Lu, J.; Luo, X.; Wu, T.; Du, P.; Zhang, X.; Ren, Y.; Wen, J.; Miller, D. J.; Miller, J. T.; et al. Synthesis of porous carbon supported palladium nanoparticle catalysts by atomic layer deposition: application for rechargeable lithium–O2 battery. *Nano Lett.* **2013**, *13*, 4182–4189.

(8) Qin, Y.; Lu, J.; Du, P.; Chen, Z.; Ren, Y.; Wu, T.; Miller, J. T.; Wen, J.; Miller, D. J.; Zhang, Z.; et al. In situ fabrication of porous-carbon-supported α-MnO_2 nanorods at room temperature: application for rechargeable Li–O 2 batteries. *Energy Environ. Sci.* **2013**, *6*, 519–531.

(9) Lu, Y.-C.; Gasteiger, H. A.; Parent, M. C.; Chiloyan, V.; Shao-Horn, Y. The influence of catalysts on discharge and charge voltages of rechargeable Li–oxygen batteries. *Electrochem. Solid-State Lett.* **2010**, *13*, A69–A72.

(10) Yang, Y.; Zhang, T.; Wang, X.; Chen, L.; Wu, N.; Liu, W.; Lu, H.; Xiao, L.; Fu, L.; Zhuang, L. Tuning the morphology and crystal structure of Li2O2: a graphene model electrode study for Li–O2 battery. *ACS Appl. Mater. Interfaces* **2016**, *8*, 21350–21357.

(11) Song, H.; Xu, S.; Li, Y.; Dai, J.; Gong, A.; Zhu, M.; Zhu, C.; Chen, C.; Chen, Y.; Yao, Y.; et al. Hierarchically Porous, Ultra-thick,"Breathable" Wood-Derived Cathode for Lithium-Oxygen Batteries. *Adv. Energy Mater.* **2018**, *8*, No. 1701203.

(12) Beattie, S.; Manolescu, D.; Blair, S. High-capacity lithium–air cathodes. *J. Electrochem. Soc.* **2009**, *156*, A44–A47.

(13) Adams, B. D.; Radtke, C.; Black, R.; Trudeau, M. L.; Zaghib, K.; Nazar, L. F. Current density dependence of peroxide formation in the Li–O 2 battery and its effect on charge. *Energy Environ. Sci.* **2013**, *6*, 1772–1778.

(14) Horstmann, B.; Gallant, B.; Mitchell, R.; Bessler, W. G.; Shao-Horn, Y.; Bazant, M. Z. Rate-dependent morphology of Li2O2 growth in Li–O2 batteries. *J. Phys. Chem. Lett.* **2013**, *4*, 4217–4222.

(15) Li, X.; Huang, J.; Faghri, A. A critical review of macroscopic modeling studies on Li O 2 and Li–air batteries using organic electrolyte: Challenges and opportunities. *J. Power Sources* **2016**, *332*, 420–446.

(16) Zhang, W.; Shen, Y.; Sun, D.; Huang, Z.; Huang, Y. Objectively Evaluating the Cathode Performance of Lithium-Oxygen Batteries. *Adv. Energy Mater.* **2017**, *7*, No. 1602938.

(17) Read, J.; Mutolo, K.; Ervin, M.; Behl, W.; Wolfenstine, J.; Driedger, A.; Foster, D. Oxygen transport properties of organic electrolytes and performance of lithium/oxygen battery. *J. Electrochem. Soc.* **2003**, *150*, A1351–A1356.

(18) Mohazabrad, F.; Wang, F.; Li, X. Experimental Studies of Salt Concentration in Electrolyte on the Performance of Li-O2 Batteries at

DOI: 10.1021/acsomega.8b00808
ACS Omega 2018, 3, 6006–6012

Various Current Densities. *J. Electrochem. Soc.* **2016**, *163*, A2623−A2627.
(19) Schmitz, D.; Anlauf, R.; Rehrmann, P. Effect of air content on the oxygen diffusion coefficient of growing media. *Am. J. Plant Sci.* **2013**, *4*, 955−963.
(20) Xu, W.; Xiao, J.; Zhang, J.; Wang, D.; Zhang, J.-G. Optimization of nonaqueous electrolytes for primary lithium/air batteries operated in ambient environment. *J. Electrochem. Soc.* **2009**, *156*, A773−A779.
(21) Zhang, Y.; Zhang, H.; Li, J.; Wang, M.; Nie, H.; Zhang, F. The use of mixed carbon materials with improved oxygen transport in a lithium-air battery. *J. Power Sources* **2013**, *240*, 390−396.
(22) Chen, M.; Jiang, X.; Yang, H.; Shen, P. K. Performance improvement of air electrode for Li/air batteries by hydrophobicity adjustment. *J. Mater. Chem. A* **2015**, 3, 11874−11879.
(23) Malmberg, C.; Maryott, A. Dielectric Constant of Water from 00 to 1000 C. *J. Res. Natl. Bur. Stand.* **1956**, *56*, 1−8.
(24) Choi, J. W.; Cheruvally, G.; Shin, Y. J.; Ahn, H. J.; Kim, K. W.; Ahn, J. H. Effect of Various Lithium Salts in TEGDME Based Electrolyte for Li/Pyrite Battery. *Solid State Phenomena*; Trans Tech Publications, 2007; pp 971−974.
(25) Amanchukwu, C. V.; Harding, J. R.; Shao-Horn, Y.; Hammond, P. T. Understanding the chemical stability of polymers for lithium−air batteries. *Chem. Mater.* **2015**, *27*, 550−561.
(26) Papp, J. K.; Forster, J. D.; Burke, C. M.; Kim, H. W.; Luntz, A. C.; Shelby, R. M.; Urban, J. J.; McCloskey, B. D. Poly (vinylidene fluoride)(PVDF) Binder Degradation in Li−O2 Batteries: A Consideration for the Characterization of Lithium Superoxide. *J. Phys. Chem. Lett.* **2017**, *8*, 1169−1174.
(27) Sow, P. K.; Lu, Z.; Talebian, H.; Damron, L.; Mérida, W. Double Layer Capacitance Measurements To Characterize the Water Intrusion into Porous Materials. *J. Phys. Chem. C* **2016**, *120*, 24794−24802.
(28) Xia, C.; Bender, C. L.; Bergner, B.; Peppler, K.; Janek, J. An electrolyte partially-wetted cathode improving oxygen diffusion in cathodes of non-aqueous Li−air batteries. *Electrochem. Commun.* **2013**, *26*, 93−96.
(29) Mohazabrad, F.; Wang, F.; Li, X. Influence of the Oxygen Electrode Open Ratio and Electrolyte Evaporation on the Performance of Li−O2 Batteries. *ACS Appl. Mater. Interfaces* **2017**, *9*, 15459−15469.
(30) Geaney, H.; O'Dwyer, C. Examining the role of electrolyte and binders in determining discharge product morphology and cycling performance of carbon cathodes in Li-O2 batteries. *J. Electrochem. Soc.* **2016**, *163*, A43−A49.
(31) Liu, G.; Chen, H.; Xia, L.; Wang, S.; Ding, L.-X.; Li, D.; Xiao, K.; Dai, S.; Wang, H. Hierarchical Mesoporous/Macroporous Perovskite La0. 5Sr0. 5CoO3−x Nanotubes: A Bifunctional Catalyst with Enhanced Activity and Cycle Stability for Rechargeable Lithium Oxygen Batteries. *ACS Appl. Mater. Interfaces* **2015**, *7*, 22478−22486.
(32) Liu, G.; Zhang, L.; Wang, S.; Ding, L.-X.; Wang, H. Hierarchical $NiCo_2O_4$ nanosheets on carbon nanofiber films for high energy density and long-life Li−O_2 batteries. *J. Mater. Chem. A* **2017**, *5*, 14530−14536.

DOI: 10.1021/acsomega.8b00808
ACS Omega 2018, 3, 6006−6012

Paper P2

Discharge Li-O_2 Batteries with Intermittent Current

Journal of Power Sources 394 (2018) 50–56

Contents lists available at ScienceDirect

Journal of Power Sources

journal homepage: www.elsevier.com/locate/jpowsour

Discharge Li-O_2 batteries with intermittent current

Fangzhou Wang, Xianglin Li*

Department of Mechanical Engineering, University of Kansas, Lawrence, KS 66046, USA

HIGHLIGHTS

- Applying intermittent current (> 1 mA/cm^2) enhances O_2 diffusion in the electrode.
- The battery capacity is increased by more than 50% with intermittent discharge.
- Hydrophilic electrodes benefit the most from the intermittent discharge strategy.
- Discharging with descending currents maximizes capacity with a given cutoff voltage.

ARTICLE INFO

Keywords:
Li-O_2 battery
High current discharge
O_2 diffusion
Electrode wettability
Discharge capacity

ABSTRACT

This study periodically rests Li-O_2 batteries (for 5–10 min) between each 2–10 min discharge to improve the oxygen transfer within the porous electrode. Periodically resting the battery increases the specific discharge capacity by at least 50% at various current densities (0.1–1.5 mA/cm^2). Multistep discharge at decreasing current rates (2.0, 1.5, and 1.0 mA/cm^2) is also proposed to increase the overall discharge capacity with a given cutoff voltage. The performance improvement is mainly due to the enhanced O_2 diffusion during rest between intermittent discharge. The lyophilic electrode has the highest increase rate of discharge capacity after applying intermittent current while the electrode with mixed wettability achieves the highest specific discharge capacity. The resting and discharging time of electrodes with mixed wettability are then optimized at 1.0 mA/cm^2. Cycling tests with 1000 mA h/g and 1500 mAh/g cut-off capacities at 1.0 mA/cm^2 are also performed. The batteries completed similar numbers of cycles with a higher cut-off capacity (1500 mAh/g) applying intermittent discharge, compared with applying continuous current (1000 mAh/g cut-off capacity). This study emphasizes the importance of O_2 diffusion and provides practical strategies to improve the deep discharge capacity of Li-O_2 batteries, especially at high current rates (> 1.0 mA/cm^2).

1. Introduction

The rapid growth in technologies such as electrical vehicles and mobile electronic devices and the urgent need to reduce environmental pollution require energy storage systems with higher energy density. Nowadays, Li-ion batteries have been commercialized and widely utilized for decades but the energy density of the state-of-art Li-ion batteries (~300 Wh/kg) is limited by the intercalation chemistry. The Li-O_2 battery is considered at one of the most promising energy storage technology replacing Li-ion battery due to the extremely high theoretical energy density of ~3500 Wh/kg [1,2]. The electrochemical reactions occurring in Li-O_2 batteries are shown in Eqs. (1)–(3). The theoretical voltage of the reaction E^0 is 2.96 V [3].

$$\text{Anode: } 2Li \underset{\text{Charge}}{\overset{\text{Discharge}}{\rightleftharpoons}} 2Li^+ + 2e^- \quad (1)$$

$$\text{Cathode: } 2Li^+ + 2e^- + O_2 \underset{\text{Charge}}{\overset{\text{Discharge}}{\rightleftharpoons}} Li_2O_2 \quad (2)$$

$$\text{Overall: } 2Li + O_2 \underset{\text{Charge}}{\overset{\text{Discharge}}{\rightleftharpoons}} Li_2O_2 \quad (3)$$

When the Li-O_2 batteries are discharged, the Li metal is oxidized to Li^+ at the anode and O_2 is reduced on the cathode, generating solid Li_2O_2. During charge, the reversed cathodic reaction decomposes Li_2O_2 and releases O_2 and Li^+. The Li metal is deposited on anode by the reversed anodic reaction. Although the above electrochemical reactions have extremely high theoretical energy density, the practical energy density is only ~1000 Wh/kg [4]. Multiple challenges exist in developing Li-O_2 batteries for commercial applications. The fundamental issues related to Li-O_2 batteries, including the reaction mechanism, the electrochemical stability of cathode, electrolyte and Li anode are not be fully understood [5,6]. Besides, the low discharge/charge rate

* Corresponding author.
E-mail address: xianglinli@ku.edu (X. Li).

https://doi.org/10.1016/j.jpowsour.2018.05.033
Received 4 February 2018; Received in revised form 26 April 2018; Accepted 8 May 2018
Available online 15 May 2018
0378-7753/

capability, poor cycle life and low round-trip efficiency are the crucial factors that impede the practical operation of Li-O_2 batteries [7–9]. Research find that the reaction over-potential is mainly caused by cathode reactions [10]. The cathode passivation deteriorates as the discharge current density increases and the discharge current density is a key parameter that can affect the performance of Li-O_2 batteries.

The practical applications of electrical vehicles require discharging the current density that is two orders of magnitude higher than the present current density applied in discharging the Li-O_2 batteries (e.g. 0.1 mA/cm^2) [11]. Therefore, it is urgent to discharge the Li-O_2 batteries at higher current density to facilitate the commercialization. Multiple numerical and experimental studies demonstrated that the discharge capacity would be reduced significantly if the Li-O_2 batteries are discharged at high current density [12–19]. For instance, Han et al. [14] stated that the discharge voltage plateau decreased by 0.2 V and discharge capacity decreased from 6219 to 1251 mAh/g when the current density increases from 0.1 mA/cm^2 to 0.4 mA/cm^2. Mohazabrad et al. [19] showed that the specific discharge capacity decreased from 461.53 mAh/g to 106.07 mAh/g when the current density increased from 0.1 mA/cm^2 to 0.5 mA/cm^2. Tremendous efforts have been paid to clarify the dominated factor that affect the discharge capacity of Li-O_2 batteries at high current density. The electrical passivation of cathode caused by Li_2O_2 film and poor O_2 transportation limited by pore clogging are claimed as two major factors that limit the discharge capacity. For example, Adams et al. [20] reported that Li_2O_2 particles nucleated at low current densities (5–25 μA/cm^2), and amorphous thin films of Li_2O_2 formed by electro-reduction reaction on the electrode surface at high current densities (50–100 μA/cm^2). The investigation by Adams et al. [20] also showed that the direct electron transfer would incur a significant voltage drop at high current density which indicates the thickness and conductivity of the Li_2O_2 film become more important for discharging Li-O_2 batteries at high current density. The electrical conductivity of Li_2O_2 film was investigated both experimentally and numerically [21]. Results show that the critical thickness of Li_2O_2 film is ~5 nm above which the exchange current density fell rapidly below ~10^{-7} A/cm^2 and the ORR was no longer supported, leading to "sudden death" of Li-O_2 batteries. The electrical conductivity of Li_2O_2 was estimated to be in the range of 10^{-12} to 10^{-13} S cm^{-1} and the critical thickness of 5 nm was confirmed by Lu et al. [22]. Mirzaeian et al. [16] examined the operation effect on the performance of Li-O_2 batteries systematically. The discharge capacity decreased from 2387 mAh/g to 364 mAh/g as the current density varied from 10 mA/g to 150 mA/g. The discharge ceased when the discharge products occupied almost all the pores at lower current density. Another study [23] argued that the Li_2O_2 deposition only covers the electrode external surface by forming a thin film rather than filling the interior pores in the electrode at high current density. Therefore, the capacity loss can be attributed to the fast deposition of Li_2O_2 on the electrode surface which limits the transportation of O_2 and Li^+ and blocks the inner active surface. However, the morphology of discharge products such as the primary product of Li_2O_2 is not only influenced by the current density but other factors such as the electrode structure [24] and the electrolyte [25,26]. Thus, it is very challenging to control the morphology of discharge products to improve the rate capability of Li-O_2 batteries.

On the other hand, studies [27,28] claimed that the poor rate capability of Li-O_2 batteries was mainly due to sluggish O_2 transportation in the organic electrolyte of flooded electrodes, which was also reported by the numerical studies [13,29]. The 1 M electrolytes with different constituents display various viscosity such that the corresponding O_2 diffusion coefficients estimated by Stokes-Einstein equation are also different [28]. For example, 1 M Li hexafluorophosphate ($LiPF_6$) in propylene carbonate (PC) has the viscosity of 8.06 cP while the viscosity of 1 M LiPF6 in PC: dimethoxyethane (DME) (1:2) is 1.98 cP. When discharge the Li-O_2 batteries with 1 M $LiPF_6$/PC and 1 M $LiPF_6$/PC:DME (1:2) at 0.1 mA/cm^2, the discharge capacities were 380 and 1095 mAh/g, respectively. When discharging those batteries at 0.5 mA/cm^2, the discharge capacity corresponding to 1 M $LiPF_6$/PC was 85 mAh/g while it was 363 mAh/g for 1 M $LiPF_6$/PC:DME (1:2). The three times increase of capacity showed that promoting O_2 diffusion in the electrode can reduce the capacity loss at high current density. In other words, the poor O_2 diffusion may dominate the performance of Li-O_2 batteries at high current density.

The debate on the determining factor of capacity loss of Li-O_2 batteries at high current density may continue until the fundamental mechanism is fully understood. However, possible approaches which include intermittent operating procedure and modifying the electrode wettability [30] can be applied to enhance the O_2 diffusion in the electrode and thus improve the rate capability of Li-O_2 batteries. In this study, intermittent discharge strategies were proposed and investigated for Li-O_2 batteries with electrodes of different wettability at various current densities (0.1–2.0 mA/cm^2), and compared with batteries discharged at continuous current densities. Cycling experiments on Li-O_2 batteries were also studied to determine the effect of discharge strategy on discharge-charge cycles.

2. Experimental methodology

The cathode electrode used in this study was prepared by coating conductive acetylene black (MTI Corporation) on the AvCarb 1071 HCB plain carbon cloth (Fuel Cell Store) [30]. Firstly, the acetylene black was mixed with the binder such as polytetrafluoroethylene (PTFE) or polyvinylidene fluoride (PVDF) at 15% mass fraction in ethanol solution. After dipping the substrate carbon cloth in the slurry and drying it in the atmosphere for 24 h for three times, the electrode was heat treated at 350 °C for 30 min. The electrodes containing 15% PVDF carbon coatings and the ones with mixed layers of carbon coatings (both 15% PTFE and 15% PVDF) were also prepared as described above. The structures of three types of the customized electrodes are shown in Figure S1. The measured carbon loadings of the fabricated electrodes were 3.0 ± 0.2 mg/cm^2.

The battery structure was displayed in Fig. 1 and the oxygen diffuser, customized cathode electrode, separator and Li chip are compressed together to guarantee the good contact between each component. The open ratio of oxygen diffuser was 50% [18] and the separator was a Whatman GF/B glass fiber filter from Fisher Scientific with the diameter of 2.1 cm. The PTFE gasket and O-ring were inserted between current collectors to avoid the short circuit and prevent O_2 leaking. The electrolyte consisted of dissolving bis(trifluoromethylsulfonyl)amine Li salt (LiTFSI) in tetraethylene glycol dimethyl ether (TEGDME). The concentration of prepared electrolyte was 1 M and the volume added in the battery was 120 μL. All these fabricating processes were completed in the Mikrouna glovebox with water and oxygen concentrations less than 1 ppm.

The electrochemical performance of the Li-O_2 batteries were examined by a 4-channel Arbin MSTAT4 battery tester at room temperature (20 °C). All the tests were set with the discharge cut-off voltage of 2.0 V, unless stated otherwise. Each group of the test was initiated after resting the battery for 1 h and repeated at least three times. All the experimental cases, with different combinations of discharge strategies and various customized electrodes, were listed in Table S1. The discharge strategies included continuous current and intermittent current at which the Li-O_2 batteries were discharged and rested periodically.

The acetylene black carbon is examined using a N_2 adsorption technique. The physisorption measurement is performed at 77 K by the surface and pore size analyzer (NOVAtouch N2TLX – 1, Quantachrome Instrument, U.S.). The sample weight is approximate 0.1 g which is degassed at 300 °C for 3 h before adsorption/desorption measurements. The amount adsorbed vs. the adsorptive pressure (P), relative to the saturated vapor pressure over the bulk liquid (P_0) is obtained and used for analysis. According to the isotherms of adsorption and desorption, the surface area is analyzed by Brunauer, Emmet and Teller (BET) method, the pore size distribution is evaluated by Barrett, Joyner and

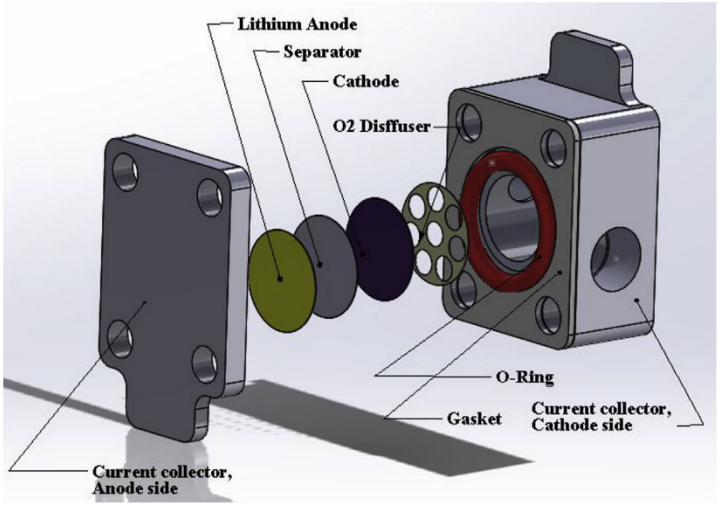

Fig. 1. Li-O_2 battery frame with its components [18].

Halenda (BJH) and Density Function Theory (DFT) methods.

3. Results and discussion

3.1. Intermittent discharge current

This study first compares the specific discharge capacities of Li-O_2 batteries under intermittent discharge currents and those under continuous currents. The electrode with 15% PTFE binder, lyophobic with the static contact angle of 128.4°, achieves higher discharge capacity than that of lyophilic electrode [30]. Thus, electrodes with PTFE 15% binder are tested in this subsection. Fig. 2 shows the results of specific discharge capacities when Li-O_2 batteries are discharged under continuous or intermittent currents of 0.1, 0.5, 1.0, and 1.5 mA/cm^2. The intermittent current strategy discharges the battery at the given current for certain time and rests the battery for 10 min periodically. The time for discharge is proportional to the given current. For example, the battery is discharged for 10 min at 0.5 mA/cm^2 and for 5 min at 1.0 mA/cm^2. The discharge and rest times are estimated based on O_2 consumption and diffusion rates in Table S2. It can be clearly seen on Fig. 2 that both the continuous discharge capacity and the intermittent

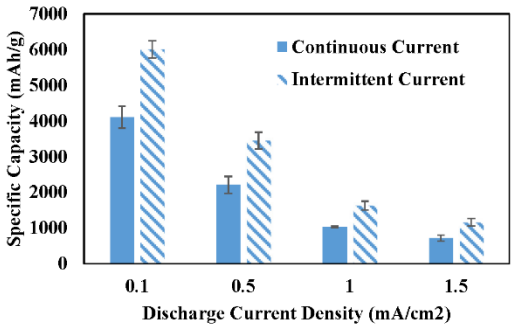

Fig. 2. Specific discharge capacities of Li-O_2 batteries with PTFE 15% electrodes at continuous and intermittent current densities.

discharge capacity decrease when the current density increases from 0.1 to 1.5 mA/cm^2. The discharge capacity is lower at higher current density because of the increased polarization of cathode electrode, which has been already examined in other studies [19]. The specific discharge capacities of Li-O_2 batteries discharged by intermittent current are ~50% higher than these obtained by continuous current. For example, the specific discharge capacity is 1629.5 ± 124.0 mAh/g at intermittent discharge current of 1.0 mA/cm^2 while it is 1031.0 ± 22.8 mAh/g at continuous discharge current of 1.0 mA/cm^2. Since the O_2 diffusion plays a significant role in determining the discharge capacity, the Li-O_2 battery will achieve higher discharge capacity if more O_2 is available. When the Li-O_2 battery is discharged intermittently, O_2 can diffuse into the electrode while the battery is at rest and compensate the O_2 consumed during discharge. Thus, the capacity loss caused by sluggish O_2 diffusion is alleviated and the discharge capacity is increased by ~50% at various current densities. Fig. 3 displays the discharge curves of Li-O_2 batteries with continuous and intermittent 0.5 mA/cm^2. The voltages of Li-O_2 batteries discharged intermittently jump back to ~2.8 V when the batteries are at rest. The discharge curves suffer potential dips at the beginning of discharge, which are consistent with the previous study on discharge curves [31]. Discharge plateaus are elongated and stabilized when the Li-O_2 batteries are discharged intermittently, which is shown in Fig. 3 as well. The Type IV isotherm is observed in N_2 adsorption/desorption measurement in Figure S2. The relatively long linear part indicates the completion of the monolayer and the isotherm characterizes a mesoporous structure in the porous electrode. Results calculated based on the isotherm also show that the acetylene black carbon has the BET surface area of 76.5 m^2/g and most of the pores are in the range of 2–50 nm. The results of surface area and pore size distribution confirms that the electrode has a mesoporous structure and the O_2 diffusion will not be impeded due to the electrode structure. After discharge, electrodes are measured by SEM and shown in Figure S3-S5. At low current, the needle-like Li_2O_2 (confirmed by Rama Spectra in Figure S6) can be detected on the electrode surface and the film-like Li_2O_2 forms at high current. The discharge products merge gradually to form large agglomerates that hinder the O_2 mass transfer. The morphologies of Li_2O_2 were similar when they are deposited under intermittent and continuous discharge current, which demonstrates that the increase of discharge capacity at intermittent current has no relationship with the

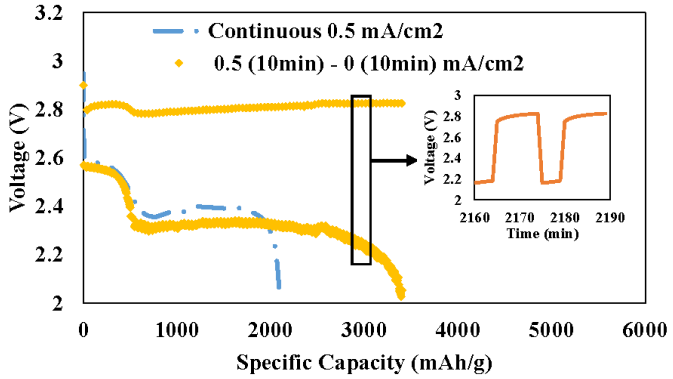

Fig. 3. Discharge curves of Li-O_2 batteries with PTFE 15% electrodes at continuous and intermittent 0.5 mA/cm^2.

morphological variations of Li_2O_2. In general, the discharge capacity can be improved due to sufficient O_2 supply by periodically resting the Li-O_2 battery.

3.2. Multi-step discharge

The existing studies usually report the Li-O_2 batteries discharged at current density on the order of 0.1 mA/cm^2, which is too low from the commercializing requirement. This study tries to increase the capacity at much higher current rates. The Li-O_2 battery with the PTFE 15% electrode is discharged under continuous and intermittent current of 2.0 mA/cm^2 (Fig. 4 (a)). When the discharge cut-off voltage is set as 2.0 V, the continuous discharge capacity is 423.4 ± 29.1 mAh/g and the intermittent discharge capacity is 436.4 ± 45.5 mAh/g. Thus, the intermittent discharge strategy only slightly increases the specific discharge capacity by 3%. However, when the discharge cut-off voltage is changed into 1.0 V, the intermittent discharge capacity reaches 1683.9 ± 148.7 mAh/g while it is only 800.2 ± 162.1 mAh/g at continuous discharge current. Fig. 4 shows the discharge curves at 2.0 V cut-off voltage drop linearly towards 2.0 V without forming a discharge plateau. The battery stops discharging because the over-potential caused by polarization exceeds the difference between open-circuit voltage and cut-off voltage of 2.0 V. When the cut-off voltage is set at 1.0 V, the plateaus are built and the discharge capacities are increased. This reveals that the battery may be further discharged even after it reaches the cut-off voltage at high current density. This finding leads to the study of multistep discharging at decreasing current rates. The discharge curve of Li-O_2 batteries at multistep discharge current (2.0-1.5-1.0 mA/cm^2) is shown in Fig. 4(b). The discharge capacity is 517 mAh/g when the voltage reaches 2.0 V at 2.0 mA/cm^2. Pores inside the electrode are not fully clogged by discharge products, the battery still possesses the potential to be discharged. Therefore, the discharge capacity is increased to 855 ± 49.9 mAh/g when the battery is further discharged at 1.5 and 1.0 mA/cm^2.

3.3. The electrode wettability

The O_2 diffusion is also affected significantly by the electrode wettability which has been systematically investigated in previous literature report [30]. The electrode with 15% PVDF binder is lyophilic and the electrolyte will spread into the electrode as soon as it is added on the electrode surface. Thus, the static contact angle cannot be measured. The static contact angle of mixed 15% electrode of 118.8° is slightly lower than that of PTFE 15% electrode (128.4°) due to the lyophilic layer in the middle of electrode coatings. These three kinds of electrodes for Li-O_2 batteries are selected and studied in this subsection.

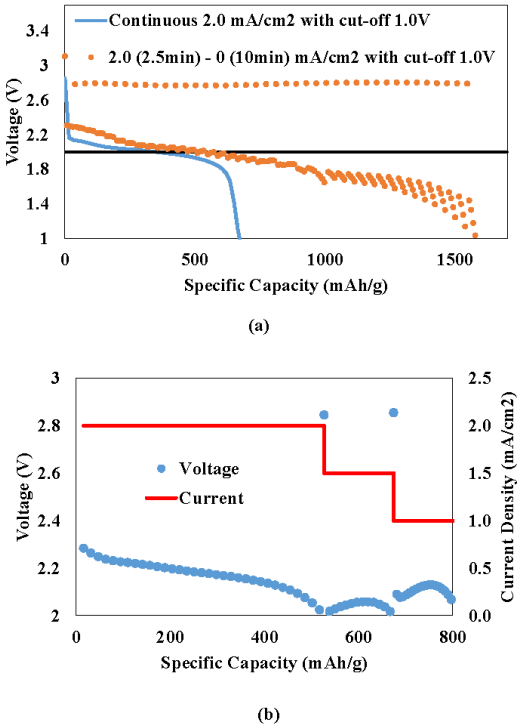

Fig. 4. Discharge curves of Li-O_2 batteries with PTFE 15% electrodes discharged at (a) 2.0 mA/cm^2 continuously and intermittently and (b) at multi-step current.

Fig. 5 exhibits the specific discharge capacities of all types of electrodes discharged at 1.0 mA/cm^2 continuously and intermittently. The specific discharge capacity of Li-O_2 battery with mixed binders increases from 1645.9 ± 98.3 mAh/g to 2256.7 ± 225.8 mAh/g when the operation changes from continuous discharge current to intermittent discharge current. The specific discharge capacity of the PVDF 15% electrode is 1664.8 ± 259.6 mAh/g at intermittent current but it is only 807.6 ± 137.6 mAh/g at continuous 1.0 mA/cm^2. The discharge

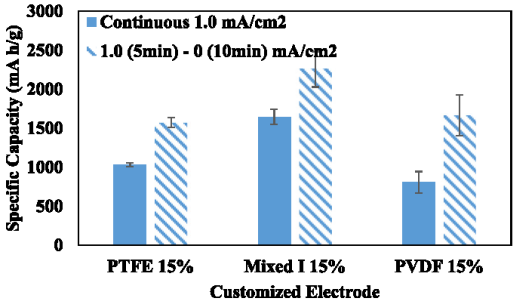

Fig. 5. Specific discharge capacities of Li-O_2 batteries with electrodes of different wettability discharged at 1.0 mA/cm^2 continuously and intermittently.

capacity is improved by 106.2%, much higher than those of the PTFE 15% electrode (51%) and the mixed 15% electrode (38%). The lyophilic PVDF 15% electrode is completely wetted by the electrolyte. The number of reaction sites increases but the O_2 diffusion is impeded due to the low O_2 diffusivity in the liquid electrolyte. Therefore, enhancing O_2 supply may be more urgent in this case. Experimental results demonstrate that Li-O_2 batteries with lyophilic electrodes are more sensitive to the intermittent discharge current and the discharge capacity can be increased more significantly. The mixed 15% electrode results in the highest discharge capacity which coincides well with results in previous study [30]. This is because the balance is achieved between dried regions for fast O_2 diffusion and wetted areas for electrochemical reactions. The discharge curves shown in Fig. 6 followed the trend in Fig. 3 in general. At the end of discharge, the potential decreases significantly and then increase gradually every time when the battery is discharged after the rest. As more Li_2O_2 is deposited in the electrode, the potential drop when the current changes from 0 to 1.0 mA/cm^2 is more obvious. When the potential drops below 2.0 V, the "sudden death" occurs and the battery stops discharging. The voltage of discharge plateau of the Li-O_2 battery with mixed 15% electrode is slightly higher ($0.05\ V < \Delta V < 0.1\ V$) than these of the batteries with the other two kinds of electrodes, which agrees well with its highest discharge capacity. Experiments in this subsection show that the discharge capacity of lyophilic electrode can increase more with periodical rests and the mixed 15% electrode obtains the highest capacity.

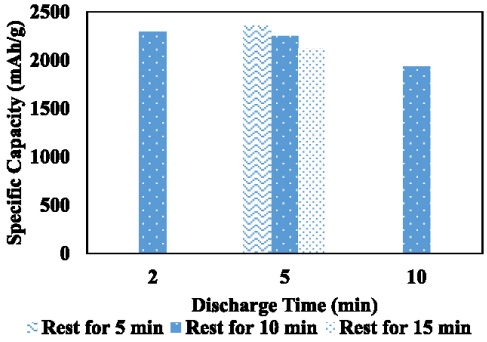

Fig. 7. Specific discharge capacities of Li-O_2 batteries with mixed 15% electrodes at 1.0 mA/cm^2 with different intermittent discharge strategies.

3.4. The intermittent discharge strategy

Since electrode is compressed when assembling the battery, the porous structure inside the electrode may be changed and thus the O_2 diffusion is affected. The estimated time schedule of discharging for 5 min and resting for 10 min may not be the best strategy. Thus, different intermittent discharge strategies are investigated experimentally and shown in Fig. 7. The subsection tests the mixed 15% electrode at discharge current of 1.0 mA/cm^2. With the rest time of 10 min, the specific discharge capacities decrease slightly from 2298.1 ± 135.1 mAh/g to 2256.7 ± 225.8 mAh/g as the discharge time varies from 2 min to 5 min. Although the capacity difference is negligible, the strategy of intermittent current 1.0 (2min) – 0 (10min) mA/cm^2 is less time-efficient. Discharging the battery for 10 min and resting for 10 min suffers the lack of O_2 supply which results in lower discharge capacity of 1941.6 ± 110.3 mAh/g. When the discharge time is set to be 5 min, the specific discharge capacity decreases gradually from 2357.5 ± 138.2 mAh/g to 2121.0 ± 191.8 mAh/g when the rest time increases from 5 min to 15 min, which may be mainly due to the electrolyte evaporation [18]. Considering the time efficiency and the capacity increase, the optimized strategy for the Li-O_2 battery with the mixed 15% electrode at 1.0 mA/cm^2 is discharging for 5 min and resting for 5 min. The intermittent discharge strategy may need to be customized based on the wettability and discharged current densities.

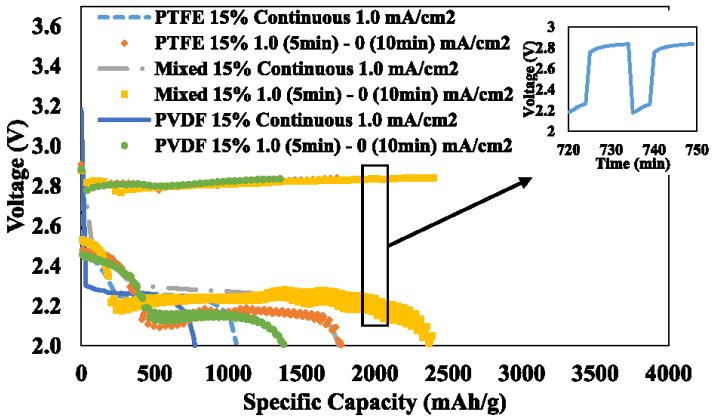

Fig. 6. Discharge curves of Li-O_2 batteries with electrodes of different wettability discharged at 1.0 mA/cm^2 continuously and intermittently.

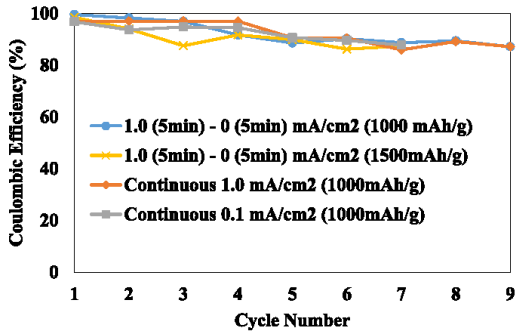

Fig. 8. Coulombic efficiencies of Li-O_2 batteries discharged in the cycling tests.

3.5. Cycling performance

The electrodes with mixed 15% binders are discharged and charged with cut-off capacities of 1000 mAh/g and 1500 mAh/g, respectively. Discharge strategies include continuous current at 0.1 mA/cm^2 and 1.0 mA/cm^2 and intermittent 1.0 (5min) – 0 (5min) mA/cm^2 but all batteries are charged at a continuous current of 0.1 mA/cm^2. The coulombic efficiencies of Li-O_2 batteries are shown in Fig. 8 and the cycling curves are shown in Figure S7, respectively. It can be clearly shown that the cycle numbers vary between 7 and 9 and the coulombic efficiencies are above 85%. After the last cycle, the voltages of Li-O_2 batteries reach the cut-off voltage of 2.0 V and thus the tests stop. The cycling performance of Li-O_2 batteries are similar despite of the discharge current. We speculate that failures of cycling tests are mainly attributed to the Li anode which may be contaminated by the water in the atmosphere. The symmetrical battery with Li chips on both anode and cathode are cycled and analyzed to validate the assumption. Results of cell potentials shown in Figure S8 demonstrate that the overpotential caused by water contamination on Li chip is more than 1.0 V after 14 cycles. The cycle can continue with almost 100% coulombic efficiency after replacing the Li chip. The contamination of water from the air also coincides with results from previous study [32] and will deteriorate the cycling performance of Li-O_2 batteries. The discharge plateau of the 7th cycle at continuous 0.1 mA/cm^2 in Figure S7 (a) and that of the 9th cycle in Figure S7 (c) descend more apparently which are due to the Li chip contamination. Applying the intermittent discharge strategy is advantageous over the continuous discharge strategy since it can cycle the batteries with higher cut-off capacity (e.g. 1500 mAh/g). The cycling performance of Li-O_2 batteries with 1500 mAh/g cut-off capacity has also been demonstrated in Fig. 8 and Figure S7 (d).

4. Conclusion

In conclusion, this study quantitatively examines the importance of enhancing O_2 diffusion in the Li-O_2 batteries during discharge. The intermittent discharge approach applied in this study can also serve as a practical way to improve the deep discharge capacity even at high current rates (> 1.0 mA/cm^2). The Li-O_2 batteries were discharged and rested periodically when intermittent strategy was applied. The intermittent discharge current can enhance the O_2 diffusion and increase the discharge capacity due to sufficient O_2 supply. Battery stacks for transportation or stationary applications will likely be composed of thousands of single cells. These single cells can be easily grouped and controlled separately following strategies investigated in this study: while some cells are discharging, other cells could be at rest to recover the oxygen.

The discharge capacities of Li-O_2 batteries with PTFE 15% electrodes increased by 50% when these batteries were discharged at intermittent currents of 0.1, 0.5, 1.0 and 1.5 mA/cm^2. The discharge capacity was doubled when the battery was discharged at intermittent 2.0 mA/cm^2 with 1.0 cut-off voltage. Besides, the Li-O_2 batteries can be further discharged at lower current densities (1.5, 1 mA/cm^2 etc.) after it reaches the discharge cut-off voltage at a high current (2.0 mA/cm^2). The Li-O_2 batteries with lyophilic electrodes such as PVDF 15% electrodes were more sensitive to the intermittent discharge current. More than 100% increase on the discharge capacity was observed when the Li-O_2 batteries with PVDF 15% electrodes were discharged at intermittent 1.0 mA/cm^2. Mixed 15% electrodes balanced the wetted regions for reactions and dried paths for O_2 diffusion and increased the discharge capacity. The Li-O_2 batteries with mixed 15% electrodes gained the highest capacity of 2256.7 ± 225.8 mAh/g at the intermittent current of 1.0 mA/cm^2. The optimized intermittent discharge strategy depended on the electrode wettability and discharge current. For the Li-O_2 batteries with mixed 15% electrode at intermittent 1.0 mA/cm^2, the discharge time was determined to be 5 min and resting time for O_2 diffusion was also 5 min.

Acknowledgements

The authors wants to thank the financial support from New Faculty General Research Fund and the General Research Fund (2234801) provided by the University of Kansas.

Appendix A. Supplementary data

Supplementary data related to this article can be found at http://dx.doi.org/10.1016/j.jpowsour.2018.05.033.

References

[1] P.G. Bruce, S.A. Freunberger, L.J. Hardwick, J.-M. Tarascon, Nat. Mater. 11 (2012) 19–29.
[2] F. Li, T. Zhang, H. Zhou, Energy Environ. Sci. 6 (2013) 1125–1141.
[3] Y.-C. Lu, H.A. Gasteiger, M.C. Parent, V. Chiloyan, Y. Shao-Horn, Electrochem. Solid State Lett. 13 (2010) A69–A72.
[4] D. Aurbach, B.D. McCloskey, L.F. Nazar, P.G. Bruce, Nat. Energy 1 (2016) 16128.
[5] D. Sharon, D. Hirshberg, M. Afri, A.A. Frimer, M. Noked, D. Aurbach, J. Solid State Electrochem. (2017) 1–18.
[6] T. Vegge, J.M. Garcia-Lastra, D.J. Siegel, Lithium–oxygen batteries: at a crossroads? Curr. Opin. Electrochem. 6 (2017) 100–107.
[7] Y.-C. Lu, D.G. Kwabi, K.P. Yao, J.R. Harding, J. Zhou, L. Zuin, Y. Shao-Horn, Energy Environ. Sci. 4 (2011) 2999–3007.
[8] G. Girishkumar, B. McCloskey, A. Luntz, S. Swanson, W. Wilcke, J. Phys. Chem. Lett. 1 (2010) 2193–2203.
[9] A. Débart, J. Bao, G. Armstrong, P.G. Bruce, J. Power Sources 174 (2007) 1177–1182.
[10] S.S. Zhang, D. Foster, J. Read, J. Power Sources 195 (2010) 1235–1240.
[11] F.T. Wagner, B. Lakshmanan, M.F. Mathias, J. Phys. Chem. Lett. 1 (2010) 2204–2219.
[12] X. Li, J. Huang, A. Faghri, Energy 81 (2015) 489–500.
[13] X. Li, A. Faghri, J. Electrochem. Soc. 159 (2012) A1747–A1754.
[14] S.-M. Han, J.-H. Kim, D.-W. Kim, J. Electrochem. Soc. 161 (2014) A856–A862.
[15] B. Kumar, J. Kumar, R. Leese, J.P. Fellner, S.J. Rodrigues, K. Abraham, J. Electrochem. Soc. 157 (2010) A50–A54.
[16] M. Mirzaeian, P.J. Hall, F.B. Sillars, I. Fletcher, M.M. Goldin, G.O. Shitta-Bey, H.F. Jirandehi, J. Electrochem. Soc. 160 (2013) A25–A30.
[17] X. Chen, V. Bevara, P. Andrei, M. Hendrickson, E. Plichta, J. Zheng, J. Electrochem. Soc. 161 (2014) A1877–A1883.
[18] F. Mohazabrad, F. Wang, X. Li, ACS Appl. Mater. Interfaces 9 (2017) 15459–15469.
[19] F. Mohazabrad, F. Wang, X. Li, J. Electrochem. Soc. 163 (2016) A2623–A2627.
[20] B.D. Adams, C. Radtke, R. Black, M.L. Trudeau, K. Zaghib, L.F. Nazar, Energy Environ. Sci. 6 (2013) 1772–1778.
[21] V. Viswanathan, K.S. Thygesen, J. Hummelshøj, J.K. Nørskov, G. Girishkumar, B. McCloskey, A. Luntz, J. Chem. Phys. 135 (2011) 214704.
[22] Y.-C. Lu, Y. Shao-Horn, J. Phys. Chem. Lett. 4 (2012) 93–99.
[23] M. Mirzaeian, P.J. Hall, J. Power Sources 195 (2010) 6817–6824.
[24] Y. Yang, T. Zhang, X. Wang, L. Chen, N. Wu, W. Liu, H. Lu, L. Xiao, L. Fu, L. Zhuang, ACS Appl. Mater. Interfaces 8 (2016) 21350–21357.
[25] N.B. Aetukuri, B.D. McCloskey, J.M. García, L.E. Krupp, V. Viswanathan, A.C. Luntz, Nat. Chem. 7 (2015) 50–56.
[26] H. Geaney, C. O'Dwyer, Meeting Abstracts, The Electrochemical Society, 2014547–547.
[27] J. Read, J. Electrochem. Soc. 149 (2002) A1190–A1195.
[28] J. Read, K. Mutolo, M. Ervin, W. Behl, J. Wolfenstine, A. Driedger, D. Foster, J.

Electrochem. Soc. 150 (2003) A1351–A1356.
[29] P. Andrei, J.P. Zheng, M. Hendrickson, E.J. Plichta, J. Electrochem. Soc. 157 (2010) A1287–A1295.
[30] Fangzhou Wang, X. Li, ACS Omega (2018) Under review.
[31] Y. Yin, A. Torayev, C. Gaya, Y. Mammeri, A.A. Franco, J. Phys. Chem. C 121 (2017) 19577–19585.
[32] S. Meini, N. Tsiouvaras, K.U. Schwenke, M. Piana, H. Beyer, L. Lange, H.A. Gasteiger, Phys. Chem. Chem. Phys. 15 (2013) 11478–11493.

Paper P3

Pore-Scale Simulations of Porous Electrodes of Li–O_2 Batteries at Different Saturation Levels

ACS APPLIED MATERIALS & INTERFACES

Research Article

Cite This: ACS Appl. Mater. Interfaces 2018, 10, 26222−26232

www.acsami.org

Pore-Scale Simulations of Porous Electrodes of Li−O_2 Batteries at Different Saturation Levels

Fangzhou Wang and Xianglin Li*

Department of Mechanical Engineering, University of Kansas, Lawrence, Kansas 66045, United States

Supporting Information

ABSTRACT: This study reconstructs pore-scale structures of battery electrodes from scanning electron microscopy images, quantitatively studies the distribution of the electrolyte at various saturations, and simulates the discharge performance of Li−O_2 batteries. This research sheds lights on the critical role of liquid−gas two-phase mass transfer within the porous electrode on the electrochemical performance of batteries. It is found that fully saturated electrodes (100% saturation) have high oxygen-transfer resistance, which will impede the battery performance at typical electrode thickness (~200 μm). On the contrary, overdried battery (with <50% saturations) electrodes have poor electrochemical performance because dry pores are inactive for electrochemical reactions. In addition, the low electrolyte saturation level leads to low ionic conductivity and high mass transfer resistance of the lithium ion. Carefully designed electrodes with the mixture of lyophilic and lyophobic pores could achieve similar discharge capacity (>7 A h/g) at high current (20 A/m^2) with lyophilic electrodes that are fully saturated by the electrolyte at low current (1 A/m^2). The findings from this study enable further research to significantly increase (by orders of magnitude) the operating current and power of the Li−O_2 battery and accelerate its deployment to transport and stationary applications.

KEYWORDS: *Li−O_2 battery, pore-scale simulation, electrode tomography, digital electrode reconstruction, liquid−vapor two-phase model, electrode wettability, electrolyte saturation*

1. INTRODUCTION

The Li−O_2 battery is considered to be a promising alternative to current rechargeable batteries (mainly the lithium-ion battery) because of the high specific energy of lithium metal (12 kW h kg^{-1}) and the inexhaustible cathode oxygen from the ambient.[1−3] Among different types of Li−O_2 batteries, batteries using the nonaqueous electrolyte (typically consisting of carbonates, ethers, and esters[4−6]) have high electrochemical window and relatively high charging and discharging efficiency and will be studied in this work. Among all of the chemical and electrochemical reactions involved in Li−O_2 batteries, the following two-electron reaction is widely accepted when an organic electrolyte is used[7]

$$2Li^+ + 2e^- + O_2 \leftrightarrow (Li_2O_2)_s \qquad E_{rev} = 2.96\ V \qquad (1)$$

The electrochemical performances of Li−O_2 batteries are often governed by mass transfer in porous electrodes. The mass transfer in porous electrodes are complex because of the following reasons: (1) the pore size distributes over a wide range (from less than 1 nm to more than 1 μm[8,9]); (2) the pore shapes are irregular; and (3) the pores are often filled with a liquid−gas two-phase fluid. Because the diffusivity of a substance in the gas phase is typically tens of thousands of times higher than that in the liquid phase and its diffusivity in the solid phase is negligible,[10] effective transport characteristics through porous electrodes are strongly determined by the filling fluid. When electrodes of Li−O_2 batteries are saturated with the liquid electrolyte, the mass transfer is more sluggish because oxygen has to dissolve into the electrolyte and transfer to the reaction sites on the interface of the electrolyte and electrode. Our previous studies[11] and other published literature[12−14] indicate that the limited specific energy of Li−O_2 batteries is a result of the insufficient utilization of reaction sites in the electrode due to the limited oxygen transfer. The sluggish oxygen transfer in the liquid electrolyte limits the oxygen supply in porous electrodes and only a fraction of the reaction sites close to the oxygen channel have sufficient oxygen supply. The majority of the electrode suffers from insufficient oxygen concentration because of the low solubility[15] and diffusivity of oxygen[16] in the nonaqueous electrolyte.

The sluggish oxygen diffusion through the nanometer-sized pores filled with the liquid electrolyte results in low operating current and power. If the Li−O_2 battery is applied to power an electric vehicle, its specific energy determines the driving range, whereas its current/power density determines the acceleration performance and driving speed of the vehicle. The operating current density of Li−O_2 batteries is several orders of magnitude lower than the operating current density of Li-ion batteries (~50 mA cm^{-2}) and the corresponding specific power (≤5 W kg^{-1})[17] of the Li−O_2 battery is much lower than that of the Li-ion battery (~300 W kg^{-1}).[18−20]

Received: April 23, 2018
Accepted: July 16, 2018
Published: July 16, 2018

DOI: 10.1021/acsami.8b06624
ACS Appl. Mater. Interfaces 2018, 10, 26222−26232

Charge and discharge current rates of $Li-O_2$ batteries using organic electrolytes need to be improved by at least 2 orders of magnitude to be feasible for practical applications.[21,22] The extremely low oxygen diffusivity in the organic electrolyte determines that the improvement of oxygen transfer in the gas phase is critical for batteries to operate at high current and power. Therefore, the mechanism of oxygen transfer in a liquid−gas two-phase fluid within the porous electrode is critical and will be the focus of this study.

The spatial distributions of the liquid and vapor phases in the porous electrode change by the evaporation of the electrolyte, volume change of solid materials, pore size, wettability, and connectivity of pores. Our recent study of $Li-O_2$ batteries indicated that the amount of the electrolyte strongly affected the specific discharge capacity.[23] The discharge capacity is strongly affected by both the initial amount of the electrolyte and its evaporation rate (controlled by the cathode open ratio). The maximum discharge capacity was achieved at 25% open ratio among the selected open ratios (0−100%) at the current density of 0.1 mA/cm^2. As the open ratio increased from 25 to 100%, the specific discharge capacity decreased from 995 to 397 mA h/g_{carbon}. The fast evaporation of the electrolyte at higher open ratios resulted in the decrease of the discharge capacity with increasing open ratio. A similar experiment carried out by Jiang et al.[24] also studied the effects of the oxygen window on the capacity of $Li-O_2$ batteries. In this work, a single hole with different diameters was machined on the oxygen side of the coin-cell battery as the oxygen window. It should be noted that the maximum open ratio (ratio between the oxygen window area to the total electrode surface area) was only 19.5%. The battery used 50 μL of $LiCF_3SO_3$−TEGDME (1:4 molar ratio) as the organic electrolyte solution. The first discharge−charge cycle of the $Li-O_2$ batteries at a current of 0.1 mA showed that the battery capacity increases linearly with the size of the oxygen window.

During the charge and discharge cycles of the battery, the volumes of both solid materials change significantly because of the consumption/generation of Li_2O_2 at the cathode and the deposition/consumption of Li metal at the anode. As a result, the electrolyte redistributes in pores during the battery operation. Yoo et al.[25] developed a model to study the significance of the volume change of the Li anode corresponding to the discharge performance of the battery. During discharge, the decomposition of lithium metal at the anode leads to a gap between the separator and Li anode. The gap grew bigger with discharge because of the decomposition of lithium metal, and the gap was assumed to be always filled with the electrolyte. Meanwhile, the porosity and pore volume of the cathode electrode decreased with discharge because of the deposition of Li_2O_2, which expelled excess electrolyte from the cathode. The leakage of the electrolyte is proportional to the discharge capacity and 2.15% of the electrolyte leaked out at the specific capacity of 650 mA h/g.

The direct measurement of the distribution and evaporation of the electrolyte by experiments is very challenging because of the small pore size and complex geometry of the pores. Therefore, models provide detailed information on the transport phenomena in liquid−vapor two-phase flow in the porous electrode. Our recent study[23] has employed a simple model to simulate the discharge capacity considering the evaporation of the electrolyte. The model simplified the evaporation of the electrolyte as the electrolyte−air interface moved at a constant speed (which is proportional to the cathode open ratio). Huang and Faghri[26] developed a two-dimensional (2D) model that captured electrolyte evaporation into the air chamber of the battery. The evaporation rate was a function of the partial pressure of solvent vapor and air chamber size. A highly volatile electrolyte, dimethylformamide (DMF), and a less volatile electrolyte, tetraethylene glycol dimethyl ether (TEGDME), were compared in this study. The evaporation rate decreased with discharge and stopped once the partial pressure of the solvent in the air chamber reached saturation. The evaporation of the electrolyte had a significant influence on the Li_2O_2 distribution and discharge capacity. The reaction sites with the fastest reaction rate moved with the electrolyte−air interface away from the air inlet. The whole electrode was better utilized because of the improved oxygen supply. After considering the evaporation of the electrolyte, the specific discharge capacity of the battery increased by 22.5 and 14.9% with DMF and TEGDME electrolytes, respectively. It was also demonstrated that the size of the air chamber was critical, that is, increasing the air chamber radius from 5 to 15 cm led to a capacity increase of 72%. The analytical model developed by Ye et al.[27] also showed that a flooded electrode negatively impacts the battery performance. A partially wetted electrode was preferred to promote the diffusion in the gas phase and decrease the concentration overpotential.

The wettability of the electrode, which determines the distribution of the electrolyte, is a critical factor on battery capacity. Our experimental studies customized battery electrodes using acetylene black carbon powder and different polymer binders [polyvinylidene fluoride (PVDF) and polytetrafluoroethylene (PTFE)].[28] The different surface energies of the polymer binders lead to variations of electrode wettability. It was found that slightly lyophobic electrodes (with 15 wt % PTFE) are more favorable than lyophilic electrodes (with 15 wt % PVDF) for higher discharge capacities. The higher discharge capacity is resulted from the improved oxygen transfer due to more available gas phase. Strongly lyophobic electrodes (with 30 wt % PTFE), however, have low discharge capacity because of overdrying the electrode. Considering the balance of improved mass transfer with the available reaction sites, this study proposed electrodes with combined lyophilic and lyophobic layers. The specific capacity of the electrode with mixed wettability (5149.5 mA h/g) was more than three times higher than that of the lyophilic electrode (1665.8 mA h/g). Although the improved mass transfer at the pore scale results in superior electrochemical performance, direct observations of the pore-scale transport phenomena by experiments are extremely difficult. The distribution of the electrolyte and mechanism of the liquid−gas multiphase transfer at the pore scale are unclear. Therefore, it is important to study the pore-scale distribution of each phase to resolve key scientific issues and engineer advanced battery electrodes to meet the target-specific energy and current density.

Only limited number of experiments[9,29−31] and numerical simulations[32−34] studied the pore size distribution of $Li-O_2$ batteries. Because smaller pores lead to higher surface area per volume and provide more reaction sites, experiments attempted to decrease the pore size to increase the specific capacity of the battery. However, there is no obvious correlation between the specific energy of the battery and the surface area or porosity.[31] Numerical simulations also try to consider the effect of pore size on the discharge capacity of batteries. Xue et al.[32] developed a model that considers the passivation of the electrode surface by the deposition of Li_2O_2.

DOI: 10.1021/acsami.8b06624
ACS Appl. Mater. Interfaces 2018, 10, 26222−26232

The model assumed that the pore becomes inactive either if it is completely blocked by the Li_2O_2 film or if the thickness of Li_2O_2 is more than 10 nm. The performances of two electrodes with different pore size distributions made from Super P and Ketjen black, respectively, are the compromise between the high initial surface area and low degradation rate of active surface area. Andrei and Bevara[33] simplified the battery electrode as a bunch of cylindrical pores with a distribution of diameters. It was found that electrodes with the same mean diameter (20 nm) but different standard deviations could have very different discharge performance because of the different characteristics of small and large pores.

The different mass transfer characteristics of pores with different sizes lead to the hypothesis that micropores that are smaller than the critical pore size do not contribute to the discharge and charge of electrochemical devices because of the limited mass transfer capability.[34] To understand the effect of critical pore size, Li[34] developed a statistics model to simulate the microstructural evolution of porous electrodes. The model assumed that pores smaller than a critical pore size have too high mass transfer resistance so that they do not contribute to the discharge of the battery. The microstructural change was also coupled with a computational fluid dynamics model to simulate the discharge performance. Effects of electrode properties and operating parameters, as well as the pore size distributions have been investigated. At a given critical pore size (10 nm), the discharge capacity first increased with the increase of the average pore size (from 10 to 50 nm) because of the improved mass transfer, followed by a capacity decrease when the average pore size further increased to 100 nm due to the decrease of the effective surface area.

The detailed distributions of the electrolyte and pore require a clear understanding of the pore-scale structure of the electrode. However, the complex microstructure of electrodes is very difficult to measure and reconstruct and none of the previously mentioned studies directly measure and consider the spatial distributions of pores and the electrolyte. Although pore-scale structure reconstruction and simulations have been carried out in fuel cells,[35−39] the authors are not aware of detailed measurements and model simulation pore structures of Li−O_2 or Li−air battery electrodes. To fill this knowledge gap, this work will develop an electrochemical model, based on reconstructed pore-scale geometries of porous electrodes, to simulate the discharge performance (current, voltage, local reaction rates, etc.) of the electrode with various saturations of the electrolyte. This model considers the multiphase mass transfer in porous electrodes and sheds lights on the critical role of liquid−gas two-phase mass transfer within the porous electrode on the electrochemical performance of batteries. The findings from this study enable further research to significantly increase (by orders of magnitude) the operating current and power of the Li−O_2 battery and accelerate its deployment to transport and stationary applications.

2. RECONSTRUCTION OF DIGITAL BATTERY ELECTRODES

This study will begin with reconstructing pore-scale structures of battery electrodes from scanning electron microscopy (SEM) images using the correlation function method.[40,41] The SEM images have the resolution of 1.34 nm per pixel to capture the pore structures of the electrode slices. The field of view, however, is limited to be 1.136 × 1.136 μm^2. The small field of view cannot provide a representative unit of the electrode (~200 μm thick) to investigate the mass transfer coupled with electrochemical reactions. Therefore, this study will generate a digital battery electrode (with the size of 186.0 × 5.8 μm^2) with detailed pore-scale structures using correlation functions as a representative unit of the model simulation. Details of the reconstruction will be discussed in the following sections and the Supporting Information. The representative images of the electrodes with gray scale were processed to binary image and used to reconstruct the target two-point correlation function. It should be noted that although noise reduction of the SEM images does not result in noticeable different target correlation functions in this study, proper noise reduction algorithms may need to be applied before image processing.[42] The target two-point correlation function was then used to reconstruct electrodes iteratively. The generation of the two-point correlation function and reconstruction procedure is explained as follows.

2.1. Target Correlation Function. The microstructure of the [2D or three-dimensional (3D)] electrode can be reconstructed using a stochastic reconstruction method from random spatial distributions of two phases (solid and gas phases for electrodes). The distribution of each phase within the electrode, F, can be described by the following index function

$$F(\vec{x}) = \begin{cases} 0 & \text{gas} \\ 1 & \text{solid} \end{cases} \tag{2}$$

where $\vec{x}$ is the position of the selected point. The two-point correlation function will be used to describe the distribution of each phase.[40] The two-point correlation function calculates the probability that two randomly selected points $\vec{x_1}$ and $\vec{x_2}$ fall into the same phase (solid phase in this study)

$$s_2(\vec{x_1}, \vec{x_2}) = \langle F(\vec{x_1})F(\vec{x_2})\rangle \tag{3}$$

For statistically homogeneous media, the two-point correlation function only depends on the relative displacements ($r = |\vec{x_2} - \vec{x_1}|$) of the selected points, not on their absolute positions.[41,43] Therefore, the two-point correlation function can be simplified as $s_2(r)$. The two-point correlation function contains significant information on the microstructure of porous media. For instance, the porosity of the electrode, ε, can be calculated by

$$s_2(0) = 1 - \varepsilon \tag{4}$$

The specific surface of a 3D medium, S, which is defined as the area of the two-phase interface per unit total volume of the medium, can be calculated from the slope of the two-point probability function at $r = 0$[44]

$$\left.\frac{ds_2(r)}{dr}\right|_{r=0} = -S/4 \tag{5}$$

Two porous electrodes with the same two-point correlation functions are considered to have similar distributions of phases and similar statistical properties. The goal of this study is to generate large 2D digital electrodes using a target two-point correlation function derived from small SEM images. The large digital electrode has a microstructure similar to that in the SEM images.

2.2. Reconstruction of the Electrode. The reconstruction of the digital structure starts with porous media with two

DOI: 10.1021/acsami.8b06624
ACS Appl. Mater. Interfaces 2018, 10, 26222−26232

randomly distributed phases (gas and solid). The two-point correlation function of the initial structure is quite different from the target two-point correlation function. The difference between these two correlation functions are quantified by the energy E

$$E^0 = \sum_r [s_2^0(r) - s_{2,\text{target}}(r)]^2 \tag{6}$$

Then, the reconstruction of the microstructure is formulated as an energy minimization problem. To minimize the energy, two randomly picked points (one in the gas phase and another in the solid phase) in the generated electrode will be switched. The corresponding two-point correlation function, s_2^1, and the new energy E^1 will be calculated

$$E^1 = \sum_r [s_2^1(r) - s_{2,\text{target}}(r)]^2 \tag{7}$$

If the energy decreases after the switch ($\Delta E = E^1 - E^0 < 0$), the switched structure will be the new microstructure of the digital electrode. If the energy change is positive, the probability to switch the two selected points is nonzero to avoid local minima. The probability is determined by the energy change as well as an artificially introduced temperature T.[45] In brief, the criterion to switch two selected points is

$$p = \begin{cases} 1 & \text{when } \Delta E < 0 \\ \exp\left(-\dfrac{\Delta E}{T}\right) & \text{when } \Delta E > 0 \end{cases} \tag{8}$$

The temperature T should be selected so that the switch probability when the energy change is positive should be approximately 0.5.[41,46] Random numbers that are uniformly distributed between 0 and 1 will be generated to compare with the probability. If the random number is less than the probability, the original microstructure will be restored before moving to the next step. Instead of using a constant temperature in the Metropolis algorithm,[45] the energy minimization problem can be optimized at various temperatures, imitating the annealing process.[47] During the annealing process, the temperature will gradually decrease with iterations until the system "freezes" and cannot be changed

$$T_k = T_0 \lambda^k \tag{9}$$

where T_0 is the initial temperature and T_k is the temperature at iteration k. The coefficient λ is slightly less than 1 (0.995 in this work) to have a slow freezing process. The iteration will continue until the energy, which reflects the difference between the current structure and the target structure, is less than a small value

$$E \leq 10^{-4} \tag{10}$$

It can be seen from the previous simulation approach that the two-point correlation functions need to be calculated at each iteration. The two-point correlation function calculation determines the computational time of the overall reconstruction. The sampling of the two-point correlation function in all directions is very time consuming (the number of operation is on the order of N^4). To significantly decrease the computational time, only the change of two-point correlation functions caused by switching the two selected points was calculated at each iteration to save the computational time. The change of the number of operation to calculate the change of correlation function is on the order of N^2.

2.3. Validation of Reconstructions. Once a digital electrode is numerically generated, its pore size distribution and the effective surface area can be derived statistically using the erosion−dilation method.[48] The erosion process will erase any foreground pixel (pore) that has at least one neighbor, that is, the background pixel (solid) in the binary images, whereas the dilation process will erase any background pixel (solid) that has at least one neighbor, that is, the foreground pixel (pore). The erosion and dilation processes will start with a small circular structuring element (with only one voxel) and will be repeated with larger and larger circular structuring elements. The change of the cumulative volume fraction of the foreground pixel with the size of circles will lead to the histogram of pore size distribution. The surface area of the digital electrode is calculated by tracking the amount of the carbon/pore interface. The accuracy of the reconstructed geometries will be validated by comparing the pore size distributions and effective surface area of the numerically generated electrode with experimental measurements by the NovaTouch pore size analyzer (Supporting Information). Once the digital electrode is reconstructed and validated, it will be applied to electrochemical models to simulate the species distribution, reaction rate, and pore-scale structure change of the electrode during discharge.

3. ELECTROCHEMICAL MODEL

Once the digital electrode is reconstructed, the detailed structure can be imported in to the finite volume method (FVM)-based computational fluid dynamics (CFD) models to simulate the mass transfer coupled with electrochemical reactions in pore scale. To save computational time and limit the number of grids required for the CFD simulation, each pixel is considered as a unit volume in the CFD model. Oxygen and the electrolyte cannot diffuse into the control volumes in the solid phase (1) because the mass diffusivity is close to zero in the solid phase. However, in the scenario that the electrode is saturated with the electrolyte (lyophilic electrodes), all control volumes in the void phase (0) are filled with the liquid electrolyte. Therefore, the mass diffusivity and ionic conductivity in the electrolyte phase are applied to the mass transfer equation of oxygen and lithium ion. In scenarios that the electrode is partially filled with the electrode (lyophobic electrodes), the electrolyte tends to fill large pores first because the capillary pressure is lower in large pores. This study will identify dry and wetted pores based on the pore size and the given saturation. Properties of the liquid electrolyte will be applied to control volumes filled with the electrolyte, whereas properties of dry oxygen will be applied to control volumes that are not wetted by the electrolyte.

3.1. Governing Equations. The governing equations of mass transfer and electrochemical reactions apply to the whole computational domain,[11,34,49,50] whereas various mass transfer and reaction coefficients are applied to local control volumes depending on the material. Because electrochemical reactions occur only at the electrolyte−carbon interface, reactions could only exit in active control volumes that are filled with the electrolyte and are next to the carbon phase. The concentration of the lithium ion, ω_{Li^+}, is only solved in the electrolyte phase

DOI: 10.1021/acsami.8b06624
ACS Appl. Mater. Interfaces 2018, 10, 26222−26232

$$\frac{\partial(\rho_{EL}\omega_{Li^+})}{\partial t} = \nabla\cdot(\rho_{EL}D_{Li^+}\nabla\omega_{Li^+}) - \nabla\cdot\left(\frac{i_{EL}t_+}{F}M_{Li^+}\right) + \dot{m}_{Li^+} \quad (11)$$

where $\dot{m}_{Li^+}$ is the consumption rate of the lithium ion, i_{EL} is the current density, and t_+ is the transference number of Li^+. To simplify the model, the concentration of oxygen is treated as a constant in the gas phase because the oxygen diffusivity in the gas phase (0.219 cm^2/s)[10] is several orders of magnitude higher than that in the electrolyte phase ($\sim 10^{-5}$ cm^2/s).[28] The concentration of oxygen in the electrolyte, ω_{O_2}, is solved using the following equation.

$$\frac{\partial(\rho_{EL}\omega_{O_2})}{\partial t} = \nabla\cdot(\rho_{EL}D_{O_2}\nabla\omega_{O_2}) + \dot{m}_{O_2} \quad (12)$$

where $\dot{m}_{O_2}$ is the consumption rate of oxygen. It should be noted that both consumption rates of lithium ion and oxygen are only nonzero in active control volumes (at the electrolyte–carbon interface). The impact of the 2D pore-scale structure and distribution of the liquid electrolyte are automatically considered in the species equation because the species in the liquid phase has to transfer a longer distance, bypassing the solid and gas phases, to reach the reaction sites. The consumption rates in the species equations of Li^+ and O_2 are proportional to the local reaction rate

$$\dot{m}_{Li^+} = -\frac{R_{ORR}}{F}M_{Li^+} \quad (13)$$

$$\dot{m}_{O_2} = -\frac{R_{ORR}}{2F}M_{O_2} \quad (14)$$

where R_{ORR} is the reaction rate of the oxygen reduction reaction (ORR) and M is the molecular weight. The local volume fraction of Li_2O_2, $\varepsilon_{Li_2O_2}$, is calculated based on the amount of accumulated Li_2O_2

$$\varepsilon_{Li_2O_2}(t) = \frac{\int R_{ORR}\cdot dt}{2F}\frac{M_{Li_2O_2}}{\rho_{Li_2O_2}} \quad (15)$$

The local ORR rate of the Li–O_2 battery is determined by concentrations of lithium ion and oxygen, the standard constant rate of ORR, k_{ORR}, the active surface area of the electrode, A_{active}, per volume of the electrode, V_{ED}, the transfer coefficient of, α, and the overpotential, η, by the Butler–Volmer equation[34]

$$R_{ORR} = k_{ORR}\cdot\frac{A_{active}}{V_{ED}}\cdot\left\{\left(\frac{\omega_{Li^+}}{\omega_{Li^+}^{ref}}\right)^2\cdot\left(\frac{\omega_{O_2}}{\omega_{O_2}^{ref}}\right)\cdot\exp\left(\frac{\alpha F\eta}{RT}\right) - \left(\frac{\omega_{Li_2O_2}}{\omega_{Li_2O_2}^{ref}}\right)\cdot\exp\left[-\frac{(1-\alpha)F\eta}{RT}\right]\right\} \quad (16)$$

It should be mentioned that the battery model is built based on lab-scale batteries with small sizes (on the order of 1 cm) and low discharge current density (on the order of 0.1 mA/cm^2). Therefore, the temperature increase of the battery during operations is negligible. The battery temperature is assumed to be the same as the room temperature (25 °C) in this study. The total surface area, A_{ED}, per volume of the electrode, V_{ED}, was measured by the N_2 absorption method. The measurements of the specific surface area and the specific pore volume of acetylene black carbon are 76.5 m^2/g and 0.22 cm^3/g, respectively. Therefore, the surface area per volume is calculated to be 3.584×10^8 m^2/m^3 and the average pore size is calculated to be 13.95 nm. Because reactions occur only on the carbon surface that is wetted by the electrolyte, the active surface area of the electrode considers only the amount of the surface that is available for electrochemical reactions. As a result, the active surface area is calculated from the total surface area of the electrode, A_{ED}, and the fraction of the carbon surface that is wetted by the electrolyte, x_{EL} (which can be calculated from the distribution of the electrolyte)

$$A_{active} = A_{ED}\cdot x_{EL} \quad (17)$$

The effect of the electrode passivation caused by the Li_2O_2 precipitation during discharge is considered by a segmental equation of the standard rate constant[34,S1]

$$k_{ORR} = \begin{cases} i_0\cdot\frac{A_{active}}{V_{ED}}\cdot\left(1 - 0.9\cdot\frac{q}{7}\right) & \text{for } q \le 7\ C/m^2 \\ 0.15245 i_0\cdot\frac{A_{active}}{V_{ED}}\cdot 10^{-0.02616q} & \text{for } q > 7\ C/m^2 \end{cases} \quad (18)$$

where i_0 is the exchange current density and the quantity of discharged electricity per active surface area of the electrode, q, is calculated from the accumulated local reaction rate and active surface area of the electrode per volume A_{active}/V_{ED}

$$q(t) = \frac{\int R_{ORR}\cdot dt}{A_{active}/V_{ED}} \quad (19)$$

3.2. Boundary Conditions. The computational domain includes the whole porous electrode (partially) filled with the electrolyte. To save the computational time, a representative unit is selected and applied to the electrochemical model. As shown in Figure 2, symmetric boundaries are applied to the upper and lower boundaries (I) of the representative computational unit

$$\frac{\partial\omega_{Li^+}}{\partial y} = \frac{\partial\omega_{O_2}}{\partial y} = 0 \quad (20a)$$

When the electrode is customized to have alternating wettability along the y direction, the nonflux boundary is applied to the lithium ion and the constant concentration boundary condition is applied to oxygen at the upper and lower boundaries (I)

$$\left.\frac{\partial\omega_{Li^+}}{\partial y}\right|_{(I)} = 0 \text{ and } \omega_{O_2}|_{(I)} = \omega_{O_2}^0 \quad (20b)$$

At the interface of the separator with the electrode (II), the flux of the lithium ion is proportional to the discharge current density and the flux of oxygen is 0

$$\rho D_{Li^+}\left.\frac{\partial\omega_{Li^+}}{\partial x}\right|_{(II)} = \frac{I}{F}M_{Li^+} \text{ and } \left.\frac{\partial\omega_{O_2}}{\partial x}\right|_{(II)} = 0 \quad (21)$$

At the electrode–oxygen interface (III), the nonflux boundary applies to the lithium ion and the oxygen concentration is set as the reference concentration

DOI: 10.1021/acsami.8b06624
ACS Appl. Mater. Interfaces 2018, 10, 26222–26232

$$\left.\frac{\partial \omega_{Li^+}}{\partial x}\right|_{(III)} = 0 \text{ and } \omega_{O_2}|_{(III)} = \omega_{O_2}^0 \quad (22)$$

The above governing equations are discretized based on the FVM[52] and solved by a home-made code developed with Fortran. Because each pixel is considered as a unit volume in the model, the grid number is 4096 × 128 and the time step is 0.1 s. The cell voltage when the battery discharges at a given current rate is calculated by the following equation at each time step

$$V = E^0 - \eta - I \times \frac{0.5\delta_{ED}}{\sigma_{ED}^{eff}} \quad (23)$$

where δ_{ED} is the thickness of the electrode and σ_{ED}^{eff} is the effective ionic conductivity of the electrode. The coefficient 0.5 considers the fact that the average transport distance of the lithium ion roughly equals to half of the thickness of the electrode. The ohm overpotential of the electric transfer in the solid carbon phase is neglected in the above equation because of the high electric conductivity compared with the ionic conductivity. In the following discussions, if not otherwise specified, the battery is discharged at a constant current of 1 A/m^2. Values of transport parameters are obtained from published data of the electrolyte of 1 M $LiPF_6$ in propylene carbonate/dimethoxyethane (1:2 wt) and are presented in Table 1.

Table 1. Electrochemical and Physical Parameters Used in the Model

parameter	symbol	value
active area of electrode per volume	A_{ED}	3.584×10^8 m^2/m^3
thermodynamic equilibrium voltage	E^0	3.1 V[53]
solubility of oxygen in electrolyte		4.395×10^{-3} mol/L[15]
reference concentration of O_2	$\omega_{O_2,ref}$	1.23×10^{-4} kg/kg
reference concentration of lithium ion	$\omega_{Li^+,ref}$	8.866×10^{-2} kg/kg
conductivity of electrolyte	σ_{EL}	5×10^{-3} S/cm
conductivity of the electrode	σ_{ED}	3 S/cm
conductivity of Li_2O_2	$\sigma_{Li_2O_2}$	1×10^{-12} S/cm
density of carbon	ρ_C	2.26 g/cm^3
density of lithium peroxide	$\rho_{Li_2O_2}$	2.31 g/cm^3
density of the electrolyte	ρ_{EL}	1.011 g/cm^3[15]
exchange current density	i_0	3.11×10^{-6} A/m^2[11]
diffusivity of oxygen in the electrolyte	$D_{O_2,EL}$	9.12×10^{-10} m^2/s[15]
diffusivity of lithium ion in the electrolyte	$D_{Li^+,EL}$	8×10^{-11} m^2/s[16]

4. RESULTS AND DISCUSSION

4.1. Reconstructions and Validations of Digital Electrodes. The reconstruction of the 3D electrode starts from the SEM images of a customized battery electrode made from acetylene black and PTFE mixture.[28] The original gray-scale image is first processed to a binary image with the porosity of the electrode (Figure S3). The correlation functions of the binary image are then derived based on eq 3. *It should be noted that only a fraction of the electrode (128 × 128 pixels out of the 4096 × 128 pixels) are included in figures throughout the paper to show the detailed distribution of each phase and species concentration.* The reconstruction of digital electrodes will use the average correlation function of 10 SEM images as the target function of the annealing process to represent the 2D structure of the electrode. The annealing process starts with the initial porous electrode with two randomly distributed phases (gas and solid). The iteration completes when the energy (the difference between the target correlation function and the correlation function of the generated electrode) is less than 10^{-4} (Figure S4). The pore size distribution of the reconstructed digital electrode is also derived using the erosion−dilation method[48] and compared with the N_2 absorption measurements. Results in Figure S5 indicate that the reconstructed digital electrode has pore size distribution similar to that of the customized electrode. Therefore, the following section will apply the reconstructed digital electrode to electrochemical models to simulate the battery performance.

The typical battery electrodes have very high aspect ratios. The height of the electrode is on the order of centimeter, whereas the thickness of the electrode is on the order of dozens or hundreds of micrometers. Because the transport phenomena along the height of the electrode are very similar or follow a repeat pattern, it is not uncommon to simulate a representative unit of the electrode to save computational time. As a result, this model simulates a representative unit of a lithium−oxygen battery electrode with a thickness of 186.0 μm and height of 5.8 μm (Figure 1). The model is validated by comparing simulated specific capacities with experimental results (Figure S6). Fabrication and testing of customized electrodes are described in the Supporting Information and discharge curves of customized electrodes are available in Figure S1.

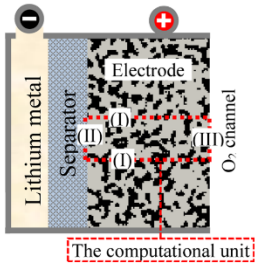

Figure 1. Computational domain and the boundary conditions of a lithium−O_2 battery using an organic electrolyte.

4.2. Electrodes Fully Saturated by the Electrolyte. The distributions of reactions (O_2 and Li^+) and product (Li_2O_2) at the end of the discharge at 1 A/m^2 are plotted in Figure 2. As

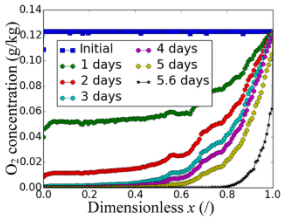

Figure 2. Distributions of O_2 when the battery is discharged at 1 A/m^2.

DOI: 10.1021/acsami.8b06624
ACS Appl. Mater. Interfaces 2018, 10, 26222−26232

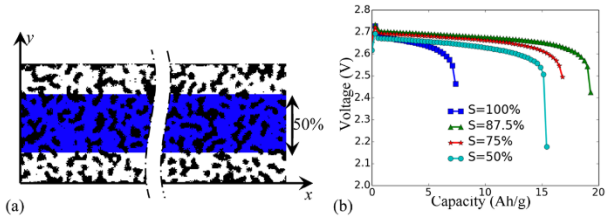

Figure 3. (a) Distribution of the electrolyte (blue) within the porous electrode (black) at the saturation of 50% and (b) corresponding discharge performance of electrodes with various electrolyte saturations at 1 A/m^2.

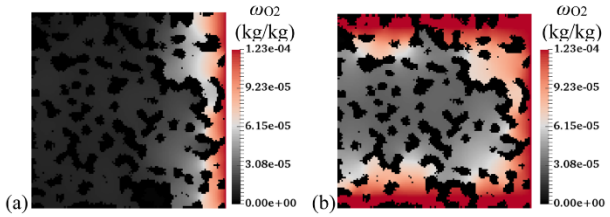

Figure 4. Distributions of O_2 in electrodes with (a) 100 and (b) 87.5% electrolyte saturations after discharging at 1 A/m^2 for 24 h (3.18 A h/g).

can be seen from the plot, the oxygen concentration decreases from the saturated oxygen concentration (1.23×10^{-4} kg/kg) due to reactions. The deposition of Li_2O_2 reduces the porosity of the porous electrode and therefore increases the mass transfer resistance of oxygen and lithium ion in the electrolyte. Most of the Li_2O_2 generated by the reaction deposits at the vicinity of the oxygen channel and blocks the transfer of oxygen (Figure 2). At the end of the discharge, the oxygen concentration reduces to less than 1.0×10^{-4} kg/kg in most of the electrode. As a result, reaction within the electrode stops because of the lack of oxygen. The high oxygen concentration gradient along the depth of the electrode is caused by the low diffusivity of oxygen in the liquid electrolyte (2.17×10^{-6} cm^2/s). As a comparison, oxygen diffusivity in the gas phase (0.219 cm^2/s) is about 5 orders of magnitudes higher than that in the liquid electrolyte. To facilitate the oxygen transfer within the electrode and improve the electrochemical reaction deep in the electrode, this study investigates electrodes that are partially saturated by the electrolyte. The gas phase serves as the oxygen-transfer media and significantly improves the mass transfer of oxygen.

4.3. Electrodes with Different Saturations. The investigations start with simplified distributions of the electrolyte. The electrolyte is assumed to occupy pores in the middle of the electrode first. The volume fraction of the pores occupied by the electrolyte is proportional to the given saturation (100, 87.5, 75%, etc.). Figure 3a shows an example of the electrolyte (blue) distribution within the porous electrode (black) when the saturation is set at 50%. The discharging performances of batteries with various electrolyte saturations (100, 87.5, 75, and 50%) are simulated based on the given governing equations and boundary conditions. Results in Figure 3b indicate that the discharge capacity increases significantly from 7.41 to 19.31 A h/g when the saturation decreases from 100 to 87.5% because oxygen is more abundant. The increase of the discharge capacity is mainly driven by the improved oxygen transfer within the electrode. When the electrolyte fully saturates the electrode, the oxygen concentration within the electrode (blue in Figure 3a) is relatively low, whereas the oxygen concentration is much higher when the electrode is partially (87.5%) saturated by the electrolyte. The availability of the dry pores at the top and bottom of the electrode (white in Figure 3a) significantly improves the oxygen transfer through the gas phase. Therefore, the oxygen supply is more sufficient during discharge in partially saturated electrodes. On the other hand, when the saturation is further decreased to 75 and 50%, the discharge capacity decreases to 16.94 and 15.41 A h/g, respectively. The decrease of the capacity is caused by the balance of improved oxygen transfer and availability of active reaction sites within the electrode. Because the discharge reaction (ORR) requires both oxygen and lithium ion, only carbon surface that has direct contact with the electrolyte can serve as the active reaction site. Reactions only happen when oxygen and lithium ion, which are dissolved within the electrolyte, reach the electric-conductive carbon surface. This model quantitatively examines the active surface area of the electrode by checking the pixels that are in the electrolyte phase and have carbon as neighbor cells.

Figure 4a,b compares the oxygen concentration after electrodes with 100 and 87.5% of electrolyte saturations are discharged for 24 h. The equivalent discharge capacity is 3.18 A h/g for both electrodes. Most of the oxygen has been consumed in the electrode with 100% saturation after 24 h discharge (Figure 4a). The evolution of the volume fraction of Li_2O_2 (Figure S6a) indicates that the volume fraction in the majority of the electrode is below 0.2 at the end of discharge, although the porosity of the electrode is 0.65. The volume fraction of Li_2O_2 is proportional to the discharge capacity. Although the electrode with 100% saturation is still capable to host more solid product, the insufficient oxygen supply stopped the discharge. The depletion of oxygen within the electrode saturated by the electrolyte leads to the death of the battery fully saturated by the electrolyte. For comparison, the

DOI: 10.1021/acsami.8b06624
ACS Appl. Mater. Interfaces 2018, 10, 26222−26232

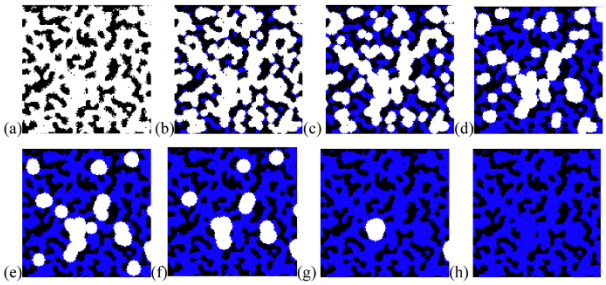

Figure 5. Battery electrodes with (a) 0, (b) 16.57, (c) 36.13, (d) 58.88, (e) 72.91, (f) 84.66, (g) 93.46, and (h) 100% saturations. The porosity of the electrode is 0.65, the solid matrix is black, the electrolyte is blue, and the gas is white.

oxygen concentration in the electrode with 87.5% saturation is still relatively high after 24 h discharge (Figure 4b). As a result, most of the electrode has sufficient O_2 for discharge and the volume fraction of Li_2O_2 reaches above 0.4 at the end of discharge (Figure S6b). The dry pores near the top and bottom of the computational unit provide a fast oxygen path. The diffusional length of oxygen in the liquid electrolyte is significantly decreased from the thickness of the electrode (~200 μm) to the height of the representative unit (~5 μm), which greatly improves the oxygen transfer. As a result, the electrode with 87.5% saturation did not stop discharging until the generated Li_2O_2 completely filled pores.

Because the electrolyte is assumed to occupy the center of the electrode, the amount of the active reaction sites changes in proportional to the saturation: 48.49% (50% saturation), 73.22% (75% saturation), 85.38% (87.5% saturation), and 100% (fully saturated). In real electrodes that are partially saturated by the electrolyte, the distribution of the electrolyte is governed by the capillary pressure. As a result, the amount of the action reaction sites depends not only on the saturation but also the spatial distribution of the electrolyte. The solid matrix of the porous electrode is composed of carbon and a binding polymer (PVDF, PTFE, Nafion, etc.). The properties and distributions of carbon and binding polymers lead to different distributions of the wettability and pore size. Both the pore size and the wettability (contact angle) determine the capillary pressure and therefore the distribution of the electrolyte. This study further investigates the distribution of the electrolyte with a given saturation. If the electrode matrix is assumed lyophilic (when Nafion or PVDF is applied as the binding polymer), the electrolyte will occupy small pores first because of the higher capillary pressure in small pores.

4.4. Distributions of the Electrolyte within the Electrode. This study applies the ball-moving approach[54] to identify the diameter of pores in the regenerated porous electrode. When the electrolyte fills the electrode, it will occupy small pores first because of the high capillary pressure within small pores. Figure 5 shows electrodes with different saturations (0–100%) of the electrolyte. The percentages of the active electrode surface (surface that is wetted by the electrolyte) are 0, 40.87, 65.07, 83, 91.07, 95.98, 98.60, and 100% at the saturation levels of 0, 16.57, 36.13, 58.88, 72.91, 84.66, 93.46, and 100%, respectively.

The discharge performance of electrodes with simulated distributions of the electrolyte in Figure 5 is compared with the performance of the electrode saturated with the electrolyte in Figure 6. Because pore surfaces in the electrode are assumed to be lyophilic, the electrolyte prefers to wet the electrode surface.

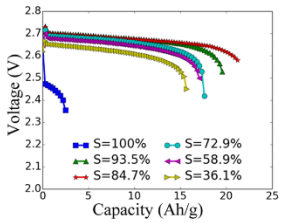

Figure 6. Discharge curves of batteries with various electrolyte saturations at 1 A/m^2.

The simulated discharge capacity increases from 7.41 to 21.38 A h/g when the saturation decreases from 100 to 84.66% (which has 95.98% active surface area). In the electrode that is fully saturated by the liquid electrolyte, the insufficient oxygen concentration deep inside the electrode limits the reaction rates and the discharge current. When the saturation of the electrode decreases due to the available gas phase, oxygen could transfer deep into the electrode much easier through the gas phase. The improved oxygen transfer leads to significant increase of discharge capacity. However, when the saturation of the electrode is further reduced to 36.14%, only 65.07% of the electrode is wetted by the electrolyte and a large fraction of the electrode becomes inactive. As a result, the discharge capacity decreases to 15.79 A h/g. The electrode with 36.14% saturation stops discharging because active pores have been completely filled with Li_2O_2, although sufficient oxygen is still available within the electrode (Figure S7).

Considering the improvement of mass transfer and the loss of active reaction sites after introducing gas phase, the saturation of the electrode needs to be close to 100%. The ideal electrode should be composed of both lyophilic and lyophobic pores[28] or a gel electrolyte with controlled dry pores.[55] The majority of the electrode pores should be lyophilic so most of the electrode surface is wetted by the electrolyte and becomes active reaction sites. Meanwhile, a small fraction of well-connected lyophobic pores will create gas paths for oxygen to significantly improve the mass transfer. It should also be noted that because most organic electrolytes applied in Li–O_2 batteries have lower boiling points than water, the evaporation of the electrolyte and the change of the

DOI: 10.1021/acsami.8b06624
ACS Appl. Mater. Interfaces 2018, 10, 26222–26232

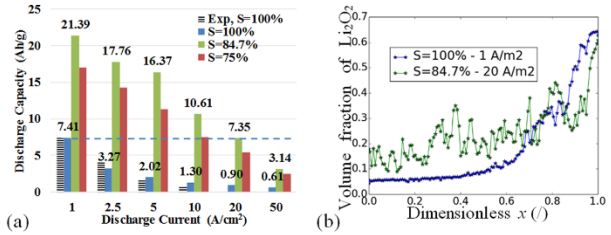

Figure 7. (a) Discharge capacities at different current rates when the electrode has different saturation levels and (b) the volume fraction of Li_2O_2 in the electrode at the end of discharge.

electrolyte saturation during operation should be considered in the design of the battery pack.

4.5. Performance of Electrodes at High Current Densities. Although 1 A/m^2 is commonly used in existing experimental and modeling studies, this extremely low current density leads to very low power density. The total active area of batteries has to be very large to provide the required power. This not only drives up the cost but also the weight of the battery pack. Li−O_2 batteries that are capable to achieve high discharge and charge capacity at current rates, much higher than 1 A/cm^2, are required for practical applications. The model employed in this study simulates discharge electrodes with different electrolyte saturations at very high current densities (up to 50 A/m^2) to investigate the feasibility of the cell design. Figure 7a compares the simulated discharge capacity at various current rates.

Results show that electrodes that are partially saturated (S = 84.7%) by the electrolyte could achieve similar capacity (7.35 A h/g) at 20 A/cm^2 with electrodes that are fully saturated with the electrolyte at 1 A/cm^2 (7.41 A h/g). In other words, the partially saturated electrode increases the power density (voltage times the current density) by 20 times. With gas pores within the electrode, the diffusion path of oxygen in the liquid electrode has been significantly decreased compared with the fully saturated electrode. Partially wetted electrodes have better utilization of the reaction sites deep into the electrode. On the contrary, a fully saturated electrode easily consumed up oxygen and stops discharge. Although partially wetted electrodes achieve similar capacity with the fully saturated electrode, the distributions of the reaction are very different. As a result, the volume fraction of Li_2O_2 at the end of the discharge, shown in Figure 7b, is significantly different. In Figure 7b, the total amount of Li_2O_2 is proportional to the discharge capacity, whereas the local volume fraction of Li_2O_2 is determined by the cumulative local reaction rates. In a fully saturated electrode, the volume fraction of Li_2O_2 next to the oxygen channel (x = 1) is close to the porosity (0.65) but the volume fraction decreases very fast moving deep into the electrode, whereas in a partially wetted electrode (S = 84.7), the distribution of Li_2O_2 volume fraction is more uniform because of the sufficient oxygen supply deep within the electrode.

Simulated results in this study, that a partially wetted electrode outperforms a fully saturated electrode, are consistent with our experiments[28,56] and applications of solid perfluorocarbons and gel electrolytes in battery electrodes.[55,57] Although the simulation does not exactly match experimental data, the overall trends are similar. The mismatch between simulation and experiments is mainly due to the fact that it is extremely difficult to engineer the distribution of wettability within the electrode by experiments to have exact electrolyte distributions simplified in models. In addition, the model assumes that all of the gas pores are connected and therefore oxygen can easily fill all of the gas pores because of the high diffusivity in gas phase. In reality, however, only gas pores that are in direct connection with the environment has access to oxygen. Because each phase connects in all three dimensions, 3D models that can capture the connectivity of all three phases will lead to more accurate simulation results on electrodes that are partially filled with the liquid electrode. Further experiments and numerical simulations are being carried out in our lab to further elucidate the impact of electrolyte saturation and electrode wettability.

5. CONCLUSIONS

The low operating current density and power density of Li−O_2 batteries are both limited by the availability of reactants (oxygen and lithium ion) during operation. This study reconstructs representative porous structures of porous electrodes from 2D SEM images, quantitatively studies the distribution of the electrolyte at various saturations, and simulates the discharge performance of a Li−O_2 battery. This research sheds lights on the critical role of liquid−gas two-phase mass transfer within the porous electrode on the electrochemical performance of Li−O_2 batteries. The following conclusions could be made based on this study:

- fully saturated electrodes (100% saturation) have high oxygen transfer resistance, which will impede the battery performance at typical electrode thickness (~200 μm);
- overdried battery (with 50% or less saturations) electrodes have poor electrochemical performance because of low conductivity of the electrolyte phase. It leads to not only the low ionic conductivity of the electrolyte but also the high mass transfer resistance of the lithium ion;
- the evaporation of the electrolyte results in dynamic change of the saturation and distribution of the electrolyte. The evaporation of the electrolyte is a critical factor that impacts the electrochemical performance of the battery;
- the mixture of lyophilic and lyophobic pores makes it possible to achieve high discharge capacity (>7 A h/g) at high current (~20 A/cm^2); and
- the design of the battery electrode should consider both the thickness of the electrode, the initial amount of the electrolyte, and the evaporation of the electrolyte during operation.

DOI: 10.1021/acsami.8b06624
ACS Appl. Mater. Interfaces 2018, 10, 26222−26232

These findings enables the design of advanced Li−O_2 battery electrodes with high capacity at high operating current and power densities, which are critical to accelerate the deployment of this beyond Li-ion battery technology to transport and stationary applications.

■ ASSOCIATED CONTENT

Supporting Information

The Supporting Information is available free of charge on the ACS Publications website at DOI: 10.1021/acsami.8b06624.

Experimental fabrication and testing of electrodes; measurement of the pore size distribution within the electrode; reconstructions and validations of digital electrodes; validation of the electrochemical model; and O_2 concentration and volume fraction of Li_2O_2 in electrodes with different electrolyte saturations (100, 87.5, and 36.14%) (PDF)

■ AUTHOR INFORMATION

Corresponding Author

*E-mail: xianglinli@ku.edu. Phone: +1 (785) 864 8165.

ORCID

Xianglin Li: 0000-0002-0193-9410

Notes

The authors declare no competing financial interest.

■ ACKNOWLEDGMENTS

The authors wants to thank the financial support from KU's NFGRF and GRF.

■ REFERENCES

(1) Girishkumar, G.; McCloskey, B.; Luntz, A. C.; Swanson, S.; Wilcke, W. Lithium−Air Battery: Promise and Challenges. *J. Phys. Chem. Lett.* **2010**, *1*, 2193−2203.

(2) Luntz, A. C.; McCloskey, B. D. Nonaqueous Li-Air Batteries: A Status Report. *Chem. Rev.* **2014**, *114*, 11721−11750.

(3) Abraham, K. M. Prospects and Limits of Energy Storage in Batteries. *J. Phys. Chem. Lett.* **2015**, *6*, 830−844.

(4) Xu, K. Nonaqueous Liquid Electrolytes for Lithium-Based Rechargeable Batteries. *Chem. Rev.* **2004**, *104*, 4303−4418.

(5) Abraham, K. M. Electrolyte-Directed Reactions of the Oxygen Electrode in Lithium-Air Batteries. *J. Electrochem. Soc.* **2015**, *162*, A3021−A3031.

(6) Li, Y.; Wang, X.; Dong, S.; Chen, X.; Cui, G. Recent Advances in Non-Aqueous Electrolyte for Rechargeable Li-O2Batteries. *Adv. Energy Mater.* **2016**, *6*, 1600751.

(7) McCloskey, B. D.; Bethune, D. S.; Shelby, R. M.; Girishkumar, G.; Luntz, A. C. Solvents' Critical Role in Nonaqueous Lithium-Oxygen Battery Electrochemistry. *J. Phys. Chem. Lett.* **2011**, *2*, 1161−1166.

(8) Yu, Z.; Carter, R. N.; Zhang, J. Measurements of Pore Size Distribution, Porosity, Effective Oxygen Diffusivity, and Tortuosity of PEM Fuel Cell Electrodes. *Fuel Cells* **2012**, *12*, 557−565.

(9) Olivares-Marín, M.; Palomino, P.; Enciso, E.; Tonti, D. Simple Method to Relate Experimental Pore Size Distribution and Discharge Capacity in Cathodes for Li/O2 Batteries. *J. Phys. Chem. C* **2014**, *118*, 20772−20783.

(10) Mench, M. M. *Fuel Cell Engines*; Wiley, 2008.

(11) Li, X.; Faghri, A. Optimization of the Cathode Structure of Lithium-Air Batteries Based on a Two-Dimensional, Transient, Non-Isothermal Model. *J. Electrochem. Soc.* **2012**, *159*, A1747−A1754.

(12) Williford, R. E.; Zhang, J.-G. Air electrode design for sustained high power operation of Li/air batteries. *J. Power Sources* **2009**, *194*, 1164−1170.

(13) Chervin, C. N.; Wattendorf, M. J.; Long, J. W.; Kucko, N. W.; Rolison, D. R. Carbon Nanofoam-Based Cathodes for Li-O2 Batteries: Correlation of Pore-Solid Architecture and Electrochemical Performance. *J. Electrochem. Soc.* **2013**, *160*, A1510−A1516.

(14) Tan, P.; Shyy, W.; An, L.; Wei, Z. H.; Zhao, T. S. A gradient porous cathode for non-aqueous lithium-air batteries leading to a high capacity. *Electrochem. Commun.* **2014**, *46*, 111−114.

(15) Read, J.; et al. Oxygen Transport Properties of Organic Electrolytes and Performance of Lithium/Oxygen Battery. *J. Electrochem. Soc.* **2003**, *150*, A1351−A1356.

(16) Lu, Y.-C.; et al. The discharge rate capability of rechargeable Li-O2 batteries. *Energy Environ. Sci.* **2011**, *4*, 2999−3007.

(17) Christensen, J.; et al. A Critical Review of Li/Air Batteries. *J. Electrochem. Soc.* **2012**, *159*, R1−R30.

(18) Al Hallaj, S.; Maleki, H.; Hong, J. S.; Selman, J. R. Thermal modeling and design considerations of lithium-ion batteries. *J. Power Sources* **1999**, *83*, 1−8.

(19) Xu, B.; Qian, D.; Wang, Z.; Meng, Y. S. Recent progress in cathode materials research for advanced lithium ion batteries. *Mater. Sci. Eng., R* **2012**, *73*, 51−65.

(20) Fleischhammer, M.; Waldmann, T.; Bisle, G.; Hogg, B.-I.; Wohlfahrt-Mehrens, M. Interaction of cyclic ageing at high-rate and low temperatures and safety in lithium-ion batteries. *J. Power Sources* **2015**, *274*, 432−439.

(21) Gallagher, K. G.; et al. Quantifying the promise of lithium-air batteries for electric vehicles. *Energy Environ. Sci.* **2014**, *7*, 1555−1563.

(22) Sapunkov, O.; Pande, V.; Khetan, A.; Choomwattana, C.; Viswanathan, V. Quantifying the promise of "beyond" Li-ion batteries. *Transl. Mater. Res.* **2015**, *2*, 045002.

(23) Mohazabrad, F.; Wang, F.; Li, X. Influence of the Oxygen Electrode Open Ratio and Electrolyte Evaporation on the Performance of Li-O2 Batteries. *ACS Appl. Mater. Interfaces* **2017**, *9*, 15459−15469.

(24) Jiang, J.; et al. Research on Effective Oxygen Window Influencing the Capacity of Li-O2 Batteries. *ACS Appl. Mater. Interfaces* **2016**, *8*, 10375−10382.

(25) Yoo, K.; Banerjee, S.; Dutta, P. Modeling of volume change phenomena in a Li-air battery. *J. Power Sources* **2014**, *258*, 340−350.

(26) Huang, J.; Faghri, A. Analysis of electrolyte level change in a lithium air battery. *J. Power Sources* **2016**, *307*, 45−55.

(27) Ye, L.; et al. Analytical insight into the oxygen diffusion in wetted porous cathodes of Li-air batteries. *Energy* **2015**, *93*, 416−420.

(28) Wang, F.; Li, X. Effects of the Electrode Wettability on the Deep Discharge Capacity of Li−O2 Batteries. *ACS Omega* **2018**, *6*, 6006−6012.

(29) Tran, C.; Yang, X.-Q.; Qu, D. Investigation of the gas-diffusion-electrode used as lithium/air cathode in non-aqueous electrolyte and the importance of carbon material porosity. *J. Power Sources* **2010**, *195*, 2057−2063.

(30) Ding, N.; et al. Influence of carbon pore size on the discharge capacity of Li-O2 batteries. *J. Mater. Chem. A* **2014**, *2*, 12433−12441.

(31) Kim, M.; Yoo, E.; Ahn, W.-S.; Shim, S. E. Controlling porosity of porous carbon cathode for lithium oxygen batteries: Influence of micro and meso porosity. *J. Power Sources* **2018**, *389*, 20−27.

(32) Xue, K.-H.; Nguyen, T.-K.; Franco, A. A. Impact of the Cathode Microstructure on the Discharge Performance of Lithium Air Batteries: A Multiscale Model. *J. Electrochem. Soc.* **2014**, *161*, E3028−E3035.

(33) Andrei, P.; Bevara, V. V. Effects of Pore Size Distribution on the Discharge Characteristics of Li-Air Batteries with Organic Electrolyte. *ECS Trans.* **2014**, *61*, 193−212.

(34) Li, X. A Modeling Study of the Pore Size Evolution in Lithium-Oxygen Battery Electrodes. *J. Electrochem. Soc.* **2015**, *162*, A1636−A1645.

(35) Mukherjee, P. P.; Wang, C.-Y. Stochastic Microstructure Reconstruction and Direct Numerical Simulation of the PEFC Catalyst Layer. *J. Electrochem. Soc.* **2006**, *153*, A840−A849.

DOI: 10.1021/acsami.8b06624
ACS Appl. Mater. Interfaces 2018, 10, 26222−26232

(36) Mukherjee, P. P.; Kang, Q.; Wang, C.-Y. Pore-scale modeling of two-phase transport in polymer electrolyte fuel cells-progress and perspective. *Energy Environ. Sci.* **2011**, *4*, 346−369.
(37) Nelson, G. J.; et al. Three-dimensional microstructural changes in the Ni-YSZ solid oxide fuel cell anode during operation. *Acta Mater.* **2012**, *60*, 3491−3500.
(38) Litster, S.; Epting, W. K.; Wargo, E. A.; Kalidindi, S. R.; Kumbur, E. C. Morphological Analyses of Polymer Electrolyte Fuel Cell Electrodes with Nano-Scale Computed Tomography Imaging. *Fuel Cells* **2013**, *13*, 935−945.
(39) Shojaeefard, M. H.; Molaeimanesh, G. R.; Nazemian, M.; Moqaddari, M. R. A review on microstructure reconstruction of PEM fuel cells porous electrodes for pore scale simulation. *Int. J. Hydrogen Energy* **2016**, *41*, 20276−20293.
(40) Yeong, C. L. Y.; Torquato, S. Reconstructing random media. *Phys. Rev. E: Stat. Phys., Plasmas, Fluids, Relat. Interdiscip. Top.* **1998**, *57*, 495−506.
(41) Jiao, Y.; Stillinger, F. H.; Torquato, S. Modeling heterogeneous materials via two-point correlation functions: Basic principles. *Phys. Rev. E: Stat., Nonlinear, Soft Matter Phys.* **2007**, *76*, 031110.
(42) Dhillon, S.; Kant, R. Quantitative roughness characterization and 3D reconstruction of electrode surface using cyclic voltammetry and SEM image. *Appl. Surf. Sci.* **2013**, *282*, 105−114.
(43) Jiao, Y.; Stillinger, F. H.; Torquato, S. Modeling heterogeneous materials via two-point correlation functions. II. Algorithmic details and applications. *Phys. Rev. E: Stat., Nonlinear, Soft Matter Phys.* **2008**, *77*, 031135.
(44) Debye, P.; Anderson, H. R.; Brumberger, H. Scattering by an Inhomogeneous Solid. II. The Correlation Function and Its Application. *J. Appl. Phys.* **1957**, *28*, 679−683.
(45) Metropolis, N.; Rosenbluth, A. W.; Rosenbluth, M. N.; Teller, A. H.; Teller, E. Equation of State Calculations by Fast Computing Machines. *J. Chem. Phys.* **1953**, *21*, 1087−1092.
(46) Kim, S. H.; Pitsch, H. Reconstruction and Effective Transport Properties of the Catalyst Layer in PEM Fuel Cells. *J. Electrochem. Soc.* **2009**, *156*, B673−B681.
(47) Kirkpatrick, S.; Gelatt, C. D.; Vecchi, M. P. Optimization by Simulated Annealing. *Science* **1983**, *220*, 671−680.
(48) Soille, P. *Morphological Image Analysis*; Springer Berlin Heidelberg, 2004.
(49) Li, X.; Huang, J.; Faghri, A. Modeling study of a Li-O 2 battery with an active cathode. *Energy* **2015**, *81*, 489−500.
(50) Li, X.; Huang, J.; Faghri, A. A critical review of macroscopic modeling studies on Li O 2 and Li-air batteries using organic electrolyte: Challenges and opportunities. *J. Power Sources* **2016**, *332*, 420−446.
(51) Viswanathan, V.; et al. Electrical conductivity in Li2O2 and its role in determining capacity limitations in non-aqueous Li-O2 batteries. *J. Chem. Phys.* **2011**, *135*, 214704.
(52) Patankar, S. *Numerical Heat Transfer and Fluid Flow*; CRC Press, 1980.
(53) Abraham, K. M. A Polymer Electrolyte-Based Rechargeable Lithium/Oxygen Battery. *J. Electrochem. Soc.* **1996**, *143*, 1.
(54) Schulz, V. P.; Becker, J.; Wiegmann, A.; Mukherjee, P. P.; Wang, C.-Y. Modeling of Two-Phase Behavior in the Gas Diffusion Medium of PEFCs via Full Morphology Approach. *J. Electrochem. Soc.* **2007**, *154*, B419−B426.
(55) Chen, W.; et al. High areal capacity, long cycle life Li-O 2 cathode based on highly elastic gel granules. *Nano Energy* **2018**, *47*, 353−360.
(56) Wang, F.; Li, X. Discharge Li-O 2 batteries with intermittent current. *J. Power Sources* **2018**, *394*, 50−56.
(57) Balaish, M.; Ein-Eli, Y. Enhancing oxygen adsorption capabilities in Li-O2 battery cathodes through solid perfluorocarbons. *J. Mater. Chem. A* **2017**, *5*, 14152−14164.

DOI: 10.1021/acsami.8b06624
ACS Appl. Mater. Interfaces 2018, 10, 26222−26232

Paper P4

The Stagnant Thermal Conductivity of Porous Media Predicted by the Random Walk Theory

International Journal of Heat and Mass Transfer 107 (2017) 520–533

Contents lists available at ScienceDirect

International Journal of Heat and Mass Transfer

journal homepage: www.elsevier.com/locate/ijhmt

The stagnant thermal conductivity of porous media predicted by the random walk theory

Fangzhou Wang, Xianglin Li *

Department of Mechanical Engineering, University of Kansas, Lawrence, KS 66045, USA

ARTICLE INFO

Article history:
Received 15 June 2016
Received in revised form 1 October 2016
Accepted 21 November 2016
Available online 29 November 2016

ABSTRACT

This study developed a predictive model based on the random walk theory to calculate the stagnant thermal conductivity of porous materials considering detailed pore geometries. This model can take the connectedness of solid matrix and filling fluid into consideration and simulate porous media with a wide range of porosities and geometries. The model was calibrated by comparing simulated thermal conductivities of simplified geometries proposed in literature with the corresponding experimental data. Results indicate that the stagnant thermal conductivities of porous media are very sensitive to the connectedness (or contact resistance) of the solid matrix, especially when the conductivity of the solid matrix (e.g. Al) is much higher than the conductivity of filling fluid (air). This study also imported reconstructed three-dimensional geometries (measured by micro computed tomography) of Al foams into the model and simulated their stagnant thermal conductivities. The measured Al foams have porosities around 0.9 and different pore sizes (5, 10, 20, and 40 parts per inch). The simulated stagnant thermal conductivities of Al foams slightly increased with decreased pore size at the porosity around 0.9.

The model developed in this study is a powerful tool to predict stagnant thermal conductivity of porous media widely applied in a broad range of science and engineering disciplines. The low computational time of this model makes it a unique tool to provide real-time updates of material properties for on-site applications or other computational models. Furthermore, the solid matrix and the filling fluid in the porous medium could be multi-phase mixtures or composite materials due to the statistical nature of the random walk model.

1. Introduction

Porous media are widely used in various applications such as nuclear power plants, combustion technologies [1], biological systems [2], petroleum industry [3], electrochemical devices [4], thermal management systems [5]. Porous media applied in energy systems can generally be categorized into packed beds and open foam structures. Unconsolidated packed beds typically have lower porosity (less than 0.5) and the solid matrix are connected by point contacts. While open foam porous materials have much higher porosity (above 0.9) and the solid matrix has better connectedness. The accurate prediction of stagnant thermal conductivities (or effective thermal conductivities) of porous materials filled with stagnant fluid (liquid or gas) has a theoretical and practical significance. Considerable theoretical and experimental research on the stagnant thermal conductivity of porous materials has been carried out. Several literature reviews have categorized, compared, and discussed a great amount of studies in details [6].

The thermal conductivity of both packed beds and the solid matrix is strongly affected by properties of constituent materials and the porosity. It has also been proven that the stagnant thermal conductivity of a control volume made from two materials (the porous matrix and the filling material) is bracketed by the conductivity of two bulk materials (the volume fraction of the filling material equals the porosity) connect in parallel and the stagnant conductivity when these two materials connect in series [7,8]. When the thermal conductivity of the solid matrix and filling materials are considerably different (e.g. air in Cu foam), however, the range between the upper and lower limits of the predicted conductivity is extremely broad. Although all the stagnant thermal conductivities predicted by existing analytical models fall between the upper (parallel) and lower (series) limits, the model predictions could be significantly different from each other.

Existing analytical models only applied to either packed beds or foam materials since these models are derived based on simplified geometries of the porous medium. Table 1 summarizes some representative models that analyze the stagnant thermal conductivity of porous media. Most of these models were derived from one-dimensional, two-dimensional, or three-dimensional thermal

* Corresponding author.
E-mail address: xianglinli@ku.edu (X. Li).

http://dx.doi.org/10.1016/j.ijheatmasstransfer.2016.11.069
0017-9310/

Table 1
Analytical studies of stagnant thermal conductivity of packed beds or foam materials.

Author	Equation of stagnant thermal conductivity, k_{eff}	Notes
Packed beds		
Yagi and Kunni, 1952 [11]	$\frac{k_{eff}}{k_f}=\frac{\beta(1-\varepsilon)}{\gamma(k_f/k_s)}+\varepsilon\beta\frac{D_p h_{rv}}{k_f}$. where β and γ can be both approximate to be 1, h_{rv}, is the heat transfer coefficient of convection, φ is the ratio of effective thickness of fluid film adjacent to contact surface of two solid particles to the average diameter of the packing, and D_p is the diameter of the bed	The packing materials that are compared include iron spheres, porcelain packings, cement clinker, insulating fire brick, and Raschig rings. The experimental temperature varied from room temperature to close to 900 °C. The thermal radiation is predominant when the temperature is high (>400 °C) and the diameter and thermal conductivity of solids are large
Kunii and Smith, 1960 [12]	Packed beds of unconsolidated particles: $\frac{k_{eff}}{k_f}=\varepsilon+\frac{1-\varepsilon}{\phi+\frac{2}{3}\frac{k_f}{k_s}}$ where $\phi=\begin{cases}\phi_1 \text{ when } \varepsilon\leqslant 0.260\\ \phi_2+(\phi_1-\phi_2)\frac{\varepsilon-0.260}{0.215}0.260\leqslant\varepsilon\leqslant 0.476\\ \phi_2 \text{ when } \varepsilon\geqslant 0.476\end{cases}$. For loose packing: $\phi_1=\frac{0.5(1-\frac{1}{n})^2}{\ln\left[k-(k-1)\sqrt{1-\frac{1}{n^2}}\right]\frac{1.5}{n^2}(1-\frac{1}{n})\left(1-\sqrt{1-\frac{1}{n^2}}\right)}-\frac{2}{3k}$, the number of contact n ≈ 1.5 For close packing: $\phi_2=\frac{0.5(1-\frac{1}{n})^2/\sqrt{3}}{\ln\left[k-(k-1)\sqrt{1-1/4\sqrt{3}}\right](1-1/n)\left(1-\sqrt{1-1/4\sqrt{3}}\right)}-\frac{2}{3k}$, the number of contact $n=4\sqrt{3}$	Radiation is neglected, which applies to cases that the porous medium is filled with liquid or when the temperature is below 900 °F Consolidated porous media: $\frac{k_{eff}}{k_f}=\varepsilon'\cdot\frac{k_s}{k_f}+\frac{(1-\varepsilon')(1+\frac{2}{3}\phi)}{1+\frac{\varepsilon' k_s}{\left(\frac{2}{3}\right)k_f+\frac{D_p h_p}{k_f}}}$. where ε′ is the porosity of the consolidated media and the heat transfer through the contact surface between consolidated particles, $\frac{D_p h_p}{k_s}$, which depends on the type of consolidation and characteristic of the solid material, needs to be determined by experimental data
Masamune and Smith, 1963 [13]	$k_{eff}=\alpha\varepsilon k_f+\frac{(1-\alpha\varepsilon)(1-\delta)}{\frac{2}{3}\frac{k_f}{k_s}}+(1-\alpha\varepsilon)\delta k_s$. where $\phi=\frac{n}{(n-1)^2}\left[1-\left(\frac{n}{2}-\theta\right)\tan\theta\right]$; $\alpha=1-\frac{3}{2}\left(\frac{1-\varepsilon}{\varepsilon}\right)\phi$; $\delta=\left(\frac{1}{1-\alpha\varepsilon}\right)\frac{k_s^0}{k_s}$; $\delta=0$ when the sphere is hard sphere with point contact. $\theta=\cos^{-1}\left(1-\frac{1}{n}\right)$, and $n=6.93-5.51\frac{\varepsilon-0.260}{0.210}\varepsilon\in[0.260,0.476]$	Experimental measurements of stagnant conductivity (at the pressure of 0.01–760 mm of Hg) of packed beds made from glass beads and steel shots from 29 to 470 μm in diameter The contribution of heat transfer through the void fraction is less than 4% of the total heat transfer and may be neglected
Veinberg, 1967 [14]	Porous media with randomly distributed spheres: $\varepsilon\left(\frac{k_{eff}}{k_f}\right)^{1/3}=\frac{k_s}{k_s}\frac{k_{eff}}{k_f}$.	The model used an integral technique and gradually filled the medium with inclusions until the given volume fraction was attained
Krupiczka, 1967 [16]	$\frac{k_{eff}}{k_f}=\left(\frac{k_s}{k_f}\right)^{0.280-0.757\log_{10}\varepsilon+0.057\log_{10}\left(\frac{k_s}{k_f}\right)}$	Simplify the packed bed as a bundle of long cylinders Assume there is no temperature drop across the liquid-solid interface
Crane and Vachon, 1977 [17]	Two boundaries of the stagnant thermal conductivity: $\int_0^1\frac{k_s\cdot k_f\cdot dx}{k_s+\varepsilon(k_f-k_s)}\leqslant k_{eff}\leqslant\frac{1}{\int_0^1\frac{dx}{k_s+\varepsilon(k_f-k_s)}}$ An empirical relation of the stagnant conductivity with the conductivity was derived based on experimental data: $k_{eff}=k_{eff}^{parallel}\cdot\exp\left\{-0.1439-0.72359\ln\left(\frac{k_s}{k_f}\right)+0.020114\left[\ln\left(\frac{k_s}{k_f}\right)\right]^2+3.026\varepsilon\right\}$	Two models to describe the stagnant thermal conductivity of granular systems were derived based on resistance network in parallel and series connections respectively The layers-in-series and the layers-in-parallel models represent limiting cases for the stagnant thermal resistance
Tien and Vafai, 1978 [18]	$F_1(\varepsilon,\frac{k_s}{k_f},G)\geqslant\frac{k_{eff}}{\sqrt{k_s k_f}}\geqslant F_2\left(\varepsilon,\frac{k_s}{k_f},G\right)$ $F_1\left(\varepsilon,\frac{k_s}{k_f},G\right)=\frac{1+(1-\varepsilon)\left(\frac{k_s}{k_f}-1\right)}{\sqrt{k_s/k_f}}\left\{1-\frac{\varepsilon(1-\varepsilon)\left(\frac{k_s}{k_f}-1\right)^2}{3\left[1+(1-\varepsilon)\left(\frac{k_s}{k_f}-1\right)\right]\left[1+(1-\varepsilon)\left(\frac{k_s}{k_f}-1\right)+3\left(\frac{k_s}{k_f}-1\right)(2\varepsilon-1)G\right]}\right\}$	The lower and upper boundaries of the stagnant thermal conductivity were based on series and parallel connections of the two phases with statistical considerations of geometry of the cell The bandwidth of the stagnant thermal conductivity will decrease with more geometric or packing information

(*continued on next page*)

Table 1 (*continued*)

Author	Equation of stagnant thermal conductivity, k_{eff}	Notes
	$F_2\left(\varepsilon,\frac{k_s}{k_f},G\right)=\left\{\sqrt{k_s/k_f}\left[\frac{k_s}{k_f}-(1-\varepsilon)\left(\frac{k_s}{k_f}-1\right)\right]-\frac{4a(1-\varepsilon)\left(\frac{k_s}{k_f}-1\right)^2}{3\left[1+\frac{k_s}{k_f}+3(1-2\varepsilon)\left(\frac{k_s}{k_f}-1\right)G\right]}\right\}^1$	Packed beds with four different packing structures (body-centered cubic, face-centered cubic, simple cubic, and simple cubic with a defect) had been studied by considering their different solid faction parameters
	where G is the geometry of the cells. For three-dimensional geometries, G is 1/9 for spherical cells and 1/3 for plate like cells	This study also considered the mixture of two different packing structures
Nozad et al., 1985 [19,20]	Two-phase heat conduction is described in Eq. (3.23) [19] Three-phase heat conduction is described in Eq. (3.6) [20]	The numerical model was derived based on the one-dimensional heat conduction through an array of two-dimensional squares with and without particle contacts
Zehner and Schlunder [22] Hsu et al., 1994 [23]	$\frac{k_{eff}}{k_f}=1-\sqrt{1-\varepsilon}+\frac{2\sqrt{1-\varepsilon}}{1-\frac{k_f}{k_s}B}\left[\frac{\left(1-\frac{k_s}{k_s}\right)B}{\left(1-\frac{k_f}{k_s}B\right)^2}\right]\ln\left(\frac{k_s}{k_fB}\right)-\frac{B+1}{2}-\frac{B-1}{1-\frac{k_f}{k_s}B}$ where $B=1.25\left(\frac{1-\varepsilon}{\varepsilon}\right)^{10/9}$ (Zehner and Schlunder)	The model was derived based on a cylindrical unit cell that contained a spherical particle; The effect of finite touching area was only noticeable when the ratio of conductivity between the solid and liquid was very high (>1000)
	or $B=1.364\left(\frac{1-\varepsilon}{\varepsilon}\right)^{1.055}$ (Hsu et al.). Stagnant thermal conductivity of spheres has finite contact area: $\frac{k_{eff}}{k_f}=1-\sqrt{1-\varepsilon}+\frac{\sqrt{1-\varepsilon}}{k_f/k_s}\left[1-\frac{1}{(1+\alpha B)^2}\right]+\frac{2\sqrt{1-\varepsilon}}{1-\frac{k_f}{k_s}B+\left(1-\frac{k_f}{k_s}\right)\alpha B}$ $\times\left\{\frac{\left(1-\frac{k_f}{k_s}\right)(1+\alpha)B}{\left[1-\frac{k_f}{k_s}B+\left(1-\frac{k_f}{k_s}\right)\alpha B\right]^2}\ln\left[\frac{1+\alpha B}{(1+\alpha)\frac{k_f}{k_s}B}\right]-\frac{1+B+2\alpha B}{2(1+\alpha B)^2}-\frac{B-1}{\left[1-\frac{k_f}{k_s}B+\left(1-\frac{k_f}{k_s}\right)\alpha B\right](1+\alpha B)}\right\}$. The shape factor B is determined by: $1-\varepsilon=\frac{B^2}{(1-B)^5(1+\alpha B)^3}\left\{(B^2-4B+3)+2(1+\alpha)(1+\alpha B)\right.$ $\left.\times\ln\left[\frac{(1+\alpha)B}{1+\alpha B}\right]+\alpha(B-1)(B^2-2B-1)\right\}^2$	
Hsu et al., 1995 [24]	Stagnant thermal conductivity of square cylinders: $\frac{k_{eff}}{k_f}=\frac{r_ar_c}{k_f/k_s}+\frac{r_a(1-r_c)}{1+(k_f/k_s-1)r_a}+\frac{(1-r_a)}{1+(k_f/k_s-1)r_ar_c}$. where $1-\varepsilon=r_a^2+2r_ar_c(1-r_a)$ and $r_a=a/l$ and $r_c=\frac{c}{a}=0.01$, $r_c=0$ for non-touching square cylinders Stagnant thermal conductivity of circular cylinders: Eq. (12) in the reference Stagnant thermal conductivity of cubes: $\frac{k_{eff}}{k_f}=(1-r_a^2-2r_ar_c+2r_a^2r_c)+\frac{r_a^2r_c^2}{k_f/k_s}+\frac{r_a^2(1-r_c^2)}{1-r_a+r_ak_f/k_s)}+\frac{2(r_ar_c-r_a^2r_c)}{1-r_ar_c+r_ar_c(k_f/k_s)}$. where $1-\phi=(1-3r_c^2)r_a^3+3r_a^2r_c^2$ and $r_a=a/l$, $r_c=\frac{c}{a}=0.13$, $r_c=0$ for non-touching cubes	A one-dimensional conduction model with solid matrix geometries of two-dimensional touching and non-touching square and circular cylinders and three-dimensional touching and non-touching cubes was developed This model also involved empirical parameters such as the deformation factor or shape factor
Singh et al., 1998 [25]	$k_{eff}=\frac{k_f\left\{k_f+\left[0.806(k_s-k_f)F^{2/3}\right]\right\}}{\left\{k_f+\left[0.806(k_s-k_f)(1-1.2407F^{1/3})F^{2/3}\right]\right\}}$ (sphere) $k_{eff}=\frac{k_f\left[k_f+(k_s-k_f)F^{2/3}\right]}{k_f+(k_s-k_f)(1-F^{1/3})F^{2/3}}$ (cube) The porosity correction term, F, was determined empirically using available experimental data: $F=1-\exp\left[-0.92(1-\varepsilon)^2\log(k_s/k_f)\right]$	Developed theoretical models of one-dimensional heat conduction in three-dimensional unit cell of packed beds made from rigid and spherical particles (ε = 0.48–1.0) and rigid and cubic particles (ε = 0–1). This study then modified these models by replacing the porosity with a correction term, F, that considers the impact of porosity and ratio of thermal conductivity of the solid and fluid
Foam materials		
Dul'nev, 1965 [26]	$k_{eff}=k_st^2+k_f(1-t)^2+\frac{2t(1-t)k_f}{1-t(1-k_f/k_s)}$ where the dimensionless thickness t of the solid ligament in the unit cell is a function of the porosity: $t^3-1.5t^2+\frac{1}{2}\varepsilon=0$	The analytical solution of stagnant conductivity was also derived based on a thermal resistance model that divided the three-dimensional domain into four regions connected in parallel. Within each region, the solid matrix and the fluid were assumed connected in series
Schuetz and Glicksman [27]	$k_{eff}=\varepsilon k_f+\frac{(1-\varepsilon)}{3}k_s$	The first term considers the conductivity of fluid and the second term considers the conductivity of solid matrix
Calmidi and Mahajan, 1999 [28]	$k_{eff}=\left\{\frac{2}{\sqrt{3}}\left[\frac{r(\frac{k}{k_f})}{k_f+(1+\frac{k}{k_f})\frac{(k_s-k_f)}{3}}+\frac{(1-r)(\frac{k}{k_f})}{k_f+\frac{2}{3}(\frac{k}{k_f})(k_s-k_f)}+\frac{\frac{\sqrt{3}}{2}\frac{k}{L}}{k_f+\frac{4\sigma}{3\sqrt{3}}(\frac{k}{k_f})(k_s-k_f)}\right]\right\}^1$ where r = 0.09 and $\frac{k}{L}=\frac{r+\sqrt{r^2+\frac{2}{\sqrt{3}}(1-\varepsilon)\left[2r\left(1+\frac{1}{\sqrt{3}}\right)\right]}}{\frac{2}{3}\left[2r\left(1+\frac{1}{\sqrt{3}}\right)\right]}$ The measured stagnant thermal conductivity was fitted by: $\frac{k_{eff}}{k_f}=\varepsilon+A(1-\varepsilon)^n\frac{k_s}{k_f}$, where n is 0.763 and A is 0.181 for air and 0.195 for water	The representative unit cell had a hexagonal structure The model assumed one-dimensional heat conduction and divided the unit cell into three layers connected in series. Solid and fluid phases were connected in parallel within each layer
Boomsma and Poulikakos, 2001 [29]	$k_{eff}=\frac{\sqrt{2}}{2(R_A+R_B+R_C+R_D)}$ where $R_A=\frac{4d}{[2\varepsilon^2+\pi d(1-\varepsilon)]k_s+[4-2\varepsilon^2+\pi d(1-\varepsilon)]k_f}$;	The heat conduction model for open-celled Al foams was developed based on a three-dimensional description of the foam geometry

Table 1 (*continued*)

Author	Equation of stagnant thermal conductivity, k_{eff}	Notes
	$R_B = \frac{(e\ \ 2d)^2}{(e\ \ 2d)e^2k_s+[2e\ \ 4d+(e\ \ 2d)e^2]k_f}$; $R_C = \frac{(\sqrt{2}\ \ 2e)^2}{2\pi d^2(1\ \ 2e\sqrt{2})k_s+2[\sqrt{2}\ \ 2e\ \ \pi d^2(1\ \ 2e\sqrt{2})]k_f}$; $R_D = \frac{2e}{e^2k_s+(4\ \ e^2)k_f}$. The porosity ε was estimated by: $\varepsilon = 1-\frac{\sqrt{2}}{2}\left[de^2+\frac{\pi d^2}{2}(1-e)+\left(\frac{e}{2}-d\right)e^2+\pi d^2(1-2e\sqrt{2})+\frac{e^3}{4}\right]$, and $d = \sqrt{\frac{\sqrt{2}(2\ \ \frac{5}{2}\sqrt{2}e^3\ \ 2e)}{\pi(3\ \ 4e\sqrt{2}\ \ e)}}$, e = 0.339 (porous Al with air)	
Yao et al., 2015 [10]	$k_{eff} = \frac{1}{\lambda/k_A+(1\ \ 2\lambda)/k_B+\lambda/k_C}$, where $k_A = \frac{\sqrt{2}}{6}\pi\lambda(3-4\lambda)\frac{1+a_1^2}{a_1^2}k_s+\left[1-\frac{\sqrt{2}}{6}\pi\lambda(3-4\lambda)\frac{1+a_1^2}{a_1^2}\right]k_f$, $k_B = \frac{\sqrt{2}}{2}\pi\lambda^2\frac{1+a_1^2}{a_1^2}k_s+\left(1-\sqrt{2}\pi\lambda^2\frac{1+a_1^2}{a_1^2}\right)k_f$, $k_C = \frac{\sqrt{2}}{6}\pi\lambda^2\frac{1+a_1^2}{a_1^2}k_s+\left(1-\frac{\sqrt{2}}{6}\pi\lambda^2\frac{1+a_1^2}{a_1^2}\right)k_f$, a_1 equals 2.01 and λ is a non-dimensional parameter and can be solved from the following equation: $\varepsilon = 1-\frac{\sqrt{2}}{2}\pi\lambda^2(3-5\lambda)\frac{1+a_1^2}{a_1^2}$.	Open-cell metal foams with a concave tri-prism ligament and Kelvin tetrakaidecahedron structure The analytical model neglected convection and radiation within the metal foam and neglected the heat exchange between the foam skeleton and the filling material The unit cell was divided into three layers connected in series along the heat transfer direction. The solid matrix and the filling fluid were assumed in parallel connections within each layer. The influence of pore density on the stagnant conductivity was negligible

resistance models. The geometries of the solid matrix in these models had been simplified so they can be mathematically described (circle, square, sphere, cube particles, or metal foam with cubic, hexagonal, or tetrakaidecahedronal lattices [9,10]). The stagnant thermal conductivity of the porous material was then analyzed based on the simplified geometry of the solid matrix and the thermal resistance model.

Yagi and Kunni [11] simplified the model of heat transfer with stagnant fluid in packed bed to three layers connected in parallel: a small layer with all solid; a layer with all fluid; and a layer that the fluid and solid phases are mixed and connected in series. The layer with all solid phase (where the solid matrix has perfect contact) was very small compared with the unit cell and could be neglected. The geometry and material properties of the particle (sphere, cylinder, hexagonal prism) was considered by the model using some empirical parameters that were measured by experiments. This study also experimentally measured the stagnant thermal conductivity of a group of solid materials (iron sphere, porcelain, cement, insulating fire bricks, and Rasching rings) filled with air or H_2 or He under temperature up to 900 °C. It was found that the radiation became effective only when the temperature is above 400 °C.

Kunii and Smith [12] developed theoretical equations to predict the stagnant thermal conductivities in packed beds of unconsolidated spherical particles with loose packing and close packing respectively. The different packing mode will result in different numbers of contact per spherical particle. This study also extended the model to predict the stagnant thermal conductivity of consolidated porous media. Similar to the previous study [11], the thermal resistance model in this study divided the computational domain into several layers connected in parallel and series.

Masamune and Smith [13] experimentally measured the stagnant thermal conductivity of packed beds made from spherical glass beads and steel shot (29–470 μm) under various air pressures (0.01–760 mmHg). The heat transfer model divided the computational domain into several layers connected in series or parallel which were similar to Yagi and Kunni [11]. It was found that the contribution of heat transfer through the void (filled with air) by conduction and radiation is less than 4%. A theoretical equation that considers the pressure of filling air was also derived considering the influence of free molecular conduction.

Veinberg [14] used analogy of permeability to derive the general equation that determines the electric conductivity, dielectric constant, and thermal conductivity of porous media with spherical solid matrix. The model used an integral technique and gradually filled the medium with inclusions until the given volume fraction was attained. The increment of the thermal conductivity was calculated based on the increment of the volume content of the inclusion. By integrating the differential equation, the correlation to predict the stagnant thermal conductivity of porous media with randomly distributed spheres was derived [15].

Krupiczka [16] simplified the packed bed as a bundle of long cylinders and assumed the solid and fluid were in local thermal equilibrium (no temperature drop at the interface). The derived correlation of stagnant thermal conductivity predicted reasonably good results for packed beds saturated with liquid.

Crane and Vachon [17] developed two models to describe the stagnant thermal conductivity of granular systems based on resistance network connected in parallel and series respectively. Their results indicated that the layers-in-series and the layers-in-parallel models represented limiting cases for the stagnant thermal resistance. An empirical relation of the stagnant conductivity was derived based on the stagnant conductivity when fluid and solid were connected in parallel (upper bound) and a correction function which was determined by experimental data. This study assumed that the location of the fluid (or solid matrix) element did not influence the overall resistance. Therefore, both the solid matrix and the fluid phases were continuous in equivalent geometries after rearranging fluid elements. However, we would argue and prove in this study that locations of the fluid or solid matrix elements in the computational domain, which reflects the connectedness of solid and liquid phases, are critical to accurately predict the stagnant conductivity. The upper and lower limits of stagnant conductivities derived in this study overstate the two boundaries.

Tien and Vafai [18] generated a band of stagnant thermal conductivity for solid matrices of sphere and fibrous structures. The lower and upper boundaries of the stagnant thermal conductivity were based on series and parallel connections of the two phases with statistical considerations of the cell geometry. Beside the porosity, additional geometric information is needed to better characterize the stagnant thermal conductivity. The bandwidth of the stagnant thermal conductivity will decrease with more geometric or packing information. Different solid fraction parameters of packed beds made from spheres with four different packing structures had been analyzed: body-centered cubic, face-centered cubic, simple cubic, and simple cubic with a defect. The model derived in this study can consider the mixture of two different packing structures.

Nozad et al. [19,20] developed a numerical model based on the one-dimensional heat conduction through an array of two-dimensional squares with and without particle contacts. The contact area between particles were determined empirically. The general theory of heat conduction in two-phase porous media introduced in this study can be extended to three-phase porous media. The numerical study was followed by experimental measurements of stagnant thermal conductivity of packed beds using the transient method. The tested packed beds were made from glass, stainless steel, bronze, urea-formaldehyde, and aluminum particles filled with air, glycerol, and water. The particle diameters varied between 2.5 and 4.0 mm in this study.

Prasad et al. [21] experimentally measured the stagnant thermal conductivity of liquid-saturated porous beds of spheres. Porous media, with a series of conductivity ratios of solid to fluid, made from various combinations of solid (glass, steel and acrylic) and fluid (water and ethylene glycol) had been measured. The measured stagnant thermal conductivities were compared with analytical models developed by Kunii and Smith [12], Krupiczka [16], Zehner and Schulunder [22]. The results calculated from Krupiczka's model matched better with the experimental data than the others.

Hsu et al. [23] modified the correlation for the stagnant thermal conductivity originally developed by Zehner and Schlunder [22] based on a one-dimensional heat flow model in a cylindrical unit cell that contained a spherical particle. This model assumed the heat transfer through two parallel paths: conduction through the void filled with gas in the outer cylinder and conduction through the solid/gas in the inner cylinder. It was found that the Zehner-Schlunder model under-estimated the stagnant thermal conductivity of packed beds because the model assumed that spheres were in point contacts (infinitely small touching area). The modified model developed by Hsu et al. [23] considered the finite touching area and this study found that the effect of the touching area was only noticeable when the ratio of conductivity between the solid and liquid was very high (>1000). Inspired by the previous work, Hsu et al. [24] developed a one-dimensional conduction model with solid matrix geometries of two-dimensional touching and non-touching square and circular cylinders and three-dimensional touching and non-touching cubes. It should be noted that both models proposed by Hsu and Zehner and Schlunder involved empirical parameters such as the deformation factor or shape factor.

Singh et al. [25] first developed theoretical models of one-dimensional heat conduction in three-dimensional unit cell of packed beds made from rigid and spherical particles (their porosities varied from 0.48 to 1.0) and rigid and cubic particles (their porosities varied from 0 to 1). This study then modified these models by replacing the porosity with a correction term. The porosity correction term was determined empirically using available experimental data and considered the impact of porosity and ratio of thermal conductivity of the solid and fluid.

In addition to the above analytical studies of packed beds, many analytical models that predicted the stagnant thermal conductivity of foam materials had also been derived based on thermal resistance models. Dul'nev [26] neglected the convection and radiation in the unit cell and assumed the solid matrix has the cubic frame structure. The dimensionless thickness of the solid ligament in the unit cell was a function of the porosity. The computational domain was then divided into four regions (with pure fluid, pure solid, and mixtures of fluid and solid) connected in parallel along the heat transfer direction. Within the mixture region, the solid matrix and fluid were connected in series along the heat transfer direction. Schuetz and Glicksman [27] proposed a simple correlation of stagnant thermal conductivity of open-cell foam with porosity and the thermal conductivity of fluid and solid matrix. The thermal conductivity of solid matrix was multiplied by a factor (1/3) to consider the fact that one-third of the solid matrix is oriented in the heat transfer direction. Calmidi and Mahajan [28] developed a one-dimensional conduction model in a two-dimensional computational domain and assumed that the metal foam in the unit cell had a hexagonal structure. The representative unit cell was divided into three layers connected in series along the heat transfer direction. Each layer was mixed with solid and fluid and these two phases were assumed to connect in parallel within each layer. This study also experimentally measured thermal conductivities of high porous open-cell Al foams saturated with air and water and fitted the experimental data with an empirical function of porosity and conductivities of solid, k_s, and fluid, k_f. The porosity of tested foams ranged from 0.905 to 0.978 and the pore size varied from 5 to 40 pores per inch (PPI).

Boomsma and Poulikakos [29] proposed a one-dimensional heat conduction model for Al foams based on a Kelvin tetrakaidecahedron foam geometry. The three-dimensional geometry of the foam network was simplified with cubical nodes and cylindrical ligaments. The model also divided the representative unit cell (1/16 of a single tetrakaidecahedron cell) into four discrete layers connected in series along the heat transfer direction. Similar to previously mentioned models, the solid and fluid phases within each layer was assumed to connect in parallel (which neglected the heat exchange between the foam matrix and the filling material). The thickness of these four layers were directly related to the porosity of the foam and at least one of these parameters should be determined empirically with experimental data. The predicted stagnant thermal conductivity matched very well with experimental data measured by Calmidi and Mahajan [28].

Inspired by the model developed by Boomsma and Poulikakos [29], E.N. Schmierer and A. Razani [9] and Yao et al. [10] proposed models with Kelvin tetrakaidecahedron foam geometry. Instead of the cubical nodes in Boomsma and Poulikakos's model, E.N. Schmierer and A. Razani [9] assumed that nodes of the tetrakaidecahedron foam network were spherical. Geometric parameters (such as surface area, volume, and pore diameter) of the foam were measured by micro computed tomography (MicroCT) and processed with various image analysis software. The stagnant thermal conductivity of the unit foam cell was then simulated by computational fluid dynamics (CFD) model. Similar to the Boomsma and Poulikakos's method, Yao et al. [10] also divided the three-dimensional Kelvin tetrakaidecahedron foam cell into three layers connected in series along the heat transfer direction. The foam structure in Yao's study was assumed to have concave tri-prism ligament. The cross-sectional shape of the ligament, however, was found to have negligible influence on the stagnant thermal conductivity. Besides the theoretical analyses, Yao et al. [10] experimentally measured the stagnant thermal conductivity of Cu foams with various porosities (0.895–0.978) and pore densities (10, 20, 40 parts per inch) filled with air, water, or paraffin.

Most of the aforementioned models considered the heat conduction within the solid matrix material, within the filling material, and between the matrix and filling materials with specific simplifications. Fig. 1 summarizes the variations of stagnant conductivities with the ratio of solid to fluid thermal conductivity when the porosity equals (a) 0.36 (packed beds) and (b) 0.9 (foam), respectively. Most of existing analytical or semi-analytical (some parameters are fitted by experimental data) models can predict the stagnant porosity of given porous media with reasonable accuracy. The major limitation of these models is that most of these models only apply to certain geometry of matrix material, or a narrow range of the porosity, or a range of fluid conductivities. Typically, models derived based on packed beds do not apply to foam materials and vice versa because the connectedness of packed beds are considerably different from that of foam materials. The errors between the predicted stagnant conductivity and the experimental measurements are unacceptable (some models' predictions even become diverged) when models derived from packed beds are applied to predict stagnant conductivity of metal foams and vice versa. For instance, none of the three models derived based on metal foams (Dul'nev [26], Calmidi [28], and Boomsma and Poulikakos [30]) applies to packed beds when the porosity is 0.36. The simulated conductivities could even exceed the lower and upper limits of the boundary set by the series and parallel models. The limited predictive capability of existing models can also be seen clearly when the porosity of porous materials varies while solid and fluid materials keep unchanged (Fig. 2).

From the previous literature review, we can conclude that there is a lack of universal model that can predict the stagnant thermal conductivity considering the detailed pore geometry (sphere, cube, or irregular; no contact, point contact or surface contact etc.), material properties (conductivities of solid matrix and the filling material) and porosity (from less than 0.5 to higher than 0.9). This study will develop a unique model that integrates the random walk theory [31] with the thermal resistance approach to simulate the stagnant thermal conductivity. The newly developed model generally applies to porous media filled with multi-phase fluids and can consider the geometry of pores, porosity of the porous medium, connectedness of solid matrix (or fluid) and thermal conductivity of the solid matrix and fluid.

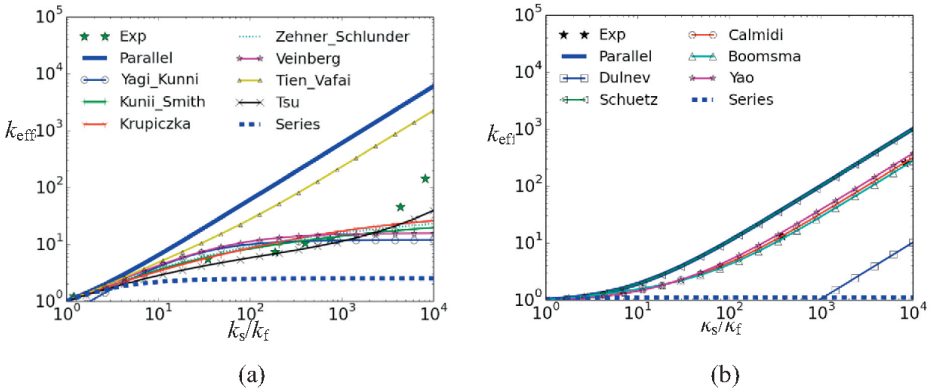

Fig. 1. Comparisons of models (a) based on pack beds and $\varepsilon = 0.4$ and (b) based on Al foam and $\varepsilon = 0.90$ with experimental data published in literature [17,20,28].

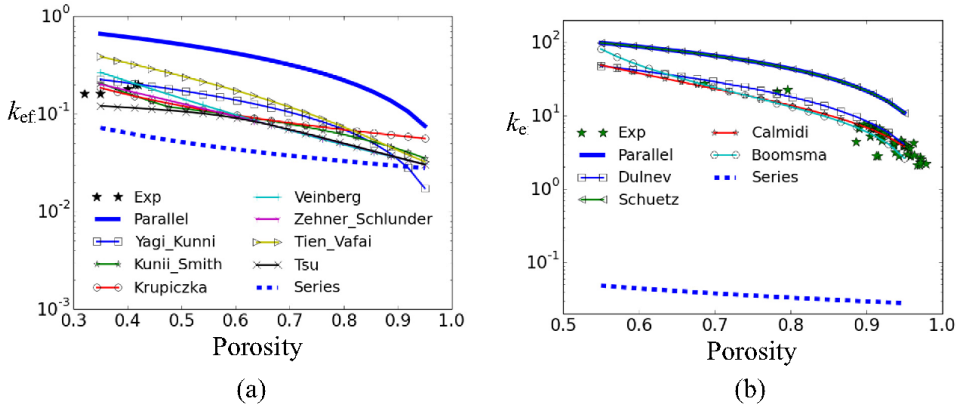

Fig. 2. Comparisons of experimental data published in literature [17,20,28] and simulated results of (a) packed beds made from glass and filled with air and (b) Al foam filled with air with various porosities.

2. Model descriptions

2.1. Thermal resistance model

Fig. 3(a) shows an example of two-dimensional thermal resistance model with heat conduction along the x direction. The computational domain is meshed by $m \times n$ grids. To consider all the heat conduction mechanism under steady state among neighbor cells, the thermal resistance model could be very complex and includes $m \times n$ thermal resistors (Fig. 3). As we mentioned before, previous analytical models divided the unit cell of the porous medium (regardless of the geometry of the solid matrix) into several layers connected in series or parallel to make the theoretical calculations manageable. The analytical solutions of the stagnant thermal conductivity are then derived based on the assumed geometry of solid matrix and the simplified layout of the heat transfer structure. All of these studies in Table 1 simplified the thermal resistance model by either neglecting the heat transfer (infinite thermal resistance) or neglecting the temperature difference (zero thermal resistance) between the matrix and filling materials in a certain direction in some calculated regions. In extreme cases, the two-dimensional thermal resistance model can be simplified to one-dimensional thermal resistance model with parallel connection, Fig. 3(b), or series connection, Fig. 3(c). The model with layers connected in parallel assumes the heat transfer resistance perpendicular to the heat transfer direction (y direction) is infinity. In other words, the heat fluxes among these layers connected in parallel are 0. On the contrary, models with layers connected in series assumes the heat transfer resistance perpendicular to the heat transfer direction is 0. Therefore, the temperature at the same heat transfer depth (x) are identical. These two assumptions either over-estimate or under-estimate the heat transfer resistance. Therefore, the parallel connection and the series connection of solid matrix with fluid set the lower and upper boundaries of the stagnant heat transfer resistance (or the upper and lower boundaries of the stagnant thermal conductivity).

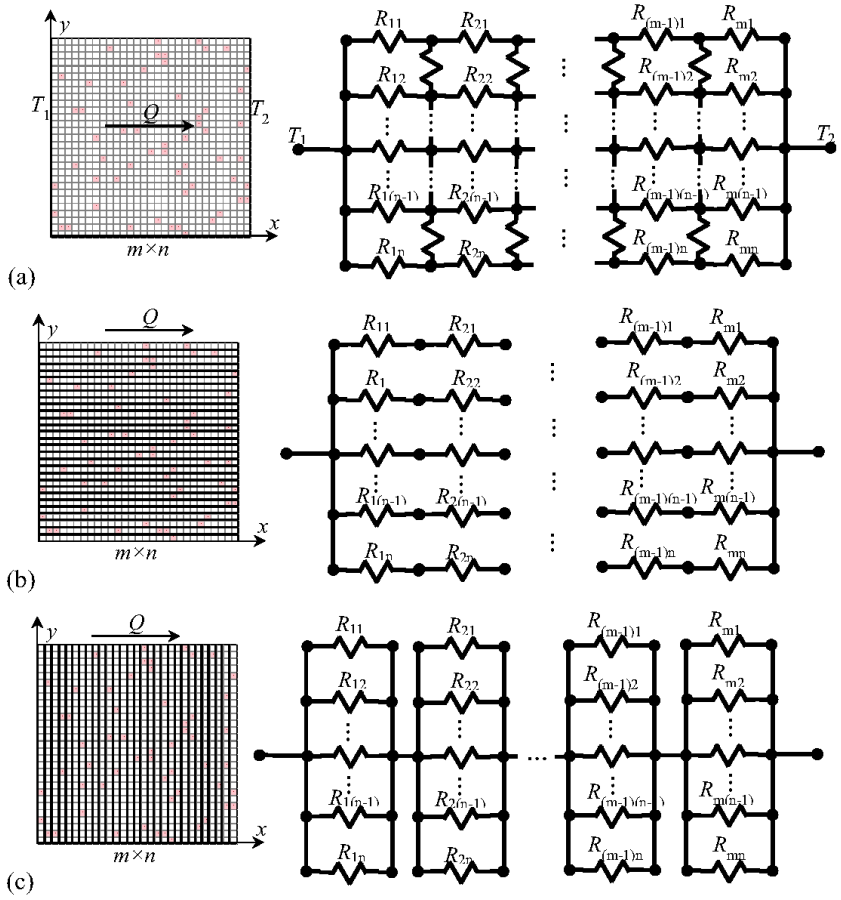

Fig. 3. (a) A two-dimensional thermal resistance model and (b) simplified thermal resistance models with layers connected in parallel and (c) simplified thermal resistance models with layers connected in series. These thermal resistance models represent a porous media with random distributions of matrix material (colored) and filling material (white). (For interpretation of the references to colour in this figure legend, the reader is referred to the web version of this article.)

The model developed in this study integrates random walk theory with detailed three-dimensional thermal resistance network without any simplifications. The unique model approach does not neglect thermal resistance or temperature difference among thermal nodes and could consider the pore (or matrix material) geometry in detail. The thermal resistance network can be generated from either simplified geometries proposed in literature or from reconstructed three-dimensional geometry measured by advanced imaging technologies. This study will start with simulation of stagnant thermal conductivity of simplified geometries (sphere and cubic frame). The simulated conductivity will be compared with experimental data or analytical solutions reported in literature to validate the model. The model validation will be followed by simulation of Al foam with various pore sizes using reconstructed three-dimensional geometries measured by MicroCT. Details of the model and results will be discussed in following sections.

2.2. Random walk theory

The random walk theory is applied to simplified or reconstructed two-dimensional or three-dimensional domains. The random walk theory treats the transport of a studied object (species, electron, or energy carrier) using a statistically significant numbers of random walkers [32]. Random walkers are mathematical objects that describe paths of the studied object. At each computational step, the random walker jumps to its neighboring sites according to probability distribution. The overall properties of the studied object (diffusivity, electric conductivity, and heat conductivity etc.) are statistically determined by paths of all random walkers and their transport resistance at each computational step. This model assumes one-dimensional heat conduction in a three-dimensional domain and tracks the movement of each random walker that starts from the $x = 0$ plane (Fig. 4). The assumptions in the model are:

- Each random walker will transfer heat independently;
- Each random walk can move freely in x, y, or z direction based on the local thermal conductivity;
- The thermal resistance of each random walker, $R(y, z)$, equals to the summary of thermal resistance of each cell this random walker has passed.
- Since all random walkers are assumed to move independently from each other, the overall thermal resistance of the computational domain equals to the thermal resistance of all random walkers connected in parallel.

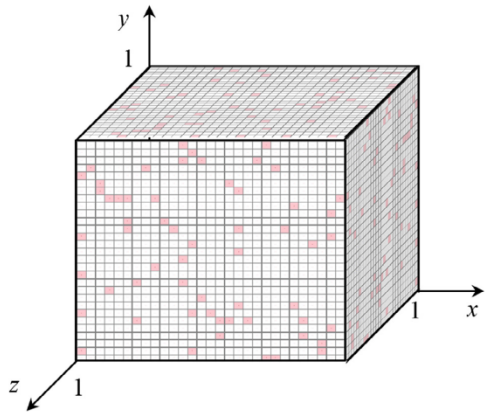

Fig. 4. The 3-D computational domain of a representative porous material with porosity of 0.5 and randomly distributed matrix materials. The matrix material is in color and the filling material is in white.

The computational domain in Fig. 4 is assumed to be a $1 \times 1 \times 1$ cube and is discretized to $m \times n \times l$ grids. Each unit cell is labeled as (i, j, p), where $i \in [1, m]$, $j \in [1, n]$, $p \in [1, m]$. The computational domain is composed with solid matrix material with the conductivity of k_m and a filling material (gas or liquid or solid) with the conductivity of k_f. The volume fraction of the filling material in the total volume of the computational domain equals the porosity (ε). Assume the heat transfer is one-dimensional and is along the x direction and all the walkers start from the $x = 0$ plane. These walkers move in the y (up or down) and z (in or out) directions randomly in the computational domain but they can only move towards right in the x direction (to be consistent with the heat transfer direction). Eventually, all walkers will reach the $x = 1$ plane which completes the simulation. To take different conductivities of the matrix material and the filling material into consideration, conductivities of all neighbor cells, except the left neighbor, of the cell (i, j, p) are used to evaluate the possibility of each walker's moving direction at the next step:

$$\{\text{Right} : k(i+1,j,p); \text{Down} : k(i,j-1,p); \text{Up} : k(i,j+1,p); \text{Out} : k(i,j,p-1); \text{In} : k(i,j,p+1)\} \quad (1)$$

The possibility of the walker that moves towards {Right, Down, Up, Out, In} is weighted by the conductivity of the neighbor cells:

$$\{k(i+1,j,p)/\text{sum}(k_{\text{neighbor}}), k(i,j-1,p)/\text{sum}(k_{\text{neighbor}}), k(i,j+1,p)/\text{sum}(k_{\text{neighbor}}), k(i,j,p-1)/\text{sum}(k_{\text{neighbor}}), k(i,j,p+1)/\text{sum}(k_{\text{neighbor}})\} \quad (2)$$

The following Fig. 5 shows an example of two-dimensional traces (on the $z = 0$ plan in Fig. 4) of three representative random walkers (colored in red, blue, and green, respectively) in the porous medium with random distributions of porous matrix. It should be noted that the anisotropic structures of metal foams caused during the manufacturing process result in anisotropic properties of the metal foam [33]. The MicroCT measurement can capture the anisotropic structures of metal foams, therefore, the random walk theory applied to the measured MicroCT structure can calculate anisotropic thermal conductivity of the metal foam. Although this study only simulates the thermal conductivity along the length of the cylindrical sample, the model could be conveniently applied to other heat transfer directions and simulate properties at other directions.

2.3. Stagnant thermal resistance

The increase of thermal resistance of the random walker after each step is calculated based on the thermal conductivity of the unit cell. If the random walker passes the matrix material with the conductivity of k_s, the equivalent thermal resistance of the walker will increase by:

$$\left\{\text{Right} : \frac{dx}{dy \cdot dz} \cdot \frac{1}{k_s}; \text{Down} : \frac{dy}{dx \cdot dz} \cdot \frac{1}{k_s}; \text{Up} : \frac{dy}{dx \cdot dz} \cdot \frac{1}{k_s}; \text{Out} : \frac{dz}{dx \cdot dy} \cdot \frac{1}{k_s}; \text{In} : \frac{dz}{dx \cdot dy} \cdot \frac{1}{k_s}\right\}. \quad (3)$$

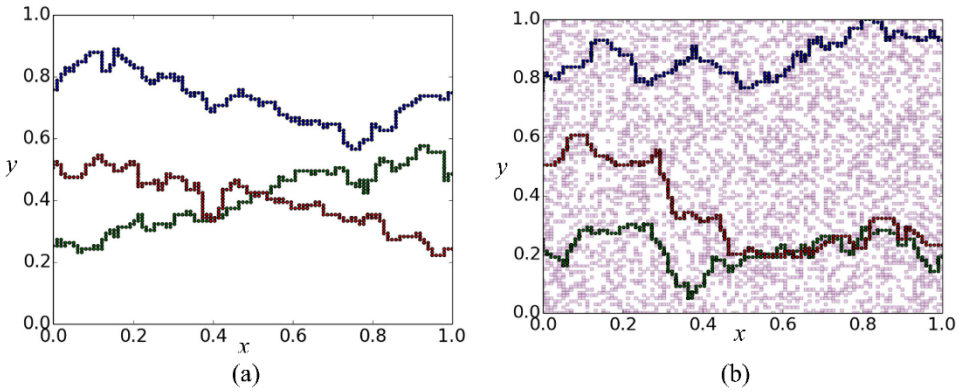

Fig. 5. Two-dimensional traces of three representative random walkers in (a) pure fluid and (b) a porous material with porosity of 0.5 and randomly distributed matrix materials.

Similarly, if the random walker passes the filling material with the conductivity of k_f, the equivalent thermal resistance of the walker will increase by:

$$\left\{\text{Right}:\frac{dx}{dy\cdot dz}\cdot\frac{1}{k_f};\ \text{Down}:\frac{dy}{dx\cdot dz}\cdot\frac{1}{k_f};\ \text{Up}:\frac{dy}{dx\cdot dz}\cdot\frac{1}{k_f};\right.$$
$$\left.\text{Out}:\frac{dz}{dx\cdot dy}\cdot\frac{1}{k_f};\ \text{In}:\frac{dz}{dx\cdot dy}\cdot\frac{1}{k_f}\right\}. \quad (4)$$

After all random walkers reach the $x = 1$ plane, the total stagnant thermal resistance, R_{eff}, and the stagnant thermal conductivity, k_{eff}, of the porous medium are calculated by:

$$\frac{1}{R_{eff}}=\frac{1}{dy\cdot dz}\cdot\frac{1}{R(y,z)}. \quad (5)$$

It should be noted that the stagnant conductivity is underestimated because the average number of steps that random walkers transfer is more than the number of steps if all random walkers transfer from $x = 0$ to $x = 1$ plane in straight lines. Therefore, this model calculates the stagnant thermal conductivity, k_{eff}, using the relative thermal conductivity, k_r, defined as the ratio of simulated conductivities between the given porous media and the pure (matrix or filling) materials. The effective thermal resistance of a given porous media is divided by the thermal resistance of a pure filling material to calculate the relative thermal conductivity:

$$k_r=\frac{k_{eff}}{k_f(\text{or}k_s)}=\frac{\left.\frac{1}{R_{eff}}\right|_{porousmedium}}{\left.\frac{1}{R_{eff}}\right|_{purematerial}}. \quad (6)$$

The thermal conductivities of filling materials, k_f, (or solid matrix, k_s) can be easily measured or found from literature. Consequently, the stagnant thermal conductivity of the porous material, k_{eff}, is calculated using the conductivity of fluid, k_f, (or solid matrix, k_s) and the relative thermal conductivity, k_r. For instance, when the grid number of the three-dimensional computational domain is $400 \times 400 \times 400$, the simulated thermal resistances of Al foam filled with air are 93.95, 3.44, and 1.21×10^{-2} (K·m)/W at the porosity of 1.0, 0.5, and 0.0, respectively. The relative conductivity at the porosity of 0.5, compared with the conductivity at the porosity of 1.0, is 27.3 (93.95/3.44). Using the thermal conductivity of air, 0.0265 W/m/K, and Eq. (6), the stagnant thermal conductivity at the porosity of 0.5 is calculated to be 0.72 W/m/K. It should be noted that the simulated thermal resistance ratio of pure Al to pure air equals to the thermal conductivity ratio of pure air to Al.

3. Model validation

The grid independence study has been conducted by comparing the calculated stagnant thermal conductivities of an Al sphere filled with air when grid numbers changed from $40 \times 40 \times 40$–$400 \times 400 \times 400$. The porosity of the porous material varies between 0.3, 0.4, and 0.5 in Fig. 6. Comparisons in Fig. 6 indicate that variations of the simulated stagnant thermal conductivity are less than 1% when the grid size is more than $160 \times 160 \times 160$. It should also be noted that this model requires minimum computational time. The computational time to simulate a three-dimensional structure with $400 \times 400 \times 400$ mesh size is on the order of one minute using a desktop computer with an Intel® i7-4770 CPU @ 3.4 GHz and 8 GB memory. If not explicitly stated otherwise, the following model results are simulated with the grid number of $400 \times 400 \times 400$. The new model was also validated by comparing simulated stagnant thermal conductivities of Al-air and Al-water systems with various matrix geometries and porosities with data reported in literature.

3.1. Two phases in series or parallel connections

To access the accuracy of the model, this model simulated stagnant thermal conductivities of porous materials with different conductivity ratios between the solid phase and fluid phase at various

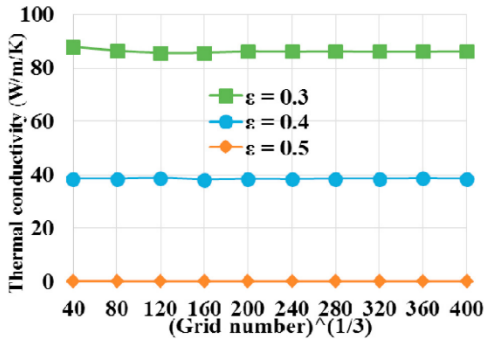

Fig. 6. Grid independence study of spherical Al particles filled with air at various porosities.

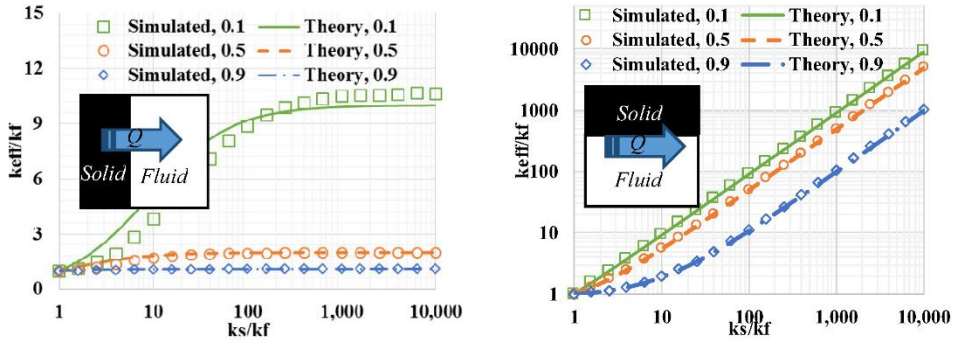

Fig. 7. Comparisons between simulated (markers) and theoretical (lines) stagnant thermal conductivities of solid-fluid systems at various porosities: (a) series and (b) parallel connections.

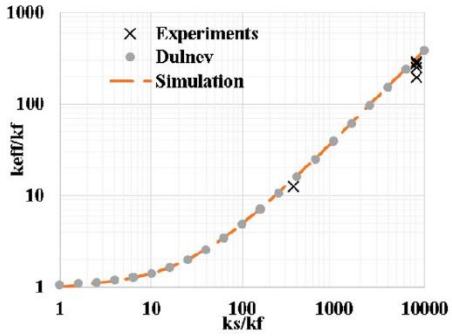

Fig. 8. Comparisons of simulated stagnant thermal conductivity with experimental data [28,34–36] and Dul'nev' model. Porosity equals 0.9 in this simulation.

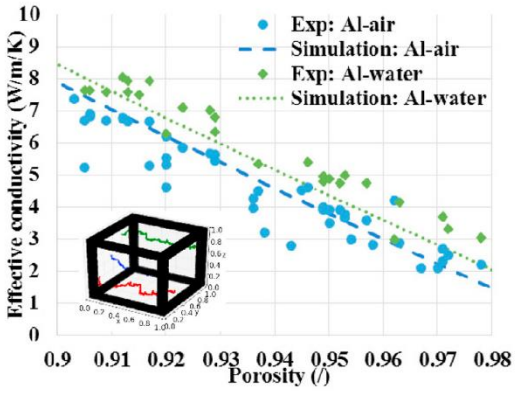

Fig. 9. Comparisons of simulated stagnant thermal conductivity of Al-air system and Al-water system when the Al foams have different porosities. The Al foams are assumed to have cubic frame structure (shown in the inserted plot).

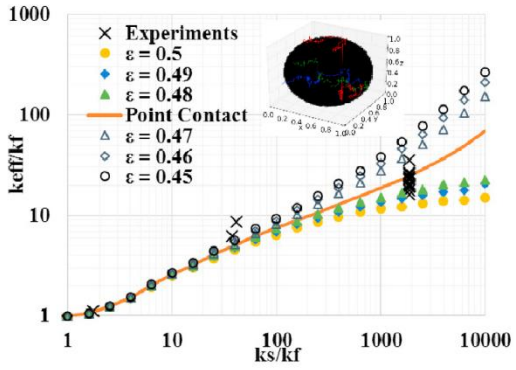

Fig. 10. Sensitivity of the stagnant thermal conductivity of a packed bed on the connectedness of the phase with higher thermal conductivity (solid). The solid matrix of the packed bed has spherical shape (black in the inserted plot).

porosities. These two phases were assumed to connect in series or parallel in order to compare with theoretical thermal conductivities predicted by the following equations for series and parallel connections, respectively:

$$\text{Series}: \quad 1/k_{\text{eff}} = \varepsilon/k_{\text{f}} + (1-\varepsilon)/k_{\text{s}}. \tag{7}$$

$$\text{Parallel}: \quad k_{\text{eff}} = \varepsilon \cdot k_{\text{f}} + (1-\varepsilon) \cdot k_{\text{s}}. \tag{8}$$

It should be noted that the theoretical thermal conductivity of two phases in series connection neglects the heat transfer perpendicular to the heat transfer direction. The random walkers' movements in directions perpendicular to the heat transfer direction (y and z) were prohibited, which was consistent with the theoretical analysis, to derive results in Fig. 7. It could be seen from the figure that the simulated stagnant thermal conductivities of these two phases connected in series or parallel match very well with theoretical values.

3.2. Simplified metal foam

To future validate the model, the stagnant thermal conductivity of metal foams with simplified foam geometry was simulated

using the newly developed random walk approach and compared with experimental data. Dul'nev [26] simplified metal foams into cubic frames with uniform thickness and derived the analytical solution of the stagnant thermal conductivity. This study generated cubic frames (based on the porosity) using Dul'nev's method. Fig. 8 compares the stagnant thermal conductivity of porous media with the porosity of 0.9 and various ratios of k_s/k_f calculated by this model and results generated Dul'nev's model. Fig. 9 compares the stagnant thermal conductivity of Al-air and Al-water systems with various porosities (0.9–0.98). It could be seen from both figures that results calculated by our newly developed model match well with those predicted by Dul'nev's model and experimental data reported in literature [28,34–36].

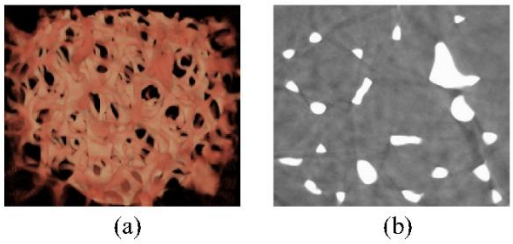

Fig. 11. The (a) three-dimensional view and (b) a two-dimensional slice of an aluminum metal foam sample (25 mm in diameter and 7 mm in height) with the pore size of 10 PPI. The bright color indicates metal.

4. Effect of pore geometry on the stagnant thermal conductivity

After model validation, the model was applied to study porous media with various pore geometries since the stagnant thermal conductivity of porous media is affected by properties of the matrix and filing materials as well as the characteristics of the porous medium such as porosity and connectedness. As indicated by previous studies, although the size of contact area between solid particles is small in packed beds [23], its impact on the stagnant thermal conductivity is significant, especially when the conductivity of the solid matrix is much higher than that of the filling material. This study will investigate porous media with various geometries to quantitatively illustrate the impacts of geometries.

4.1. Spherical matrix material

The stagnant thermal conductivity of a repeating unit of packed beds with different ratios of k_s over k_f was simulated. The packed beds are made from spherical particles filled with fluids (the inserted plot in Fig. 10). The porosity of the packed beds changes around 0.4767 (where these particles just have point contacts). Many studies in literature have experimentally measured stagnant

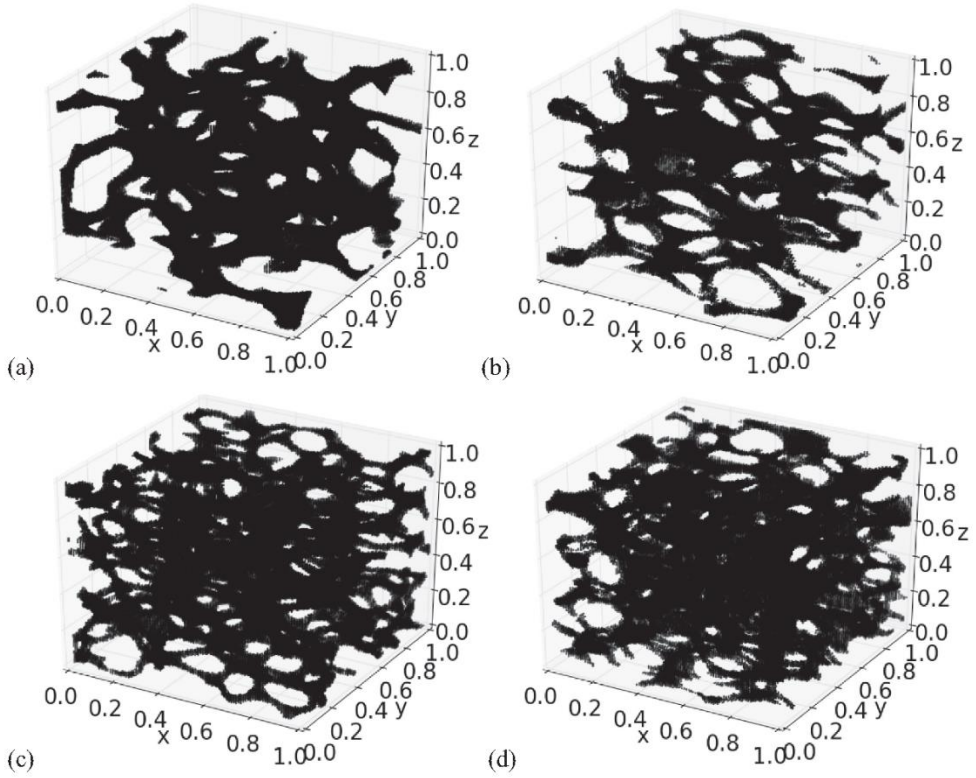

Fig. 12. Reconstructed three-dimensional structures of Al foams with pore size of (a) 5 PPI, (b) 10 PPI, (c) 20 PPI, and (d) 40 PPI on non-dimensional coordination. Their corresponding porosities were measured to be 0.907, 0.899, 0.909, 0.874, respectively.

thermal conductivity of packed beds filled with fluids (glass-air; glass-water; steel-air; steel-water, etc.) [37]. The simulated thermal conductivities at various ratios of k_s/k_f are compared with reported data in literature. It can be seen that the simulations are very sensitive to the porosity which directly determines the connectedness of the solid matrix. When spheres are in perfect point contacts with each other ($\varepsilon = 0.4767$), the ratio of stagnant conductivity to the conductivity of fluid is 68.69 when the conductivity ratio of solid to liquid is 7735.8 (Al-air). The ratio of stagnant thermal conductivity to the conductivity of fluid remarkably decreased to 22.50 when the porosity slightly increased to 0.48. The significant decrease of the stagnant thermal conductivity is due to the disconnection of the solid phase. On the contrary, the ratio of stagnant thermal conductivity to the conductivity of fluid increased to 152.25 when the porosity decreased slightly to 0.47. In this case, the spheres are in area contact instead of point contact (e.g. particles are pressed with high pressures). The better connectedness of the solid phase (which dominates the heat conduction) leads to the significant increase of the stagnant thermal conductivity of the porous medium shown in Fig. 10.

The sensitivity of the results indicates the importance of connectedness of the solid matrix if the conductivity of the solid phase dominants. Therefore, the detailed structure of the porous medium is critical to accurately determine its stagnant thermal conductivity. The statistical nature of this model determines that it can consider all detailed structure of the porous medium without increasing computational time. Therefore, it is a powerful tool to simulate complex pore geometries without simplification or neglecting heat transfer perpendicular to the heat transfer direction. In the following section, the stagnant thermal conductivity of Al foams with various geometries and pore sizes will be simulated to indicate the importance of both of these two parameters.

4.2. Reconstructed metal foam

The above literature review and simulations using our home-developed model indicates that the geometry of the porous media is as important as the porosity and conductivities of the constituent materials to accurately predict the stagnant conductivity of the porous medium. The stagnant conductivity of porous media with the same porosity could be vastly different due to the different pore geometry (or connectedness of the matrix material). The previous model validations and simulations still used simplified geometries such as spheres and cubic frames with various porosity. The model has the capability to simulate the stagnant thermal conductivity of measured pore geometries with any simplifications on their pore geometry. The statistical nature of the random walk model and fact that the model does not require intensive mesh to represent complex geometries of each phase save computational time. Instead of using simplified geometries of the matrix, this study experimentally measured and reconstructed the geometry of the metal foams measured by MicroCT. The stagnant thermal conductivity of Al foams will be directly simulated using pore geometries measured by MicroCT.

In this study, Al foams with different pore sizes, 5, 10, 20, and 40 PPI purchased from ERG Aerospace Corporation were experimentally measured. The stagnant thermal conductivities of ERG's Al foams with different porosities and pore sizes had been experimentally measured by previous studies [9,34,38,39]. Porosities of Al foams with 5, 10, 20, and 40 PPI (measured by Archimedes' principle using water as the fluid) are 0.907, 0.899, 0.909, and 0.874, respectively. MicroCT of cylindrical Al foam samples (with 25 mm in diameter and 7 mm in height) were measured with an Xradia MicroXCT-400 tomographic X-ray microscope. The resolution of the micro CT image is 1 μm. Fig. 11 shows a three-dimensional view and a representative two-dimensional slice (out of 994 slices) of an Al foam sample with the pore size of 10 PPI. The three-dimensional image in Fig. 11(a) was obtained by the image processing software of the X-ray microscope and it was used to validate reconstructed images. We processed (remov-

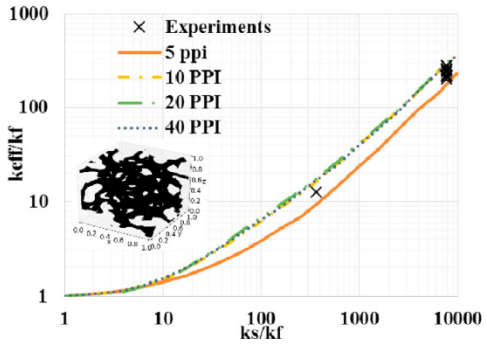

Fig. 14. Simulated stagnant thermal conductivities of Al foams with various pore sizes: 5 PPI, 10 PPI, 20 PPI, and 40 PPI.

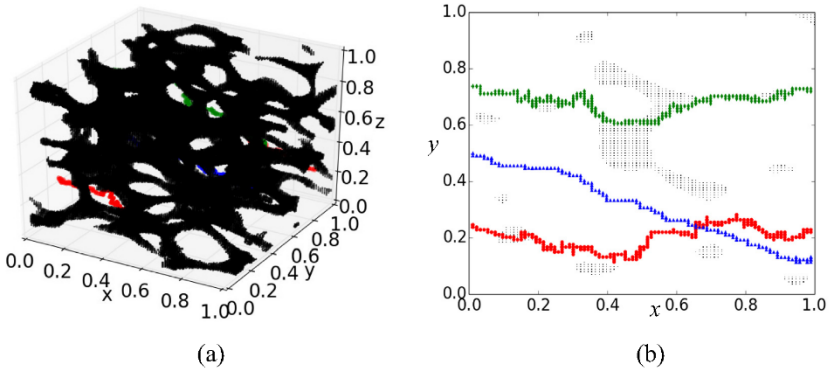

Fig. 13. (a) Reconstructed three-dimensional geometry of the metal foam with 10 PPI measured by MicroCT and traces of three representative random walkers in the computational domain and (b) two-dimensional slice of the geometry and the traces of three representative random walkers.

ing noise and converting images from grayscale to binary) all two-dimensional slices, Fig. 11(b), using home-written codes based on Python 2.7.6. The processed binary data of each slice were exported, read by Intel® Fortran, and reconstructed to three-dimensional computational domain to run the random walk model. Porosities of all reconstructed three-dimensional images matched exactly with measured porosities to guarantee accuracy of the processed images.

Reconstructed three-dimensional geometries of four samples with similar porosities but different pore sizes are shown in Fig. 12. After all three-dimensional structures were reconstructed, geometries of these samples were imported into the validated random walk model to simulate the stagnant thermal conductivities. Fig. 13 shows three-dimensional and two-dimensional (in the $z = 0.5$ plane) traces of three representative random walkers in an Al foam sample with 10 PPI pore size. Since the sample is considered as a representative unit of the porous medium, the random walker re-enters the computational domain once it escapes from either the y plane or the z plane.

The stagnant thermal conductivities of Al foams with different pore sizes and filling fluid are compared with experimental data [9,34,38,39] in Fig. 14. The measured (or interpolated) stagnant thermal conductivity of Al foam saturated with air in literature falls between 4.84 and 8.08 W/m/K when the porosity of Al foam is close to 0.9. The results in Fig. 14 indicates that the stagnant thermal conductivity varies with the pore geometry and pore size, especially at large ratios of solid to liquid thermal conductivities. The simulated stagnant thermal conductivities of Al foam filled with air are 4.86, 7.71, 7.76, and 7.79 W/m/K at the pore size of 5, 10, 20, and 40 PPI, respectively. The simulated results in this study follow similar trend with experimental measurements reported by J.W. Paek et al. [38] that the thermal conductivity slightly decreased when the pore size increased (the porosity keeps unchanged).

5. Conclusion

This study developed a universal predictive model that calculates the stagnant thermal conductivity of porous media considering both the porosity and the pore geometry. The model can simulate either simplified geometries such as sphere, cube, cubic frame that were applied in literature (listed in Table 1) or detailed geometries that are directly measured by imaging technologies such as MicroCT. This model does not need to fit geometric parameters from experiments, does not need to arbitrarily neglect the heat transfer between two different phases, and does not need to neglect the heat flux or heat transfer resistance in certain directions (e.g. directions that are perpendicular to the heat transfer direction). It can be seen from previous results and discussions that this novel model can simulate stagnant thermal conductivity with reasonable accuracy and results match with experimental measurements reported in literature across a wide range of porosity, geometries, and materials. Results also shows that stagnant thermal conductivities of porous materials are sensitive to the connectedness (or contact resistance) of the solid matrix, especially when the conductivity of the solid matrix (Al) is much higher than the conductivity of filling fluid (air). Likewise, if the conductivity of the filling fluid is much higher than that of the solid matrix, the connectedness of the fluid is critical to determine the stagnant thermal conductivity.

The low computational time of this model makes it a unique tool to provide real-time updates of material properties for on-site applications or other computational models. The developed model can also be conveniently applied to porous media filled with multi-phase fluid (e.g. gas/liquid mixtures or liquid/liquid mixtures) or porous media made from composite materials (e.g. metal alloys or other solid mixtures). As long as the geometry of each phase can be measured and reconstructed, the model can accurately predict the stagnant thermal conductivity of the porous medium. Although this model only considers conductive heat transfer and neglects convective and radiative heat transfer, it still has wide applications in porous media without fluid flow or high temperature gradients such as electrodes of electrochemical devices, thermal management systems, geological samples, water percolation process, food processing, fossil fuel recovery, biomechanical devices, and additive manufacturing. Furthermore, this model can be conveniently converted to simulate tortuosity of porous media and predict effective diffusivities of species in porous media.

Acknowledgement

The authors greatly appreciate Dr. Qiang Ye at BERC for providing training on the use of MicroCT equipment.

References

[1] M.A. Mujeebu, M.Z. Abdullah, M.Z.A. Bakar, A.A. Mohamad, M.K. Abdullah, Applications of porous media combustion technology – a review, Appl. Energy 86 (2009) 1365–1375.
[2] A.-R.A. Khaled, K. Vafai, The role of porous media in modeling flow and heat transfer in biological tissues, Int. J. Heat Mass Transfer 46 (2003) 4989–5003.
[3] C.-L. Lin, J.D. Miller, Pore Scale Analysis of Oil Shale/Sands Pyrolysis, vol. 33, University of Utah, 2011.
[4] J.W. Long, B. Dunn, D.R. Rolison, H.S. White, Three-dimensional battery architectures, Chem. Rev. 104 (2004) 4463–4492.
[5] W. Libeer et al., Two-phase heat and mass transfer of phase change materials in thermal management systems, Int. J. Heat Mass Transfer 100 (2016) 215–223.
[6] P. Ranut, On the effective thermal conductivity of aluminum metal foams: review and improvement of the available empirical and analytical models, Appl. Therm. Eng.
[7] R.G. Deissler, J.S. Boegli, An investigation of effective thermal conductivities of powders in various gases, Trans. Am. Soc. Mech. Eng. 80 (1958) 4283517.
[8] W. van Antwerpen, C.G. du Toit, P.G. Rousseau, A review of correlations to model the packing structure and effective thermal conductivity in packed beds of mono-sized spherical particles, Nucl. Eng. Des. 240 (2010) 1803–1818.
[9] E.N. Schmierer, A. Razani, Self-consistent open-celled metal foam model for thermal applications, J. Heat Transfer 128 (2006) 1194–1203.
[10] Y. Yao, H. Wu, Z. Liu, A new prediction model for the effective thermal conductivity of high porosity open-cell metal foams, Int. J. Therm. Sci. 97 (2015) 56–67.
[11] S. Yagi, D. Kunii, Studies on effective thermal conductivities in packed beds, AIChE J. 3 (1957) 373–381.
[12] D. Kunii, J.M. Smith, Heat transfer characteristics of porous rocks, AIChE J. 6 (1960) 71–78.
[13] S. Masamune, J.M. Smith, Thermal conductivity of beds of spherical particles, Ind. Eng. Chem. Fundam. 2 (1963) 136–143.
[14] A.K. Veinberg, Permeability, electrical conductivity, dielectric constant and thermal conductivity of a medium with spherical and ellipsoidal inclusions, Sov. Phys. Dokl. 11 (1967) 593.
[15] C. Beckermann, R. Viskanta, Natural convection solid/liquid phase change in porous media, Int. J. Heat Mass Transfer 31 (1988) 35–46.
[16] R. Krupiczka, Analysis of thermal conductivity in granular materials, Int. Chem. Eng. 7 (1967) 122–144.
[17] R.A. Crane, R.I. Vachon, A prediction of the bounds on the effective thermal conductivity of granular materials, Int. J. Heat Mass Transfer 20 (1977) 711–723.
[18] C. Tien, K. Vafai, Statistical bounds for the effective thermal conductivity of microsphere and fibrous insulation, Prog. Astronaut. Aeronaut. 135–148 (1979).
[19] I. Nozad, R.G. Carbonell, S. Whitaker, Heat conduction in multiphase systems—I, Chem. Eng. Sci. 40 (1985) 843–855.
[20] I. Nozad, R.G. Carbonell, S. Whitaker, Heat conduction in multiphase systems—II: experimental method and results for three-phase systems, Chem. Eng. Sci. 40 (1985) 857–863.
[21] V. Prasad, N. Kladias, A. Bandyopadhaya, Q. Tian, Evaluation of correlations for stagnant thermal conductivity of liquid-saturated porous beds of spheres, Int. J. Heat Mass Transfer 32 (1989) 1793–1796.
[22] P. Zehner, E.U. Schlünder, Thermal conductivity of granular materials at moderate temperatures, Chem. Ingr. Tech. 42 (1970) 933–941.
[23] C.T. Hsu, P. Cheng, K.W. Wong, Modified Zehner-Schlunder models for stagnant thermal conductivity of porous media, Int. J. Heat Mass Transfer 37 (1994) 2751–2759.

[24] C.T. Hsu, P. Cheng, K.W. Wong, A lumped-parameter model for stagnant thermal conductivity of spatially periodic porous media, J. Heat Transfer 117 (1995) 264–269.
[25] K.J. Singh, R. Singh, D.R. Chaudhary, Heat conduction and a porosity correction term for spherical and cubic particles in a simple cubic packing, J. Phys. Appl. Phys. 31 (1998) 1681.
[26] G. Dul'nev, Heat transfer through solid disperse systems, J. Eng. Phys. 9 (1965) 275–279.
[27] M.A. Schuetz, L.R. Glicksman, A basic study of heat transfer through foam insulation, J. Cell. Plast. 20 (1984) 114–121.
[28] V.V. Calmidi, R.L. Mahajan, The effective thermal conductivity of high porosity fibrous metal foams, J. Heat Transfer 121 (1999) 466–471.
[29] K. Boomsma, D. Poulikakos, On the effective thermal conductivity of a three-dimensionally structured fluid-saturated metal foam, Int. J. Heat Mass Transfer 44 (2001) 827–836.
[30] K. Boomsma, D. Poulikakos, The effects of compression and pore size variations on the liquid flow characteristics in metal foams, J. Fluids Eng. 124 (2001) 263–272.
[31] M.A.B. Promentilla, S.M. Cortez, R.A.D. Papel, B.M. Tablada, T. Sugiyama, Evaluation of microstructure and transport properties of deteriorated cementitious materials from their X-ray computed tomography (CT) images, Materials 9 (2016) 388.
[32] P. Salamon, D. Fernàndez-Garcia, J.J. Gómez-Hernández, A review and numerical assessment of the random walk particle tracking method, J. Contam. Hydrol. 87 (2006) 277–305.
[33] P. Magnico, Analysis of permeability and effective viscosity by CFD on isotropic and anisotropic metallic foams, Chem. Eng. Sci. 64 (2009) 3564–3575.
[34] E. Sadeghi, S. Hsieh, M. Bahrami, Thermal conductivity and contact resistance of metal foams - metal foam.pdf, J. Phys. Appl. Phys. 44 (2011) 125406.
[35] E. Bianchi et al., An appraisal of the heat transfer properties of metallic open-cell foams for strongly exo-/endo-thermic catalytic processes in tubular reactors, Chem. Eng. J. 198–199 (2012) 512–528.
[36] M. Fetoui, F. Albouchi, F. Rigollet, S.B. Nasrallah, Highly porous metal foams: effective thermal conductivity measurement using a photothermal technique, J. Porous Media 12 (2009).
[37] F. Gori, C. Marino, M. Pietrafesa, Experimental measurements and theoretical predictions of the thermal conductivity of two phases glass beads, Int. Commun. Heat Mass Transfer 28 (2001) 1091–1102.
[38] J.W. Paek, B.H. Kang, S.Y. Kim, J.M. Hyun, Effective thermal conductivity and permeability of aluminum foam materials, Int. J. Thermophys. 21 (2000) 453–464.
[39] K. Lafdi, O. Mesalhy, S. Shaikh, Experimental study on the influence of foam porosity and pore size on the melting of phase change materials, J. Appl. Phys. 102 (2007) 83549.

Paper P1 Copyright Permission

Regarding Incident 2707455 Request Copyright Permissions

support@services.acs.org

周四 2019/4/25 18:55

收件人:Wang, Fangzhou <fangzhouwang@ku.edu>;

Dear Dr. Wang:

Thank you for contacting ACS Publications Support.

Your permission request is granted and there is no fee for this reuse. In your planned reuse, you must cite the ACS article as the source, add this direct link (https://pubs.acs.org/doi/full/10.1021/acsomega.8b00808) and include a notice to readers that further permissions related to the material excerpted should be directed to the ACS.

I hope this information helped. Please let me know if I can be of further assistance.

Sincerely,

Kryxie J. Ramirez
ACS Customer Services & Information
https://help.acs.org

Incident Information:

Incident #: 2707455
Date Created: 2019-04-25T03:37:45
Priority: 3
Customer: fangzhouwang@ku.edu
Title: Request Copyright Permissions
Description: Hello there,

I am a PhD student from the University of Kansas. As I am preparing my thesis, I hope to request the copyright permission of my first-authored paper.

The detailed information of this paper is shown below.

- https://pubs.acs.org/doi/full/10.1021/acsomega.8b00808
- I want to reuse the entire article for my thesis.
- The entire paper will be placed at the end of the thesis.

I would appreciate if you can give me the reuse permission.

Thank you very much!
Fangzhou Wang
University of Kansas

Paper P2 Copyright Permission

Copyright Clearance Center

Confirmation Number: 11809863
Order Date: 04/24/2019

Customer Information

Customer: Fangzhou Wang
Account Number: 3001354194
Organization: Fangzhou Wang
Email: fangzhouwang@ku.edu
Phone: +1 (785) 505-0588
Payment Method: Invoice

This is not an invoice

Order Details

Journal of power sources

Billing Status: **N/A**

Order detail ID: 71884502
ISSN: 0378-7753
Publication Type: Journal
Volume:
Issue:
Start page:
Publisher: ELSEVIER S.A.

Permission Status: Granted
Permission type: Republish or display content
Type of use: Thesis/Dissertation
Order License Id: 4575541424943

Requestor type	Academic institution
Format	Print, Electronic
Portion	chapter/article
Number of pages in chapter/article	7
The requesting person/organization	Fangzhou Wang
Title or numeric reference of the portion(s)	Discharge Li-O2 batteries with intermittent current
Title of the article or chapter the portion is from	Discharge Li-O2 batteries with intermittent current
Editor of portion(s)	N/A
Author of portion(s)	Fangzhou Wang, Xianglin Li
Volume of serial or monograph	394
Issue, if republishing an article from a serial	N/A
Page range of portion	1-7
Publication date of portion	2018/8/1
Rights for	Main product and any product related to main product
Duration of use	Life of current edition
Creation of copies for the disabled	no
With minor editing privileges	no

For distribution to	Worldwide
In the following language(s)	Original language of publication
With incidental promotional use	no
Lifetime unit quantity of new product	Up to 4,999
Title	Experimental and Numerical Investigations of Wettability of Positive Electrodes for Li–O2 Batteries
Institution name	University Of Kansas
Expected presentation date	May 2019

Note: This item was invoiced separately through our **RightsLink service.** More info **$ 0.00**

Total order items: 1 **Order Total: $0.00**

Paper P3 Copyright Permission

Paper P4 Copyright Permission

Copyright Clearance Center

Confirmation Number: 11809865
Order Date: 04/24/2019

Customer Information

Customer: Fangzhou Wang
Account Number: 3001354194
Organization: Fangzhou Wang
Email: fangzhouwang@ku.edu
Phone: +1 (785) 505-0588
Payment Method: Invoice

This is not an invoice

Order Details

International journal of heat and mass transfer

Billing Status: **N/A**

Order detail ID: 71884504
ISSN: 0017-9310
Publication Type: Journal
Volume:
Issue:
Start page:
Publisher: PERGAMON

Permission Status: Granted
Permission type: Republish or display content
Type of use: Thesis/Dissertation
Order License Id: 4575550204239

Requestor type	Academic institution
Format	Print, Electronic
Portion	chapter/article
Number of pages in chapter/article	14
The requesting person/organization	Fangzhou Wang
Title or numeric reference of the portion(s)	The stagnant thermal conductivity of porous media predicted by the random walk theory
Title of the article or chapter the portion is from	The stagnant thermal conductivity of porous media predicted by the random walk theory
Editor of portion(s)	N/A
Author of portion(s)	Fangzhou Wang, Xianglin Li
Volume of serial or monograph	107
Issue, if republishing an article from a serial	N/A
Page range of portion	1-14
Publication date of portion	2017/4/30
Rights for	Main product and any product related to main product
Duration of use	Life of current edition
Creation of copies for the disabled	no

With minor editing privileges	no
For distribution to	Worldwide
In the following language(s)	Original language of publication
With incidental promotional use	no
Lifetime unit quantity of new product	Up to 4,999
Title	Experimental and Numerical Investigations of Wettability of Positive Electrodes for Li–O2 Batteries
Institution name	University Of Kansas
Expected presentation date	May 2019

Note: This item was invoiced separately through our **RightsLink service.** More info **$ 0.00**

Total order items: 1 **Order Total: $0.00**